Application of a CuBr Laser to the UV Spectroscopy of NaI

by

Wenhua Qin (MSc)

Thesis Submitted for the Degree of Doctor of Philosophy

Department of Physics and Mathematical Physics

University of Adelaide

June 1996

To my wife

Jian Ping

for her love, understanding and continuing support.

Contents

Summary

Many diatomic molecular systems have overlapping potential curves and it is well known that if the electronic states are of the same symmetry then the curves undergo an avoided crossing. Photo-transitions to these states have interesting spectroscopic properties including the Fano profile shapes and very narrow lines above the dissociation limit. This study investigates the non-adiabatic behaviour of such excited states, especially the predissociation of NaI by the ionic-covalent crossing.

A tunable narrow bandwidth (1 GHz) dye laser system pumped by a CuBr laser has been constructed. The frequency doubling of this dye laser radiation to UV was then used to obtain experimental data to investigate the nature of the ionic-covalent crossing of NaI. The high resolution absorption measurements show that the spectrum consists of many more band fragments than that observed with the excitation measurements. Lines in the absorption spectrum of NaI have been assigned and analyzed for the first time. Together with absorption strength determination, this data has been used to demonstrate an inconsistency in the presently accepted molecular potentials. Suggestions for resolving this conflict are presented.

Theoretical investigation was carried out on resonance structure in spectra, including resonance positions, widths and intensities, corresponding to different parameters of the potential surfaces and the coupling strength. Numerical solution of the Schrödinger equations and the complex scaling method were used to investigate the non-adiabatic behaviour of the excited states of diatomic molecules and the model was compared with the results of a semiclassical calculation. Using the assumption that the change of resonance structure from the diabatic to adiabatic limit as the coupling strength increases is smoothly continuous and that the contribution to the resonant state can be considered as part diabatic and part adiabatic, a maximum internal amplitude method is proposed for the location of resonance position and width for a two channel curve crossing system. This technique was used successfully to demon-

strate how resonance structure changes from diabatic to adiabatic limit as the coupling strength changes for a set of model potential curves. The method gives an improved understanding of the origin of the resonance changes in a curve crossing system.

Statement of Originality

This Work contains no material which has been accepted for the award of any other degree or diploma in any university or other tertiary institute and, to the best of my knowledge and belief, contains no material previously published or written by another person, except where due reference has been made in the text.

I give consent to this copy of my thesis, when deposited in the University Library, being available for loan and photocopying.

Signed:..... Wenhua Qin (M.Sc.)

Date:.....6/96..... June, 1996

Acknowledgments

It is with sincere appreciation that I thank my supervisor, Dr. Donald McCoy, for his expert guidance, invaluable ideas, continual encouragement and deep interest in all aspects of this research.

Discussions with Dr. Lee Torop and Dr. Alastair Blake were of much value and were greatly appreciated.

I would also like to thank Mr. Peter Davis, Managing Director of Norseld Pty. Ltd., for his continuing support for providing the CuBr laser tubes and other laser facilities as well as financially supporting the last year of this study.

I am indebted to Dr. J. Wang for providing her original program of optimization and for solving the coupling equation; to Dr. G. Liu for his recommendation of the graph program which was used to produce the diagram in this thesis.

I would also like to thank Mr. R. Nation for his friendly and effective technical assistance and advice; Mr. E. Hirsch for translating German literatures; Mr. R. Leeve (Norseld Pty. Ltd.) for making the NaI cell; Mr. M. Shorthose and Mr. J. Smith (Electronics Services), Mr. J. Schache and Mr. G. Eames (Student Workshop), Mr. M. Ferraretto (Computer Officer) for their technical assistance and advice.

I would also like to thank Mr. P. Foster for proof reading part of the thesis and useful discussion.

Finally I would like to thank my parents for their encouragement.

Financial support during this research was provided by a University of Adelaide Postgraduate Research Scholarship.

List of Symbols

A_{ij}	Einstein coefficient
A_{int}	electronic coupling strength
B	rotational constant
B_{ij}	Einstein coefficient
Bz	Boltzmann factor
c	speed of light
E	energy
E_i	energy level
e	electronic charge
F_{ij}	motion coupling strength
FC	Franck-Condon factor
G_{ij}	motion coupling strength
g	statistical weight
H	Hamiltonian
h	Planck's constant
$\hbar$	$= h/2\pi$
h_x	electronic coupling strength
I	intensity
J	total angular momentum (rotational quantum number)
k	Boltzmann's constant
k	wave vector
L	cavity length
l	litre
l_g	length of the illumination part of the grating
M	Molar
M	mass of nucleus

m	mass of electron
N	population
N_x	quantum number function
P_{ij}	transition rate
P	possibility
P	power
P	amplitude of semiclassical wavefunction
Q	partition function
R	branch parameter
R	radius of mirror
r	internuclear separation
r_e	equilibrium position of potential curve
r_x	crossing point
S_J	Hönl-London factor
T	absolute temperature
T	time
t	time
V	potential energy
V_{ij}	electronic coupling strength
v	vibrational quantum number
W	watt
w	beam radius
w	width
x	mixing parameter
x	collective electronic coordinates
Y_{ij}	Dunham parameters
α	phase
β	phase

Γ	line width
λ	wavelength of radiation
μ	reduced mass
ν	frequency of radiation
Ω	total electronic angular momentum
ρ	energy density of photon
σ	absorption cross section
Σ	electronic state with $\Lambda = 0$
ξ	$= (r - r_e)/r_e)$
$\varphi(x\|r)$	wavefunction for electronic motion
$\chi_i(r)$	wavefunction for nuclear motion
Ψ	molecular wavefunction

Super- and sub-script

i,j,k,n,m	iteration index
1,2,+,−	identifies components of a paired quantity
$'$	first derivative
$''$	second derivative
a	adiabatic representation
d	diabatic representation
b	bound state
c	continuum state
e	electron
+	adiabatic upper state
−	adiabatic lower state
$'$	upper state in a transition
$''$	lower state in a transition

Chapter 1

Introduction

1.1 Introduction

Much of our knowledge about the structure of atoms and molecules is based on spectroscopic investigations. Information on molecular structure may be derived in various ways from the absorption or emission spectra generated when electromagnetic radiation interacts with the molecules.

In molecular physics, the enormous mass difference between nuclei and the electron implies a much faster motion of electrons than that of the nuclei. This allows the assumption to be made that the electronic motion is separable from that of the nuclei. Thus the electronic motion can be described by the electronic Hamiltonian and electronic wavefunctions for fixed nuclear positions. This is the so-called Born-Oppenheimer approximation (Born and Oppenheimer, 1927). In the Born-Oppenheimer approximation, the nuclei move along the adiabatic electronic potential curves representing the variation of the effective potential energy of the nuclei in different electronic states such that each electronic state is characterized by a definite potential curve. Detailed analysis of the spectroscopic structure allows a better understanding of these potential curves and therefore of the molecular structure. If adiabatic

potential curves with the same symmetry approach with changing internuclear separation, they will exhibit an avoided crossing according to the non-crossing rule (von Neumann and Wigner 1929, Landau and Lifschitz 1958). However, it has been found that the avoided crossing phenomena can cause a break down of the Born-Oppenheimer approximation showing that non-adiabatic behaviour can become significant. Transitions occur between the two adiabatic states which are described by the Landau-Zener non-adiabatic transition probability P_{LZ}. (Landau 1932(a), (b) and Zener 1932).

If one of the non-crossing pair of potential curves supports a bound state for nuclear motion and the other a near energy continuous state, the molecules initially prepared in the bound state will decay into the continuous state due to non-adiabatic transitions between the two adiabatic states. This is called predissociation. It has been shown that in such cases the molecular system is better described by electronically coupled states in the diabatic representation (O'Malley, 1971). The diabatic potential curves cross at the location of the avoided crossing in the adiabatic representation. Fig. 1.1(i) gives a typical example, taken from potential curves of NaI, where the dotted lines represent the non-crossing adiabatic states. For the same total energy, if the electronic coupling between the two crossing diabatic states is strong, then the Born-Oppenheimer approximation is valid and the upper adiabatic state is a bound state. If the electronic coupling is very weak, the Born-Oppenheimer approximation completely breaks down, the molecular system behaves diabatically and the upper state leads to a continuous spectrum.

Interesting cases arise for intermediate coupling between the two electronic states when there are quasi-bond states which predissociate. These states are neither adiabatic nor diabatic. The resonance structures of these states may vary from very sharp lines to very broad lines. The complexity of the spectrum and the discontinuous rotational line progression between bands makes it very difficult to determine the spectroscopic constants from the experimental data. In the case of NaI, this complexity is

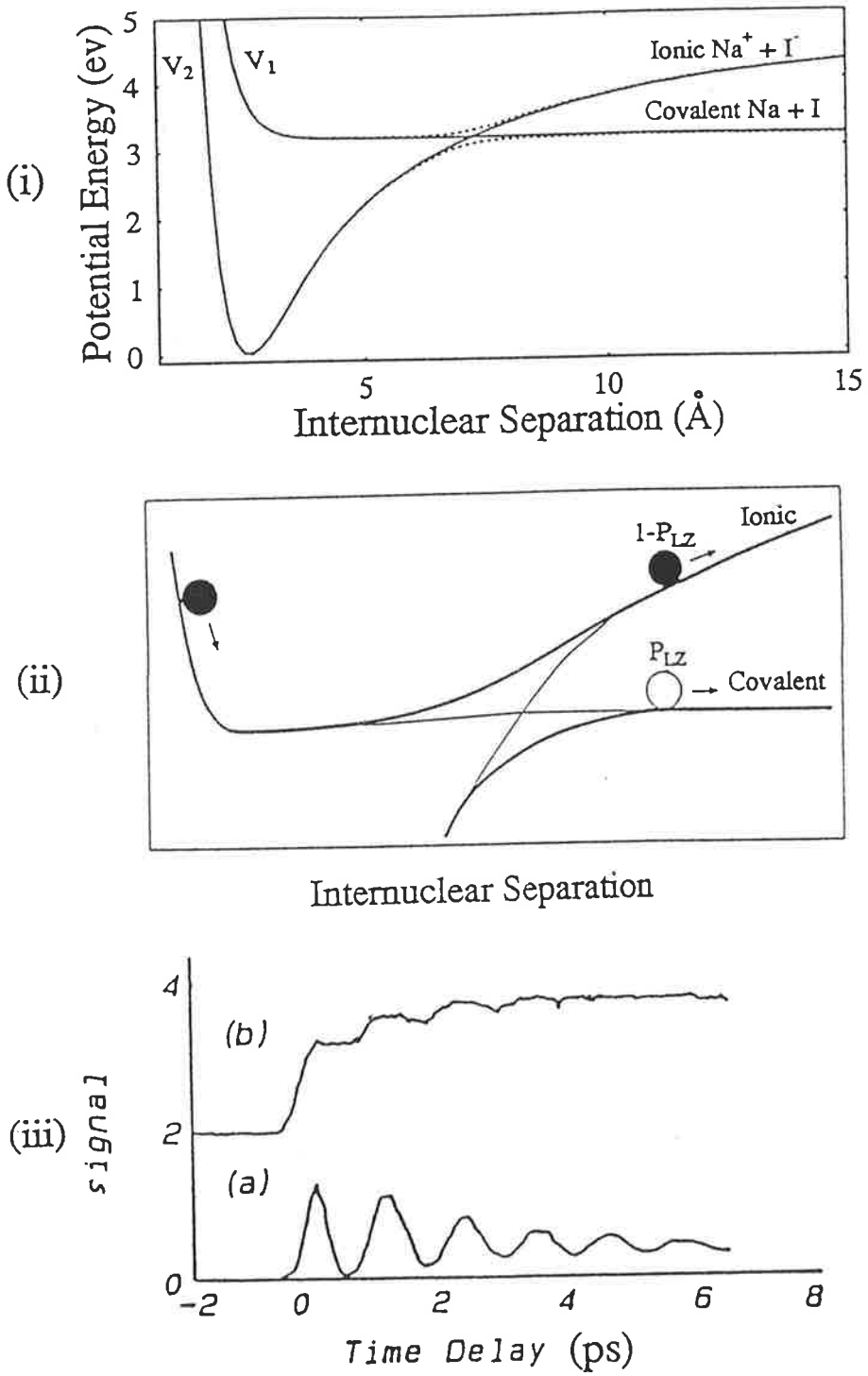

Figure 1.1: (i) Some potential curves of NaI with an avoided crossing; (ii) the classical description of the dynamics in the avoided crossing region; and (iii) the FTS experimental results on the NaI transition states (a) and free Na atoms (b).

further compounded by the high temperature of the vapour used in the experiment.

1.2 Spectroscopic Investigation on NaI

Diatomic alkali halide molecules have been the subject of numerous experimental and theoretical investigations. Their ground states are $^1\Sigma^+$ ionic states consisting of an alkali metal positive ion and a halide negative ion while each low excited state is a covalent state consisting of alkali and halide atoms. The lowest optically accessible excited states are $\Omega = 0^+$ and 1 states. Much of the interest in these systems derives from the fact that the 0^+ state and the $^1\Sigma^+$ state have the same character and the two adiabatic potential curves display an avoided crossing with an interchange of ionic and covalent character.

NaI is the most interesting of the alkali halide molecules because its low excited states display a bound character and give rise to a very dense line structure in the absorption spectrum from ultraviolet to visible (Berry 1979). None of the other alkali halide molecules show this absorption line structure.

Using a classical picture, Berry (1957) described the behaviour of alkali halide molecule as follows: The absorption of light carries the molecular system vertically from the ground state to an excited state and produces a change in the electronic wave function corresponding to the transfer of an electronic charge along the internuclear axis from the halide to the metal. The nuclei then move apart across the relatively flat region of potential energy toward the crossing point. As the crossing region is reached, there are two possibilities for the behaviour of the molecule, as seen in Fig. 1(ii). The molecule may retain its electronic character as it moves further apart and dissociate into free alkali and halide atoms with the Landau-Zener probability P_{LZ}, or it can remain in the same adiabatic state and change character with the probability of $(1 - P_{LZ})$. In the second case the electronic wavefunction re-adjusts itself, and

effectively, an electron jumps back from the metal to the halogen. When this occurs electrostatic forces are rapidly set up which pull the nuclei back toward each other. As the nuclei pass the crossing point again, there will be another $(1 - P_{LZ})$ possibility that the electron returns to the metal, and the two particles, now neutral, come together once more. The molecule in the excited state will oscillate in this way until it dissociates or fluoresces as discussed later.

Time-resolved spectroscopy on a femtosecond time scale allows direct observation of such nuclear motion on a potential energy surface. Recently Rose et al (1988, 1989) have applied this technique to study the predissociation dynamics of molecular systems, especially NaI. Fig. 1(iii) gives a typical picture of the time evolution in such an experiment. A pump laser pulse places the NaI molecules in the excited state. The molecular system will then oscillate in the way described above. A second probe laser pulse, after an adjustable delay, monitors the formation of Na product. When the probe pulse is tuned on resonance with the Na D-line it probes the population of free Na atoms from dissociation. When tuned to off resonance, the probe pulse detects the population of the perturbed Na atoms still trapped in the "transition state" ([Na...I]) where the internuclear distance is large. The oscillation of NaI molecules trapped in the adiabatic state was then monitored until they eventually dissociate into free Na and I atoms. The experimental observations are shown in Fig. 1.1(iii) where the time series has a damped oscillatory structure, whose damping frequency reflects the motion of the wave packet in the excited state and the damping reflects predissociation rate. This femtosecond "transition state" spectra (FTS) is a new tool for the spectroscopic study of transition processes and allows direct measurement of the wave packet evolution, potential width, the Landau-Zener parameter and thus the electronic coupling strength.

Although NaI has received extensive experimental and theoretical study, there is still very limited information about the excited states. Several authors have at-

tempted to obtain information about the potential curves for the excited state. However the currently published potential curves cannot explain all the experimental data and do not agree with each other within the experimental errors. Analysis of the absorption spectrum was plagued by its high density of lines and the discontinuous band fragments. On the other hand, the broad band nature of the femtosecond pulses limits the energy resolution of the FTS technique to perform accurate analysis of the potential curves.

Extensive study of the absorption spectrum over a broad wavelength region was reported by Davidovits and Brodhead in 1967 on NaI and they presented a potential curve which covers the transitions to the $\Omega = 1$ state as well as 0^+ state.

Van Veen et al (1981) distinguished between absorption into the 0^+ and 1 state using the photo-fragmentation spectroscopy method for wavelengths between 300–334 nm and derived the potential curves for these two states.

In a UV laser spectroscopy investigation, Schaefer et al (1982, 1984) measured the fluorescent excitation spectrum of NaI which is simpler than the absorption spectrum, and 28 rotational band fragments were analyzed and assigned using the early version of Child's semiclassical theory (Child, 1976, 1991(a)). The observed energy levels were then fitted to the Dunham series for the upper adiabatic bound state and the $X^1\Sigma^+$ diabatic bound state. The result of the best fit with a minimum standard deviation was used to assign the vibrational quantum numbers and the corresponding Dunham parameters were used to calculate the vibrational energy levels and their rotational constants outside the observed energy region. Potential curves were constructed based on these calculated values with the RKR method (Schaefer et al, 1984). However, the location of the upper state potential curve relys on the accuracy of the lower vibrational states that were not measured but proposed from theoretical extrapolation of the Dunham parameters found from a limited region of the spectrum at much higher energy. The extrapolation would be expected to produce large errors at the

lower energy region of the potential curve. This may be the reason that their upper state potential curve locates at a smaller internuclear distance than that of van Veen et al (1981) with a discrepancy cannot be explained with experimental errors.

Telle and Tambini (1989) noted a controversy in the relative position of the 0^+ state and 1 state. They found that the 0^+ potential curve given by Schaefer et al (1984) actually lies below that of the 1 state derived from the experimental data of Davidovits and Brodhead (1967) which contradicts the measurement of van Veen et al (1981) and the theoretical studies of Zeiri and Balint-Kurti (1983) that the 0^+ state lies above the 1 state for alkali halide molecules. Their investigation, however, was unable to clarify the controversy.

Wang et al (1990) questioned the potential curves of Schaefer et al (1984) and suggested that they indicate an electronic coupling strength between the two diabatic states about 4 times bigger than that of their own estimation in deriving the potential curves. They then presented analytical expressions for the $^1X\Sigma^+$ and $A0^+$ diabatic states of NaI to fit the term energies given by Schaefer et al with a numerical optimization procedure. The resulting 0^+ potential curve is in good agreement with that given by van Veen et al although the B values for both potential curves are slightly smaller than that of the potential curve given by Schaefer et al.

Most of the work of this thesis is aimed at investigating the controversy discussed above and to derive a more accurate potential curve which is consistent with the known facts.

1.3 This Study

A general description of the quantum mechanical and semiclassical theory for analyzing predissociation caused by the crossing of two diabatic electronic potential curves having the same symmetry is presented in Chapter 2. Particular attention will be given

to the breakdown of the Born-Oppenheimer approximation, the adiabatic and diabatic description of molecular systems, the solution of the coupled equations, Child's semi-classical theory for predissociation and the complex scaling method to locate resonance positions and widths.

A high resolution tunable UV laser was designed and set up to carry out a spectroscopic absorption investigation of NaI. Details of the principle and performance of the laser system are given in Chapter 3. This UV laser facility uses a CuBr laser to pump a folded cavity dye jet laser system containing a grazing incidence grating dye oscillator and an external amplifier employing a dye jet. The band width of the dye laser is about 1 GHz. A BBO crystal is used to frequency double the visible laser radiation to the ultra-violet for the experiment.

Chapter 4 gives a general description of the spectroscopic characters of NaI. A modification of the numerical optimization program of Wang et al (1990) was employed to fit analytical potential curves to the spectroscopic data given by Schaefer et al (1984) and to optimize the Dunham parameters so that the position of sharp lines of the observed rotational band fragments occur in better coincidence of the hypothetic diabatic and adiabatic levels. Chapter 5 reports measurements of the high resolution absorption spectrum with the tunable UV laser described in Chapter 3. The spectrum is then analyzed with Child's semiclassical theory and the Dunham parameters presented by Schaefer et al (1984). The analysis extracts new information about the position of the excited state potential curve and found that a departure from the excited state potential curve given by Schaefer et al (1984) is necessary to account for the absorption spectrum. A new potential curve is then derived which is consistent with the observed results.

In the last Chapter, a theoretical investigation on resonance structures, including resonance positions, widths and intensities, corresponding to different parameters of the potential surfaces and the coupling strength is presented. Semiclassical scatter-

ing theory, numerical solution of the coupled Schrödinger equations and the complex scaling method were used to investigate the non-adiabatic behavior of a crossing system. This study has successfully demonstrated how resonance structure changes from diabatic to adiabatic limit as the coupling strength changes for a model potential curves of MgH and is an aid to understanding the origin of the resonance behaviour in a curve crossing system.

Chapter 2

Predissociation of Diatomic Molecule by Curve Crossing

2.1 Introduction

Predissociation induced by the crossing of two diabatic potential curves is of very frequent occurrence in diatomic molecules. The coupling of the vibrational levels of an excited electronic state to a vibrational continuum will cause broadening and shift of the energy levels. The level shifts are of about the same order as the broadening and may be difficult to observe. The widths of the resonance show very strong variations. They may vanish at some special positions and become very broad at some others (Child, 1991). When the width is broad, some of the lines may overlap and become unresolvable so that in general one may find sharp lines, broad lines and continuous regions in the absorption spectrum. The complexity of the spectrum and the discontinuous line progression between band fragments makes it very difficult to analyze the observed spectrum. Over many years, the nature of this coupling has attracted much interest with the aim of understanding its quantum mechanical properties.

The basic idea of the quantum mechanical description of a molecular problem

is to take advantage of the enormous mass difference between nuclei and the electrons which implies a much slower motion for the nuclei with respect to the electronic motion in low energy molecular physics. From this one can assume that the electronic motion is separable from the nuclear motion and atoms move along adiabatic electronic potential energy curves. This is the well known Born-Oppenheimer approximation (Born and Oppenheimer 1927) which has been at the foundation of molecular physics for decades. In the Born-Oppenheimer approximation if two potential curves of the same symmetry come close together they will exhibit an avoided crossing according to the non-crossing rule (von Neumann and Wigner 1929, Landau and Lifschitz 1958). This corresponds to an intuitive picture of a fast moving electronic cloud adiabatically adjusting to the slowly moving nuclei. Although this model is generally successful, such an approximation can fail in some cases when the adiabatic electronic potential curves exhibit an avoided crossing, suggesting that nonadiabatic behavior must be considered. It has been shown that diabatic states have proved to be extremely useful in the interpretation of the nonadiabatic behavior (O'Malley 1971, Whetten et al 1985, Balint-Kurti and Shapiro 1985, Torop et al 1987, Kirby and Dishoeck 1988, Wang 1989).

2.2 Adiabatic and Diabatic Representation

In quantum mechanics a molecular system is described by the solution of the Schrödinger equation

$$(H - E)\Psi = 0. \tag{2.1}$$

The much slower motion of nuclei with respect to the electronic motion due to their enormous mass difference make it possible to separate the nuclei kinetic energy operator T_r from the rest of the Hamiltonian H_e (O'Malley, 1971):

$$H = T_r + H_e. \tag{2.2}$$

For non-rotating diatomic molecule T_r is given by:

$$T_r = -\frac{\hbar^2}{2\mu}\frac{d^2}{dr^2} \tag{2.3}$$

with $\mu = m_a m_b/(m_a + m_b)$ the reduced mass of the nuclei and r the internuclear distance. H_e is then the electronic Hamiltonian:

$$H_e = \sum_i^N \left(-\frac{\hbar^2}{2m_e}\nabla_i^2 - \frac{Z_a e^2}{x_{ia}} - \frac{Z_b e^2}{x_{ib}} + \sum_{j\neq i}\frac{e^2}{x_{ij}} \right) + \frac{Z_a Z_b e^2}{r} \tag{2.4}$$

where the sum is over all N electrons, m_e is the electron mass, Z_a and Z_b are the nuclear charges of the nuclei a and b, and x_{ia}, x_{ib}, x_{ij} are the distances of electron i from nuclei a, b, and electron j respectively.

For a basis set of the electronic Hamiltonian $\{\phi_i(x : r)\}$, where x denotes all the electronic coordinates, the full wave function for a non-rotating diatomic molecule can be expanded in the basis set each multiplied by a nuclear motion wave function $\chi_i(r)$ as

$$\Psi(x, r) = \sum_i \phi_i(x : r)\chi_i(r) \tag{2.5}$$

Substituting into Eq. (2.1) and multiplying both side on the left by ϕ_i^* in turn and integrating over all the electronic coordinates give (O'Malley, 1971):

$$(T_r + G_{ii} + V_{ii}(r) - E)\chi_i(r) = -\sum_{j\neq i}(V_{ij} + F_{ij} + G_{ij})\chi_j(r) \tag{2.6}$$

which is the formal set of coupled equations for the nuclear wave functions, where

$$V_{ij}(r) = < \phi_j|H_e|\phi_i > \tag{2.7}$$

$$F_{ij} = -2(\hbar^2/2\mu) < \phi_i|\nabla_r|\phi_j > \cdot\nabla_r \tag{2.8}$$

$$G_{ij} = (\hbar^2/2\mu) < \phi_i|\nabla_r|\phi_j > . \tag{2.9}$$

The diagonal matrix elements of the electronic Hamiltonian H_e are the electronic potential curves. The electronic coupling terms V_{ij} $(i \neq j)$ are the electronic couplings of the electronic states and F_{ij} and G_{ij} represent the kinematic coupling of nuclear and electronic motions. There are two possible choices of the basis set to represent the adiabatic or diabatic behavior of the molecular states which be described in the following sections.

2.2.1 Adiabatic representation

In the adiabatic representation, the basis set is chosen to be the electronic eigenfunctions ϕ_i^a of the electronic Hamiltonian H_e satisfying the eigenvalues equation

$$H_e|\phi_i^a>=E|\phi_i^a> . \tag{2.10}$$

In this case $V_{ij}^a =< \phi_i^a|H_e|\phi_j^a >$ are diagonal and the adiabatic electronic potential curves undergo an avoided crossing if they have the same symmetry in accordance with the non-crossing rule. The basis set $\{\phi_i^a\}$ constitutesthe adiabatic representation of the electronic molecular states. The coupled equations for the nuclear wave function Eq. (2.6) become

$$(T_r + G_{ii} + V_{ii}^a(r) - E)\chi_i^a(r) = -\sum_{j\neq i}(F_{ij} + G_{ij})\chi_j^a(r). \tag{2.11}$$

For low-lying molecular bound states, the motion coupling terms G_{ij} and F_{ij} are generally very small and can be neglected so that the nuclei move as if in a static field of electronic charge. That is, the electrons are considered to move so rapidly compared with the nuclear motion that their effect on the nuclei is a spatial distribution of the electronic cloud which depends on the relative position of the nuclei and the energy of the electronic state, but does not depend on the details of the electron dynamics. This results in the Born-Oppenheimer approximation and the set of uncoupled Schrödinger equations

$$(T_r + V_{ii}^a(r) - E)\chi_i^a(r) = 0. \tag{2.12}$$

The electronic energy eigenvalue $V_{ii}^a(r)$ becomes the potential energy for nuclear motion. Because the adiabatic states $\phi_i^a\chi_i^a$ are uncoupled, they are stationary states and give an excellent description of the ground and low-lying electronic states of molecules.

However in some cases, especially when the two potential curves of the same symmetry come close together and undergo an avoided crossing, the motion coupling terms may become large in the avoided crossing region and induce strong transitions

between the adiabatic molecular states known as nonadiabatic transitions. In such a situation the adiabatic description of molecular states as stationary states becomes invalid in the regions of strong nonadiabatic coupling.

2.2.2 Diabatic representation

Another choice of the basis set is one that makes the motional coupling (G_{ij} and F_{ij}) zero and then the off diagonal electronic coupling matrix elements ($V_{ij}^d =< \phi_i^d|H_e|\phi_j^d >$) are non zero. Thus, the electronic wavefunctions are not eigenvalues of H_e. Such a basis set forms the diabatic representation of the electronic states and the diabatic coupled equations, from Eq. (2.6), are

$$(T_r + V_{ii}^d(r) - E)\chi_i^d(r) = -\sum_{j\neq i} V_{ij}^d(r)\chi_j^d(r) \tag{2.13}$$

where the superscript 'd' denotes the diabatic representation. The two diabatic electronic potential curves cross in the region where the adiabatic potential curves suffer an avoided crossing. The nonadiabatic transitions between the molecular states are caused by the configuration interaction, represented by the off-diagonal matrix elements V_{ij}^d as shown in Eq. (2.13).

Although setting the motion coupling terms G_{ij} and F_{ij} to zero does not provide an acceptable general definition of diabatic electronic states (Torop et al, 1987), it can be taken at least as an adequate approximation for the current study. In practice the diabatic representation has been proved to be extremely useful in the interpretation of experimental results concerning the non-adiabatic behavior.

2.2.3 Coupled equations for two states problems

Usually, in curve crossing problems, only two interacting states are involved or only the interaction between two states are considered important because of their energy

separation from other states. Therefore, the following study will focus on the two state problem where the diabatic coupled equations become

$$\begin{aligned}\left(-\frac{\hbar^2}{2\mu}\frac{d^2}{dr^2}+V_{11}^d(r)-E\right)\chi_1^d(r) &= -V_{12}^d(r)\chi_2^d(r)\\ \left(-\frac{\hbar^2}{2\mu}\frac{d^2}{dr^2}+V_{22}^d(r)-E\right)\chi_2^d(r) &= -V_{21}^d(r)\chi_1^d(r).\end{aligned} \tag{2.14}$$

Since the diabatic and adiabatic electronic wavefunctions both form a complete set and the quantum mechanics requires that they are orthogonal, it is possible to write the adiabatic electronic wave functions as a linear combination of the diabatic electronic wave functions and vice versa. The transformation between the diabatic and adiabatic electronic wave function has the form of (Torop et al 1987)

$$\begin{aligned}\phi_1^a &= \phi_1^d cos\theta + \phi_2^d sin\theta\\ \phi_2^a &= -\phi_1^d sin\theta + \phi_2^d cos\theta\end{aligned} \tag{2.15}$$

where θ is defined as

$$\theta = \frac{1}{2}tan^{-1}\left(\frac{V_{11}^d(r)-V_{22}^d(r)}{V_{12}^d(r)}\right) \tag{2.16}$$

which changes rapidly in the crossing region. With such a transformation the adiabatic nuclear motion coupling matrix can be calculated and the adiabatic coupling Eq. (2.11) can be written as

$$\begin{aligned}\frac{\hbar^2}{2\mu}\left(-\frac{d^2}{dr^2}+V_{11}^a(r)+\frac{\hbar^2}{2\mu}(\frac{d\theta}{dr})^2-E\right)\chi_1^a(r) &= -\frac{\hbar^2}{2\mu}\left(\frac{d^2\theta}{dr^2}+2\frac{d\theta}{dr}\frac{d}{dr}\right)\chi_2^a(r)\\ \frac{\hbar^2}{2\mu}\left(-\frac{d^2}{dr^2}+V_{22}^a(r)+\frac{\hbar^2}{2\mu}(\frac{d\theta}{dr})^2-E\right)\chi_2^a(r) &= \frac{\hbar^2}{2\mu}\left(\frac{d^2\theta}{dr^2}+2\frac{d\theta}{dr}\frac{d}{dr}\right)\chi_1^a(r).\end{aligned} \tag{2.17}$$

The relationships between the diabatic and adiabatic nuclear wave function and potential curves are:

$$\begin{aligned}\chi_1^a &= \chi_1^d cos\theta + \chi_2^d sin\theta\\ \chi_2^a &= -\chi_1^d sin\theta + \chi_2^d cos\theta,\end{aligned} \tag{2.18}$$

and

$$\begin{aligned}V_{11}^a &= \frac{1}{2}\left(V_{11}^d+V_{22}^d+\sqrt{(V_{11}^d-V_{22}^d)^2+4V_{12}^2}\right)\\ V_{22}^a &= \frac{1}{2}\left(V_{11}^d+V_{22}^d-\sqrt{(V_{11}^d-V_{22}^d)^2+4V_{12}^2}\right).\end{aligned} \tag{2.19}$$

Eq. (2.19) also imply that the diabatic coupling term $V_{12}^d(r)$ has a significant contribution to the adiabatic potentials only around the crossing region. The minimum

separation between the two adiabatic potential curves locates the internuclear distance where the diabatic potential energy curves cross and is equal to $2V_{12}^{d}(r_x)$. Sometimes the adiabatic potentials are denoted as V_+ and V_- for the upper (V_{11}^{a}) and lower (V_{22}^{a}) potential curves. For convenience the superscript d for the electronic Hamiltonian matrix elements and the nuclear wavefunctions will be neglected in the following discussion.

Examples for the changes of the diabatic (solid lines) and adiabatic (dotted lines) potential curves, θ, $\frac{d\theta}{dr}$, and $\frac{d^2\theta}{dr^2}$ as a function of the internuclear distance for NaI and KI are shown in Fig. 2.1 based on the values given by Rittner (1951) except the coupling strength used for the adiabatic potential curves are 5 times stronger than the actual value to emphasis the noncrossing region.

Rotational effect

There are two additional modes of motion in a diatomic molecule which do not occur for atoms. One is that the nuclei can vibrate relative to each other through the internuclear axis which has been described in Chapter 1. The potential curves represent the potential energy of such vibration. The other is that the molecule can rotate as a whole about an axis passing through the center of gravity and, in most cases especially for large J, perpendicular to the internuclear axis. To account for the rotational motion of the nuclei, an extra energy term $\frac{J(J+1)\hbar^2}{2\mu r^2}$ is added to the potential energy:

$$V(r) = V_0(r) + \frac{J(J+1)\hbar^2}{2\mu r^2} \tag{2.20}$$

where $V_0(r)$ is the potential energy with no rotation and J is the rotational quantum number. This extra term is associated with the centrifugal force due to the rotational angular momentum (Herzberg 1950 p.426).

Numerical methods for obtaining solution of bound state or coupled channel Schrödinger equations have been developed and used over many years. Among them

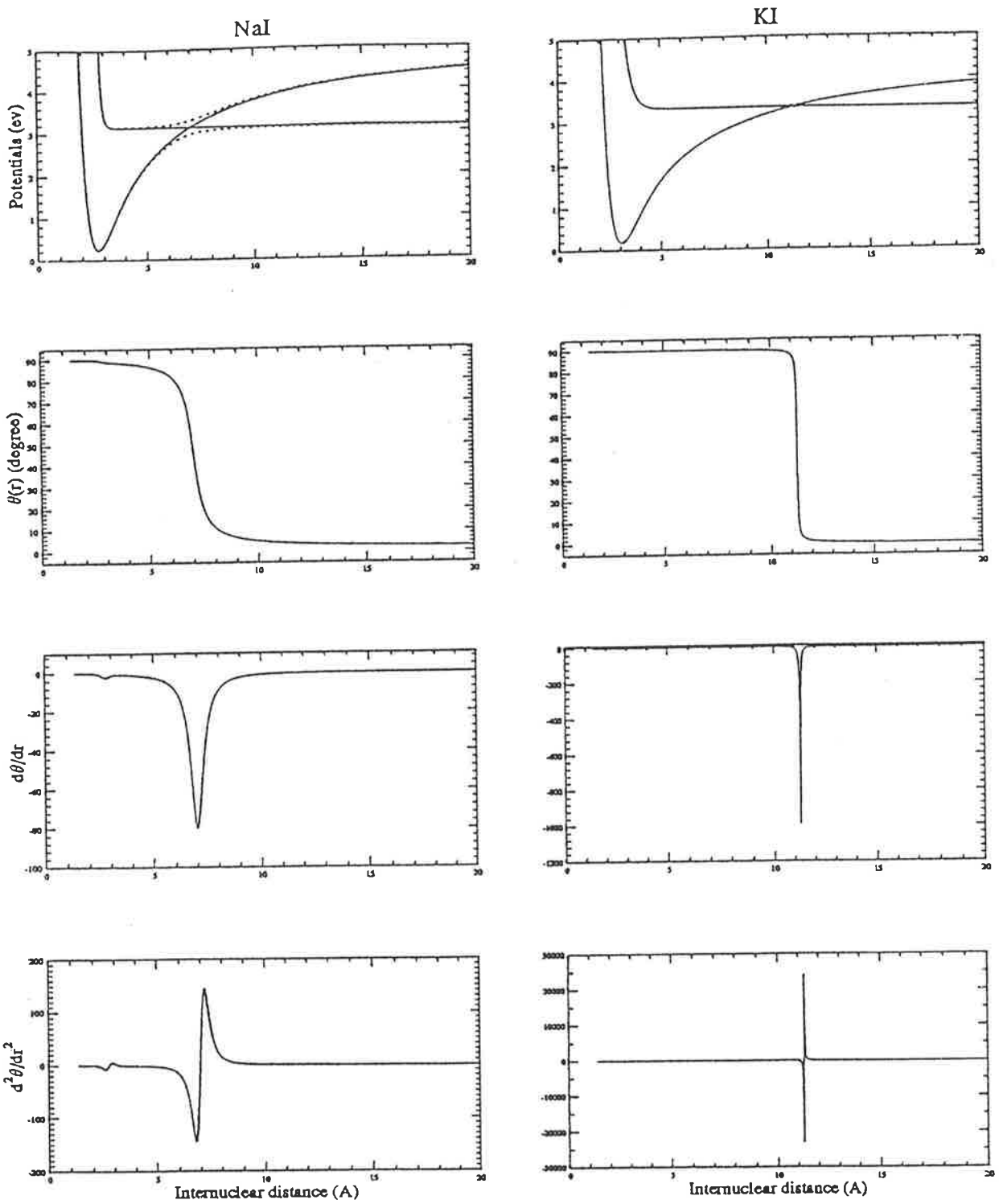

Figure 2.1: Examples for the changes of the diabatic (solid lines) and adiabatic (dotted lines) potential curves, θ, $\frac{d\theta}{dr}$, and $\frac{d^2\theta}{dr^2}$ as a function of the internuclear distance based on the values given by Rittner (1951). The coupling strength for the adiabatic potential curves are 5 times greater than the given values to emphasis the non-crossing region.

the renormalized Numerov method developed by Johnson (1977, 1978) provides one of the most efficient. It has the advantage of speed of computation, quick convergence, stable solutions and ease of programming. A description of the renormalized Numerov method for solving the Schrödinger equation is presented in Appendix A.

As an example, the coupled equations are solved for a typical crossing system:

$$\begin{aligned} V_1(r) &= 18154.95\ exp[2.2039(r-2.48)] - 8000\ \ cm^{-1} \\ V_2(r) &= 15000\ [1 - exp(-1.9685(r-1.6))]^2\ \ cm^{-1} \end{aligned} \tag{2.21}$$

with $V_{12} = 705\ cm^{-1}$ and r in Å. The transition strength factor, similar to the Franck-Condon factor, given by

$$I = < \chi_g | \chi_1 + \chi_2 >^2 \tag{2.22}$$

is show in Fig. 2.2 for transitions from ground states with potential minimum which favor the transitions to the repulsive edge of V_2 and V_1. It is assumed that the electronic transition dipole moment for the states are equal and constant. The diabatic and adiabatic potential curves and their wavefunctions corresponding to different energy positions are shown in Fig. 2.3.

2.2.4 Near diabatic and near adiabatic case

The diabatic and adiabatic representations are theoretically equivalent. But a number of considerations may weigh in favor of the choice of one or the other for representing that molecular potential.

In the two limiting cases where the electronic coupling or the motion coupling terms approach zero, the resonance of the molecular states approach the diabatic or adiabatic bound states respectively. In the near diabatic case, the electronic coupling strength is so small that the resonance character is close to the diabatic behaviour and the resonance positions are close to the eigenvalues of the diabatic bound states. As the electronic coupling strength increases the mixing of the two diabatic wavefunctions

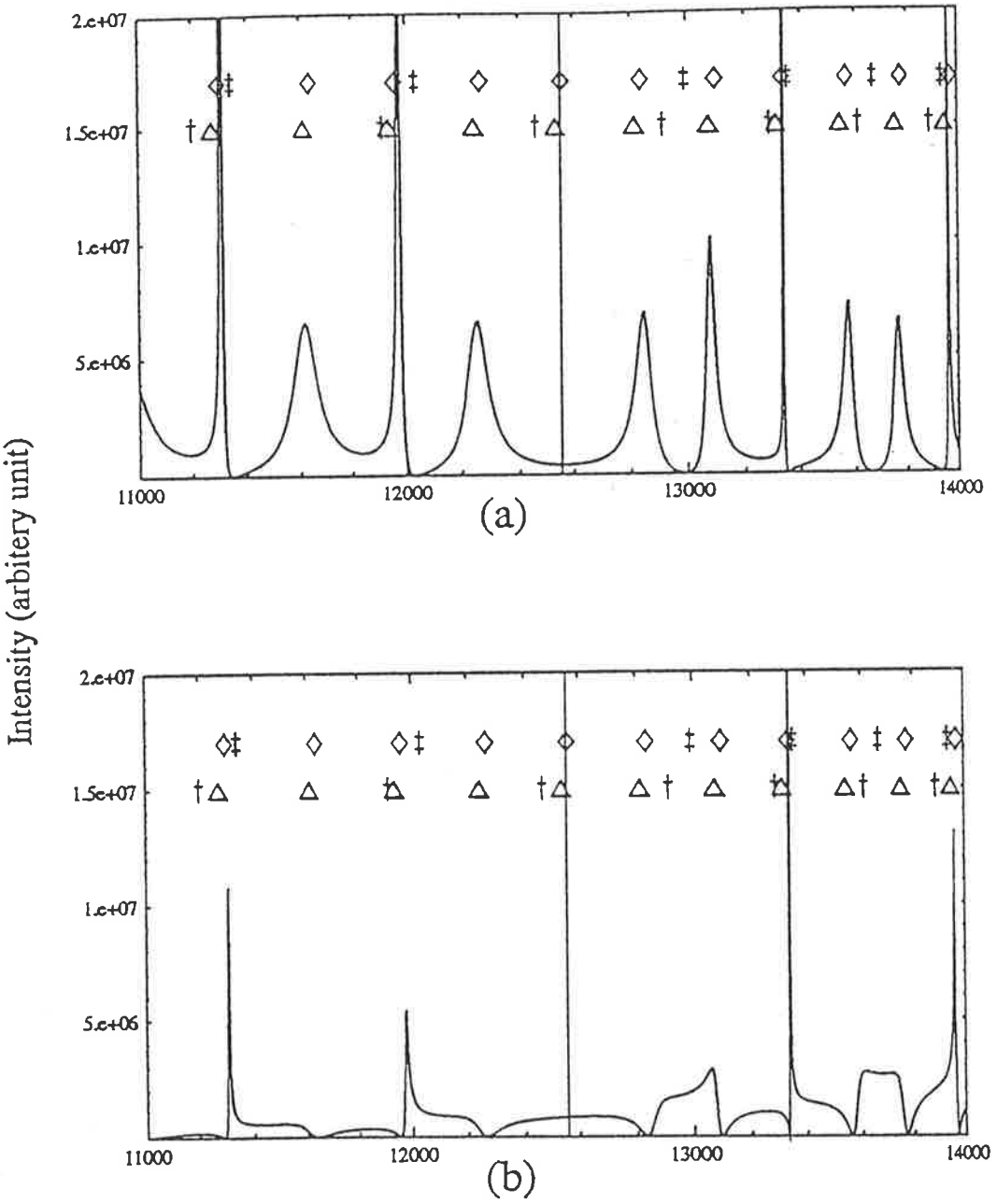

Figure 2.2: Examples of the transition strength factors I as a function of energy for a typical crossing system, Eq. (2.21), with transitions to the repulsive edges of V_2 (a) and V_1 (b). The $\triangle$ and $\diamond$ are the positions of the diabatic levels calculated from the Schrödinger equation and the Child's semiclassical theory (Child 1991) respectively, likewise † and ‡ are calculated for adiabatic levels with $n_d = 21$ and $n_a = 0$ from the left. The wavefunctions for different energy positions representing sharp resonance, broad resonance and off resonance are shown in Fig. 2.3.

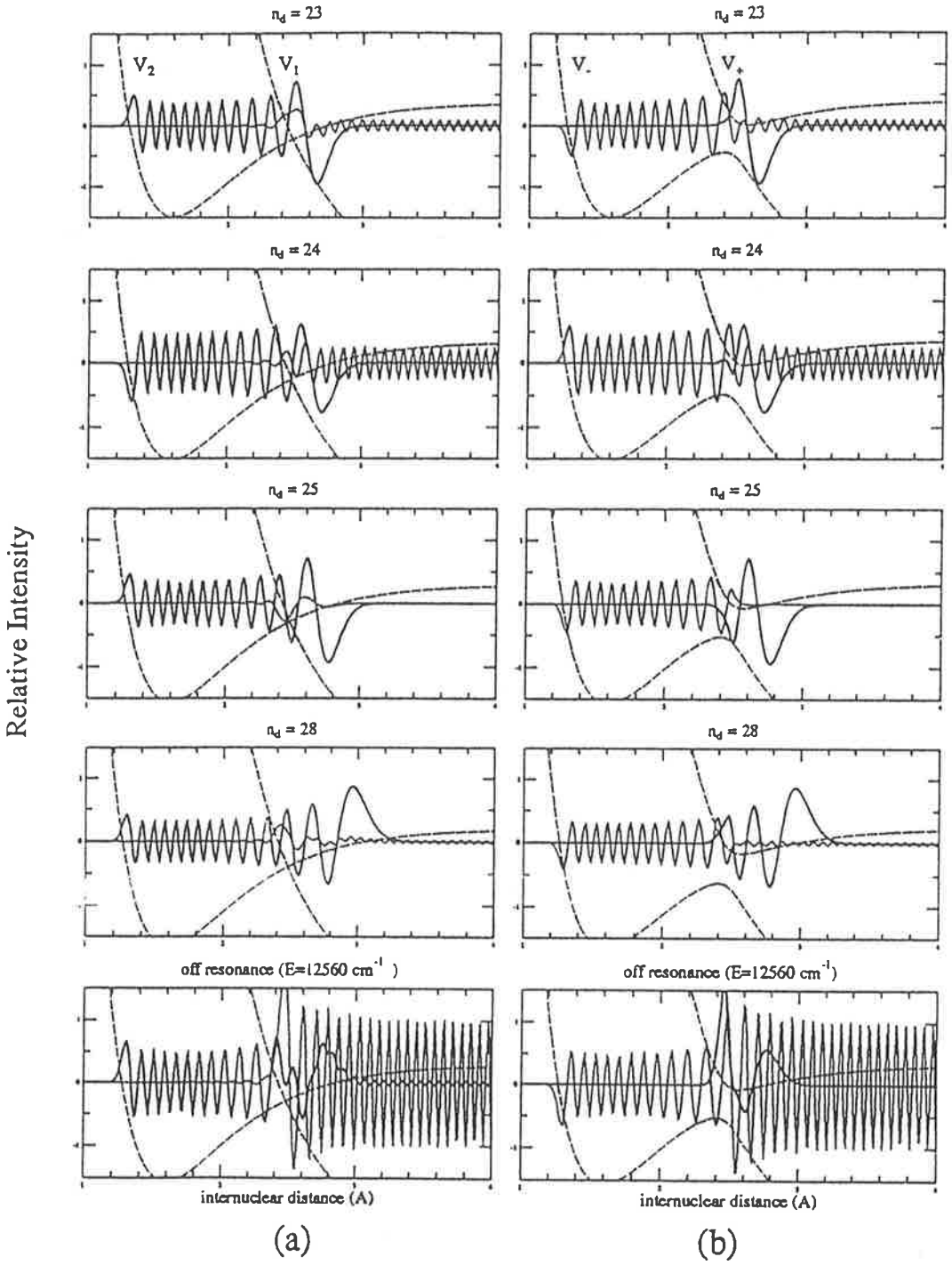

Figure 2.3: Examples of diabatic (a) and adiabatic (b) wavefunctions for on resonance and off resonance corresponding to different positions in Fig. 2.2. n_d denote the nearest eigenvalues of the diabatic bound state V_2. The diabatic (a) and adiabatic (b) potential curves are also marked.

increases. When the electronic coupling strength is very large, the adiabatic character becomes dominant and the resonance positions are close to the eigenvalues of the adiabatic bound state.

The non-adiabatic transition probability

The presence of motion coupling between the two adiabatic electronic states allows the transition from one adiabatic state to the other. The transition probability for a single passage through the crossing region known as the Landau-Zener nonadiabatic transition probability, is given by (Landau 1932, Zener 1932):

$$P_{lz} = exp\left(-\frac{2\pi V_{12}^2}{\hbar v \Delta F}\right) \tag{2.23}$$

where V_{12} is the electronic coupling strength at the crossing point, while v and ΔF are the relative velocity of the two nuclei and the slope difference of the two diabatic electronic potential curves at the crossing point respectively, given by

$$\begin{aligned} v &= (\frac{2}{\mu}(E - E_x))^{1/2} \\ \Delta F &= \frac{d}{dr}(V_{11}(r_x) - V_{22}(r_x)) \end{aligned}$$

with $E_x = V_{11}(r_x) = V_{22}(r_x)$.

The Landau-Zener nonadiabatic transition probability provides an indication, in a particular situation, of whether the near diabatic or near adiabatic case gives a better description of the molecular states. If P_{lz} is small (when V_{12} is very large), there is little transition between the two adiabatic electronic states and the molecular state will mainly remain in the same adiabatic electronic state and the molecular states are near adiabatic. If P_{lz} approaches to 1 (when $V_{12} \rightarrow 0$), a nearly complete transition from one adiabatic to the other adiabatic electronic state occurs. Then the molecular states will mainly stay in the same diabatic electronic states. and this is a near diabatic case. In the region of intermediate electronic coupling strength. where $P_{lz} \approx 0.5$, the

two states are strongly mixed. A theoretical study for the transition from near diabatic to near adiabatic case by varying the coupling strength is given in Chapter 6.

Fig. 2.4 shows the changes of Landau-Zener nonadiabatic transition probabilities as the energy changes for different coupling strength for the potential curves of NaI. The actual coupling strength for NaI is taken to be 0.055 ev.

Explanation of the diabatic and adiabatic cases

Berry (1957) provided an intuitive picture to explain the near diabatic and near adiabatic cases for diatomic alkali halide molecules. As described in Chapter 1, upon passing through the crossing region an electron may jump from one nuclei to the other and the electronic wavefunction re-adjusts itself to the sudden change of character to form a bound adiabatic state. To indicate whether such a jump is possible, an estimate can be made of the relative velocity between the nuclei and the electron as well as the distance they travel in such a jump. The mass difference implies that the electronic velocities are about 40 times faster than that of the nuclei. Therefore in the time that the nuclei move 0.1 Å, the electron can move about 4 Å. Thus, an electron jump from one nuclei to the other would be possible if the crossing region is long enough and hence the molecular system will be a near adiabatic case. Otherwise, it will be a near diabatic case.

Although diatomic alkali halide molecule NaI and KI have similar electronic character and potential curves, that is both have an ionic ground state and a covalent excited state which undergoes an avoided crossing at a large internuclear distance, their behaviour is completely different. For example, the absorption spectrum for NaI is a very rich band spectrum in the UV while that for KI is a continuum. The physical interpretation given by Berry (1957) for such a similar molecule resulting in a very different behaviour is that the crossing region, where θ changes rapidly, for KI lies at a greater internuclear distance and is narrower than that of NaI. This is shown in

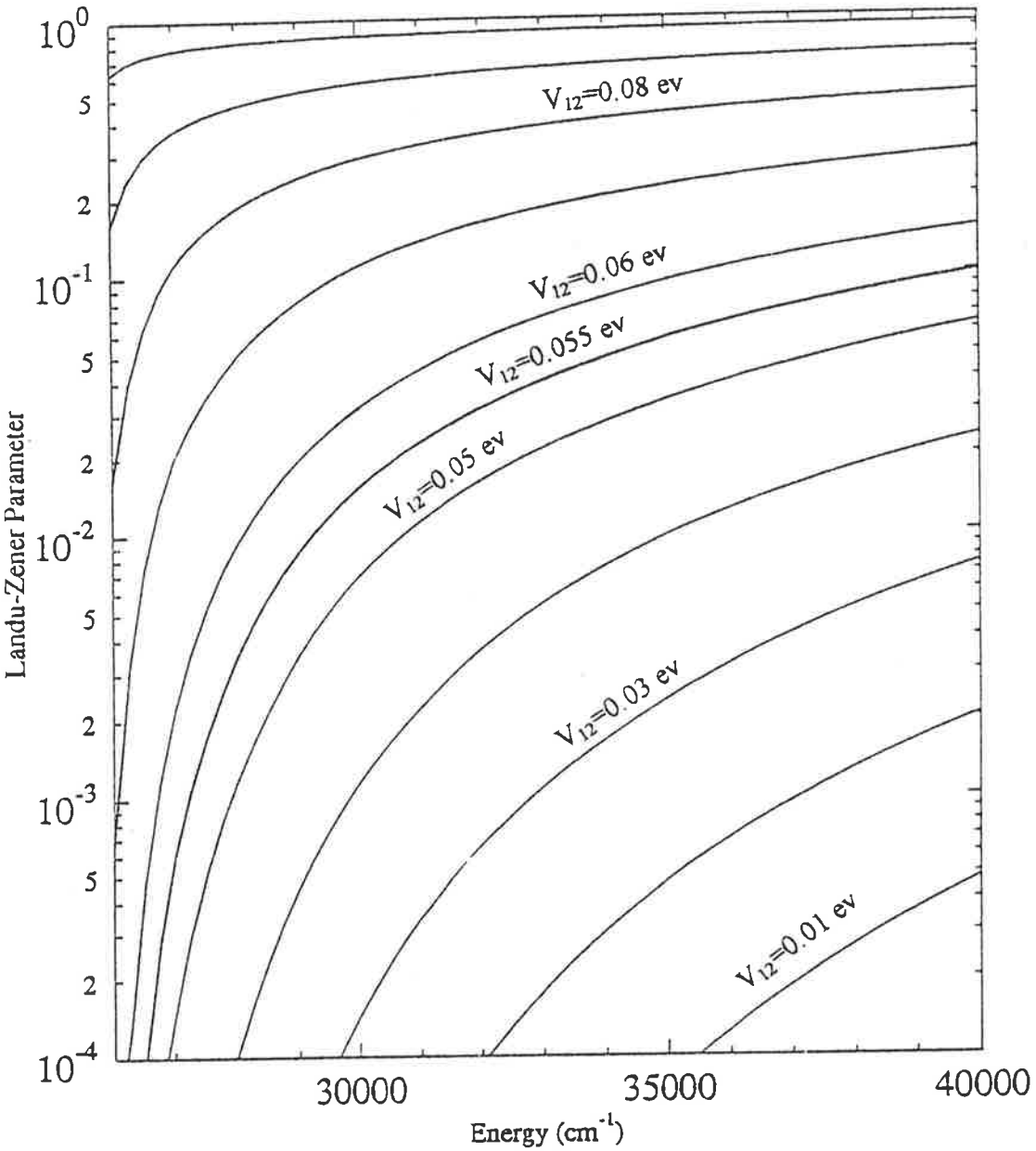

Figure 2.4: The changes of Landau-Zener nonadiabatic transition probabilities plotted against the energy measured from the potential minimium of the ground state for different coupling strength for NaI. The bold line represents the actual situation of NaI with a coupling strength taken to be 0.055 ev.

Fig. 2.1. Thus an electron jump can occur for NaI but not for KI. In another words, for KI, the Born-Oppenheimer approximation breaks down completely and the electronic motion is not separable from that of the nuclei so the electronic wavefunctions do not change their character and the KI molecule behaves diabatically.

2.2.5 Resonance states

In the study of the discrete energy spectrum of molecules, the excited states are found to be very long-lived and are described by the uncoupled, bound state Schrödinger Equation (2.12). The wavefunctions exist only at energies corresponding to the energy eigenvalues of the bound state. When a bound state is perturbed, for example by a vibrational continuum of the same symmetry as investigated in this study, its lifetime is reduced, and the eigenstate of the bound potential becomes a quasistationary or metastable state. Such states can be regarded as resonant states of the molecular system if their lifetimes are long enough to be well characterized. The wavefunctions exist at any energy and can be calculated by the coupled equations. A resonance is characterized by the resonance energy and its width or lifetime. The simplest theoretical description of resonance states is that they resemble bound stationary states in that they are "localized" in space (at t=0), and their time evolution is given by:

$$\psi_r(t) = exp\left(-i(E_r - i\frac{\Gamma}{2})t/\hbar\right)\psi_r(0) = exp(-iE_Rt/\hbar)\psi_r(0), \tag{2.24}$$

where

$$E_R = E_r - i\Gamma/2 \tag{2.25}$$

is a complex resonance energy. E_r and Γ are real and $\Gamma > 0$. The presence of the $-i\Gamma/2$ term represents a decaying state.

Experimentally resonances are usually associated with a sharp variation of the cross section as a function of energy. Analysis of resonance spectra is one of the most interesting and important features of spectroscopy. Resonant phenomena

have been studied for many decades, but nevertheless some aspects are not yet fully understood. Rather than looking for a general explanation of resonances it may well be more appropriate to distinguish between various kinds of resonance phenomena (Volker 1984). In this section, we restrict ourselves to the area of molecular optical spectroscopy and introduce some definitions for resonance which are related to this study.

Shape resonance is a simple example which is closely related to the curve crossing problem. It can be that the lower state V_- produced by the avoided crossing of a bound state with a continuum state creates a potential barrier, such as that is shown in Fig. 2.3(b), or is the result of centrifugal barrier effects.

The most straightforward and perhaps the most productive approach for single channel resonance is through the calculation of phase shifts. It is shown that (Child 1974, 1991) the phase of the wavefunction in the asymptotic region will undergo a π phase shift on resonance which corresponds to the creation or cancellation of a node in the wavefunction within the barrier region.

In many cases, a resonance may be very broad with the π phase shift occurring over a broad energy region and it is necessary to find a suitable definition for the resonance energy in this case. Allison (1969) suggested that an alternative definition for resonance position is the energy where the amplitude of the wavefunction inside the potential barrier, or the internal wavefunction, normalized by its asymptotic amplitude reaches a maximum. A similar definition for the curve crossing problem is proposed in Chapter 6 to describe the resonance behaviour in the intermediate coupling region.

For the multichannel case, one can use Feshbach projector operators to define resonance (Feshbach 1958, 1962). However, definition of the operators is so difficult for systems with many electrons that it has not yet been demonstrated that such an approach provides a practical method for calculating resonance parameters to arbitrary accuracy (Bardsley, 1978).

The most fruitful definition for resonance is the "outgoing wave only" boundary condition. According to Siegert "the cross section being the ratio of the intensities of outgoing and incoming wave becomes singular if there is only the outgoing wave" (Siegert, 1939). Such a definition has been widely used in semiclassical (Child 1991, Korsch 1986) as well as quantum mechanical methods (Junker 1982 and Reinhardt 1982) to investigate resonance structure. More discussion about the Siegert state can be found in §2.4 and Chapter 6.

It has been noted by Child (1991) that *the precise equivalence between the resonance positions and width associated with the three different prescriptions – internal amplitude, phase shift jump, and Siegert eigenvalue – applies only in the sharp resonance limit.* This is observed in Chapter 6 for broad resonances.

2.3 Semiclassical Theory

Only a few quantum mechanical problems have exact analytical solutions. In practice one has almost always to resort to an appropriate approximate methods or to numerically solve the Schrödinger equation. Semiclassical approximations is the short wavelength link between classical and quantum mechanics. Besides simplifying the calculations and providing reasonably accurate numerical results, semiclassical approximations offer a conceptual way of understanding quantum processes. This is often impossible in a pure quantum mechanical treatment. A very useful method is the JWKB approximation for the wave function (Child 1974) and will be used in the following discussion.

In this section, the results of semiclassical theory on curve crossing developed by Child (1970, 1974, 1976, 1979, 1991) are presented and the characteristics of the resonance position and its width are discussed.

2.3.1 Child's semiclassical theory

Because Child's semiclassical method is based on the assumption that the coupling effect is only significant near the crossing point, the central problem for a curve crossing system reduces to an investigation of the general solution of coupled equations in the crossing region. Outside the crossing region the Schrödinger equation is uncoupled and its solutions can be approximated by the JWKB wavefunction $\chi_{\pm}(r)$ for the potential curves of $V_{\pm}(r)$ (Child 1974, 1991). In the semiclassical regions which are far away from the crossing point and the turning points, $\chi_{\pm}(r)$ is given by

$$\chi_{\pm}(r) \overset{r \ll r_x}{\approx} k_{\pm}^{-1/2}(r)[P'_{\pm} exp(i\int_{r_x}^{r} k_{\pm}(r)dr) + P''_{\pm} exp(-i\int_{r_x}^{r} k_{\pm}(r)dr)] \quad (2.26)$$

$$\overset{r \gg r_x}{\approx} k_{\pm}^{-1/2}(r)[Q'_{\pm} exp(i\int_{r_x}^{r} k_{\pm}(r)dr) + Q''_{\pm} exp(-i\int_{r_x}^{r} k_{\pm}(r)dr)] \quad (2.27)$$

where

$$k_{\pm}(r) = [2\mu(E - V_{\pm}(r))]^{1/2}/\hbar. \quad (2.28)$$

The basic idea of Child's semiclassical theory is to follow the changes in the amplitudes of the wavefunction (P and Q) in the nonclassical region. A diagrammatic approach is developed and the connection matrix (see Appendix B) is used to follow changes in the amplitudes and phases of the various JWKB terms in passing from one semiclassical region to another. Fig. 2.5 gives a typical picture of a curve crossing system and the corresponding diagram showing the transmission of fluxes through the crossing region. Elements of the connection matrix including free propagation, reflection from a classical turning point and passing through a curve crossing region are given in Appendix B.

2.3.2 Application for curve crossing

Following the flow in Fig. 2.5 and applying the connection formulas to the wave functions together with the outgoing wave only boundary condition for resonance, one finds

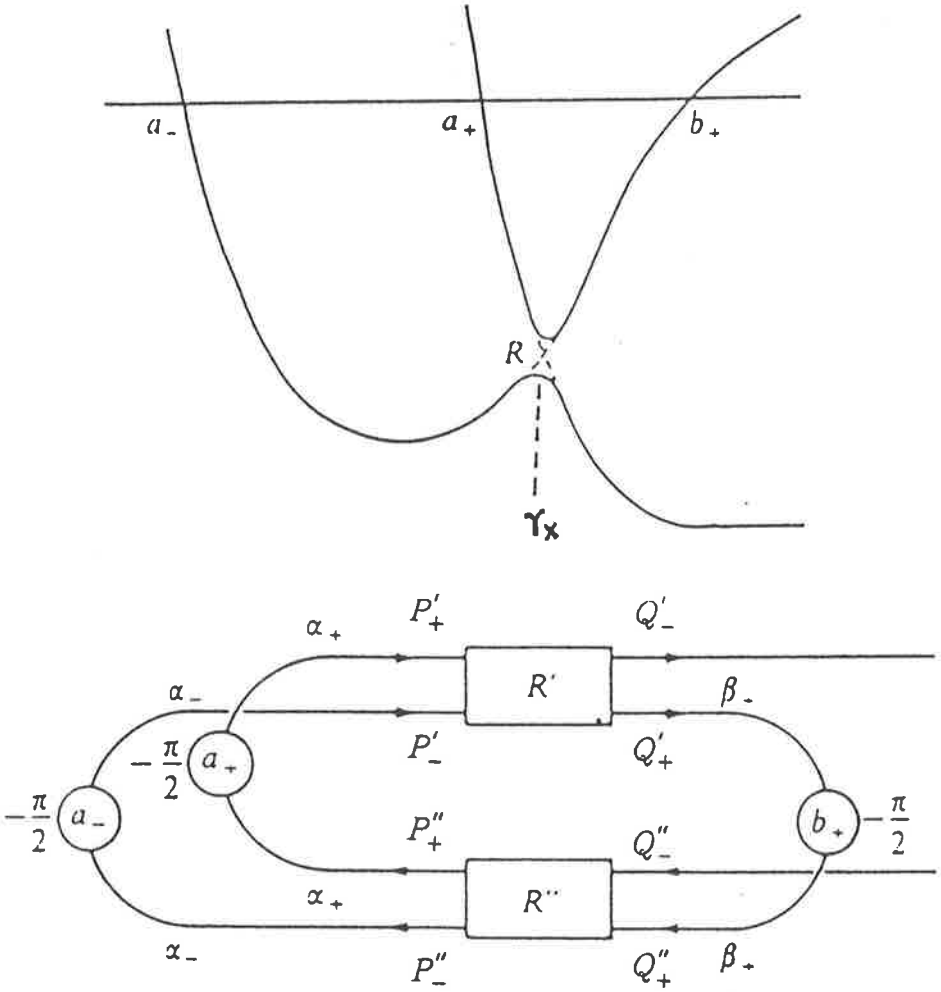

Figure 2.5: Potential curves and connection diagram for predissociation by curve crossing (after Child 1991).

that (Appendix B)

$$\begin{pmatrix} Q'_+ \\ Q'_- \end{pmatrix} = \begin{pmatrix} (1-\lambda^2)exp(2i\theta_+) + \lambda^2 exp(2i\theta_2) \\ \lambda(1-\lambda^2)^{1/2}exp(-i\chi)(exp(2i\theta_+) - exp(2i\theta_2)) \end{pmatrix} (-Q'_+). \quad (2.29)$$

where

$$\alpha_\pm = \int_{a_\pm}^{r_x} k_\pm(r)dr \quad (2.30)$$

$$\beta_+ = \int_{r_x}^{b_+} k_+(r)dr \quad (2.31)$$

$$\theta_2 = \alpha_- + \beta_+ \quad (2.32)$$

$$\theta_+ = \alpha_+ + \beta_+ + \chi \quad (2.33)$$

$$\lambda = exp(-\pi\nu) \quad (2.34)$$

$$\nu = -\frac{i}{2\pi}(\int_{r_-}^{r_+}[k_-(r) - k_+(r)]dr) \quad (2.35)$$

$$\chi = arg\Gamma(i\nu) - \nu ln\nu + \nu + \pi/4. \quad (2.36)$$

In the above equations, $a_\pm$ and b_+ are the semiclassical turning points, r_+ and r_- are the complex crossing points of the adiabatic upper V_+ and lower V_- potential curves in the complex coordinate plane, θ_2 and θ_+ are the diabatic and the adiabatic phase integrals, and χ is a phase shift caused by the curve crossing. Eq. (2.29) requires that

$$(1-\lambda^2)exp(2i\theta_+) + \lambda^2 exp(2i\theta_2) = -1. \quad (2.37)$$

The semiclassical levels of the diabatic and adiabatic bound state are deduced from the Bohr quantization condition:

$$\theta_2(E_2) = (v_2 + \frac{1}{2})\pi \quad (2.38)$$

$$\theta_+(E_+) = (v_+ + \frac{1}{2})\pi. \quad (2.39)$$

Since these level schemes are never observable they were also called hypothetical levels (Schaefer et al, 1984). Analytical expressions for the resonance energy shift Δ from the bound state level and the predissociation line width Γ were given by (Child, 1974):

$$\Delta_2 = \frac{\hbar\omega_2}{\pi} u sin\theta_+ cos\theta_+, \qquad \Gamma_2 = \frac{2\hbar\omega_2}{\pi} u cos^2\theta_+ \quad (2.40)$$

for the diabatic case; and

$$\Delta_+ = \frac{\hbar\omega_+}{\pi} u^{-1} sin\theta_2 cos\theta_2, \qquad \Gamma_+ = \frac{2\hbar\omega_+}{\pi} u^{-1} cos^2\theta_2 \tag{2.41}$$

for the adiabatic case. In these equations $u = \lambda^{-2} - 1$.

A more general formula, for any coupling strength, for the region in the neighborhood of certain arbitrarily sharp lines is given by the equations (Child 1976, 1991):

$$E = (E_2 + xE_+)/(1+x) \tag{2.42}$$

$$\Gamma = 2\pi x(1+\gamma x)(E_2 - E_+)^2/[\hbar\bar{\omega}_2(1+x)^3] \tag{2.43}$$

where $x = u\hbar\bar{\omega}_2/\hbar\bar{\omega}_+$ is the mixing parameter and $\gamma = \hbar\bar{\omega}_2/\hbar\bar{\omega}_+$.

It can be seen from the above equations that the predissociation line position and width depend on the two nearby diabatic (E_2) and adiabatic (E_+) hypothetic levels, their local level spacings ($\hbar\omega_2$ and $\hbar\omega_+$) and the mixing parameter (x).

2.3.3 The vanishing predissociation line width

The analytical expressions for the predissociation line width predict that the sharp lines (or the vanishing line width) always occurs when the hypothetical diabatic and adiabatic levels are accidentally coincident. This is a very important characteristic of the lines which can be used to identify the hypothetic level positions and may help lead to final assignment of the spectrum. This technique was first successfully applied to the assignment of IBr (Child 1976), and was more recently applied for NaI (Schaefer et al 1984).

As seen in the previous discussion of this section, two sets of energy levels can be considered. One is the set of eigenvalues of the Schrödinger equation Eq. (2.12) for the diabatic (V_2) and adiabatic (V_+) bound states. The other is the set of semiclassical hypothetical levels defined by the Bohr quantization conditions (Eq. (2.38) and Eq. (2.39)) in Child's semiclassical theory. It has to be pointed out that there are

differences between the hypothetical levels from the bound state eigenvalues. Apart from the semiclassical approximation, the adiabatic hypothetic levels differ from the adiabatic bound state eigenvalue by a modified phase χ which is caused by the crossing. From Table B.1 in Appendix B and Eq. (2.39) one finds that for weak coupling $\chi \sim \pi/4$ which will cause an energy shift equal to one quarter of the vibrational spacing and this shift will reduce and then approach zero as the electronic coupling strength V_{12} increases. Calculations for NaI in this study showed that this shift is only about 2 cm^{-1} for the adiabatic levels.

The hypothetical diabatic levels are the eigenvalues of a "modified" diabatic bound state which is:

$$V = \begin{cases} V_- & (r < r_x) \\ V_+ & (r > r_x) \end{cases} \tag{2.44}$$

with a discontinuous step at r_x (see Fig. 2.5.). Calculation in this study showed that the eigenvalues of such a "modified" diabatic bound state differ from those of the actual diabatic bound state (V_2) by about one vibrational level spacing for NaI. In the analysis of the NaI spectrum reported by Schaefer et al (1984), the diabatic and adiabatic hypothetic levels are regarded as the isolated bound state (V_2 and V_+) eigenvalues. The resulting potential curves, therefore, will not be in agreement with the later version of Child's theory (Child 1991(a)) and need to be re-calculated.

Fig. 2.6 shows the strength factors for a spectral region of NaI and the corresponding hypothetic levels and the bound states eigenvalues. Two kinds of electronic coupling functions were used for the calculation with one being constant with r while the other is a Gaussian function about the crossing region. It was found that while the coincidence of the two hypothetic levels provides a good approximation for the position of a sharp line, the eigenvalues of the bound states seem to have little relationship with the occurrence of the sharp lines. Calculations show that for a constant coupling strength, the coincidence of the two bound state eigenvalues may be near the broadest line. For a Gaussian function coupling strength, the coincidence may move from the

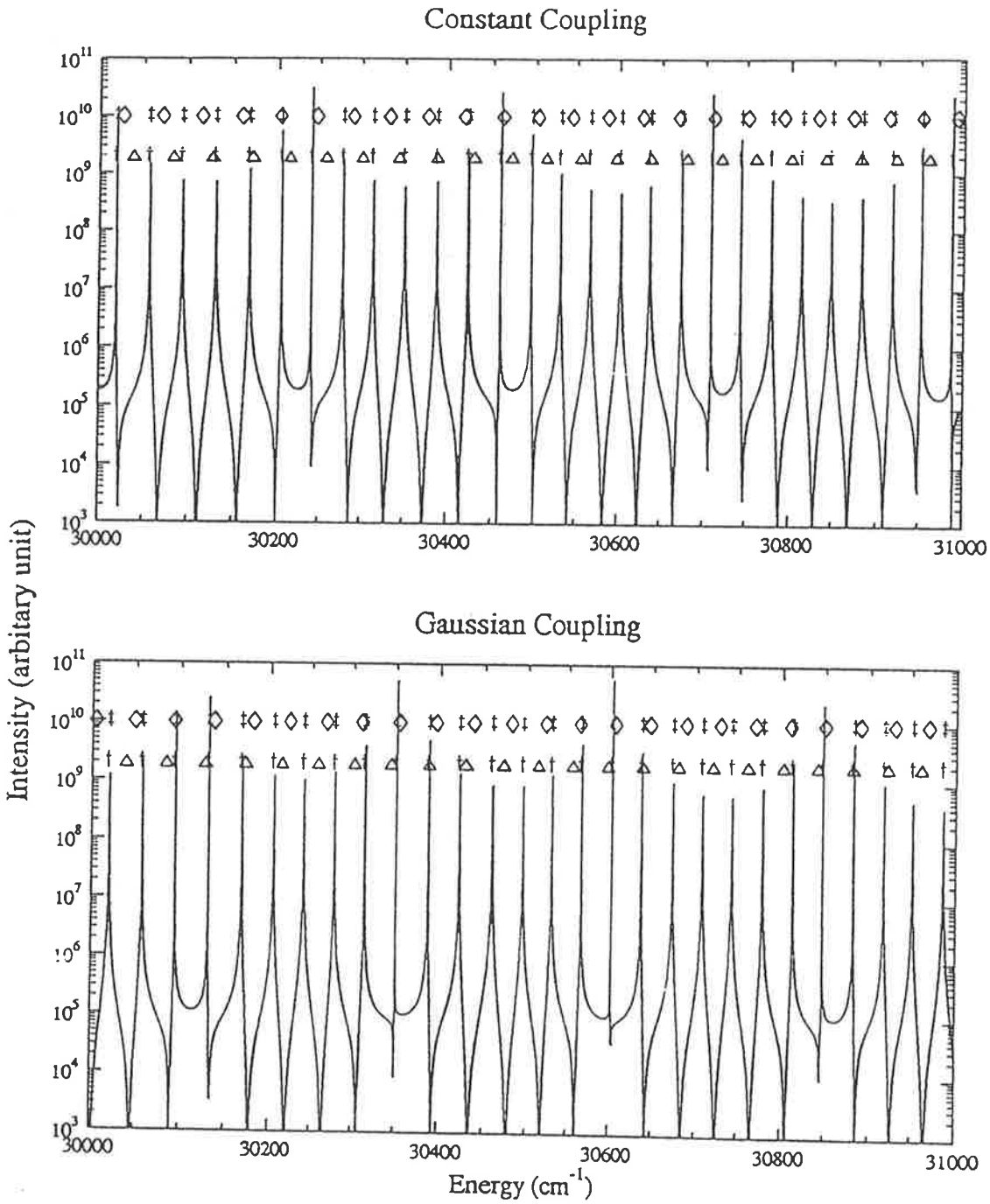

Figure 2.6: Fragment of the strength factors defined in Eq. (2.22) for NaI with the the positions of the hypothetic levels and the bound state eigenvalues for a constant coupling strength (a) and a Gaussian coupling function (b). In both cases, the sharp lines occur at the position of the closest coincident of the two hypothetic levels. The symbols are the same as those in Fig. 2.2.

broadest line towards the sharpest line as the width of the Gaussian function reduces. There is no clear explanation for such behavior. However, a possible reason may be that as the width of the Gaussian coupling strength reduces, the electronic coupling function approximates more closely the semiclassical electronic coupling function which has a constant coupling strength in the crossing region and has zero coupling outside the crossing region.

Although it is unambiguously evident that the vanishing line width occurs at the energy of the coincidences of the diabatic and adiabatic hypothetic levels, a physical understanding of the reason for the sharp resonance is not clear. There is no satisfactory interpretation directly from the coupled equations, diabatic or adiabatic, which can be used to explain the occurrence of sharp resonances and the suppression of the outgoing wave through coupling at such a particular condition.

One possible physical explanation, in the semiclassical theory, comes from the examination of the leakage rate of the curve crossing system. which is directly related to the line width (Lefebvre 1988, 1990a, and Lefebvre and Child 1989):

$$\Gamma/2 = \frac{\hbar^2}{2\mu} k|A|^2, \tag{2.45}$$

where A is the normalized amplitude of the outgoing wave and k is the asymptotic wave number. From Fig. 2.5, the amplitude of the out going wave is Q'_-. It is zero, from Eq. (2.29) and Eq. (2.37), only on the condition that

$$exp(2i\theta_+) = exp(2i\theta_2) = -1. \tag{2.46}$$

Therefore

$$\theta_+ = (v_+ + 1/2)\pi \tag{2.47}$$

$$\theta_2 = (v_2 + 1/2)\pi \tag{2.48}$$

or $E_+ = E_2$. This means zero leakage rate or zero predissociation line width can only occur when the two hypothetic energy levels coincident.

2.3.4 The asymptotic analysis of the line width

For a curve crossing system which normalization is performed through the closed channel with the bound state wavefunction $\chi_b(r)$:

$$\int_{-\infty}^{+\infty} |\chi_b(r)|^2 dr = 1. \tag{2.49}$$

the asymptotic amplitude of the open channel wavefunction χ_c provides a measure of the dissociation rate of the molecular system (Lefebvre 1988, 1990a, and Lefebvre and Child 1989).

With the semiclassical wavefunctions describing the curve crossing system, as shown in Fig. 2.5, Child (1976) suggested that the amplitudes on the left turning points a_- and a_+ are related to the normalization of the bound states. If a standard normalized JWKB wave function

$$\chi_b(r) = \left(\frac{2\mu\hbar\omega_b}{\pi\hbar^2}\right)^{1/2} k_b^{-1/2}(r) sin\left(\int_a^r k_b(r)dr + \pi/4\right) \tag{2.50}$$

is used for bound state wave functions, then the amplitude for the traveling wave will be half that of the standing wave

$$|A_b| = (\mu\hbar\omega_b/2\pi\hbar^2)^{1/2} \tag{2.51}$$

In the diabatic case, from the connection matrix in Appendix B, $|A_b| = |P'_-| = |P''| = |Q'_+|/\lambda$ when there is no incoming wave. From Eq. (2.27) and Eq. (2.29) the square of the normalized amplitude of the outgoing wave is

$$\begin{aligned} |A|^2 &= k_-^{-1}(r)|Q'_-|^2 && (2.52)\\ &= 4k_-^{-1}(r)\lambda^2(1-\lambda^2)sin^2(\theta_2-\theta_+)|Q'_+|^2 && (2.53)\\ &= \frac{2\mu\hbar\omega_2}{\pi\hbar^2}k_-^{-1}(r)(1-\lambda^2)sin^2(\theta_2-\theta_+) && (2.54) \end{aligned}$$

Substituting this into Eq. (2.45) with $k(r) = k_-(r)$ gives

$$\Gamma = \frac{2\hbar\omega_b}{\pi}(1-\lambda^2)sin^2(\theta_2-\theta_+) \tag{2.55}$$

and with $\theta_2 \simeq (v_2 + 1/2)\pi$ the line width is

$$\Gamma = \frac{2\hbar\omega_2}{\pi}\lambda^2 u cos^2\theta_+ \tag{2.56}$$

Similarly, in the adiabatic case, $|A_b| = |P'_+| = |Q'_+|/(1-\lambda^2)^{1/2}$ and

$$|A|^2 = k_-^{-1}(r)|Q'_-|^2 \tag{2.57}$$

$$= 4k_-^{-1}(r)\lambda^2(1-\lambda^2)sin^2(\theta_2 - \theta_+)|Q'_+|^2 \tag{2.58}$$

$$= \frac{2\mu\hbar\omega_+}{\pi\hbar^2}k_-^{-1}(r)\lambda^2 sin^2(\theta_2 - \theta_+) \tag{2.59}$$

and with $\theta_+ \simeq (v_+ + 1/2)\pi$ the line width is

$$\Gamma = \frac{2\hbar\omega_+}{\pi}(1-\lambda^2)u^{-1}cos^2\theta_2 \tag{2.60}$$

Eq. (2.56) and Eq. (2.60) agree with Eq. (2.40) and Eq. (2.41) except for a factor of λ^2 and $(1-\lambda^2)$ respectively which approach unity in the weak and strong coupling case. A similar result for weak coupling case was obtained by analysis based on the stabilization method (Lefebvre and Child, 1989).

2.4 Complex Scaling Method

The operators in quantum mechanics representing physical observables are all self-adjoint and therefore have real eigenvalues if the corresponding eigenfunctions fulfill the standard boundary conditions. Thus one obtains an energy spectrum of real eigenvalues for the Hamiltonian, which are either discrete (corresponding to bound states) or continuous (corresponding to continuous or quasibound states). However, if one "properly changes" the boundary conditions, so that the Hamiltonian H is no longer self-adjoint, then H may have complex eigenvalues $E = E_r - i\Gamma/2$ corresponding to resonance states with the resonance energy E_r and a finite lifetime Γ. The eigenfunctions of such states, which are often called Siegert states or Gamow states, have an asymptotic characteristic of being an outgoing wave. Such a "proper change" of the

conventional boundary conditions is associated with a certain mathematical extension of the standard quantum mechanical formalism through the introduction of complex variables. This idea was brought to a firm mathematical basis by Balslev and Combes (1971), which is known as the complex scaling method (CSM), also called the complex coordinate method or the complex dilation theory.

In the complex scaling method resonance is defined by the Siegert outgoing wave only boundary condition and its corresponding wavefunction has a complex energy $E = E_r - i\Gamma/2$, where E_r is the resonance energy and Γ is the resonance width. This also leads to a complex wave vector

$$k = \sqrt{\frac{2\mu}{\hbar^2}[E - V(r)]}. \tag{2.61}$$

For a Siegert resonance state the asymptotic behavior of the wave function for large internuclear distance r is an outgoing wave

$$\chi(r) \propto exp(ikr) \tag{2.62}$$

with

$$k = k_0 - ik_1 \ \ (k_0,\, k_1 > 0) \tag{2.63}$$

or

$$k = Ke^{-i\beta} \ \ (K > 0,\, \beta > 0). \tag{2.64}$$

where

$$\beta = tan^{-1}\frac{k_1}{k_0} \quad or \quad \frac{1}{2}tan^{-1}\frac{E_r - E_0}{\Gamma/2}. \tag{2.65}$$

with E_0 the dissociation energy of V(r).

It is clear from Eq. (2.62) and Eq. (2.63) that the amplitude of the outgoing wave will diverge exponentially as r increases. This asymptotic divergence can be avoided through the use of complex rotation of coordinates (Brandas 1987) by the transformation

$$r \rightarrow r\,e^{i\theta} \tag{2.66}$$

provided that the rotation angle θ is greater than the critical angle β define in Eq. (2.65). Therefore we can write

$$\chi(r) \propto exp(ikr) = exp[iKr\,cos(\theta - \beta)]\,exp[-Kr\,sin(\theta - \beta)] \tag{2.67}$$

which approaches zero in the asymptotic region. Such a complex rotation of coordinates is only a mathematical tool for the calculation of the complex energy eigenvalue and has no physical meaning. The method for numerically calculating the complex energy eigenvalues is essentially the same as that for a bound state and is detailed in Appendix C.

The development of complex scaling method provides an approach to the direct study of resonance through the introduction of complex variables. It is an attempt to treat resonance states as bound states. Its application in a typical curve crossing system is described in Chapter 6.

Chapter 3

A Tunable Ultraviolet Laser System

3.1 Introduction

Laser, light amplification by simulated emission of radiation, produces intense light sources with spectral energy densities which may exceed those of incoherent sources by several orders of magnitude. Furthermore, because of their extremely small bandwidth, single-mode lasers allow a spectral resolution which far exceeds that of conventional spectrometers. Many experiments which could not be done before because of lack of intensity or insufficient resolution are now readily performed with a laser source. This brought about a revolution in optical technology and spectroscopy, and had a far-reaching influence in various fields of science and technology.

This Chapter describes a tunable UV laser designed and set up in this work for the spectroscopic study of NaI. It consists of a pulsed copper bromide (CuBr) laser with a 16 kHz repetition rate which pumps a dye laser with a narrow bandwidth of 1-2 GHz and a tunable range from 528 nm to near infrared using different dyes. The output of the dye laser is frequency doubled by a beta-barium borate (BBO) crystal

to provide a tunable UV source from 290 nm to 350 nm. This tunable UV laser is then used to obtain a high resolution absorption spectrum of NaI to investigate the nature of its non-adiabatic crossing potentials, which will be presented in Chapter 5.

3.1.1 Theory of operation

If a molecule with energy levels E_1 and E_2 absorbs a photon of energy $h\nu = E_2 - E_1$, it is excited from the lower energy level E_1 to the higher energy level E_2 as shown in Fig. 3.1(a). This process is called induced absorption with a total transition rate of

$$P_{12} = B_{21}\rho N_1 \tag{3.1}$$

which is proportional to the Einstein coefficient of induced absorption B_{21}, the energy density of the electromagnetic radiation ρ and the total population N_1 of level E_1.

After the excitation, the molecule in the excited state may spontaneously make a transition to the lower energy level with the emission of a photon as seen in Fig. 3.1(a) in an arbitrary direction.

The radiation field can also induce molecules in the excited state E_2 to make a transition to the lower state E_1 by stimulated emission of a photon possessing the same energy, phase and direction of travel as the inducing photon. The total transition rate of emission is therefore given by

$$P_{21} = (A_{21} + B_{12}\rho)N_2 \tag{3.2}$$

where A_{21} is the Einstein coefficient of spontaneous emission, B_{12} is the Einstein coefficient of stimulated emission and N_2 is the population in the higher energy level E_2.

In thermal equilibrium, the population distribution N_i is given by the Boltzmann distribution

$$N_i = \frac{g_i}{Q} N \, exp(-E_i/kT) \tag{3.3}$$

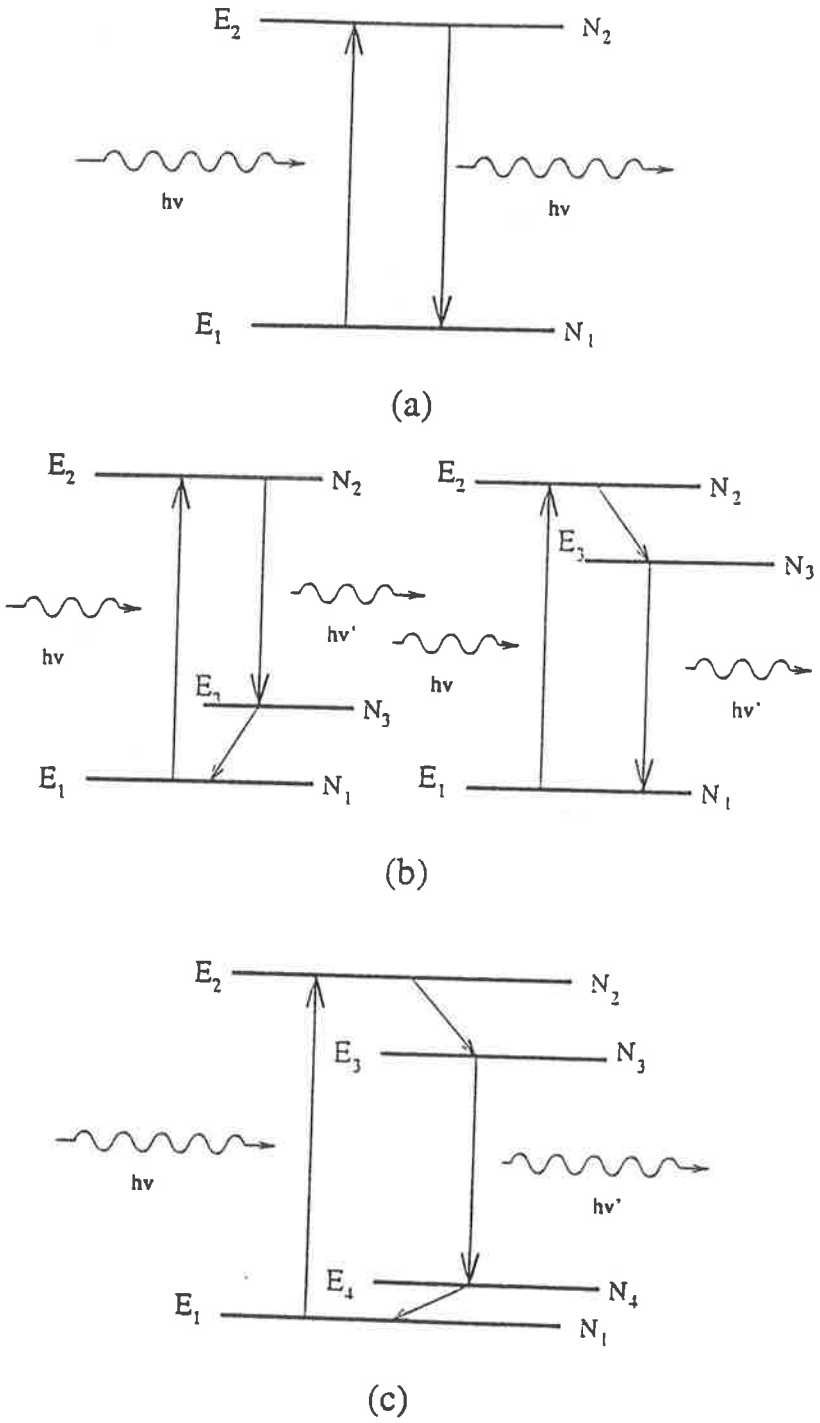

Figure 3.1: The energy levels for absorption and emission of radiation in a two level system (a), three level system (b) and four level system (c).

where the statistical weight g_i gives the number of degenerate sublevels of the energy level E_i and

$$Q = \sum_i g_i exp(-E_i/kT) \tag{3.4}$$

acts as a normalization factor which ensures $\sum N_i = N$.

In the steady state field, the total absorption rate has to equal the total emission rate. It can be shown that because the field obeys the Planck's black body radiation law (Planck, 1900), the relationships between the Einstein coefficients are (Einstein, 1917):

$$B_{12} = \frac{g_2}{g_1} B_{21}, \tag{3.5}$$

$$A_{21} = \frac{8\pi h\nu^3}{c^3} B_{21}. \tag{3.6}$$

Eq. (3.5) states that for levels E_2, E_1 with equal statistical weights $g_2 = g_1$ the probability of induced emission is equal to that of induced absorption. When an external signal is applied to the molecular system (or the active medium), the net transition rate induced is then proportional to the population difference in the upper and lower energy levels. If the lower level is more heavily populated, the signal will be attenuated by induced absorption. On the other hand, if the upper level is more heavily populated, the signal will be amplified by stimulated emission. Therefore, it is necessary to obtain a population inversion between the transition levels for a laser, so that stimulated emission is the net process. This is, however, impossible for a two level system in thermal equilibrium as the Boltzmann distribution Eq. (3.3) indicates that the population in the higher energy level is always less than that in the lower level.

Population inversion can be achieved in a three or four level system as shown in Fig. 3.1(b) and 3.1(c). The ideal system for laser operation is the four level system where the pumping source pumps the population from the ground state E_1 to an excited E_2 which will then relaxes down rapidly through nonradiative processes to another excited state E_3. The population in level E_3 will then make transitions to the lowest excited state E_4 by the emission of radiation where the population will relax

back to the ground state rapidly to avoid an accumulation of the population. When the pumping rate is strong, and the nonradiative relaxation rates of the population from E_2 to E_3 and from E_4 to E_1 are fast, together with a long lifetime level E_3, population inversion can be obtained between energy level E_3 and E_4 and laser action may take place. Gas electronic discharges and optical pumping are the two most widely used pumping processes for these systems.

3.1.2 Laser oscillation and laser cavity modes

Once the population inversion is realized, it is possible to obtain stimulated light amplification by adding mirrors which form a Fabry-Perot etalon as a resonant cavity to introduce signal feedback. This is the final step necessary to produce coherent laser oscillation. In the first stage of the lasing action, spontaneous photons are emitted in every direction. The resonant cavity, by the reflection of the mirrors, will then select photons which propagate along the cavity axis, and feed them back into the active medium to be amplified. Spontaneous emission in all other directions will quickly pass out of the active medium.

The longitudinal resonance for a cavity of optical length L can occur only at frequencies of

$$\nu = \frac{c}{\lambda} = \frac{m\,c}{2L} \tag{3.7}$$

where λ is the optical wavelength in the medium, c is the speed of light and m is an integer. These frequencies correspond to the possible standing waves of the cavity. Hence, there are an infinite number of possible oscillatory longitudinal cavity modes with separation between two adjacent modes of $\Delta\nu = c/2L$ which is the free spectral range of the cavity. However the actual number of longitudinal modes in oscillation is restricted by the bandwidth of the optical gain of the active medium and the Q factor of the resonator. Selection of the longitudinal mode is normally obtained by the insertion of wavelength selection devices into the resonator.

In addition to the longitudinal modes of oscillation, transverse modes can be sustained as well, which refer to the variation of the optical fields in the laser cavity over the cross-sectional planes perpendicular to the laser axis. The lowest order of the transverse mode is the TEM_{00} mode, which has the best beam quality and the flux density is ideally Gaussian over the beam's cross section. The lower the order of the transverse mode, the better beam quality the laser has. Thus, high beam quality is achieved by increasing the optical loss of high order transverse modes, for example, by placing a pin hole inside the cavity.

A narrow bandwidth laser must operate at TEM_{00} mode with a single or few longitudinal modes. As will be seen later, most of the wavelength selection devices are very sensitive to the incident direction of the light beam. Higher transverse modes will then have a broader bandwidth because of the divergence. Operation in a low order transverse mode for a laser pumped dye laser is normally obtained by focusing the pumping laser beam into a very small region of the active medium which limits the beam diameter together with a small pin hole to select the TEM_{00} mode.

Some laser systems have such extremely high gain that they can emit very bright and more or less quasi coherent beams from each end of the laser medium without the mirrors, simply as a result of very high gain amplification of their own internal spontaneous emission traveling along the length of the optical gain medium. This kind of behavior is called *amplified spontaneous emission (ASE), superradiance* or *superfluorescence.* Both the CuBr laser and dye laser used in this study have strong ASE.

A detailed description of the operation of a laser system, the longitudinal and transverse modes, one should refer to the work of Siegman (1986).

3.2 The Dye Laser

The most important characteristic of a dye laser is its tunability. The widest spectral range is covered by pulsed laser pumped dye lasers which can operate at any wavelength from near UV at 311 nm to near IR using different types of dye. Since the discovery of the dye laser by Sorokin in 1966, rapid progress has been achieved in dye laser technology. Tunable dye lasers have found a wide range of applications in fields such as spectroscopy, laser chemistry, isotope separation, trace analysis, cancer treatment, etc. The copper vapour laser (or CuBr laser) pumped dye is often favoured because of its high repetition rate when compared with other pulsed laser systems (YAG, N_2 and excimer lasers) and its high power level giving high conversion efficiency when compared with continuous wave (cw) lasers. This section summarized the basic technique for wavelength tuning and spectral narrowing as it relates to this study.

3.2.1 Spectral narrowing and tuning of dye lasers

Organic dyes are characterized by a strong absorption band in the visible region of the electromagnetic spectrum. The energy levels of a typical dye molecule in solution are shown in Fig. 3.2. There are a manifold of singlet electronic states, S_0 ... S_n and triplet states T_1 ... T_n which are of importance for the operation of the dye laser. Each electronic state has a number of vibrational levels superimposed on it. In addition, each vibronic level has closely spaced rotational levels superimposed on it. These rotational levels are broadened by frequent collisions with solvent molecules and form a near continuum between each vibrational level. These give rise to the characteristic broad, structureless absorption and emission bands in the electronic spectra of dye molecules in solution. In thermal equilibrium most of the molecules are in the lowest vibrational level of S_0. Thus in the absorption of pump radiation, the molecule may be excited to the first excited single state S_1, or higher excited singlet states S_n $(n > 1)$ with UV

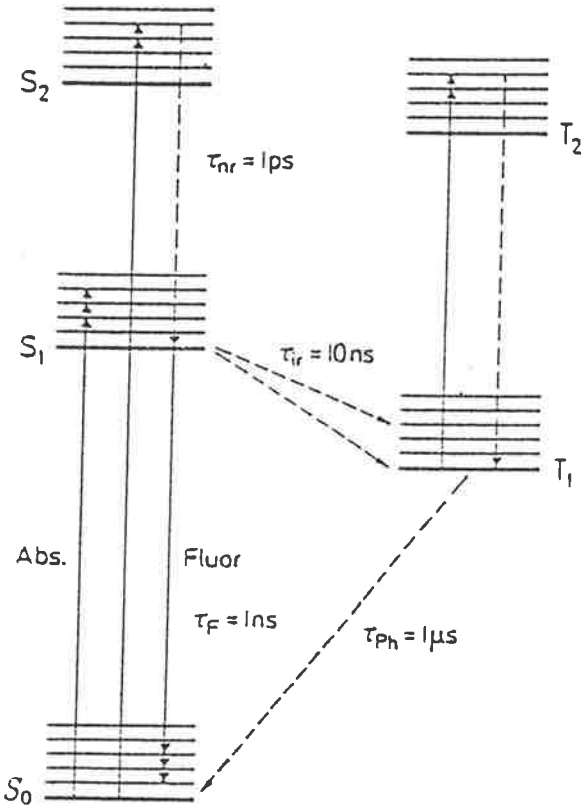

Figure 3.2: The energy levels of a typical dye molecule with radiative (solid lines) and non-radiative (broken lines) transitions.

pump sources. There are various rapid nonradiative relaxation processes in the excited states of dye molecules, which accumulate the population in the lowest states of S_1. Stimulated emission then occurs with the transition from the lowest vibronic level of S_1 to higher vibronic levels of S_0 which are initially un-populated so that population inversion is satisfied. Rapid relaxation processes through various nonradiative processes in the ground states depopulate in the lower state of the transition to the lowest state of S_0. There are also intersystem nonradiative relaxation processes which transfer population from the singlet state S_1 to the triplet state T_1. It was found that such processes are related not only to the dye molecular structure but also the environmental effects (Schäfer 1973, Nair 1982). Since transitions from the triplet states to singlet states are optically forbidden these processes are undesirable in a dye laser system and should be minimized by choosing the correct dye compound and solvent.

Spectral narrowing and simultaneous tuning of dye lasers can be obtained by introducing wavelength selective devices into the resonator. The following methods for wavelength selection are widely employed :

- Resonators including devices with spatial wavelength separation such as prisms and gratings;
- Resonators including devices for interferometric wavelength discrimination such as a Fabry-Perot etalon;
- Resonators including devices with rotational dispersion such as birefringent filters.

With these wavelength selective devices inside the resonator, the optical gain becomes strongly wavelength dependent and determines the wavelength and the bandwidth at which laser action occurs.

The spectral width of the dye laser depends mainly on the single pass bandwidth of the resonator and the number of light passes in the resonator. For the most

commonly used wavelength selection device such as prisms and gratings, the single pass bandwidth is determined by the angular dispersion of the wavelength selector and the divergence of the laser radiation incident on it. Normally, the higher the angular dispersion, the higher the optical loss the wavelength selection devices introduce in the resonator. Hence in the cw dye laser, where the optical gain is low, comparatively narrow bandwidths are obtained by the use of low dispersion tuning elements such as prisms and birefringent filters. For pulsed dye lasers, due to the high gain and only a few passes in the resonator, high dispersion elements such as gratings can be used. For narrower linewidths and single mode operation, interferometric devices such as Fabry Perot etalon are used in conjunction with the above tuning element both for pulsed and cw dye lasers.

3.2.2 Practical alignment of a pulsed dye laser

There are a large number of different grating configurations for high peak power pulsed pumping sources which have high optical gain among which are the often used Hänsch and the grazing-incidence (or Littman) configuration after the designs of Hänsch (1972) and Littman (1978). A short review of the relevant designs is presented in the following giving their strengths and weaknesses and hence the basis on which the present dye laser was built.

The Hänsch configuration

A typical arrangement for a Hänsch type cavity is shown in Fig. 3.3. It consists of a dye cell, beam expander, a diffraction grating in a Littrow mount and a plane output coupling mirror at the other end of the optical cavity. Tuning of the wavelength is obtained by the rotation of the grating. This design was first described by Hänsch (1972) with a N_2 laser of 100 Hz repetition rate as the pump source. A reverse telescope was used as the beam expander. Conversion efficiency of up to 20% was easily obtained

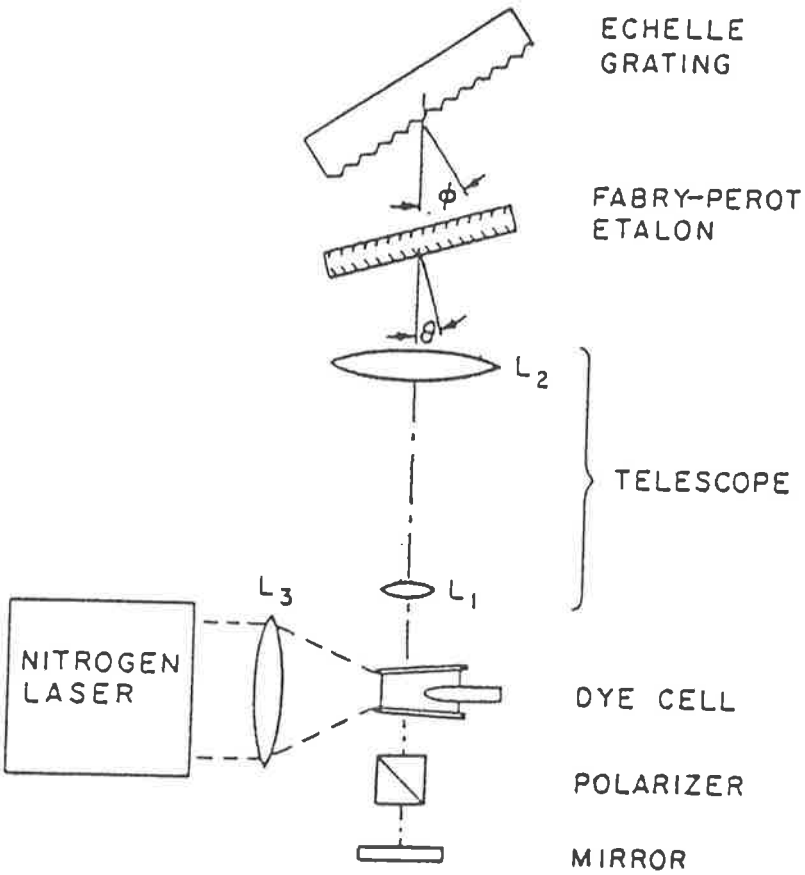

Figure 3.3: Basic components of narrow band tunable dye laser with the Hänsch configuration (After Hänsch, 1972).

with this dye laser system for operation near 600 nm using a 5×10^{-3} M/liter solution of Rhodamine 6G in ethanol. With careful adjustment of the collimating telescope, a bandwidth of 0.03 Å (FWHM) can be obtained. Insertion of a Fabry-Perot etalon with a free spectral range of 0.57 cm^{-1} into the collimated beam reduced the bandwidth to 300 MHz or less than 0.004 Å.

A pulsed dye laser is often characterized by its spectral width (exclusive of intracavity etalon) which is determined by diffraction and the beam expander-grating combination. The single pass bandwidth of a Littrow grating tuned resonator is given by (Hänsch 1972):

$$\Delta\lambda = \frac{\lambda^2}{\pi l_g sin\phi} \tag{3.8}$$

where $l_g = 2w_2/cos\phi$ is the length of the illuminated part of the grating and w_2 is the beam radius after the beam expander. It is noted that the spectral bandwidth of such a laser depends on the illuminated width of the grating l_g (perpendicular to the grooves) and not on the height, diffraction order, or groove spacing.

Because the beam diameter of the laser is normally very small, it is necessary to use a beam expander inside the cavity to achieve maximum illumination on the grating and so obtain narrow bandwidth. In recent years much effort has been devoted to find technologies for increasing the expansion ratio of the beam expander, to reduce the optical cavity length and optical loss due to the insertion of optical components in the cavity as well as to reduce alignment problems and cost. Prism beam expanders (Hnilo and Manzano 1985, Niefer and Atkinson 1988), as shown later in Fig. 3.8, which expand the beam in one dimension only are one of the most successful replacements for the telescope. Moreover since only one dimension of the beam is expanded, the large grating can be replaced with a less expensive thin strip only a few mm high.

The grazing-incidence grating configuration

An alternative cavity configuration which does not need a device to expand the beam, yet it still provides a spectrally narrow high power output was developed by Littman (1978) which is known as the Littman type or grazing-incidence configuration.

A typical dye laser oscillator in the grazing-incidence grating configuration (Littman, 1978) is shown in Fig. 3.4 where the grating is not mounted at the Littrow angle and the laser wavelength is tuned by rotation of the tuning mirror. In this Littman type cavity, the grazing-incidence grating acts as a beam expander when θ_0 is close to 90^0. Design advantages of this dye laser oscillator include:

- The expensive high quality achromatic telescope or prism expander is eliminated.
- Alignment is simple. Careful adjustment and focusing of the beam expander are not necessary.
- Elimination of the beam expander reduces the number of surfaces in the optical cavity resulting in fewer reflection losses.
- The laser can be made extremely compact so that short duration pump light can be used more effectively. Furthermore, the longitudinal modes have a large frequency separation due to the compact cavity. This makes it much easier to obtain single longitudinal mode operation.

The single pass bandwidth of a grazing incidence-grating dye laser is given by (Littman, 1978)

$$\Delta\lambda = \frac{\sqrt{2}\lambda^2}{\pi l_g(sin\theta_0 + sin\phi)} \tag{3.9}$$

which is similar to that of the Hänsch type.

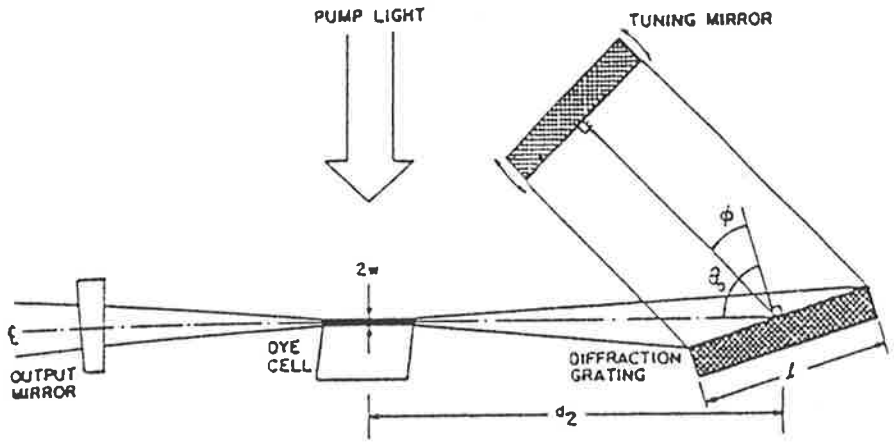

Figure 3.4: Schematic diagram of basic grazing incidence (Littman configuration) dye laser (After Littman, 1978).

Multi-pass bandwidth

Multiple passes of laser pulses inside a resonator will further compress the linewidth. An estimate of the dependence of time averaged linewidth on the resonator length or pulse width was given by Flamant (1978) for pulsed dye lasers which use Fabry-Pérot etalons, a grating or prisms for spectral narrowing. For times $t \gg T_{RT}$, where $T_{RT} = 2L/c$ is the time a laser pulse take a round trip inside the resonator and L is the optical length of the resonator, the laser linewidth at time t for a grating-tuned system is:

$$\delta\nu(t) = \delta\nu_0(2ln2)^{1/2}(T_{RT}/t)^{1/2}, \tag{3.10}$$

where $\delta\nu_0$ is the passive linewidth of the resonator. Therefore the time averaged laser linewidth is

$$\bar{\delta\nu} = \left(\frac{\delta\nu_0(2ln2)^{1/2}}{T}\right)\int_0^T (T_{RT}/t)^{1/2}dt \tag{3.11}$$

$$= 2(2ln2)^{1/2}\left(\frac{T_{RT}}{T}\right)^{1/2}\delta\nu_0 \tag{3.12}$$

$$= 4\left(\frac{ln2}{cT}\right)^{1/2} L^{1/2}\delta\nu_0 \tag{3.13}$$

where T is the observed pulse duration of the laser.

3.3 Copper Bromide Laser Pumped Pulsed Dye Lasers

Since the copper bromide (CuBr) laser (or copper vapour laser) pumped dye lasers fit well into the gap between a low-power cw system and a high power pulsed system with a low repetition rate, they can successfully be built using the technology which applies either to cw or pulsed dye lasers. Therefore, there are a number of cavity configurations which would be able to provide a narrow bandwidth laser operation with high conversion efficiency.

In this section, different configurations of the dye laser system related to this work are reviewed and compared. A novel design of a longitudinally pumped pulsed dye laser resonator using grazing incidence in a folded astigmatic cavity employing a free flowing dye jet from a nozzle is described. A CuBr laser pumped dye laser system with master oscillator-power amplifier (MOPA) configuration was then designed and constructed. The oscillator used a grazing incidence grating with an open dye stream jet and a three mirror folded cavity configuration. It produced good beam quality laser pulses with a bandwidth of about 1-2 GHz. The laser pulses were then amplified by an amplifier jet to obtain a total average power of about 230 mW. In the following, we will describe each part of this dye laser system. When necessary, a review of the work on related subjects by other authors is given.

3.3.1 The copper bromide (CuBr) laser

The pulsed CuBr laser used in this study is characterized by a high repetition rate, high average power, long lifetime and is a promising alternative to the copper vapor laser (CVL).

It is known that lasing transitions can occur from a resonance to a metastable level in metal atoms. One of the most important requirement and difficulties for metal vapor lasers is the need to provide a sufficient concentration of working atoms in the active volume which is normally achieved by heating the metal. The CuBr laser, however, introduces the working atoms (copper) into the active volume by the dissociation of the chemical compound, CuBr, in a pulsed discharge. This is the most important advantage of the CuBr laser because to vaporize the CuBr into the active region the temperature only needs to reach 500 ^{o}C rather than the 1600 ^{o}C for a copper vapor laser. The discharge and therefore the laser operates at a repetition rate of 16 kHz and is self-heating through the discharge with the CuBr supplied through heated CuBr reservoir. The CuBr laser as well as the copper vapor laser operates at two atomic

transitions of copper, 510.6 and 578.2 nm.

The CuBr laser used in this study was manufactured by Norseld Pty. Ltd. in Adelaide. The laser beam is 25 mm in diameter and is horizontally polarized by Brewster windows of the laser tube. The power ratio between the green (510.6 nm) and yellow (578.2 nm) lines is about 2:1 and the pulse width is about 30 ns.

Both a flat-flat mirror cavity and an unstable cavity were used in this study. While the flat-flat cavity is one of the most efficient ways to extract laser power from the CuBr laser, the unstable cavity provides a much improved beam quality and hence higher focusable power. One of the most frequently used unstable cavities for the CuBr laser (or CVL) is formed by a pair of confocal mirrors as shown in Fig. 3.5(b). The convex mirror M_2 and concave mirror M_1 form a telescope with a cavity magnification given by the ratio of their focal lengths. Light making a round trip in this cavity is expanded by this telescope so that its divergence is correspondingly reduced by a factor equal to its magnification. For example, with a magnification of 10, the light making a round trip inside the cavity will reduce its divergence by a factor of 10, two round trip will improve the beam quality by 100 times and so on until the beam quality approaches the diffraction limit. However, due to the short gain period of CuBr laser which is less than 50 ns, there are only a few round trips during each laser pulse. It is then only during the latter half of the laser pulse that good beam quality is obtained. Near diffraction limited divergence beam quality can only be obtained with high magnification (Coutts D.W. et al, 1993). Moreover, because of the high gain of the active medium, there is a strong presence of amplified spontaneous emission (ASE) in the cavity during the entire laser pulse. This severely limits the achievable beam quality because the cavity feedback includes this highly divergent ASE (Chang 1994). The higher the magnification, the higher optical loss of the cavity, and therefore the lower of the total power. In spite of the lower output power from the laser tube, the unstable cavity offers a higher focusable power which is preferable for many applications.

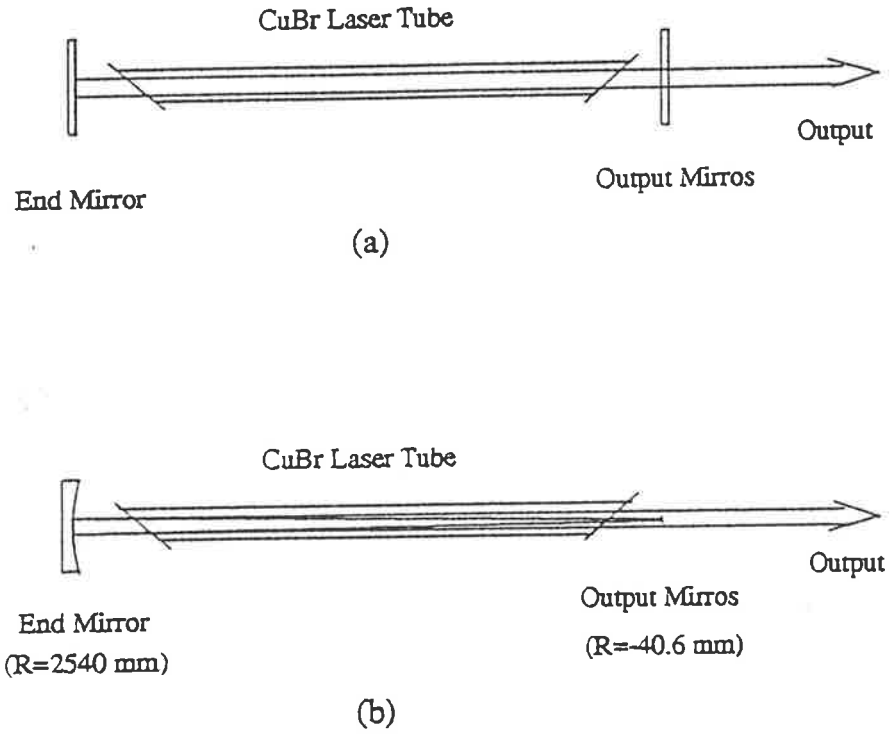

Figure 3.5: The flat-flat cavity (a) and the unstable cavity (b) of CuBr laser.

In this study, an unstable cavity with a magnification of 62.5 was used to improve the beam quality for focusing most of the laser power into a small region, about 100 μm in diameter, in the dye jet stream. The total power of the laser tube was 10 W with this unstable cavity while a total power of 13 W was obtained with the flat-flat cavity.

3.3.2 The active medium of the dye laser – a free flowing jet stream

With a high power laser as the pump source, it is very easy to damage the window of the dye cell cuvette. Furthermore the window also induces aberration losses when placed at Brewster's angle and there are problems with the seal with the metal body. In an attempt to overcome these problem Runge and Rosenberg (1972) proposed a laser where the dye solution flows in a free jet stream through the resonator of the laser. A windowless open free jet which is formed through a carefully designed polished nozzle has been successfully used to produce high output power as well as very narrow bandwidth dye lasers. It is more commonly used for cw and mode-locked dye lasers than a dye cell cuvette.

For CuBr lasers (or CVL) both jet stream and the dye cell cuvette can be used, however in addition to the advantages previous stated, a jet nozzle can also produce very high velocity dye stream which replaces the dye solution in the active zone for each successive pump pulse. This removes the heat produced by nonradiative processes and the dye molecules in the triplet states generated in the active region. Berry et al (1990) found that this is necessary to achieve high conversion efficiency operation of a narrow band width dye laser.

Although employing a free flowing jet stream in a CuBr (or CVL) pumped narrow band width dye laser system appears to have the above advantages, a thorough

literature search revealed no reports of work on such a system, except for broad band operation. One reason may be the relatively poor beam quality of the CuBr laser (or CVL) with the flat-flat cavity which prevents the laser beam being focused onto a very small spot on the jet stream. This reduces the conversion efficiency because it reduces the power density of the pump laser in the jet. Furthermore, the large size of the active zone may enable the oscillation of a second transverse mode, thus, increasing the beam divergence and the bandwidth. However, this problem can be overcome by employing an unstable cavity in the CuBr (or CVL) laser. A broad band dye laser system employing a jet nozzle pumped by a CuBr laser with unstable cavity has achieved a conversion efficiency up to 63% (Petrov et al, 1992), the highest reported.

Preliminary experiments were performed on a dye cell cuvette and a jet stream with both systems employing a prism as the tuning element. The experimental arrangements are shown in Fig. 3.6. The output coupler is a flat mirror with 45% transmission and the end mirror is a high reflectivity concave mirror with a 245 mm radius. The dye solution was a 3×10^{-3} M/l Rh-6G dissolved in ethylene glycol. The CuBr laser was a flat-flat cavity configuration. The yellow line was removed by a dielectric mirror because it is not absorbed by the dye and therefore does not contribute to the pumping. In addition it can be amplified by the dye jet, reducing the gain for the dye laser. The dye cell cuvette provided a poor performance in output power, beam quality and ASE background, while the jet stream system produced a very good result. The flow rate of the jet was about 1.2l/min and the thickness of the jet was 0.35 mm which gives a flow speed of 6m/sec. The energy conversion efficiency peaked at 36.1% when the pump power was 3.5 W. The power of the dye laser was up to 2.4 W with a very good beam quality and low ASE background with the maximum pump power of 7 W . No attempt was been made to optimize the parameters of the dye laser to increase the conversion efficiency because this study was not concerned with broad band operation.

Due to the outstanding performance of the jet stream nozzle over dye cell

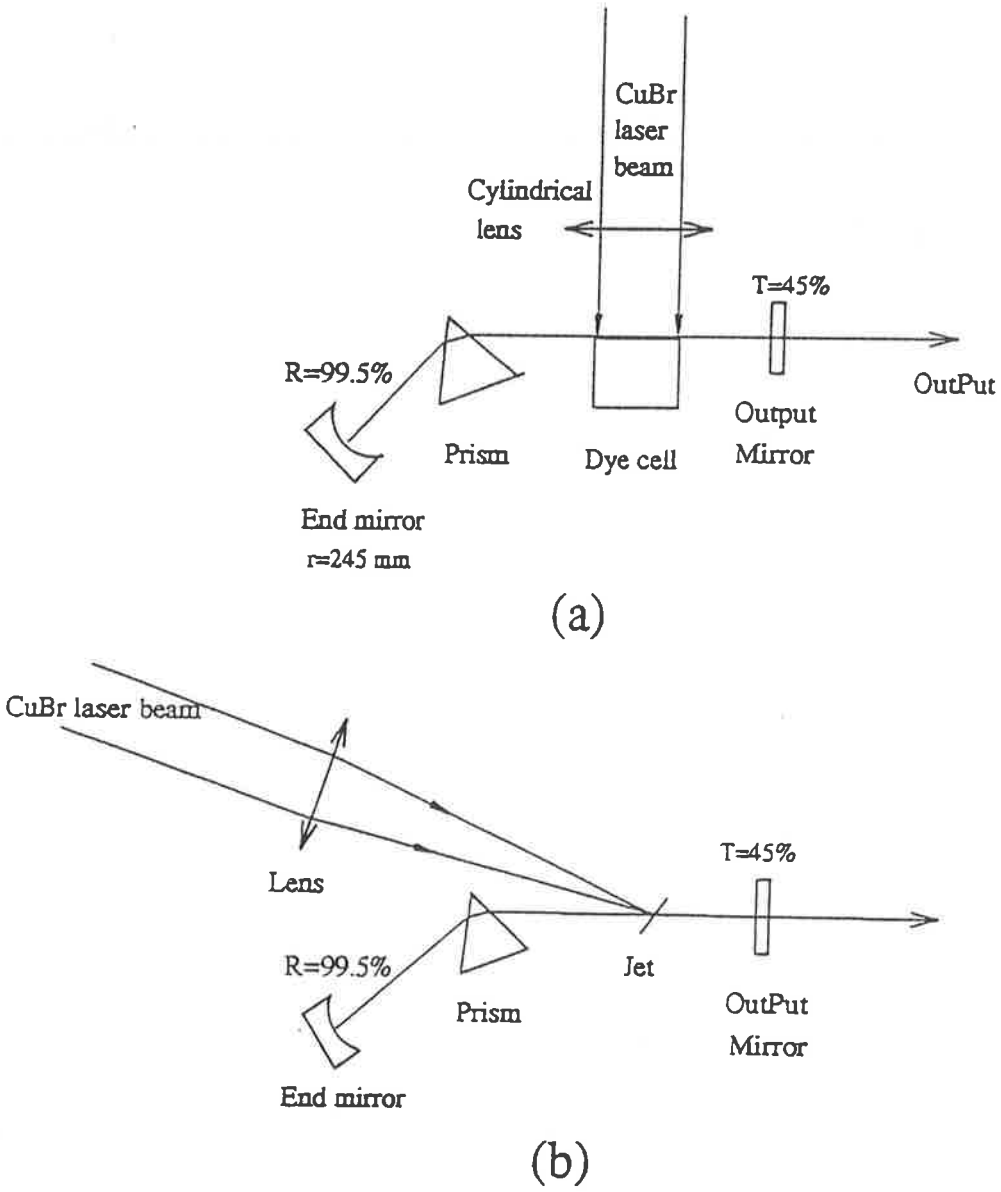

Figure 3.6: Experimental setups for the preliminary experimental test for a dye cell cuvette (a) and a dye stream jet (b).

cuvette in broad band operation, our dye laser system was constructed with free-flowing dye jet streams which were formed by flowing dyes in ethylene glycol solutions through nozzles produced by compressing stainless steel pipes against an internal spacer. With very careful polishing of the nozzle a good quality jet stream was obtained. An unstable cavity was then employed in the CuBr laser to improve the beam quality for focusing.

A dye jet stream can easily be placed at the Brewster angle to the axis of the resonator to produce polarized laser radiation. This also reduces the optical loss by reflection from the dye stream surfaces of the polarized pump beam which was focused onto the jet stream at or close to the Brewster angle.

3.3.3 Cavity design

There are a number of cavity configurations for CuBr laser (or CVL) pumped dye lasers which are able to produce narrow bandwidth laser operation with high conversion efficiency. As the CuBr laser is only commercially available from Norseld and is currently manufactured for medical applications, most of the following review were given for CVL since their lasing characters are the same.

For broadband laser operation, Huang and Namba (1981) operated a longitudinally pumped jet stream system and obtained 31% conversion efficiency. In a transversely pumped configuration, Broyer and Chevaleyre (1984) reached up to 40% conversion efficiency. Sun et al (1986) obtained 40% conversion efficiency using a longitudinally pumped jet stream in a three mirror folded cavity. A 63% broadband conversion efficiency was claimed by Petrov et al (1992) using the same configuration as Huang and Namba (1981) with a better quality jet stream.

For narrow bandwidth dye laser operation with the Hänsch design, Bernhardt and Rasmussen (1981) employed a four prism beam expander with an etalon to obtain single longitudinal mode operation with a bandwidth of 60 MHz and a conversion

Table 3.1: Measured Performance (at 5800 Å) on the Six Cavity Arrangements Shown in Fig. 3.8 and Fig. 3.9 (After Duarte and Piper, 1982)

Parameters	Dye Laser System					
	Prism cavities			Grazing-incidence cavities		
	A1	B1	C1	A2	B2	C2
ϕ_1	89.3	89.3	84.4			87
ϕ_2			84.4			
θ				89.5	89.5	85
$\Delta\lambda$(Å)	0.016	0.016	0.017	0.009	0.01	0.01
$P_0(kW)$	15	1.5	7	11.5	1.6	5.6
Energy eff (%)	23	2.2	10	16	2.3	8
ASE (%)	0.09	< 0.01	< 0.01	0.1	0.01	< 0.01

efficiency of 5%. With a Hänsch type oscillator combined with an amplifier, Lavi et al (1985) were able to obtain up to 45% total conversion efficiency with a bandwidth of 2 GHz. By using a double-prism beam expander and an intracavity etalon Yoichiro Maruyama et al (1991) obtained frequency stabilized single-mode operation with a bandwidth of 60 MHz and a frequency drift for long term operation of within 30 MHz.

The grazing-incidence configuration provides a more flexible arrangement for practical applications. Broyer and Chevaleyre (1984) reported a 20% conversion efficiency with a bandwidth of 3 GHz by a Littman design cavity as shown in Fig. 3.7(a). Second harmonic generation (SHG) of the dye laser output covered a UV range between 260 nm to 408 nm at a conversion efficiency of $\leq 5\%$.

Duarte and Piper (1982) evaluated a number of prism-expander and grazing incidence grating cavities pumped by a low repetition rate (1 Hz) CuBr laser. Experimental results are reproduced in Table 3.1 for different cavities shown in Fig. 3.8

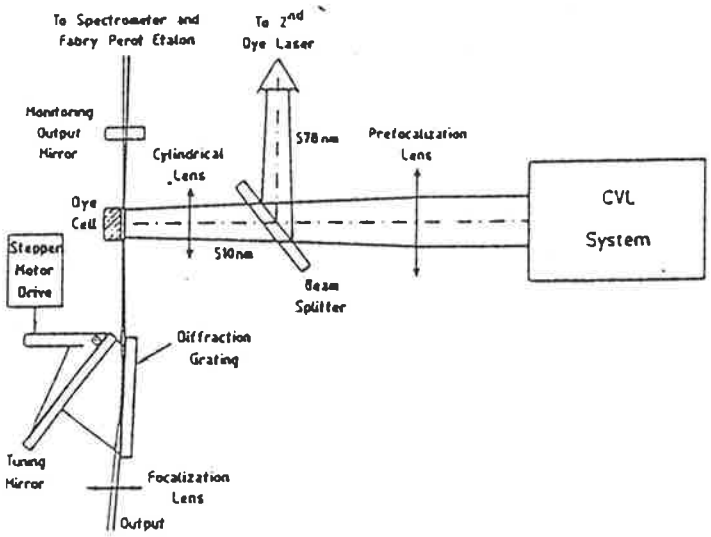

(a)

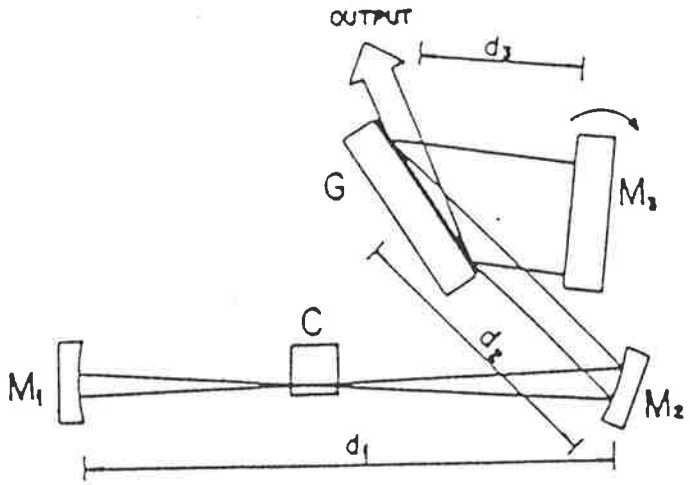

(b)

Figure 3.7: (a). Experimental setup of the CVL-pumped dye laser system operating with a grazing incidence grating cavity. (after Broyer and Chevaleyre, 1984). (b) Schematic diagram of dye laser with grazing incidence and folded cavity (after Lago et al, 1989).

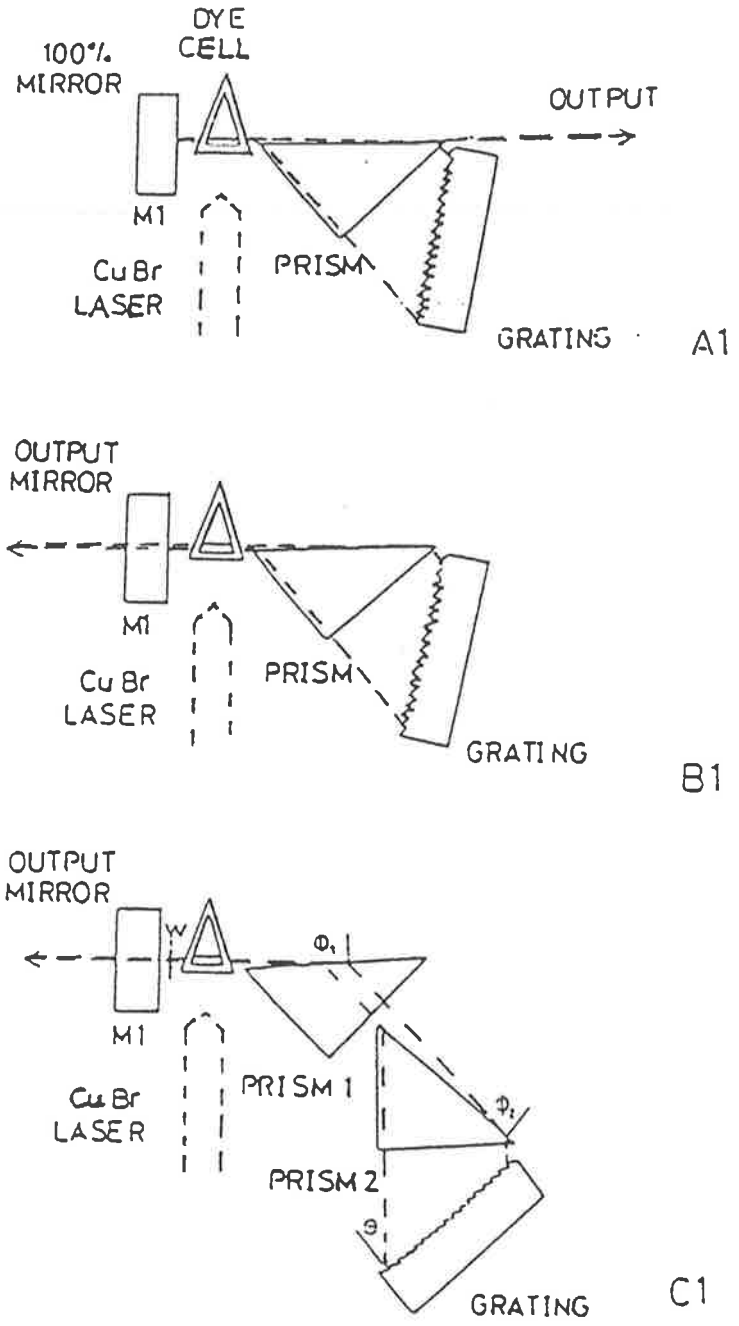

Figure 3.8: Schematic diagram of dye laser cavities incorporating prism beam expanders: A1 shows an open cavity single-prism arrangement, B1 is a closed cavity single-prism layout, and C1 shows a closed cavity double-prism configuration. (Duarte and Piper (1982)

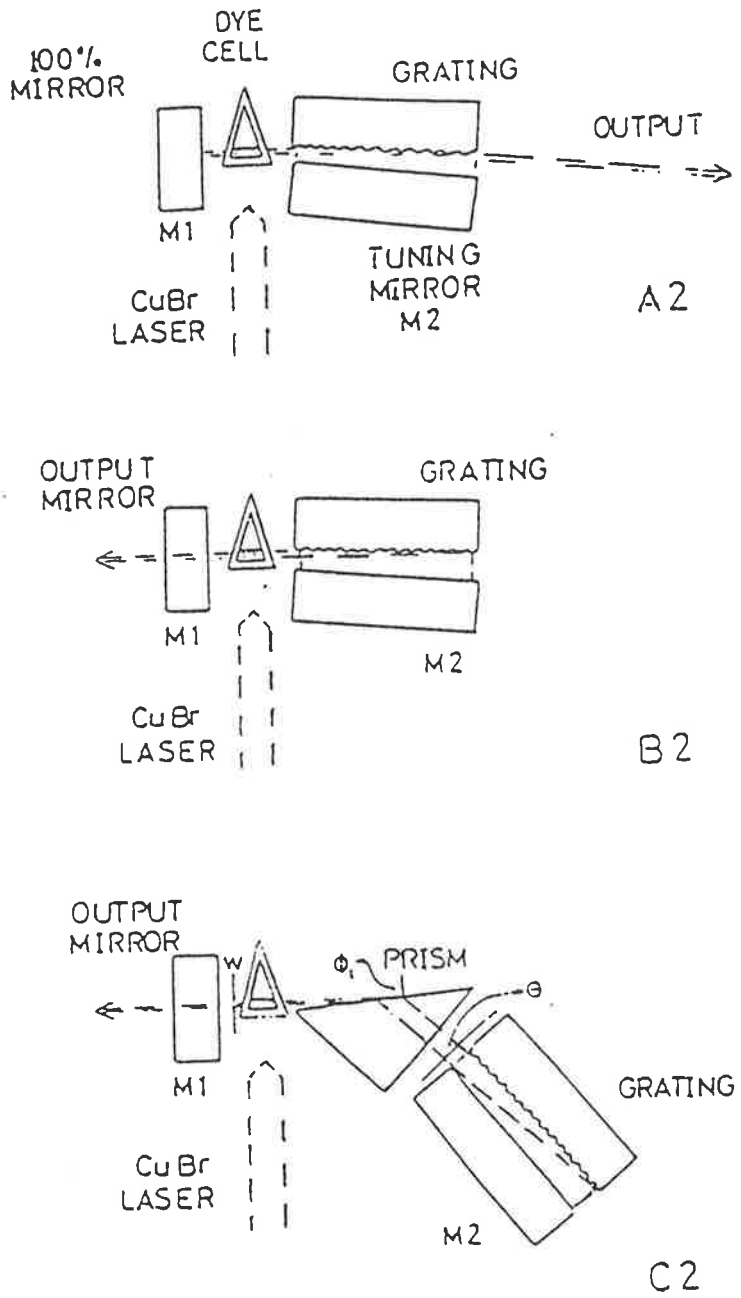

Figure 3.9: Schematic diagram of grazing-incidence dye laser oscillators. A2 shows an open cavity configuration, B2 is a closed cavity layout, and C2 shows a prism pre-expanded grazing-incidence cavity. (Duarte and Piper (1982)

and Fig. 3.9 which displays a better overall performance for the Littman designs than the Hänsch designs. Linewidths of $\sim$ 0.01 Å at an energy conversion efficiency up to 10% were obtained for a prism pre-expanded grazing-incidence grating cavity with good beam quality and low background superluminescence ($< 0.01\%$). Thus, grazing incidence configuration was employed in this study because of its advantage over the Hänsch configuration in performance, alignment and cost.

It was found that insertion of a lens in the cavity of a grazing-incidence pulsed dye laser will increase its performance with higher output power and narrower spectral width (Lisboa et al, 1983 and Yodh et al, 1984). The reason is as follows. In the grazing-incidence configuration, there is a severe limitation which concerns the overall efficiency with which the light, at a given wavelength, can be fed back to the amplifying medium. While the selection of a holographic grating having a high number of lines/mm can eliminate the additional loss of light into other unwanted diffraction orders, conversion efficiency is limited by diffraction losses which reduce the overall feedback efficiency. If the laser beam emerging from the dye cell has a beam waist of w_0, which is normally very small, it will increase in diameter quickly as it travels away from the cell because of diffraction. The beam diameter will be $w(2l)$ when it returns to the cell after the reflections from the tuning mirror and the grating, where l measures the mean distance between the cell and the mirror. Therefore only $(w_0/w(2l))^2$ of the beam is fed back to the active medium. This factor is normally about 0.1 or less. The insertion of a carefully chosen lens in the cavity increases this factor to nearly unity. Furthermore a more collimated beam incident to the grating also reduces the linewidth.

In a modified version of this design, Lago et al (1989) reported a further development of this collimated grazing incidence cavity by introducing a stable folded cavity. The divergent beam emerging from the dye cell was collimated by the folding mirror M_2 as shown in Fig. 3.7(b). The highly reflective mirror M_2 resulted in lower optical losses than the insertion of an intracavity lens. The linewidth was found to

be adjusted by changing the incidence angle in the diffraction grating and could be reduced down to 610 MHz. Conversion efficiency of about 10% was obtained for a linewidth of 1 GHz. This configuration has the advantages of increasing the output power, narrowing the bandwidth and ease of alignment.

In view of all the considerations discussed above, we adopted the grazing incidence folded cavity configuration used by Lago et al (1989) but using a dye jet stream with a thickness of about 0.5 mm rather than a dye cell cuvette.

3.3.4 Experimental performance

The experimental set up for the grazing incidence oscillator and jet amplifier is shown in Fig. 3.10. In the oscillator, the divergent beam emerging from the dye jet stream, longitudinally pumped in a folded cavity, was collimated by the folding mirror (M_2) and directed to the diffraction grating, which increases the feedback efficiency and therefore the conversion efficiency. The holographic diffraction grating used was a Jobin Yvon, 2400 lines/mm with dimensions of 58×17 mm^2. The tuning mirror (M_3) fed back the first diffracted order into the laser. Precise wavelength scanning was obtained with a DC motor driven rotational stage (Oriel standard rotator with D.C. Encoder Mike^{TM} Drive, model 13118) which was modified with an extended cantilever arm to reduce the rotational speed by 5.3 times for the tuning mirror. The readout resolution of the Encoder Mike Drive is 0.1 microns which corresponds to an angular resolution of 31 μrad or 0.06 arc sec, or a change of $10^{-3}\mathring{A}$ (70MHz) in wavelength (frequency). A spherical mirror (M_1) closed the cavity on the other side of the dye jet. The output coupling was through the zeroth order of the diffraction grating. The output from the dye laser oscillator was then focused into another dye jet stream which was used as an amplifier. It was found necessary to use a pressure buffer and soft latex tubing to remove pressure pulses in the dye circulation produced by the dye gear pump to obtain a narrow bandwidth laser system.

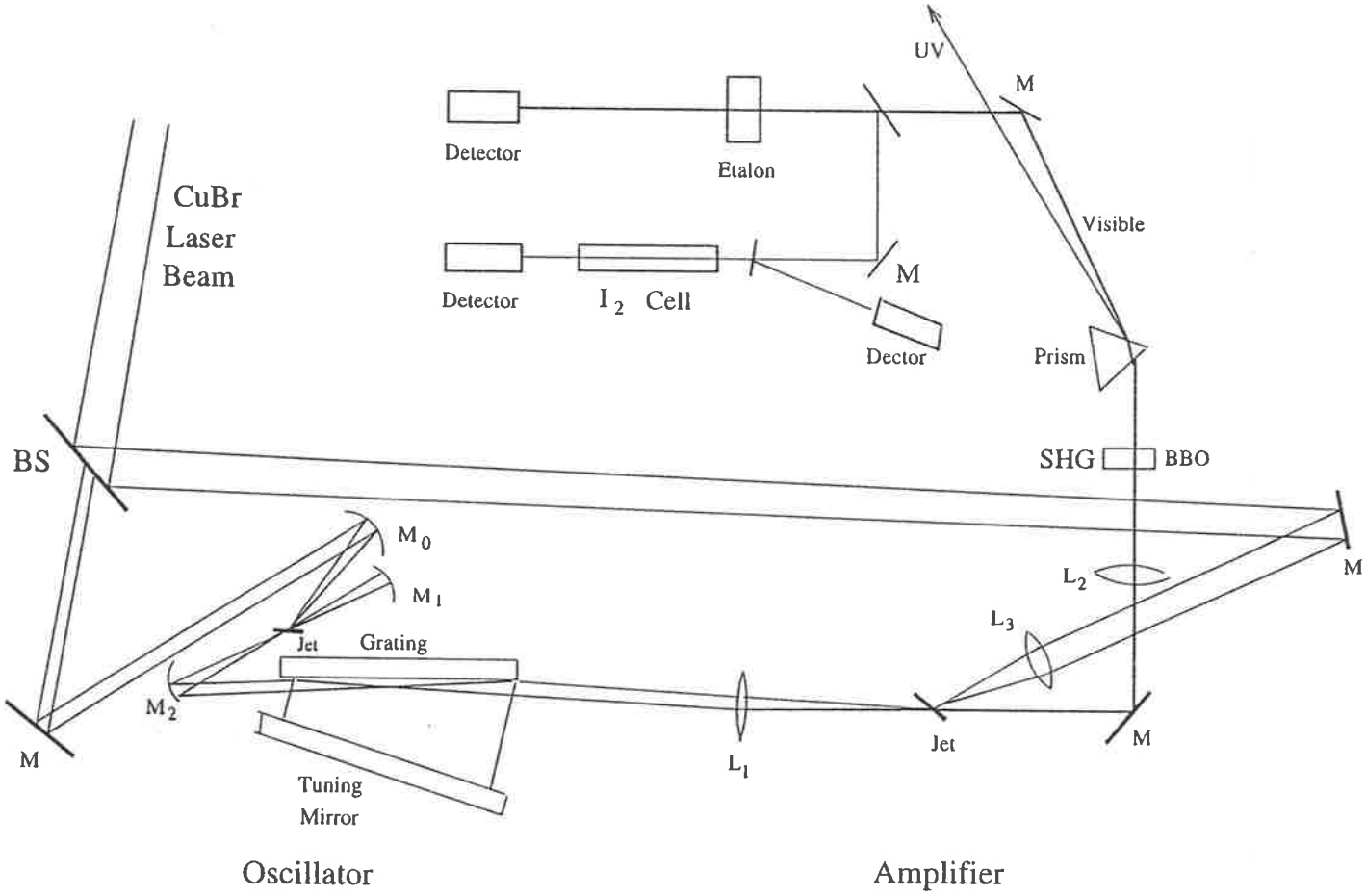

Figure 3.10: Experimental alignment of the CuBr laser pumped dye laser system operating with a folded cavity, longitudinally pumped jet stream and grazing incidence grating configuration

The pumping laser was a CuBr laser, as described before, operating at 16 kHz with a pulse width of 30 ns. It was found in this study that with a flat-flat cavity, the focused spot in the jet stream may move around in a very small region corresponding to the some unstable discharge in the CuBr laser tube which affects the intensity distribution of the laser beam. This affected the stability of the dye laser through movement of the pump laser beam on the dye jet preventing narrow band width lasing operation. It is therefore necessary to employ an unstable cavity in the CuBr laser to improve the beam quality and stability. With a magnification M=62.5 (concave mirror R=2540 mm, convex mirror R=−40.64 mm), output power of the CuBr laser was about 10 W. With a focusing mirror M_0 (R=129.20 mm), the CuBr laser beam could be focused into a spot which was sufficiently small to vaporize the dye solution and it had to be slightly defocused. A prism was used to separate the green and yellow lines when Rh-6G or DCM dye was used. The linewidth was measured by a solid etalon with a free spectral range (FSR) of 10 GHz and a finesse greater than 25 (Melles Griot, product No. 03ETA013).

A great deal of experimentation on jet design and construction was carried out including knife edge jets. The quality of the jet stream was investigated by observing the flowing pattern using a He-Ne laser and was found to be equal to those reported in the literature.

Due to the imperfections in the jet nozzle and the inherent instability of rapidly flowing fluids, the dye stream became unstable for high flow rates affecting the frequency stability and the band width. A variable speed micropump was then employed to enable variation of the flow rate. It was found that, in narrow bandwidth operation, some instability of the jet stream was still apparent even if the flow rate was kept very low and the grazing angle had to be increased to reduce the bandwidth and frequency jitter and consequently limit the power from the oscillator. To improve the dye laser performance, a master oscillator-power amplifier configuration was employed. A beam

splitter which is a high reflection mirror with a 4 mm hole in the center allows the center of the CuBr laser beam to be transmitted (about 1/3 of the total power) and pump the oscillator. The rest of the beam is directed to pump the amplifier with a delay of 3 ns after the input from the oscillator. This delay is approximately the duration of one oscillator round trip.

A dye laser oscillator cannot be efficient if the requirements for bandwidth and beam quality are to be met. In our dye laser system, the oscillator was kept just above the lasing threshold so that it had a good performance in bandwidth and beam quality. The power amplifier was then used to increase the conversion efficiency of the system. With a 1.5×10^{-3} M/liter Rhodamine 6G solution in ethylene glycol for the oscillator and amplifier, the output power from the oscillator is about 20 mW with a bandwidth of 2-3 GHz when the pumped power is 1.2 W. The pulsed width of the dye laser was found to be about 10 ns. A gain of 11 is obtained in the amplifier with a pumped power of 3 W, resulting a total output power of 230 mW and a overall conversion efficiency of more than 5%.

A bandwidth of about 1 GHz was also achieved with 3×10^{-3} M/liter DCM in 2:1 ethylene glycol and propylene carbonate solution. The total power of the dye laser is about 100 mW. Fig. 3.11 shows a Fabry-Perot scan for such operation.

3.4 Second Harmonic Generation and Wavelength Calibration

The ultraviolet radiation was produced by frequency doubling the output of the dye laser using a BBO nonlinear crystal, while the wavelength calibration was made using the fundamental wavelength with an I_2 cell.

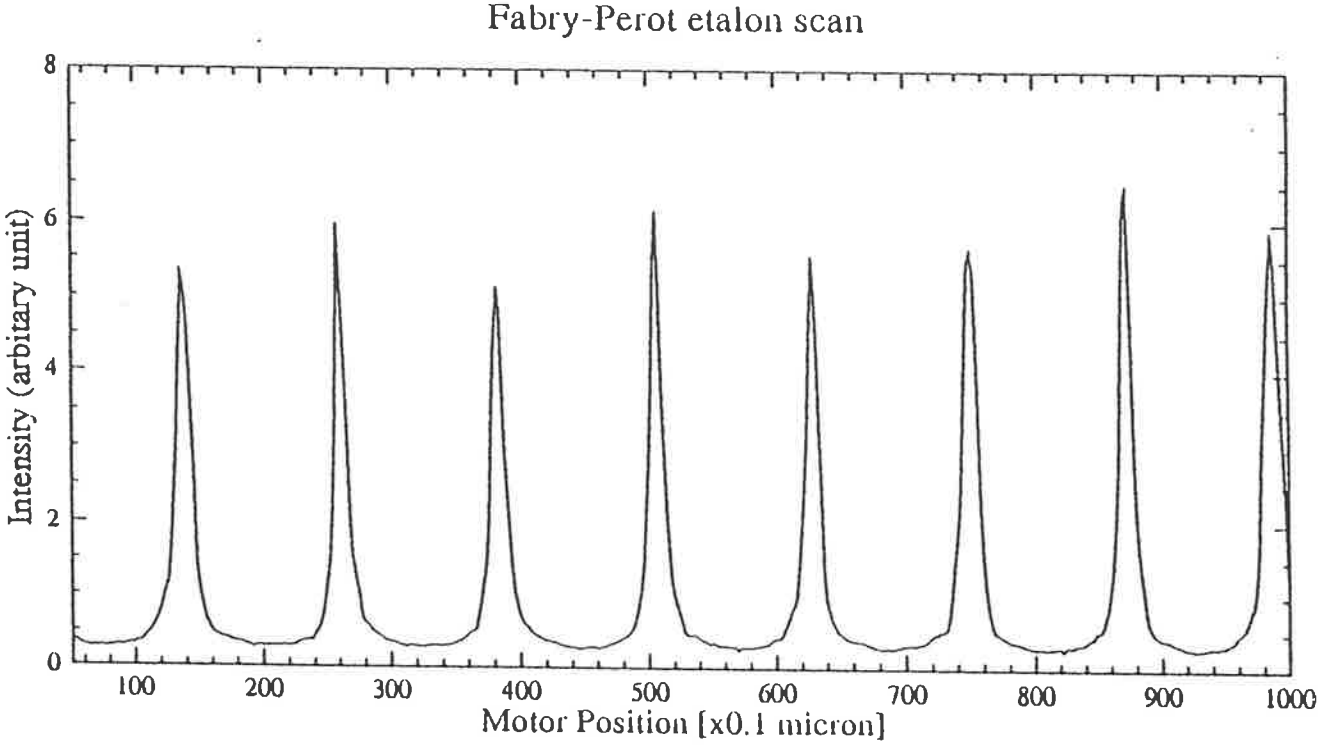

Figure 3.11: A Fabry-Perot etalon scan for the CuBr pumped dye laser with DCM. The free spectral range of the etalon is 10 GHz, indicating a 1 GHz bandwidth of the dye laser.

3.4.1 Second harmonic generation

With the advent of the intense and coherent light made available by the laser, the optical properties of a medium, such as its refractive index, become a function of the light intensity. When two or more intense coherent light waves interfere within the medium, the principle of linear superposition no longer holds. As a result, nonlinear optical phenomena can occur. Among them, second harmonic generation or frequency doubling was the first nonlinear optical phenomena observed (Bloembergen 1965).

The conversion efficiency for frequency doubling is usually quite low, therefore the intensity of the fundamental wave can be regarded as constant in the nonlinear medium. Under such an approximation, the intensity of the second harmonic is given by (Appendix D)

$$I_2 = \frac{\epsilon_0 c}{2} E_2^2 = 2K^2 L^2 c\mu_0 I_1^2 sinc^2(\frac{1}{2}\Delta kL) \tag{3.14}$$

where I in W/m^2 and E in (V/m), $sinc(x) = \frac{sinx}{x}$, and L is the total length of the nonlinear medium, $\Delta k = k(2\omega) - k(\omega)$ represents the phase matching condition. A more detailed description of the basic theory and the phase matching technology of second harmonic generation is given in Appendix D.

The beta barium borate (BBO) crystal is a new nonlinear optical material discovered recently (Chen et al. 1984, 1985). It is characterized by a wide range of transparency from the UV to the infrared. Its large birefringence allows phase matching for second harmonic generation in a large frequency region (189-1750 nm) with a large nonlinear coefficient ($5.8 \times d_{36}(KDP)$). These properties indicate that the BBO crystal is potentially useful for many applications, especially in the UV region. The optical, mechanical and thermal properties of the BBO crystal are summarized in Appendix D.

The BBO crystal used in this study is cut for type I phase matched, frequency doubling for 580-700 nm, protectively coated with a dimension of $6 \times 4 \times 7\ mm^3$ from

CASTECH. The laser beam is weakly focused into the crystal to prevent the divergence of the UV beam because a suitable quartz lens was not available for collimation after the crystal and the UV power was not a major requirement in this study. The phase matching angle was initially adjusted manually to optimise the UV output. During a scan, the personal computer controlling the scan calculated a correction to the angle and drove the BBO crystal mounting with a DC motor (Oriel D.C. Encoder Mike^{TM} Drive) which had an encoder resolution of 0.1 microns.

From Appendix D, the peak conversion efficiency of the BBO crystal is

$$\eta_{eff} = 6.78\ L^2 I^2 sinc^2(\frac{1}{2}\Delta kL) \tag{3.15}$$

where L (cm) is the length of the BBO crystal and I_1 (W/cm^2) is the intensity of the fundamental wavelength. For our system, L=0.7 cm and assuming perfect phase matching, ie $\Delta k = 0$, the conversion efficiency is

$$\eta_{eff} = 3.32 \times 10^{-8} I_1. \tag{3.16}$$

For a 200 mW average output from the dye laser pulsed at 16 kHz repetition rate and 10 ns pulse width, the peak power for each pulse is 12.5 kW. If it is focused into a 0.3 mm diameter spot in the BBO crystal, the intensity is 1.6 MW/cm^2 which indicates a 3.75% conversion efficiency and a UV output of 7.5 mW. Unfortunately, the power meter used was not sensitive enough to measure this UV power, but the UV could be easily detected by the visible fluorescent spot it produced on a sheet of paper.

3.4.2 Calibration of the wavelength

The application of tunable lasers in optical spectroscopy requires an absolute measurement of the wavelength to an accuracy approaching the linewidth of the laser. Since in most case the adjustment parameters of the laser do not provide a sufficiently accurate estimation of the wavelength, various techniques have been developed to measure

the wavelength, for example, the use of an absorption cell with a known absorption spectrum or a Fizeau wavemeter (Snyder 1977; Gardner 1985).

It is well known that the iodine absorption spectrum in the visible region provides a simple means of calibration. Therefore it received an extensive study during the 1960s to 1970s (Gerstenkorn et al 1977). As a result, a wide range and precise knowledge of the of the visible iodine molecular spectrum of the whole $B^3\Pi^+_{0+u}$-$X^1\Sigma^+_g$ electronic transition was obtained and the atlas of the absorption spectrum was given by Gerstenkorn and Luc (1978) from 14800 - 20000 cm^{-1} or 5000 - 6757 Å. The atlas contains 46, 700 lines of which 22, 850 were identified.

A 48 cm long I_2 cell was used in this study for wavelength calibration. Fig. 3.12 shows part of the I_2 absorption spectrum measured in this study and is compared with the absorption spectrum in the atlas. This study reproduced the I_2 absorption spectrum in excellent agreement with the atlas at a slightly lower resolution. Some of the very close lines were not resolved in some spectral regions due to the lower resolution of our laser system. However, since the I_2 spectrum is so dense, there are always sufficient resolved lines within the required wavelength range. In fact, only some of the resolved lines were used in the interpolation program for wavelength calculation, the rest were used as a test for the errors. Fig. 3.13(a) shows the relationship between the motor positions and the calibrated wavenumbers calculated by interpolation. The corresponding errors are shown in Fig. 3.13(b) which indicates an error of less than 0.05 cm^{-1} in the calibration. Thus the error in the UV radiation will be less than 0.1 cm^{-1}.

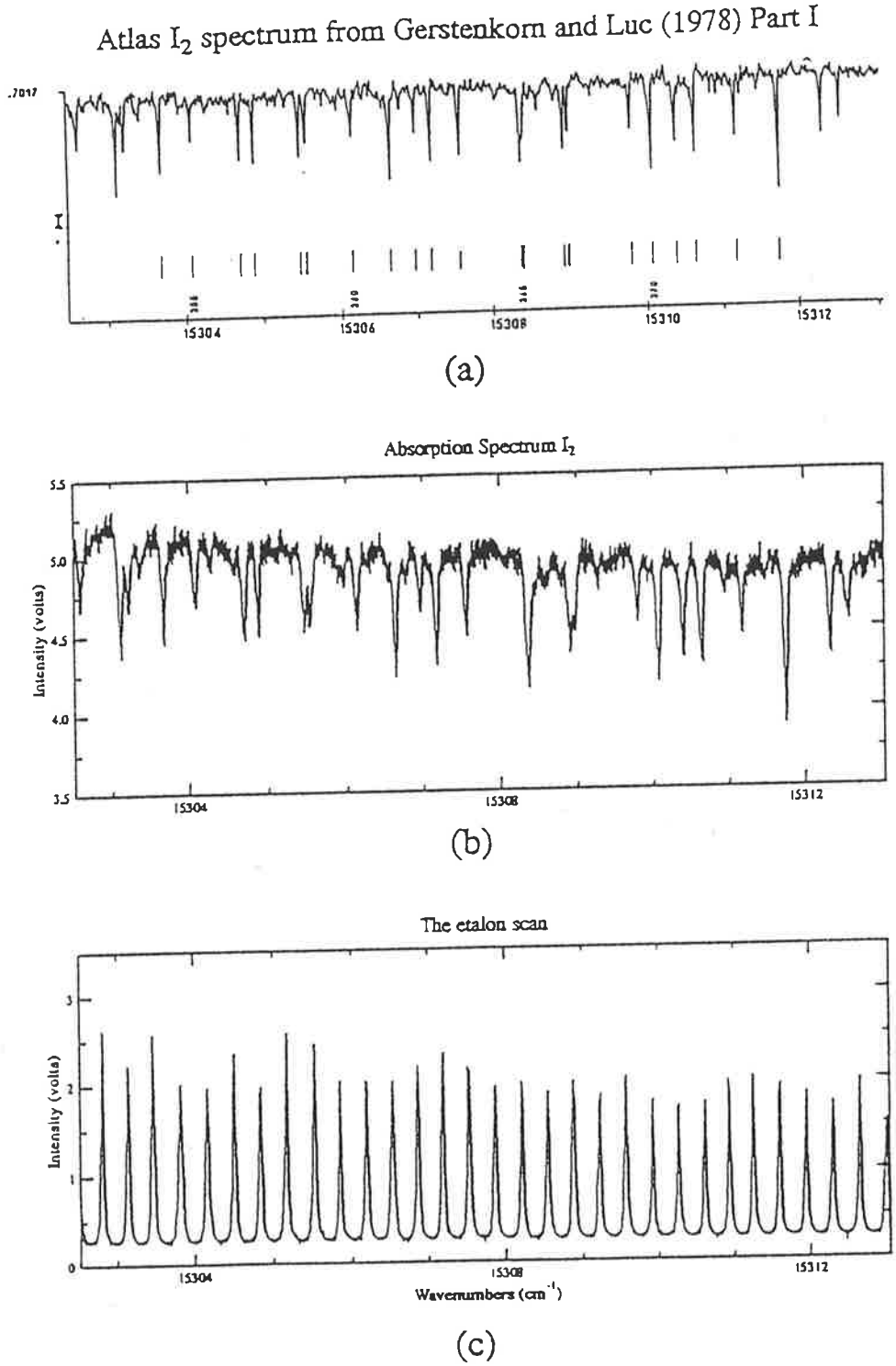

Figure 3.12: The absorption spectrum of I_2 taken from the atlas of Gerstenkorn and Luck (1978) (a), this study (b), and the etalon scan which measured the bandwidth of the dye laser (c).

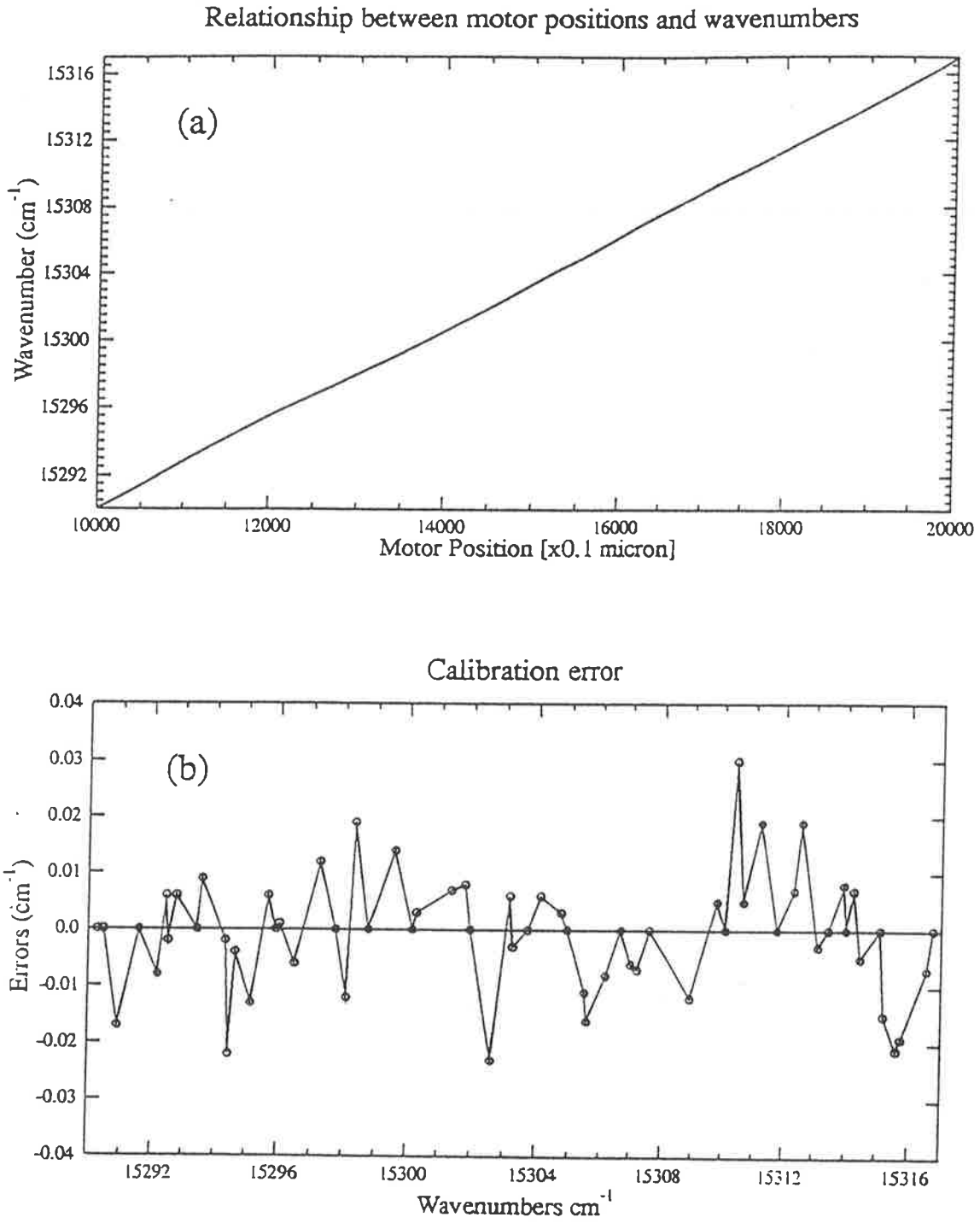

Figure 3.13: The relationship of motor positions and the calibrated wavenumbers (a) and the corresponding errors (b).

Chapter 4

Photodissociation of NaI

4.1 Introduction

The alkali halide molecules have been the subject of numerous experimental and theoretical investigation for nearly 70 years. Much of the interest derives from the fact that the two lowest adiabatic potential curves display an avoided crossing with an interchange of ionic and covalent character. The optical spectra of the alkali halide molecules have a continuous structure with very few absorption maxima. NaI is unique in that the vapour is known to have, in addition, a banded absorption spectrum superimposed on the continuous background. This makes NaI the most interesting of the alkali halide molecules for studying the process of charge transfer transition from the ionic ground state to the first electronically excited state which then dissociates into neutral atoms.

Although interest in NaI dates back to 1929 when Sommermeyer observed a long series of unresolved bands in its absorption spectrum, there is still much to be learnt about the excited electronic state and the dissociation spectra. The analysis of the photoabsorption band fragments was prevented by the high density of lines and the fragmented nature of the bands due to broadening by predissociation. Attempts have been made in more recent times to obtain the potential curvesfor the excited states.

Davidovits and Brodhead (1967), van Veen et al (1981) have constructed the potential curves for the lowest excited potential curves in the Frank-Condon region, which corresponds to vertical transitions from the lower vibrational levels, with broadband spectroscopic data.

A section of the rotational bandfragments were assigned for the first time by Schaefer et al (1982, 1984) using a high resolution laser spectroscopic study of the UV excitation spectrum. They examined the energy region above the first potential crossing of the ionic ground state and the covalent state $\Omega = 0^+$ (26900 - 33175 cm^{-1}) and produced an analysis of the fragmentary spectrum of NaI. Potential curves for the diabatic ground state and the adiabatic excited state were constructed based on the assignment of the bandfragments.

Higher excited states of NaI were studied by quenching the Na D line fluorescence by different gases (Hanson 1955 and Earl et al 1972), broad-band structured fluorescence from NaI (Bower et al, 1988) and excitation spectra (Bluhm et al 1990).

Sakai et al (1992) performed a multireference singly and doubly excited configuration interaction study of the ground ($^1\Sigma^+$) and first excited (0^+ or $^1\Sigma^+$) states on the NaI molecule. As will be shown later in Fig. 5.13, their excited state potential curve has a shallow shape above the equilibrium internuclear distance of the ground state.

This chapter will be confined to the study of the ground state and the lowest lying excited states of NaI. Some of the basic knowledge about the molecular states of NaI is introduced. In the last section, an optimization program was employed and an attempt was made to fit analytical potential curves to the experimental data given by Schaefer et al (1984). The optimization program was also applied to the Dunham parameters so that the sharp lines occur more closely to the coincidence of the diabatic and adiabatic hypothetical bound state levels than the parameters given by Schaefer et al (1984).

4.2 The electronic states of NaI

A molecule is formed by the binding of two or more atoms in such a way that the total energy is lower than the sum of the energies of the isolated constituents. The bonds are normally of ionic or covalent nature. Particularly weak bonds occur in van der Waals molecules. The electronic states of a molecule are, under the Born-Oppenheimer approximation, eigenstates of the electronic Harmitonian. The corresponding eigenvalues are the electronic potential energy surfaces.

The atomic nuclei in a molecule are bound together by the electrons. Different electronic states of a molecule are specified by different kinds of quantum number according to the coupling of the electronic spins, the electronic orbital angular momentum and the nuclear angular momentum. There are four types of coupling classified as Hund's case (a), (b), (c) and (d) (Herzberg 1950, Chapter 5).

It is believed that the ground state of NaI is described by Hund's case (a) while the excited states are best described by Hund's case (c) (Berry 1979).

4.2.1 The ground state

The ground state of NaI is an ionic state. The positive ion Na^+ and the negative ion I^- have the closed-shell electron configurations

$$Na^+ \ : \ 2s^2 2p^6$$

$$I^- \ : \ 5s^2 5p^6$$

and have ^1S ground states. According to Hund's case (a) it forms a $^1\Sigma^+$ molecular state which is also denoted as the $X\,^1\Sigma^+$ state for NaI.

4.2.2 The lower-lying excited states

The low-lying excited states are covalent states. Hence an optical transition between the ground state and the excited states can be considered as a charge transfer process (Zare and Herschbach 1965). The outer shell electron configurations of atomic Na and I are of the form

$$Na \ : \ 3s^1$$

$$I \ : \ 5s^2 5p^5$$

which lead to the atomic states of Na ($^2S_{1/2}$), and I ($^2P_{1/2}$) and ($^2P_{3/2}$). The lowest covalent state of interest in this study is formed from the atomic ground states of Na($^2S_{1/2}$)+I($^2P_{3/2}$). According to the Hund's case (c), the possible molecular states are:

$$\Omega \ = \ 0^{\pm}, \ 1, \ 2.$$

The $\Omega = 0^+$ state, usually noted as A 0^+ state, is the most interesting state, because it has the same symmetry as the ground state $X^1\Sigma^+$ and the two potential curves undergo an avoided crossing by the Born-Oppenheimer approximation under the non-crossing rule and give rise to a bound potential.

4.2.3 Selection rules

Transition probability between two electronic states is determined by the electronic dipole transition moment:

$$R_{mn} = < \phi_m | er | \phi_n > . \tag{4.1}$$

Calculations of the non-zero transition matrix elements R_{mn} provide the selection rules for the transition (Herzberg 1950, Chapter 5). For the present study the general selection rules are:

(i) For total angular momentum J

$$\Delta J \;=\; 0,\ \pm 1 \quad except \quad J = 0 \;\rightarrow\; J = 0.$$

Additional selection rules holding for Hund's case (c), where only J and Ω are well defined quantum numbers, are

(ii) For the total electronic angular momentum Ω

$$\Delta\Omega \;=\; 0,\ \pm 1.$$

Furthermore, if $\Omega = 0$ for both electronic states, then

(iii) Transitions from 0^+ to 0^- state are forbidden, so that

$$0^- \longleftrightarrow 0^- \quad 0^+ \longleftrightarrow 0^+ \quad 0^+ \not\longleftrightarrow 0^-;$$

(iv) and the following restriction holds:

$$\Delta J \;=\; 0 \;\; is \;\; forbidden \;\; for \;\; \Omega = 0 \;\rightarrow\; \Omega = 0.$$

Following these selection rules, one finds that the possible electronic transitions from the ground state of NaI are

(a) to the excited states of $\Omega = 0^+$ and 1; and

(b) $\Delta J = \pm 1$ for transitions to the $\Omega = 0^+$ state, which corresponding to the P and the R branches

$$P(J) \;=\; \nu_0 + F'(J-1) - F''(J) \tag{4.2}$$

$$R(J) \;=\; \nu_0 + F'(J+1) - F''(J) \tag{4.3}$$

while the Q branch

$$Q(J) \;=\; \nu_0 + F'(J) - F''(J) \tag{4.4}$$

is forbidden by selection rule (iv).

(c) $\Delta J = 0 \pm 1$ for transitions to the $\Omega = 1$ state which consists of all the three: P, Q and R branches.

4.3 The ground state potential curve

The ground state of NaI is an ionic state and is designated as $X^1\Sigma^+$. In this section the spectroscopic parameters obtained from the microwave spectrum are summarized in §4.3.1 and the theoretical modeling for analytical expressions for the potential curves are introduced in §4.3.2.

4.3.1 Rotational microwave spectroscopy

The first complete survey of the alkali halides by microwave absorption spectroscopy was carried out by Honig et al (1954). High resolution microwave absorption spectra were measured and analyzed by Rusk and Gordy (1962) which provides the most accurate spectral parameters for NaI for the ground state. The ground state potential curve was then obtained by fitting the molecular constants to the Dunham potential function (Dunham, 1932).

The Dunham potential function is one of the most accurate and often used procedures for representing potential curves near the equilibrium position r_e and is expressed as a series expansion in $\xi = (r - r_e)/r_e$

$$V(r) = a_0\xi(1 + a_1\xi + a_2\xi^2 + \ ...\ ) + B_eJ(J+1)(1 - 2\xi + 3\xi^2 - 4\xi^3 + \ ...\ ), \qquad (4.5)$$

where B_e is the rotational constant at r_e, J the rotational quantum number and a_i are the potential constants which are related to the molecular constants. The rovibrational

Table 4.1: Molecular constants for the $X^1\Sigma^+$ state from microwave spectroscopy (after Rusk and Gordy 1962)

a_0 (10^5 cm^{-1})	1.42	Y_{01} (MHz)	3531.7232
a_1	−3.02	$Y_{02} = -D_e$ (kHz)	−2.9183
a_2	5.9	$Y_{10} = \omega_e$ (cm^{-1})	259.20
a_3	−8	$Y_{11} = -\alpha_e$ (MHz)	−19.42
r_e Å	2.71143	$Y_{12} = -\beta_e$ (kHz)	0.0014
B_e (MHz)	3531.7187	$Y_{20} = -\omega_e\chi_e$ (cm^{-1})	−0.96
		$Y_{21} = \gamma_e$ (kHz)	43

energy levels for such a potential curve can be expressed in the Dunham series

$$T_{v,J} = \sum_{i,j} Y_{i,j}(v+\frac{1}{2})^i J^j (J+1)^j, \tag{4.6}$$

where v is the vibrational quantum number and $Y_{i,j}$ are the Dunham parameters. Experimental data can be fitted to obtained the Dunham parameters and the molecular constants can be obtained by using the relationship (Dunham, 1932)

$$\begin{aligned} &Y_{01} = B_e + O(B_e^2/\omega_e^2) \ , \quad Y_{02} = -D_e, \quad Y_{10} = \omega_e, \\ &Y_{11} = -\alpha_e, \qquad\qquad\quad Y_{12} = -\beta_e, \quad Y_{20} = -\omega_e\chi_e, \\ &Y_{21} = \gamma_e, \qquad\qquad\quad \cdots \end{aligned} \tag{4.7}$$

and

$$r_e = \left(\frac{\hbar}{4\pi B_e \mu}\right)^{1/2}. \tag{4.8}$$

Table 4.1 summarized the derived Dunham parameters from the spectroscopic data for the ground state of NaI (Rusk and Gordy 1962, Dyke 1979) from microwave spectroscopy.

4.3.2 Theoretical modeling of the potential curve

The most frequently used theoretical model for the potential curve of the ionic ground state is the Rittner (1951) model. In this model the energy binding the ions together arises from the Coulomb attraction (1/r term), the London approximation for the van der Waals attraction ($1/r^6$ term), ion-induced dipole interaction ($1/r^4$ and $1/r^7$ term) and a short distance repulsion (the exponential term), which produced an expression for the potential curve:

$$V(r) = Aexp(-r/\rho) - \frac{C}{r^6} + E_0 - \frac{e^2}{4\pi\epsilon_0}\left(\frac{1}{r} + \frac{\alpha_+ + \alpha_-}{2r^4} + \frac{2\alpha_+\alpha_-}{r^7}\right). \qquad (4.9)$$

where α_+ and α_- are the free ion polarizabilities of Na^+ and I^- respectively. Dissociation energy E_0 together with the equilibrium distance r_e are used to determine A and ρ.

Brumer and Karplus (1973) performed a quantum mechanical exchange perturbation theory to analyze the interactions in alkali halide diatomic molecules. They found that the $1/r^7$ term in the original Rittner model arises from higher order exchange independent terms in the perturbation expansion and should be excluded in the second order energy model which was employed by Rittner. They introduced the so called T-Rittner model by dropping the $1/r^7$ term

$$V(r) = Aexp(-r/\rho) - \frac{C}{r^6} + E_0 - \frac{e^2}{4\pi\epsilon_0}\left(\frac{1}{r} + \frac{\alpha^+ + \alpha^-}{2r^4}\right). \qquad (4.10)$$

where $\alpha^{\pm}$ are the effective polizabilities which will approach $\alpha_{\pm}$ at large internuclear distance.

In an attempt to avoid the undesired behavior that the Rittner potential curves become negative at small internuclear distance, Faist and Levine (1976) added a repulsive term $(B/r)^8$ to the exponential portion

$$V(r) = \left(A + \left(\frac{B}{r}\right)^8\right) exp(-r/\rho) - \frac{C}{r^6} + E_0 - \frac{e^2}{4\pi\epsilon_0}\left(\frac{1}{r} + \frac{\alpha_+ + \alpha_-}{2r^4} + \frac{2\alpha_+\alpha_-}{r^7}\right). \qquad (4.11)$$

The same term was added in the T-Ritter model and used in this study as seen in Eq. (4.23).

There are also some other attempts to model the ground state potential curves of alkali halide diatomic molecules which were discussed in the review of Jordan (1979).

4.4 Photodissociation of NaI

The lower lying excited states of NaI are designated by the quantum numbers $\Omega = 0^{\pm}$, 1, 2. They are all covalent in nature. The optical accessible excited states from the ground state are only $\Omega = 0^{+}$ and 1 states. Since the 0^{+} state has the same symmetry as the ionic ground state $^{1}\Sigma^{+}$, an avoided crossing exists in the adiabatic potential curves and coupling is present which leads to photodissociation of NaI.

4.4.1 The excited states — broadband structure

The study of absorption spectrum was first recorded by Sommermeyer (1929) and Levi (Beutler and Levi 1931, Levi 1934). The later measurements of the total absorption cross section by Davidovits and Brodhead (1967) meant that their excited state potential curve represents the combine effects of the $\Omega = 0^{+}$ and 1 states rather than the separate potential curves.

By using the technique of photofragment spectroscopy, which measures the angular and velocity distributions of photofragments, van Veen et al (1981), Anderson et al (1977, 1981), Telle and Tambini (1989) were able to distinguish the contributions from the 0^{+} state and the 1 state. For diatomic molecules, the transition dipole moment is parallel to the internuclear axis with the $\Delta\Omega = 0$ transitions and perpendicular with the $\Delta\Omega = \pm 1$ transitions. Therefore transitions to the 0^{+} state are parallel transitions and the dissociation fragments from this state recoil at a direction parallel to the

polarization of the dissociating light while those from the 1 state are perpendicular. The ratio of parallel to perpendicular transitions can be obtained by measuring the angular distributions of the Na photofragments resulting from photodissociation of a molecular beam of NaI.

Van Veen et al (1981) measured this ratio with a broadband laser source with wavelength tunable through the range 300–337 nm. By assuming that the electronic transition probabilities to the 0^+ and 1 states are equal and that the potential curves have the form

$$V(r) = A\,exp(-b(r - r_e)) \tag{4.12}$$

in the Franck-Condon region. The parameters were found to have the values of A=3.88 ev, b=8.557 $Å^{-1}$ for the 0^+ state and A=3.63 ev, b=10.03 $Å^{-1}$ for the 1 state. $r_e = 2.7$ Å is the equilibrium internuclear distance of the ground state. The resulting potential curves are shown in Fig. 4.1.

Dissociation energy

The experimental result of van Veen et al also gives a dissociation energy of 3.18 ev for the covalent states of NaI.

The dissociation limit of the ionic ground state $(Na^+(^1S_0) + I^-(^1S_0))$ differs in energy from the covalent state $(Na(^2S_{1/2}) + I(^2P_{3/2}))$ by an amount

$$Q = I.P.(Na) - E.A.(I) \tag{4.13}$$

where $I.P.$ is the ionization potential of Na and $E.A.$ is the electron affinity of I which are 5.139 ev and 3.061 ev respectively (Berry 1979). Therefore, Q=2.078 ev and the dissociation energy of the ionic ground state is 5.258 ev based on the observation of van Veen et al.

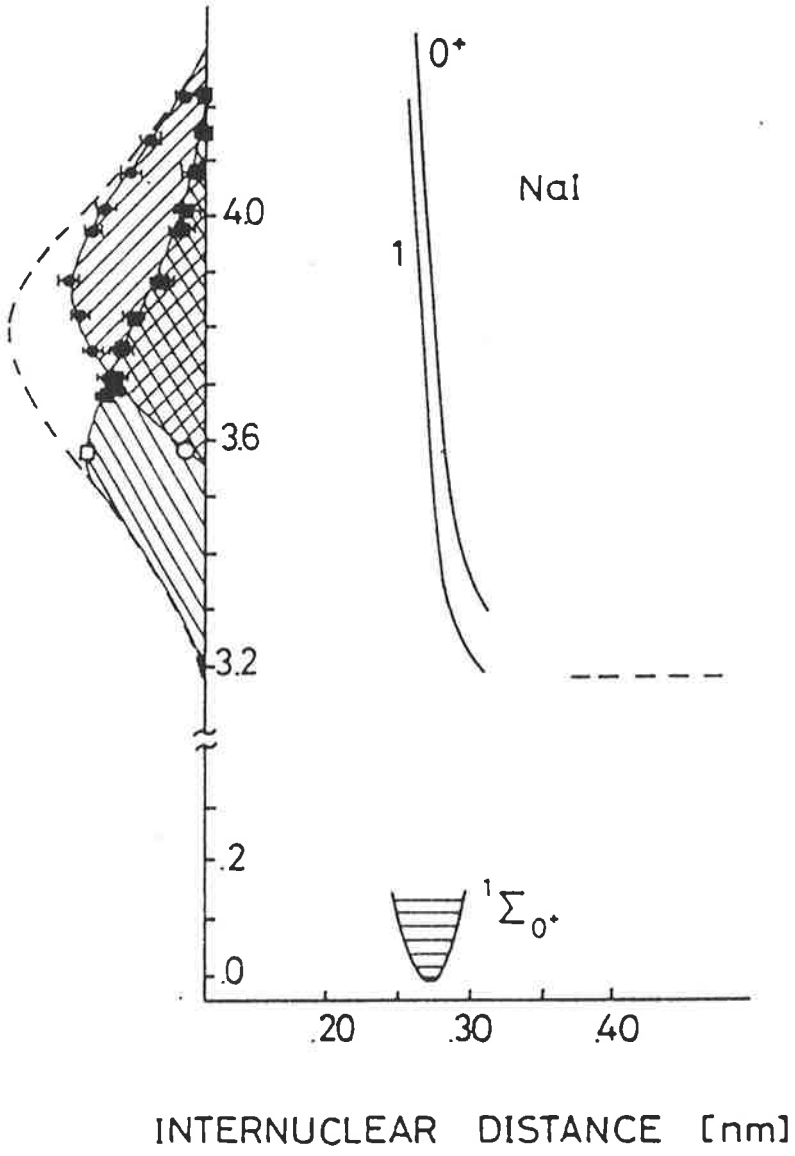

Figure 4.1: Potential curves for NaI from van Veen et al (1981)

The crossing point

The crossing point of the ionic and the covalent states can be obtained from the simple relationship

$$r_x = \frac{e^2}{Q} \tag{4.14}$$

which is based on the assumption that the potential curves can be approximated by the Coulomb curve for the ionic state and a horizontal line for the covalent state if the crossing point is at a large internuclear distance.

The electronic coupling

Since the 0^+ covalent state has the same symmetry as the $^1\Sigma^+$ ionic ground state, there exists electronic coupling between the two diabatic states and the adiabatic potential curves exhibit an avoided crossing. The values of electronic coupling matrix element at the crossing point have been evaluated by Grice and Herschbach (1974) for diatomic alkali halide molecules and is 0.055 ev for NaI. This is in reasonable agreement with the experimental result of Na+I collision (0.065 ev) (Delvigne and Los, 1973), and the later experiments of UV-laser excitation spectroscopic study on NaI (0.054 ev) (Schaefer et al, 1984) and the femto-second transition-state spectroscopy (0.046 ev) (Rose et al, 1989). This coupling strength represents a strong coupling case in the predissociation of NaI and produces a strong bound character for the $\Omega = 0^+$ state.

The shape of the coupling function is not known. However, as mentioned in §2.2, the electronic coupling matrix element only has a significant contribution to the adiabatic potential curves near the crossing point. Therefore it is usual to assume that the coupling matrix element is independent of internuclear distance and has a value equal to the coupling strength at the crossing point. Although this assumption is very useful in a practical treatment of curve crossing systems, it causes theoretical problem at large internuclear distance when atoms of the molecular system are moving freely

in space at constant speed (Torop et al 1987). By considering the fact that as the two nuclei move apart, the coupling between the two diabatic electronic states should approach zero, Faist and Levine (1976) assumed that the coupling strength decreases exponentially as internuclear distance increases:

$$V_{12}(r) = A\ exp(-r/\rho), \tag{4.15}$$

while Engel and Metiu (1989) assumed a Gaussian shape coupling centered at the crossing point r_x:

$$V_{12}(r) = A_{12} exp[-\beta(r - r_x)^2] \tag{4.16}$$

with the coupling strength A_{12} at the crossing point.

4.4.2 The discrete band fragment structure

NaI is the only alkali halide which exhibits a dense line structure in the absorption spectrum. The discrete structure was observed during the early 1930's (Beutler and Levi 1931 and Levi 1934) and its origin was not explained until 1957 when Berry presented a classical picture giving the physics of the bound character of the potential curves in NaI. Analysis of the spectrum was prevented by the high density of rotational lines which are present because of the high temperature required to vaporise the NaI ($\geq 650\ ^0C$). The high temperature causes several vibrational levels and a large number of rotational levels of the ground electronic state to be populated and so enable Franck-Condon transitions over a large energy range. High resolution absorption spectrum of NaI was described as a dense and complex spectrum that contain some very sharp lines, many overlapping lines and diffuse lines, which are caused by predissociation (Berry 1979).

Berg and Skewes (1969) reported the first rotationally resolved structure of NaI but were not able to carry out an analysis or line assignment. They claimed, however, that a spacing of rotational groups of 36 cm^{-1} to be associated with the vibrational

spacing of the upper state, suggesting that the excited potential curve is broad and shallow. Furthermore they claimed such spacings appeared throughout the region from 2945 to 5400 Å. Since at temperatures of 1000 ^{o}C there are only about five vibrational levels of the ground state populated, the extent of the spectrum, implies that the upper state has a potential well much deeper than a van der Waals well (Berry, 1979).

In order to reduce the population in high rotational levels, Ragone et al (1982) reported a UV laser spectroscopic investigation on the fluorescence excitation and emission spectra from cold NaI vapor seeded in a supersonic beam with He. With the assumption that the absorbing beam is rotationally cool and therefore only a few low J states are populated, Ragone et al assigned several bands of the excitation spectrum and made a vibrational analysis in the Franck-Condon region accessible from the ground and the first excited vibrational levels of the $X^1\Sigma^+$ state. However, because NaI is a case of intermediate coupling between states associated with adiabatic and diabatic potentials, some high J rotational lines are much stronger than the others and live long enough to fluoresce. Therefore these high J rotational lines could also appear in their observation and some lines were reassigned later (Schaefer et al 1983, Berry and Levy 1983).

In a UV laser spectroscopic study of NaI by Schaefer et al (1982, 1984), fragmentary rotational fine structure was observed in the excitation spectrum and assigned for the first time to the electronic transition $0^+ \leftarrow^1 \Sigma^+$ based on Child's semiclassical theory (Child 1976). The excitation spectrum was measured by detecting the fluorescence from the excited states with a large slit width in the monochromator while scanning the excitation wavelength. The dense and complex absorption spectrum was greatly simplified by the fact that the fluorescent intensity depends on whether the NaI molecules live long enough in the excited state to fluoresce. If the predissociation rate is too fast the molecule will dissociate quickly after being excited and no fluorescence will be detected. Only lines with a line width due to predissociation less than 300 MHz

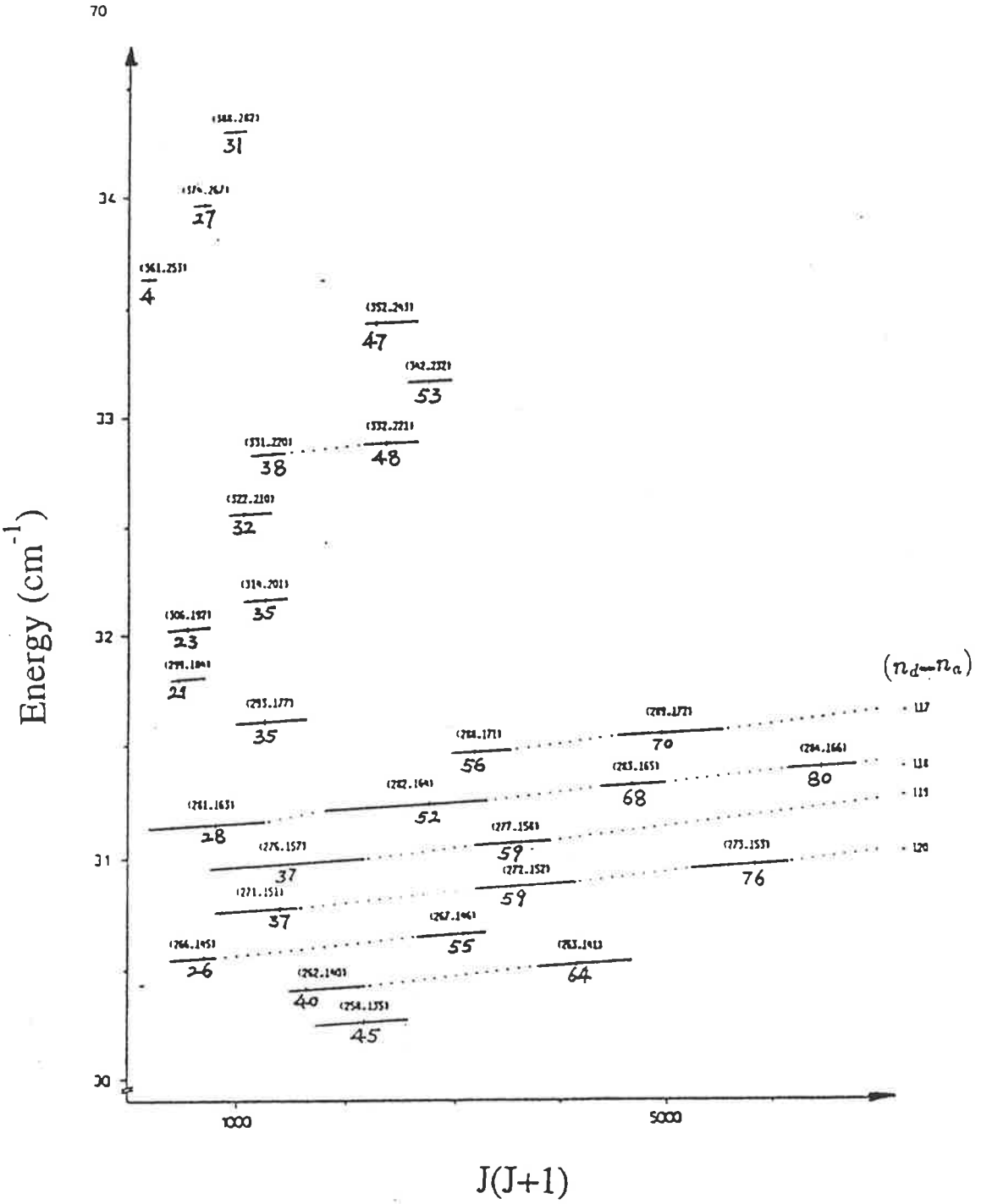

Figure 4.2: The term energies of the observed assignments, (n_d, n_a) for the diabatic and adiabatic levels with the J numbers for the center lines measured from the figure, against J(J+1) (After Schaefer et al, 1984).

were observed. Most of the absorption lines have predissociation widths broader than 300 MHz and escaped their observation. A central sharp line is observed in every fragmentary rotational band structure with the neighboring lines symmetrically broadened and decreasing in intensity.

For all the fragmentary rotational structure observed, only P and R branches and no Q branches were found, as expected for Hund's case (c) coupling.

Information on the ground state ($X^1\Sigma^+$) vibrational levels was obtained at a much higher energy region than the microwave experiment can reach (Schaefer et al, 1984). Excitation spectra of the same excited levels from different ground state vibrational levels yield very precise experimental data for $v'' = 0 - 4$. Fluorescence progressions extending up to $v'' = 78$ were observed by fixing the excitation wavelength and scanning the fluorescence spectra with a narrow slit width in the monochromator, with an accuracy of $4 - 7\ cm^{-1}$.

Since these sharp lines occur in the accidental coincidence of the hypothetic levels of the adiabatic and the modified diabatic bound states, as detailed in Chapter 2, their positions can be used to identify the corresponding vibrational and rotational energies ($E_2(E,J)$ and $E_+(E,J)$) of the hypothetic levels. Schaefer et al (1984) then fitted these energy levels to the Dunham series with a non-linear least-squares program for the diabatic ground state (V_2) and the adiabatic excited state V_+ with the coupling parameter according to Eq. (2.42). The best fit with a minimum standard deviation provides the final vibrational assignments, the Dunham parameters and a coupling strength of 0.054 ev (Schaefer et al 1984). Fig. 4.2 shows the term energies of the 28 band fragments observed and corresponding assignments. The resulting Dunham parameters, as listed in Table 4.2, were used to predict the remaining (lower) energy levels and the corresponding potential curves, as shown in Fig. 4.3, were constructed with the RKR method based on these levels.

Because the spectroscopic parameters of the lower vibrational levels for the

upper adiabatic state were obtained by the extrapolation of the Dunham parameters obtained with a few rotational band fragments in a much higher energy region, the location of the corresponding potential curve would be affected by the accuracy of the extrapolation.

As described in Chapter 2, the separation between the two adiabatic potential curves at the internuclear distance where the diabatic potential curves cross is twice the coupling strength. Therefore, the separation of the adiabatic and diabatic potential curves given by Schaefer et al (1984) at the crossing point should be the same as the coupling strength, 0.054 ev. However as noted by Wang et al (1990), the separation of their potential curve at the crossing point indicates a coupling strength of about 0.2 ev (1600 cm^{-1}) as seen in Fig. 4.3. This is not consistent with the 0.054 ev coupling strength from which the Dunham parameters for the potential curves was derived. Moreover Schaefer et al (1984) did not use the full version of Child's semiclassical theory (Child and Lefebvre 1978, Child 1991(a)), and regarded the hypothetic states as the diabatic and adiabatic bound states. As noted in §2.3, the hypothetic diabatic levels used in Child's semiclassical theory correspond to a modified diabatic potential curve:

$$V = \begin{cases} V_- & (r < r_x) \\ V_+ & (r > r_x) \end{cases}$$

where the level positions differ from the eigenvalues of the diabatic (V_2) potential curves by about one vibrational spacing for NaI. Regarding them as the same will introduce errors in fitting the Dunham parameters to the final vibrational assignments.

4.4.3 Optimization of the potential curves and Dunham parameters

An optimization procedure can be use to minimize the difference between experimental data and the calculated quantities using theoretical models. Although there are

Table 4.2: Dunham parameters for the states of NaI.

	$X0^+$ diabatic state		$A0^+$ adiabatic state	
	Schaefer et al	This work	Schaefer et al	This work
T_e	0.0	0.0	25556.125	25556.125
Y_{10}	259.056819	258.458388	27.27876	27.20254
Y_{20}	-0.9127106	-0.907696	0.1468826	0.1484409
$Y_{30}(\times 10^{-3})$	1.39339	1.38383	-0.88577	-0.897378
$Y_{40}(\times 10^{-6})$	5.8808	5.8463	1.92053	1.958117
$Y_{50}(\times 10^{-8})$	-5.4912	-5.45937	-0.157943	-0.162444
$Y_{60}(\times 10^{-10})$	2.1641	2.1490		
$Y_{70}(\times 10^{-13})$	-4.8365	-4.7960		
$Y_{80}(\times 10^{-16})$	5.8534	5.8032		
$Y_{90}(\times 10^{-19})$	-2.9748	-2.95475		
Y_{01}	0.1178056	0.11738486	0.04817098	0.04817097
$Y_{11}(\times 10^{-4})$	-6.4770	-6.4404	-1.532322	-1.532321
$Y_{21}(\times 10^{-6})$	1.430	1.422	0.14739	0.14744
$Y_{31}(\times 10^{-9})$	-3.18299	-3.17309		
$Y_{41}(\times 10^{-11})$	2.15891	2.14567		
$Y_{51}(\times 10^{-14})$	-7.3021	-7.2499		
$Y_{61}(\times 10^{-17})$	7.9978	7.9403		
$Y_{02}(\times 10^{-8})$	-9.73	-10.587	-9.4062	-9.7204
$Y_{12}(\times 10^{-11})$	5.0	5.0	29.829	31.1374
$Y_{22}(\times 10^{-13})$	5.30942	5.70596		
δ	11.25	0.087	0.015	0.004

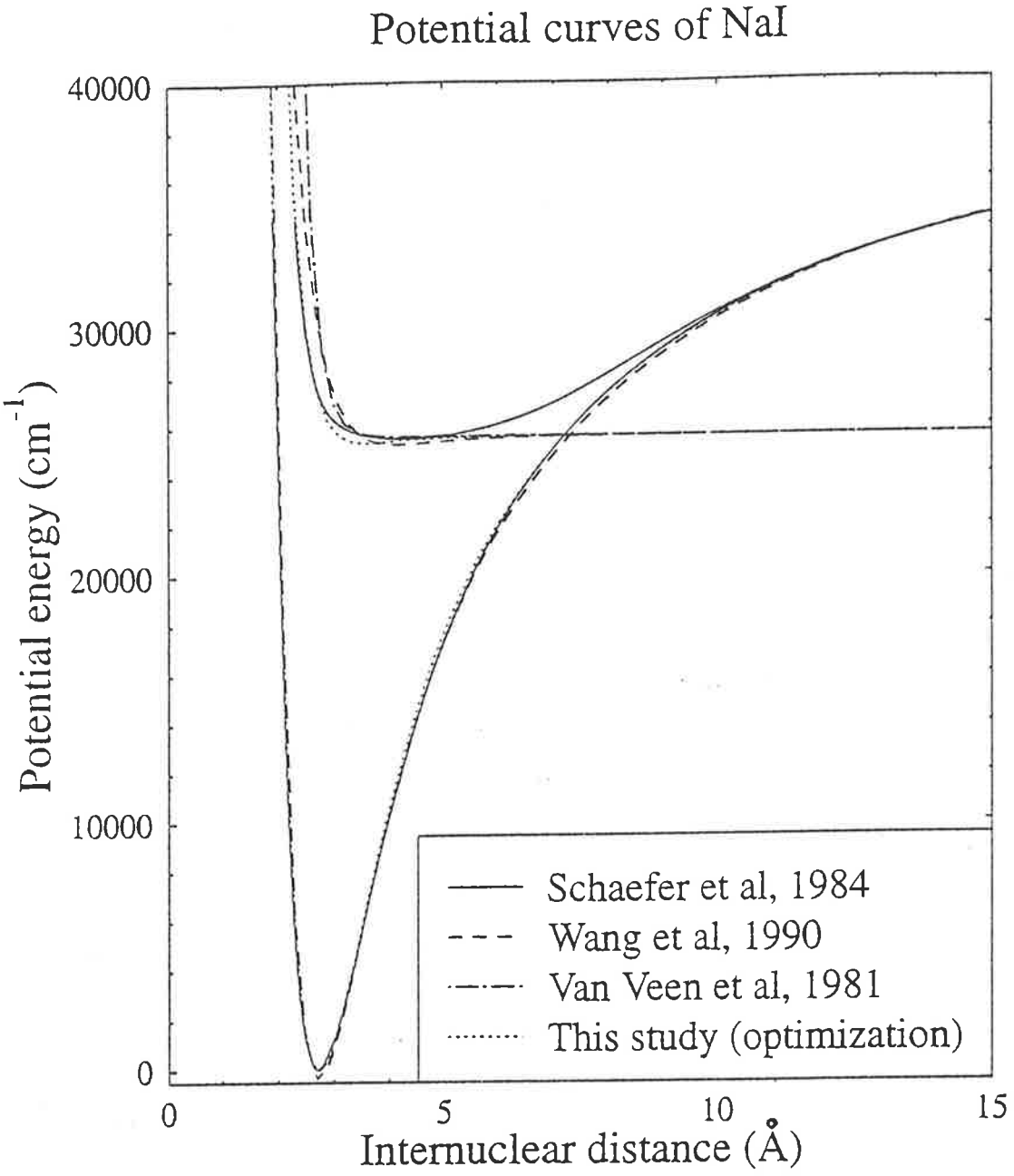

Figure 4.3: The proposed potential curves for NaI from different workers. Note that the excited state potential curve given by Schaefer et al (1984) is an adiabatic potential curve, while the others are diabatic.

possible errors in the potential curves and the corresponding vibrational assignments, as discussed above, the spectroscopic data presented by Schaefer et al (1984) in the experimental energy range is still the most accurate one so far and will be used as the basis for analyzing the absorption spectrum in the next Chapter. Thus there is a need to extract more information from their spectroscopic analysis.

It was found that the diabatic and adiabatic levels calculated by the Dunham parameters according to the assignments in Fig. 4.2, which are expected to be coincidence for each of the 28 sharp lines, have discrepancies ranging from 0.5 to 10 cm^{-1}. Therefore the position of the sharp lines predicted by the Dunham parameters are in large error with their experimental observation. This creates difficulties when attempting to predict the position of other sharp lines not observed in their experiment.

In the following, a description is given of the method used to obtain an analytical expression for the diabatic potential curves and an improvement to the Dunham parameters using a numerical optimization program. These calculations allow spectroscopic parameters such as Franck-Condon factors and more accurate sharp line positions to be calculated.

Optimization on the potential curves

The optimization of the potential curves in this study provides analytical expressions for the diabatic potential curves of the $X\ ^1\Sigma^+$ and $A0^+$ states which fit to the analysis given by Schaefer et al (1982, 1984).

In an attempt to derive analytical expressions for the diabatic potential curves for the $X\ ^1\Sigma^+$ and $A0^+$ states of NaI, Wang et al (1990) employed a numerical optimization procedure based on the flexible simplex search algorithm (Himmeblau 1972) to determine the parameters for the potential curves:

$$V_{cov}(r) = \left[A_{cov} + \left(\frac{B_{cov}}{r+r_0}\right)^{12}\right] exp\left(-\frac{r+r_0}{\rho_{cov}}\right) - \frac{C_{cov}}{(r+r_0)^6} + E_{cov}, \quad (4.17)$$

$$V_{ion}(r) = \left[A_{ion} + \left(\frac{B_{ion}}{r}\right)^8\right] exp\left(-\frac{r}{\rho_{ion}}\right) - \frac{C_{ion}}{r^6} + E_{ion}$$
$$-\frac{e^2}{4\pi\epsilon_0}\left(\frac{D_{ion}}{r} + \frac{\alpha_+ + \alpha_-}{2r^4} + \frac{2\alpha_+\alpha_-}{r^7}\right), \quad (4.18)$$

$$V_{12}(r) = h_x exp[-\beta(r - r_x)^2]. \quad (4.19)$$

Both the diabatic potential functions were taken from Faist and Levine (1976) while the coupling function was assumed to be a Gaussian (Engel and Metiu 1989). Two parameters, D_{ion} and r_0, were introduced by Wang et al (1990) to make the potential more flexible so that the optimization procedure was more efficient. The potential curve of the covalent state deduced from scattering experiments (Faist and Levine 1976), in which all the excited covalent states, the 2, 1, and $0^{\pm}$ states, contribute (Anderson et al 1977 and Kaufmann et al 1974), has its repulsive limb at a considerably larger internuclear distance than those found from optical absorption data. The parameter r_0 was then put into Eq. (4.17) to translate the covalent potential curve to the left. This modification causes the inner limb of the covalent and ionic potential curves to cross at a small internuclear distance with a very high energy. In the optimization computation of Wang et al (1990), all the parameters in the potential functions except E_{cov} were assumed to be adjustable and the initial parameters were taken from Faist and Levine (1976) as well as Engel and Metiu (1989). The criterion function δ is defined as

$$\delta = \sum (E_v^{cal} - E_v^{sh})^2 \quad (4.20)$$

where v is the vibrational number and E_v^{sh} is the corresponding term energy for the potential curves tabulated by Schaefer et al (1984) while E_v^{cal} is the term energy for the trial diabatic and adiabatic bound states. The rotational constants

$$B_v = \frac{\hbar^2}{2\mu} < \chi_v(r)|\frac{1}{r^2}|\chi_v(r) > \quad (4.21)$$

were used to imposed constraints upon the potentials. The procedure is to ensure that the calculated B values for each trial potential curve are within a constraint limit. The resulting parameters of the calculation of Wang et al (1990) for the potentials are listed

in Table 4.3 and the corresponding $A0^+$ potential curve is in good agreement with that given by van Veen et al (1981) in the experimental energy region as shown in Fig. 4.3. It was found that the rotational constants of the 0^+ state show a discrepancy with those of Schaefer et al, especially in the lower potential energy region. Wang et al suggested that the implication of this result required a revision for the assignment of the vibrational or rotational quantum numbers.

It was found in this study that because of the high J number in the experimental band fragments and because the line position is proportional to the rotational constant B and not proportional to the rotational quantum number J, it is impossible to alter the value of B by changing the rotational assignment for J while still fitting the spectrum for the rotational band fragment. The change of B values and the reassignment of J can result in an error in the line position much bigger than the experimental error. For example, the B values for the potential curve of Wang et al (1990) or van Veen et al (1981) are about $3 \cdot 10^{-4}\ cm^{-1}$ smaller than those of Schaefer et al (1984). The corresponding error in line position is $0.3\ cm^{-1}$ when J changes from 50 to 60, which is three times bigger than the experimental error of Schaefer et al, showing that it is not possible to change B by re-assigning J. Therefore, only the vibrational assignments can be changed. In the following, a modification of the work of Wang et al was carried out to obtained analytical expressions for the diabatic potential curves. These modifications are:

1. The analytical expression for the ionic state was changed to the T-Ritter model by dropping the $1/r^7$ term in Eq. (4.17) therefore the potential curves are:

$$V_{cov}(r) = \left[A_{cov} + \left(\frac{B_{cov}}{r}\right)^{12}\right] exp\left(-\frac{r}{\rho_{cov}}\right) - \frac{C_{cov}}{(r)^6} + E_{cov}, \tag{4.22}$$

$$V_{ion}(r) = \left[A_{ion} + \left(\frac{B_{ion}}{r}\right)^{8}\right] exp\left(-\frac{r}{\rho_{ion}}\right) - \frac{C_{ion}}{r^6} + E_{ion} - \frac{e^2}{4\pi\epsilon_0}\left(\frac{D_{ion}}{r} + \frac{\alpha^+ + \alpha^-}{2r^4}\right), \tag{4.23}$$

and there is no translational shift of the covalent potential curve. The coupling strength

Table 4.3: Parameters for the potential curves of NaI.

Parameters	Wang et al (Eq. (4.17-19)	This work (Eq. (4.25-27)
$A_{cov}(eV)$	3150.0	3100.0
$B_{cov}(eV^{1/12}\text{Å})$	2.710	3.33
$C_{cov}(eV\ \text{Å})$	1000.0	150
ρ_{cov} (Å)	0.4277	0.3168
E_{cov}(eV)	3.18	3.18
r_0 (Å)	0.61	0
$A_{ion}(eV)$	27580.0	1744.7
$B_{ion}(eV^{1/8}\text{Å})$	1.742	2.107
$C_{ion}(eV\text{Å})$	12.72	19.54
D_{ion}	1.072	1.0215
ρ_{ion}(Å)	0.3603	0.3910
$\alpha_+(\text{Å}^3)$	1.375	
$\alpha_-(\text{Å}^3)$	5.446	
$\alpha^+ + \alpha^-(\text{Å}^3)$		11.09
E_{ion}(eV)	5.312	5.258
h_x(eV)	0.055	0.055
β_{12}(Å$^-$2)	0.6858	0
r_x (Å)	7.293	7.14
δ	0.4	
δ_t		0.01

was taken as a constant over r

$$V_{12}(r) = h_x = 0.055\ eV. \tag{4.24}$$

to simplify the calculation.

2. The basic requirement for the potential curves is that they can reproduce the 28 band fragments observed in Schaefer's experiment and the microwave data for the ground state. The term energies given by Schaefer et al (1984) outside the experimental region are an extrapolation of the Dunham parameters which may not be correct because the incorrect shape of the potential curves around the crossing point. Therefore, instead of fitting all the term energies, the optimization program in this study only uses the position of the 28 sharp lines in the upper state and the first ten vibrational levels in the ground state.

3. It was found in this study that the constraints of Wang et al (1990) on the B values are not tight enough and the accepted B values are in error for the line position larger than the experimental error of the fluorescence excitation spectrum. However a tighter constraint resulted in the computation never terminating because the program kept looking for a trial potential curve subject to the other conditions with the right B values which are not consistent. To overcome this problem, the B values were included in the criterion function rather than used as a constraint. Thus, there are two factors included in the criterion:

$$\delta_1 = \sum (E_{cal}(n_{cal}) - E_{exp}(n_s))^2, \tag{4.25}$$

$$and \quad \delta_2 = \sum (B_{cal}(n_{cal}) - B_{exp}(n_s))^2, \tag{4.26}$$

where $E_{cal}(n_{cal})$ is the eigenvalue of the "modified" diabatic state or the adiabatic state for the vibrational quantum number n_{cal} with B_{cal} the corresponding rotational constant. Experimental data for the position of the sharp lines (E_{exp}) were taken from Schaefer et al (1984) with their vibrational assignment n_s. The first ten ground state levels were also calculated from Schaefer et al's Dunham parameters since their

experiment yielded more information on the higher vibrational levels of the ground state than the microwave experiments. The computation is then to minimize

$$\delta_t = \begin{cases} \delta_1 & (\delta_2 < 1.5 \cdot 10^{-5}) \\ \delta_1 + 600(\delta_2 - 1.5 \cdot 10^{-5}) & (\delta_2 > 1.5 \cdot 10^{-5}) \end{cases} \tag{4.27}$$

where δ_t is set in such a way that the B values will have a significant effect on it if δ_2 is bigger than $1.5 \cdot 10^{-5}$ so that the program can converge to the optimal potential quickly. In practice such an arrangement is much more efficient in computer time than using a tighter constraint and results in a smaller criterion function.

3. Because the dissociation energies of both states were known, as discussed in §4.4.1 they are not treated as adjustable.

The rest of the parameters of the potential curves were regarded as adjustable in this work without taking account of their physical meaning. The initial potential parameters were obtained by adjusting the potential curve to fit the potential curves given by Schaefer et al (1984) and then used for the computation. It was found that if the resulting potential curves were used as the initials for another calculation, it is still possible to reduced the criterion function. Thus, such process was iterated until the value of the criterion function converged to the same value. Other computation details were the same as Wang et al's (1990).

The resulting potential curves represent the optimized fit of the potential curves to the experimental data and the analysis given by Schaefer et al (1984). The optimized parameters are listed in Table 4.3 and the resulting potential curves are plotted in Fig. 4.3. The vibrational assignments for the upper states were changed for each set of calculations and the best result were found to shift up by 9 (or $n^a_{cal} - n^a_s = 9$) for the adiabatic state and 3 (or $n^a_{cal} - n^a_s = 3$) for the diabatic state. Compared with the potential curves of Wang et al (1990) the criterion function is much smaller in this study as the δ and δ_t values in Table 4.3 indicate. It should be noted that the criterion function δ defined in Eq. (4.20) does not include the contribution from the B values

as δ_t does. The repulsive limb of the optimized covalent potential curve is in excellent agreement with the potential curve of Schaefer et al. The $^1\Sigma^+$ ionic state gives a good fit for the first few vibrational levels as well as in the high energy region of interest. The potential well is slightly narrower than that of Schaefer et al. Attempts to include higher ground state levels, for example $v'' = 0 - 63$, resulted in the crossing point shifting to a larger internuclear distance. This may indicate the analytical expression used is not accurate enough to account for the ionic behavior over such a large energy region.

It was found that the error in the optimized potential curves is still too large to reproduce the position of the sharp lines due to their extreme sensitivity to the position of the energy levels of the two potential curves. However, they provided the best fit to the potential curves given by Schaefer et al that were able to be obtained and were used, as described in the next chapter, for numerical calculations such as finding the Franck-Condon factors for the potential curve of Schaefer et al.

It must be emphasized that these optimized potential curves are based on the analysis of Schaefer et al (1982, 1984). They are not the final result of this study.

Optimization on the Dunham parameters

The purpose of this calculation was to obtain a new set of Dunham parameters which not only reproduce the experimental energy values of Schaefer et al but also have a better coincidence of the diabatic and adiabatic energy levels at the center lines. Thus, the new Dunham parameters can be used to obtain a better prediction of other sharp line positions which were not observed in their experiment.

Of the 28 sharp lines observed by Schaefer et al (1982, 1984), precise positions were given for only 8 lines. It was found that the position of these eight center lines given by Schaefer et al in 1982 can be reproduced accurately using Child's semiclassical

theory, even though the two hypothetical levels calculated by their Dunham parameters (Schaefer et al, 1984) are not in their closest coincidence. It was then assumed that the position of the center lines that they observed, but only presented graphically (as shown in Fig 4.2), can be obtained with the same calculation and can be used as the experimental data. The new Dunham parameters were calculated by the optimization program with those given by Schaefer et al as the initial values. The criterion function is defined as:

$$\delta = \frac{1}{28}\sum(E_v^{cal} - E_v^c)^2 + 10^{10}\sum(B_v^{cal} - B_v^{sh})^2 \qquad (4.28)$$

where E_v^c are the position of the center lines, E_v^{cal} are the position of the calculated diabatic or adiabatic levels, B_v^{sh} are the B values calculated with the original Dunham parameters and B_v^{cal} are the calculated values with the trail parameters. For the same reason as before, the criterion function and the coefficients are set in a way to enable the program converge to the optimal parameters quickly with minimum error with the experimental data.

The resulted Dunham parameters are listed in Table 4.2. The criterion function δ, also given in Table 4.2, is greatly reduced when compared with that of Schaefer et al (1984) especially for the diabatic state. This is because the ground state vibrational levels were not included in this calculation due to the discontinuity of the modified potential shape for these levels, as described in §2.3. Thus this set of Dunham parameters can only be used to reproduce the excited state levels and not for constructing the whole diabatic potential curve. The resulting parameters reproduce better coincidence of the diabatic and adiabatic levels for all the sharp line positions. It is therefore assumed that the resulting parameters will give a better prediction for the position of other sharp lines and will be used in the next Chapter to model the absorption spectrum.

Chapter 5

Ultraviolet High Resolution Absorption Spectrum of NaI

5.1 Introduction

In an attempt to resolve the controversy on the $\Omega = 0^+$ state of NaI concerning its absolute position as well as its relative position with the 1 state as discussed in the previous Chapter, a high resolution absorption spectrum measurement on NaI was carried out. The experimental data was then analyzed and modeled with the optimized Dunham parameters calculated in the previous Chapter. A new potential curve is proposed at the end of this Chapter which is consistent with the recorded observations.

5.2 Experimental Measurements

The experimental setup is shown schematically in Fig.5.1. The narrow bandwidth dye laser system has been described in Chapter 3. Briefly, a CuBr laser is used to pump

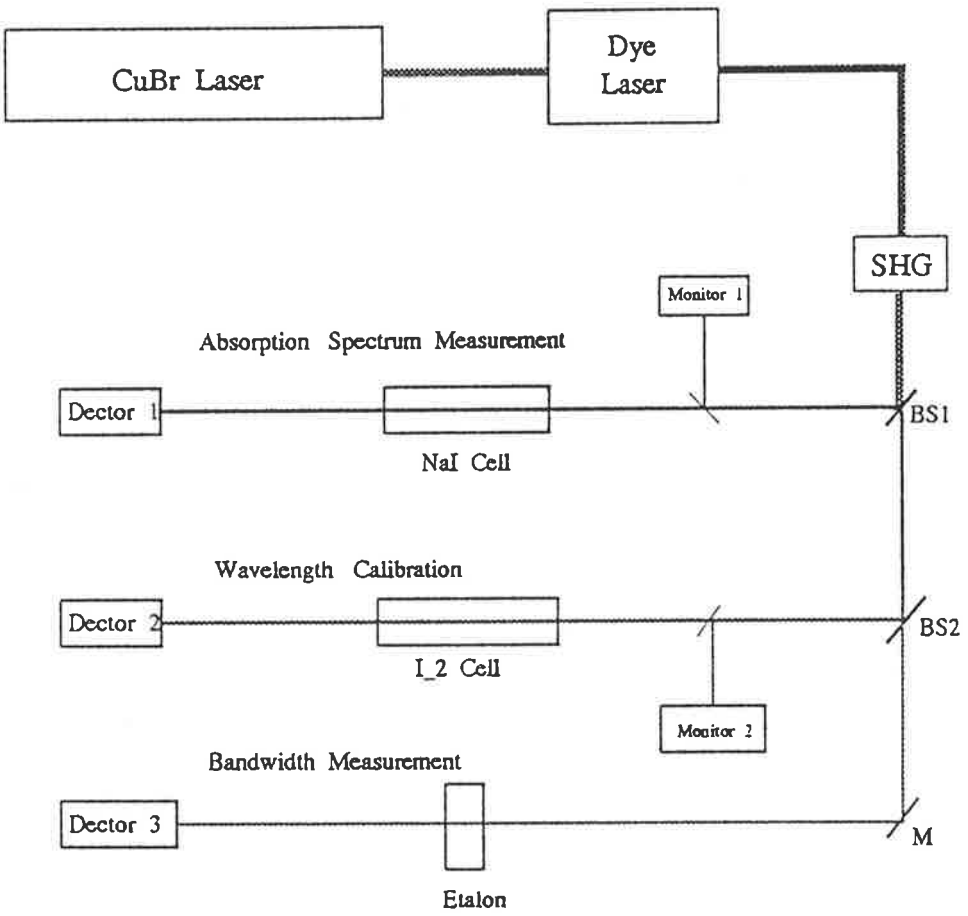

Figure 5.1: Schematic of experimental arrangement

a dye laser oscillator and amplifier. The output of the dye laser is then focused into a BBO crystal for frequency doubling. Prisms were used to separate the dye laser beam and its second harmonic (UV). The visible laser beam was directed into an I_2 cell for wavelength calibration and into an etalon to monitor the bandwidth. The UV beam was directed through a heated quartz NaI cell to measure the absorption spectrum. For the UV radiation, the error in the frequency calibration was less than 0.1 cm^{-1} and the bandwidth was about 2-3 GHz as described in Chapter 3.

The NaI cell was made of silica tube with a vertical finger in the bottom containing the salt. The cell was prepared by placing the salt in the vertical finger which was connected via a "T" junction to a vacuum line to outgas the cell at 300 ^oC overnight at a pressure lower than 10^{-6} torr while the salt was also slightly heated. After the vacuum line was sealed off, the salt was vaporized into the cell and the cell sealed off above the "T" junction forming the base of the finger. For recording the absorption spectrum the cell was placed in a vacuum chamber with quartz windows. The vapor pressure of the NaI in the cell was controlled by the temperature in the finger which was heated to 650 ^oC. The rest of the cell was heated to 690 ^oC in the main arm and 710 ^oC on the windows to prevent condensation. It was found in this study that if the windows are colder than the rest of the cell NaI will deposit on the windows to form a thin white layer which cannot be removed later by heating the window.

Fig. 5.2 illustrates the method of the data acquisition. The detectors were UV enhanced photodiodes with a high speed preamplifier and peak detector which held the peak level of the laser signal. UV transmission filters were used and together with the peak detectors, essentially eliminated the signal from background radiation produced by the hot cell. The laser signal which passed through the absorption cell and the reference signal for determining the UV intensity were both sent to a discriminator to remove the weak pulses and the very strong pulses which may saturate the amplifiers.

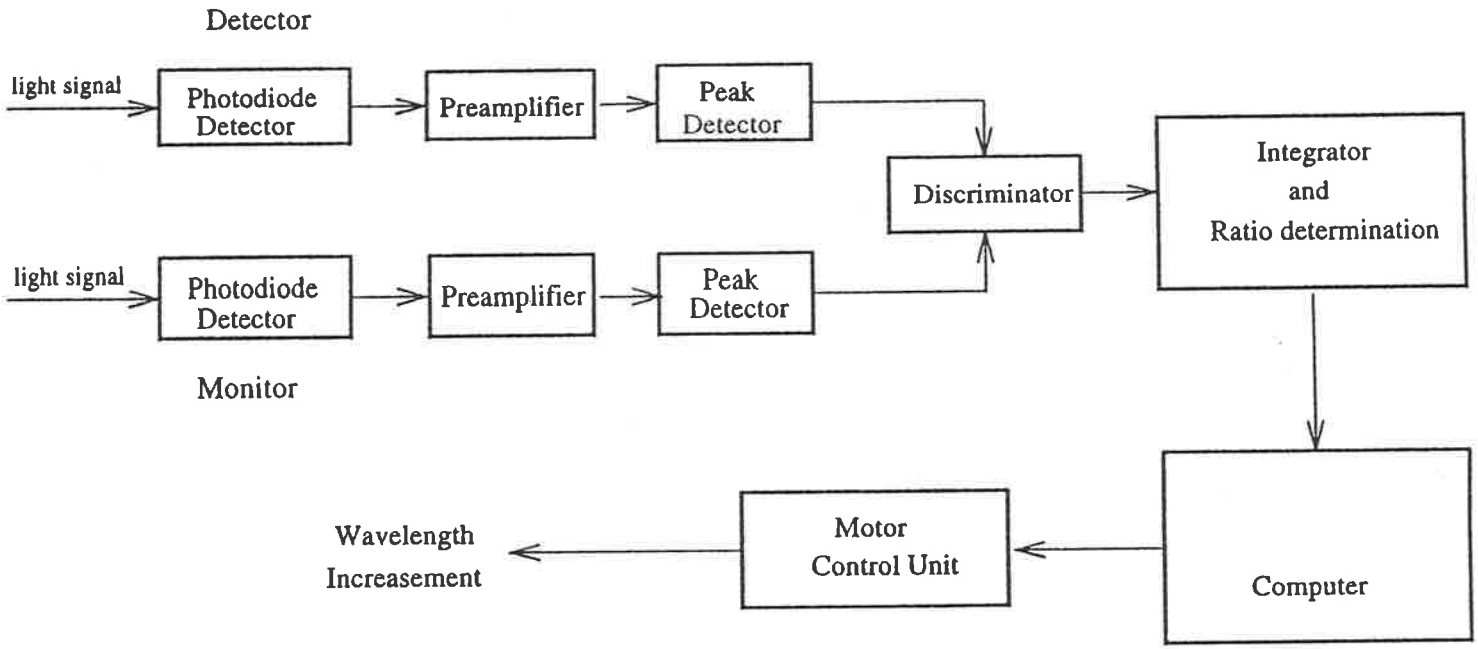

Figure 5.2: Schematic of data acquisition

The peak values were integrated and the ratio between the two channels was determined and sent to a computer. The electronic circuits for the detecting system are given in Appendix E. The computer was also used to control the master motor for scanning the wavelength and also a slave motor to rotate the BBO crystal to the corresponding phase matching angle for frequency doubling. A $PC - LPM - 16$ data acquisition board with 16 input channels from *National Instruments Corporation* was installed in the computer for data logging at every wavelength increment.

Different dyes such as Rhodamine 590, Kiton Red 620, Rhodamine 640 and DCM were used in the experiment, corresponding to the tuning regions of 281 - 289 nm, 293 - 301 nm, 305 - 312 nm and 322 - 334 nm in the UV.

A section of the absorption spectrum recorded in this study as well as the corresponding excitation spectrum reported by Schaefer et al (1982) are shown in Fig. 5.3. The absorption spectrum of NaI, which was inverted to compare with the excitation spectrum, shows much more dense line structure than the excitation spectrum. Such a dense line structure in the absorption spectra was observed throughout the experimental energy region.

It was also noted that there was a continuous absorption spectrum, with about the same intensity as the line structure, which is believed to be mainly caused by the $\Omega = 1$ continuum state. It was also observed that in some regions, the absorption lines are stronger than those in other regions and there are a few regions which are nearly fully continuum. Weak intensity fluctuations were also observed superimposed on the continuous background.

In this thesis, the absorption spectrum measured with DCM dye was analyzed. The remaining spectra needs further investigation.

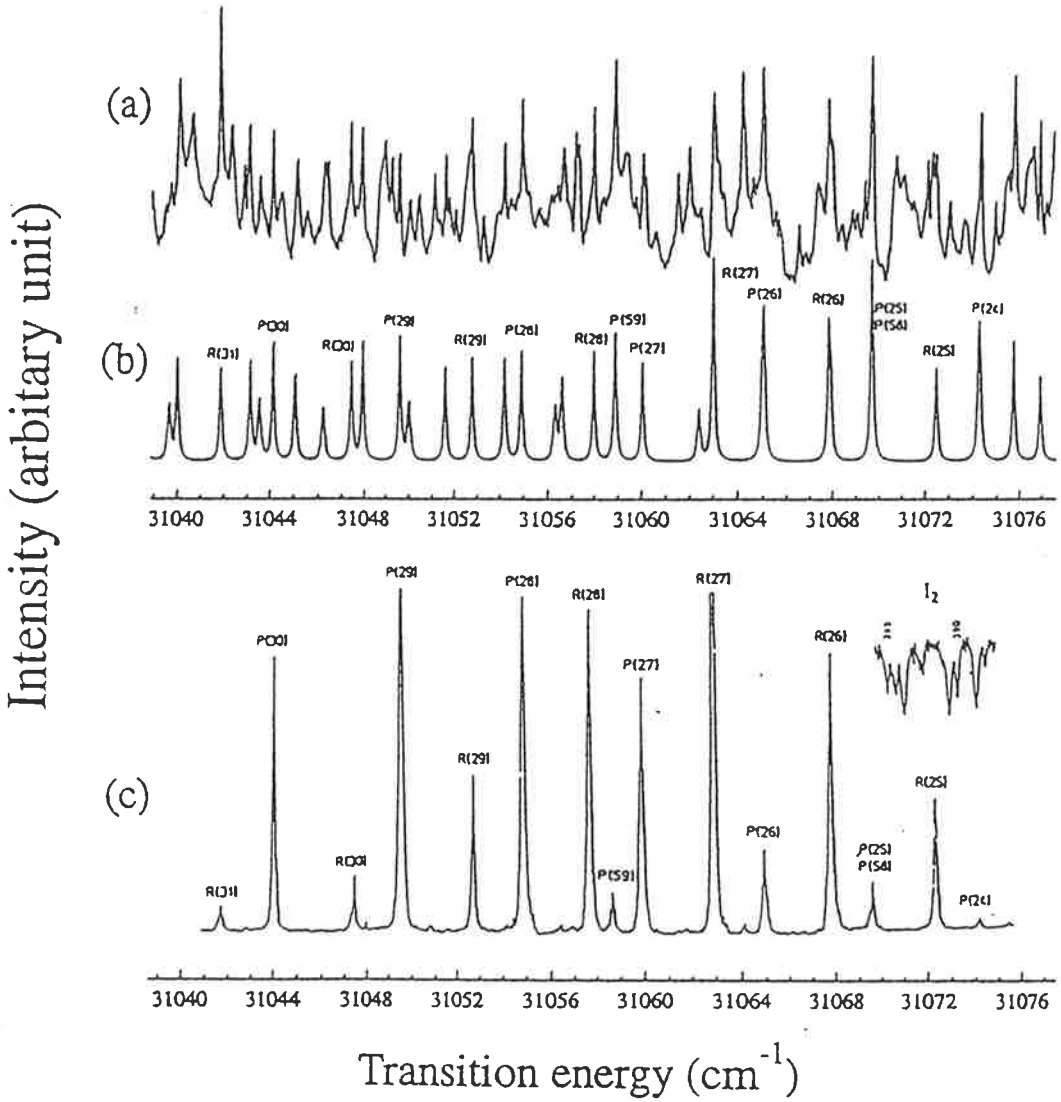

Figure 5.3: (a) Absorption spectrum of NaI (inverted), (b) the computed model with the bands observed by Schaefer et al (1984) and (c) a typical band fragment of the excitation spectrum observed by Schaefer et al (1982) in the same energy region. The modeling of (b) will be discussed later.

5.3 Analysis of the Absorption Spectrum

Analysis of the absorption spectrum of NaI has been prevented for decades because of the high density of lines. The fluorescence excitation spectrum reported by Schaefer et al (1982, 1984) produced a much less dense spectrum which allowed a break through in the assignments of the rotational band fragments. In this study use is made of the spectroscopic data they obtained to analyze the absorption spectrum and make adjustments to the shape and position of the $A0^+$ potential curve.

5.3.1 Position of lines

Predissociation of a curve crossing system was described by Child's semiclassical theory in terms of two hypothetical bound state levels: the "modified" diabatic $E_2(v_2, J)$ and the adiabatic $E_+(v_+, J)$ levels, deduced from the Bohr quantization conditions Eq.(2.38) and Eq.(2.39), as described in §2.3. The position and width of a predissociating line depends on the two nearby energy levels E_2 and E_+, the coupling parameter u and the ratio of the vibrational level spacings:

$$E = (E_2 + xE_+)/(1+x) \tag{5.1}$$

$$\Gamma = 2\pi x(1+\gamma x)(E_2 - E_+)^2/[\hbar\bar{\omega}_2(1+x)^3] \tag{5.2}$$

where $x = u\hbar\bar{\omega}_2/\hbar\bar{\omega}_+$, $\gamma = \hbar\bar{\omega}_2/\hbar\bar{\omega}_+$ and

$$u = exp(2\pi\nu) - 1 = exp\left(\frac{2\pi V_{12}^2}{\hbar v(E,J)\Delta F}\right) - 1, \tag{5.3}$$

with V_{12} the coupling strength and is taken to be 0.055 ev for NaI (Grice and Herschbach, 1974).

A useful approximate picture arises from equations 5.1 and 5.2. If the energies of the two hypothetical levels, E_2 and E_+, are plotted as a function of J(J+1), two series of approximately linear curves result, with the slopes given by the rotational constants

B. As predicted by Eq. (5.2), when the curves for the nearby levels E_2 and E_+ are close, the resonance is sharp; when the curves are further apart, the resonance is broad. Such a plot for NaI, using the optimized Dunham parameters of Table 4.2, is given in Fig. 5.4. The central line of a band fragment, the sharpest and the strongest line, is located at the intersection of the two hypothetic levels, i.e. the closest coincidence of the two rotational levels. On both sides of the central line are neighboring lines with symmetrically decreasing peak height and increasing line widths as the two levels move apart. Because of the high temperature and the similar slope for E_2 and E_+, there are a great many of these bands occurring in the absorption spectrum and there are also many lines in each band. As will be seen in the following, all the possible bands predicted by Fig. 5.4 for J values up to 100 were observed and more than 50 lines could be seen in each band for the energy region accessible with DCM dye. All of these observed bands are labelled in Fig. 5.4 with the J values of the central lines. Those band fragments observed with the excitation spectrum (Schaefer et al 1982, 1984) are also marked as "o" at the position of the central lines. It can be seen from Fig. 5.4 that those central lines locate slightly off the positions correspond to the closest coincidence of the two hypothetic levels ($\Delta J \sim 1-3$), indicating that there is a small error in the Dunham parameters. It also displays the extreme sensitivity of the central line position to the spectroscopic data of the two potential curves.

5.3.2 Intensity and the Voigt line profiles

The absorption intensity for a vapour in thermal equilibrium condition is given as (Herzberg, 1950 Chapter 4)

$$I_{abs}(v', v'') = \left(\frac{8\pi^3}{3hc}\right) I_0 \Delta x N_{v''} \nu R_e^2 [< \chi'' | \chi' >]^2 \qquad (5.4)$$

where h is Planck's constant, I_0 is intensity of the incident radiation, Δx is the length of the absorption sample, $N_{v''}$ is the population in the ground state level v'', ν is the frequency of the radiation, R_e is the electronic transition moment and the last term is

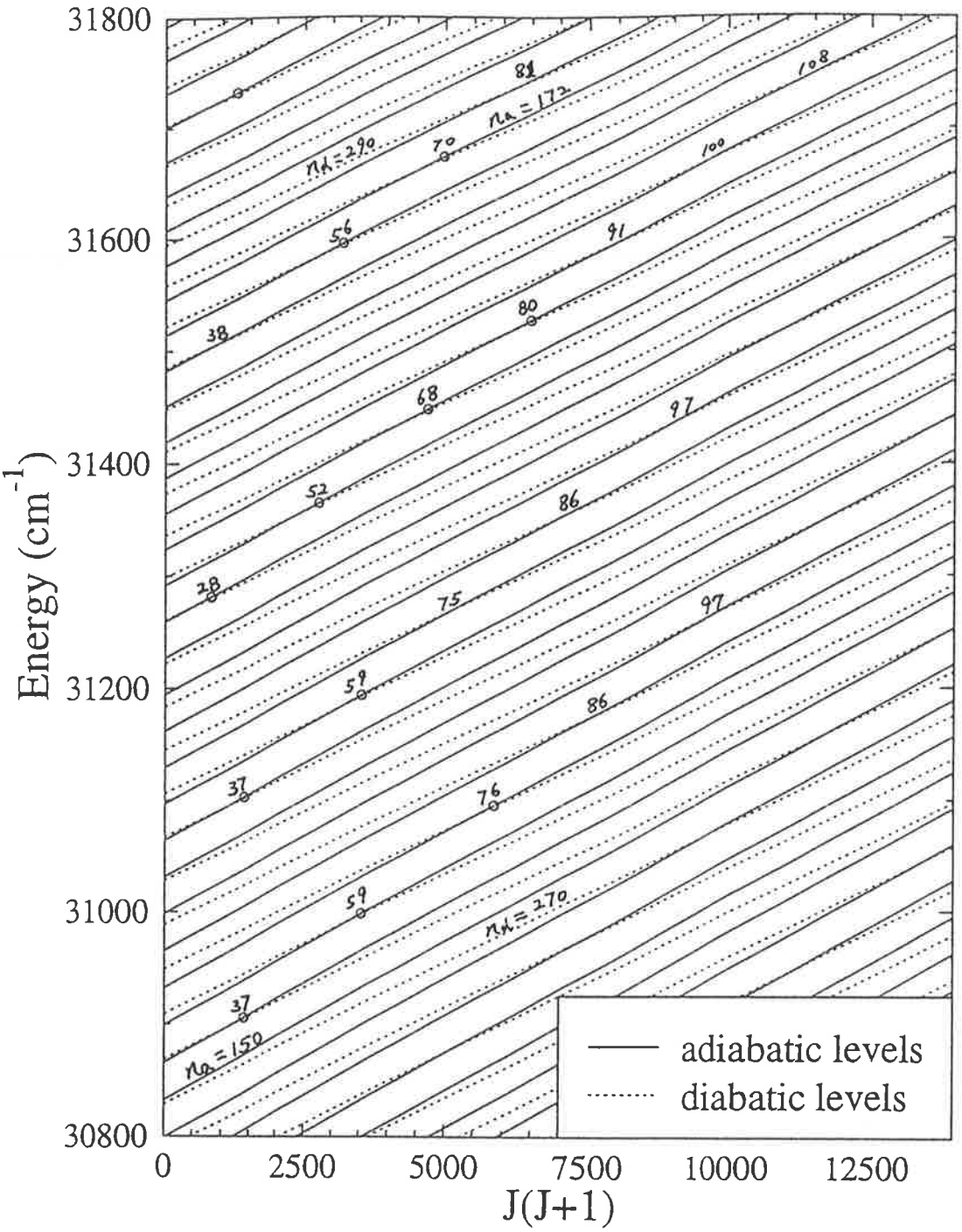

Figure 5.4: The diabatic and adiabatic energy levels relative to $v'' = 0$ against J(J+1) calculated with the Dunham parameters listed in Table 4.2. The center line rotational quantum numbers J are marked for each band observed in this study. Those band fragment observed by Schaefer et al (1984) are marked with o. The vibrational assignments were also taken from Schaefer et al.

Table 5.1: The Boltzmann Population Distribution for NaI

v''	Bz(%) 650°C	Bz(%) 1000°C	v''	Bz(%) 650°C	Bz(%) 1000°C
0	32.7	24.8	8	1.4	2.6
1	21.9	18.6	9	1.0	1.95
2	14.7	13.9	10	0.7	1.5
3	9.9	10.5	11	0.5	1.1
4	6.7	7.9	12	0.3	0.87
5	4.5	5.9	13	0.2	0.66
6	3.1	4.5	14	0.15	0.5
7	2.1	3.4	15	0.1	0.4

the Franck-Condon factor.

The Boltzmann factor

The population $N_{v''}$ in the ground state is determined by the Maxwell-Boltzmann distribution law. The percentage of the number of molecules in vibrational level v'' at temperature T is given by the Boltzmann factor:

$$Bz(v'') = exp(-E(v'')/kT)/Q_v \tag{5.5}$$

where k is the Boltzmann constant, $E(v'')$ is the term energy for the vibrational levels and

$$Q_v = \sum exp(-E(v'')/kT) \tag{5.6}$$

is the vibrational partition function. The Boltzmann factors for NaI at different temperatures are given in Table 5.1.

Intensity distribution in the rotational structure

Similarly, the percentage population of the number of molecules in rotational level J at temperature T is:

$$P_J = \frac{1}{Q_r}(2J+1)exp(-BJ(J+1)hc/kT), \tag{5.7}$$

where (2J+1) is the degeneracy of the level with an angular momentum J, B is the rotational constant and

$$Q_r = \sum(2J+1)exp(-BJ(J+1)hc/kT), \tag{5.8}$$

is the rotational partition function. The thermal distribution P_J of the rotational levels for $T = 650°C$ for NaI in the ground vibrational state is shown in Fig. 5.5 where the peak population occurs around $J = 50$ and with more than 1/4 of this population for $J \sim 100$.

The statistical weight of the lower state is $g'' = (2J+1)$, therefore the intensity distribution for rotational structure is given by (Herzberg, 1950 Chapter 3).

$$I_{abs} = \frac{2C_{abs.}\nu}{Q_r}S_J exp(-B''J''(J''+1)hc/kT) \tag{5.9}$$

where $C_{abs.}$ is a constant depending on the transition dipole moment, the Franck-Condon factor and the total number of molecules in the initial vibrational level. S_J is the Hönl-London factor. For the electronic transitions of interest in this study, which can be classified as the $^1\Sigma$ - $^1\Sigma$ transition and $\Delta\Omega = 0$, the Hönl-London factors are given by (Herzberg, 1950 Chapter 4):

$$S_J^R = J' \tag{5.10}$$

$$S_J^P = J' + 1, \tag{5.11}$$

for R and P branches. Transitions for the Q branch is optically forbidden and therefore $S_J^Q = 0$.

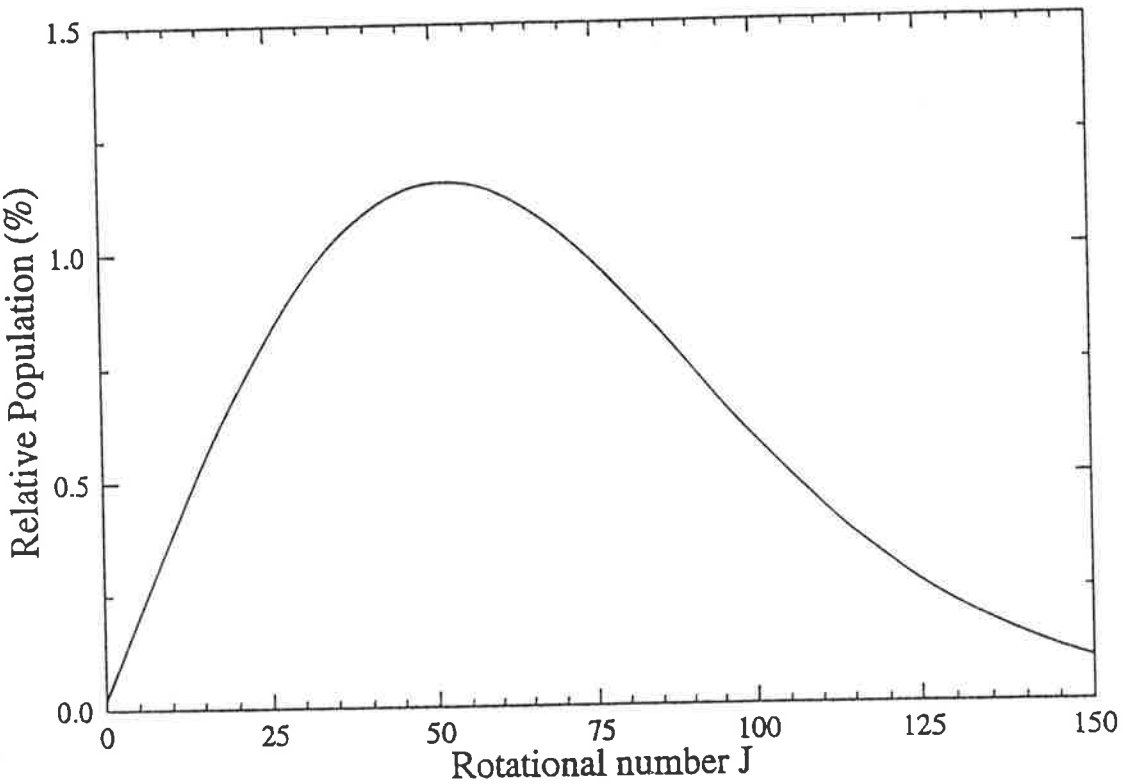

Figure 5.5: Thermal distribution of the rotational levels for $T = 650°C$ for NaI on the ground vibrational level.

The Franck-Condon factor

The intensity distribution are explained in an easily visualized manner by the Franck-Condon principle: the change in the electronic state during transitions in a molecule takes place so rapidly in comparison to the vibrational motion that immediately afterwards the nuclei still have very nearly the same relative position and velocity as before the transition. Therefore transitions vertically upward or downward in the potential energy diagram correspond to the most intense bands. Mathematically, the Franck-Condon factor can be calculated with the vibrational wavefunctions of the ground ($\chi''_{v''}$) and the upper ($\chi''_{v''}$) states:

$$FC(v'', E_t) = \int \chi''_{v''}(E'')\chi'(E')dr, \tag{5.12}$$

with the transition energy $E_t = E' - E''$.

In this study, the Franck-Condon factor for the excited state was approximated by calculation with the $\Omega = 0^+$ diabatic continuum state. Furthermore, the Franck-Condon factors are regarded as the same for the same transition energy for different J values since the centrifugal distortion is not significant in this study.

The Voigt profile

The width of an absorption line is broaden mainly due to thermal (Doppler) and natural (lifetime) broadening. Therefore the absorption line has the shape of a Voigt profile which is the convolution of the thermal and natural line profile and can be approximated by the empirical expression (Whiting 1968):

$$\begin{aligned} V(\nu) = \frac{I_\nu}{I_{\nu_G}} = \; & (1 - \tfrac{w_l}{w_v})exp[-2.772(\tfrac{\nu-\nu_G}{w_v})^2] + (\tfrac{w_l}{w_v})\tfrac{1}{1+4[(\nu-\nu_G)/w_v]^2} \\ & +0.016(1 - \tfrac{w_l}{w_v})(\tfrac{w_l}{w_v})\{exp[-0.4(\tfrac{\nu-\nu_G}{w_v})^{2.25}] - \tfrac{10}{10+(\frac{\nu-\nu_G}{w_v})^{2.25}}\}. \end{aligned} \tag{5.13}$$

The Gaussian and Lorentian profile represent thermal (Doppler) and natural (lifetime) broadening respectively:

$$I = I_{\nu_G} exp\left(-2.772(\frac{\nu - \nu_G}{w_G})^2\right) \tag{5.14}$$

$$I = I_{\nu_G} \frac{1}{1 + 4(\frac{\nu - \nu_G}{w_l})^2} \tag{5.15}$$

where w_l is the natural width, w_G the Doppler width, ν_G the line position, and I_{ν_G} the line intensity. w_v is the width of the Voigt profile and is given by

$$w_v = \frac{w_l}{2} + \sqrt{\frac{w_l^2}{2} + w_g^2}. \tag{5.16}$$

In this study, we assumed that the oscillator strengths are the same for all bands so that the intensity changes are due to thermal distribution in the ground state levels, the Hönl-London factor for rotational levels and the Franck-Condon factors. The intensity profile of a line in the experimental data was assumed to be:

$$I_\nu = \frac{I_0}{w_v} V(\nu - \nu_0), \tag{5.17}$$

where V is the Voigt profile given by Eq.(5.13). The intensity I_0 is determined by:

$$I_0 = A_0 Bz(v'') FC(v'', E_t) S_J \; exp(-BJ(J+1)hc/kT), \tag{5.18}$$

where A_0 is a constant chosen to fit the scale of the experimental data. $Bz(v'')$ is the Boltzmann population distribution and $FC(v'', E_t)$ is the relative strength of the Franck-Condon factor based on the calculation of Eq. (5.12). S_J is the Hönl-London factor and the last term accounts for the thermal distribution in rotational levels.

5.3.3 Modeling the absorption spectrum

The above model was first applied with the bands observed in the excitation spectrum, with transitions originating from the ground vibrational level ($v'' = 0$) and including 31 lines in each band fragment, to fit the absorption spectrum in the same energy region

as that in Fig. 5.3(c) and shown in Fig. 5.3(b). The corresponding absorption lines are clearly identified. Compared to the excitation spectrum, the absorption lines have much less intensity changes within a band fragment. In the excitation spectrum, the fluorescence intensity is proportional to the natural lifetime of the level and therefore reduces rapidly on each side of the central line due to predissociation. Actually, Schaefer et al (1984) could only observe lines with a natural width narrower than 300 MHz, corresponding to a maximum spacings of about 1 cm^{-1} between the nearby diabatic and adiabatic levels. For molecular states with a width broader than 300 MHz, the predissociation rate is too rapid compared with the fluorescence rate, the molecules don't have enough time to fluoresce before predissociating, so they are not observed. In the absorption spectrum, because of the Doppler broadening ($\sim$ 1.6 GHz) of all lines, it is impossible to identify the central lines by the intensity changes.

It can be seen from Fig. 5.3 that while the excitation spectrum observed by Schaefer et al (1984) contains fewer lines than that of the model spectrum the absorption spectrum has many more lines than the model. This implies that although the upper state is predissociated, the resonant structure still exists in regions far removed from the central sharp lines and can be observed with the absorption spectrum. This was confirmed by adding more lines and band fragments into the model. Because the absorption spectrum does not provide a good indication for the position of the central lines, they have to be obtained from the Dunham parameters. The optimized Dunham parameters obtained in the previous Chapter were used to calculate the position of the excited state levels with Child's semiclassical theory since they are more accurate for the coincidence of the two levels for the central lines. The locations of the center lines were shown Fig. 5.4.

With the Dunham parameters given in Table 4.1 to calculate the position of the ground state levels, the first attempt to model the absorption spectrum using Eq.(5.17) with the P and R branches was made.

For the best fit, w_G was taken to be 0.12 cm^{-1} which is about twice the Doppler width (1.6 GHz or 0.05 cm^{-1}). This is in approximate agreement with the convolution of the Doppler width with the instrument function which has a band width of about 2-3GHz (0.07-0.1 cm^{-1}). The line width of the transition is approximated by:

$$w_l = 3 \cdot 10^{-8}(\Delta J(2J_c + \Delta J + 1))^2 \ cm^{-1} \tag{5.19}$$

where $\Delta J = J - J_c$ and J_c is the J value for the central line. This is modeled according to Eq. (5.2). The other parameters were obtained from the best fit to the recorded absorption spectrum.

The model spectrum for transitions originating from $v'' = 0$ is given in Figs. 5.6 to 5.8 where a satisfactory fit was obtained for transition energies higher than 30500 cm^{-1}. For lower energies, the corresponding $v'' = 0$ transition lines in the recorded absorption are weaker than the model spectrum and there are other stronger lines which have not been accounted for as demonstrated in Fig. 5.9(a). This implies that transitions from other ground state vibrational levels are important and must be included, in particular the $v'' = 1$ level. Fig. 5.9(a-d) illustrate the changes of the spectrum resulting from changes in the relative strength of the Franck-Condon factors $FC(v'', E_t)$ for $v'' = 0$ and 1. It is obvious that a large contribution from $v'' = 1$ has to be included in the model spectrum to get a good fit to the observed spectrum as seen in Fig. 5.9(c) with $R_{FC} = 0.7$ where $R_{FC} = FC(v'' = 0, E_t)/FC(v'' = 1, E_t)$. Together with the Boltzmann factors of these two ground state vibrational levels, the transition strengths originating from these two levels are about the same. Fig. 5.10 and Fig. 5.11 show the best fit for some of the lower energy regions with increasing contribution from $v'' = 1$. In all the calculations, 25 lines on each side of the central line or 51 lines in each band fragment are used in the calculation. It is found that a 20% change of the ratio R_{FC} does not make a significant change for the best fit in the model spectrum. As the ratio changes it was noted that while some lines appeared to fit better, others may get worst. This is because the value of the ratio used here is for a continuum and

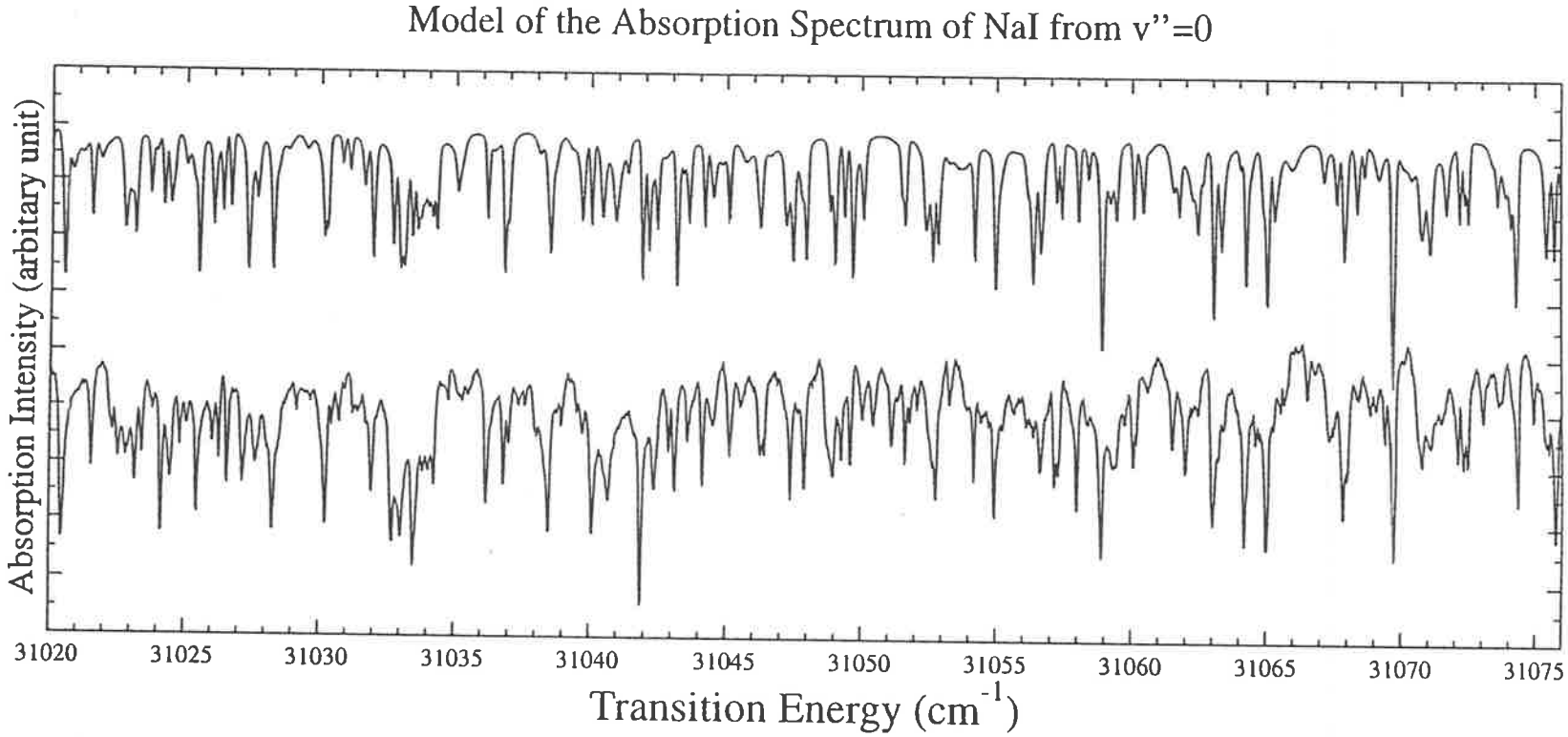

Figure 5.6: Model of the absorption spectrum of NaI according to the calculation of Eq. (5.17) for transitions from $v''=0$ (top) and the measured absorption spectrum of the study (bottom) in the same energy region as that in Fig. 5.3.

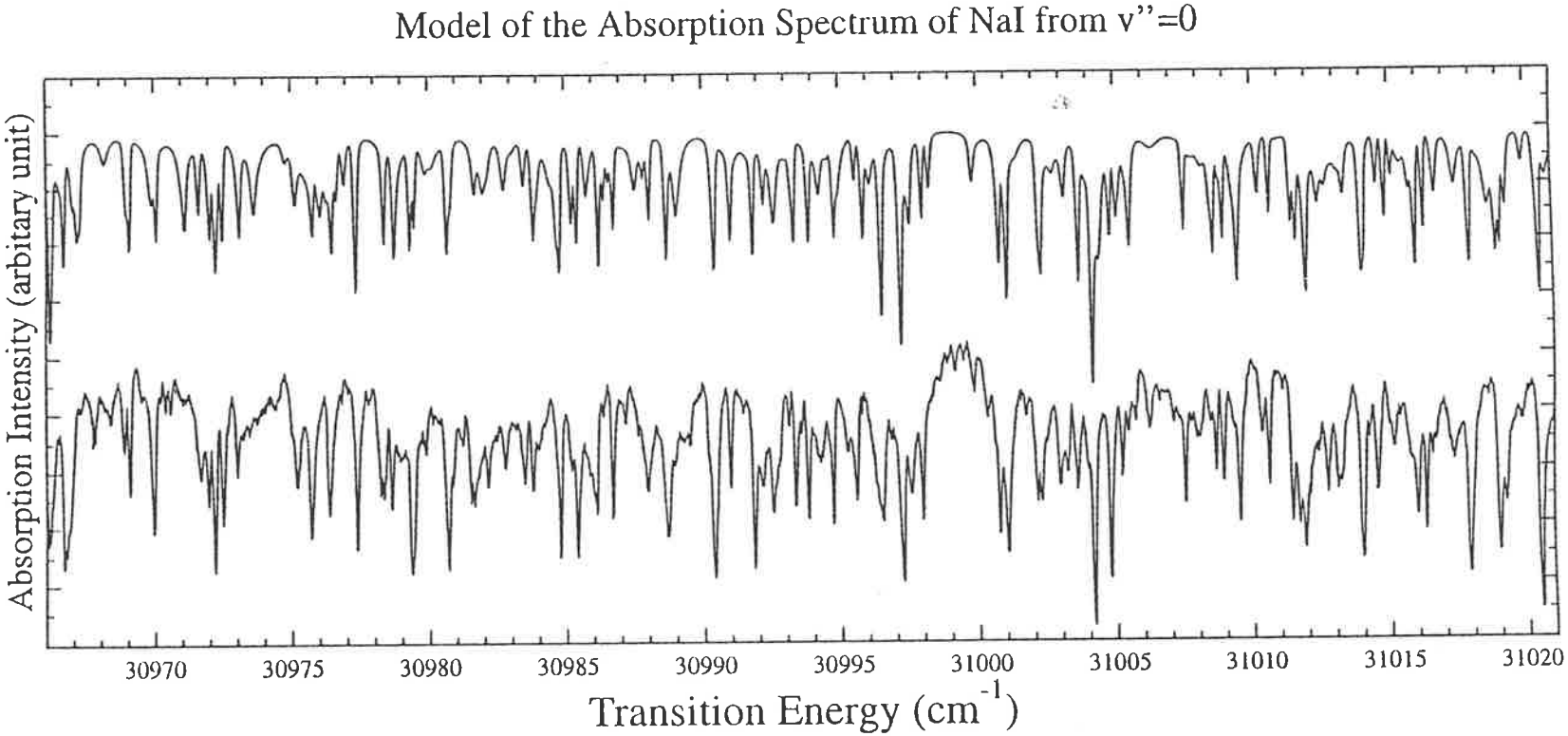

Figure 5.7: Model of the absorption spectrum of NaI according to the calculation of Eq. (5.17) for transitions from v''=0 (top) and the measured absorption spectrum of the study (bottom).

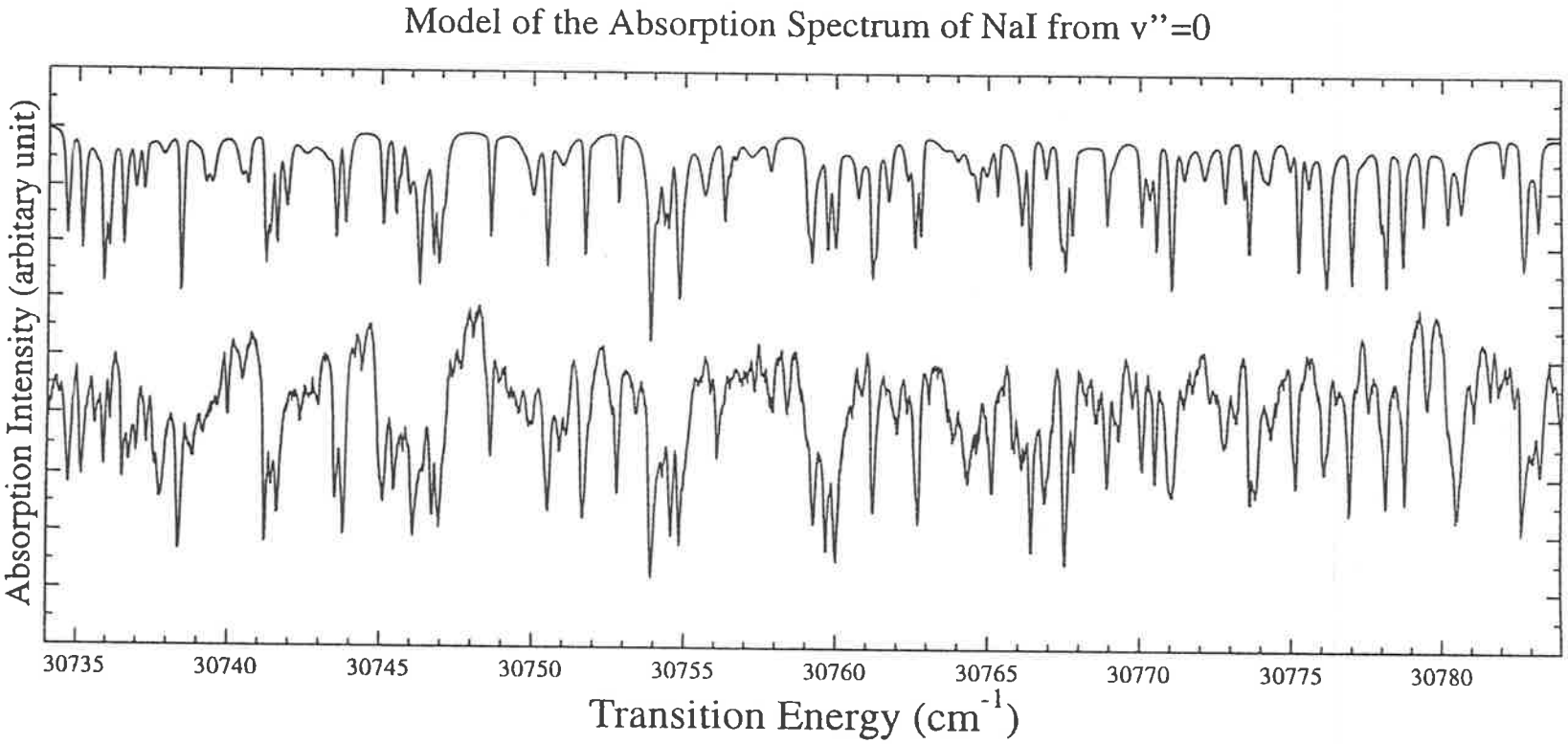

Figure 5.8: Model of the absorption spectrum of NaI according to the calculation of Eq. (5.17) for transitions from $v''=0$ (top) and the measured absorption spectrum of the study (bottom).

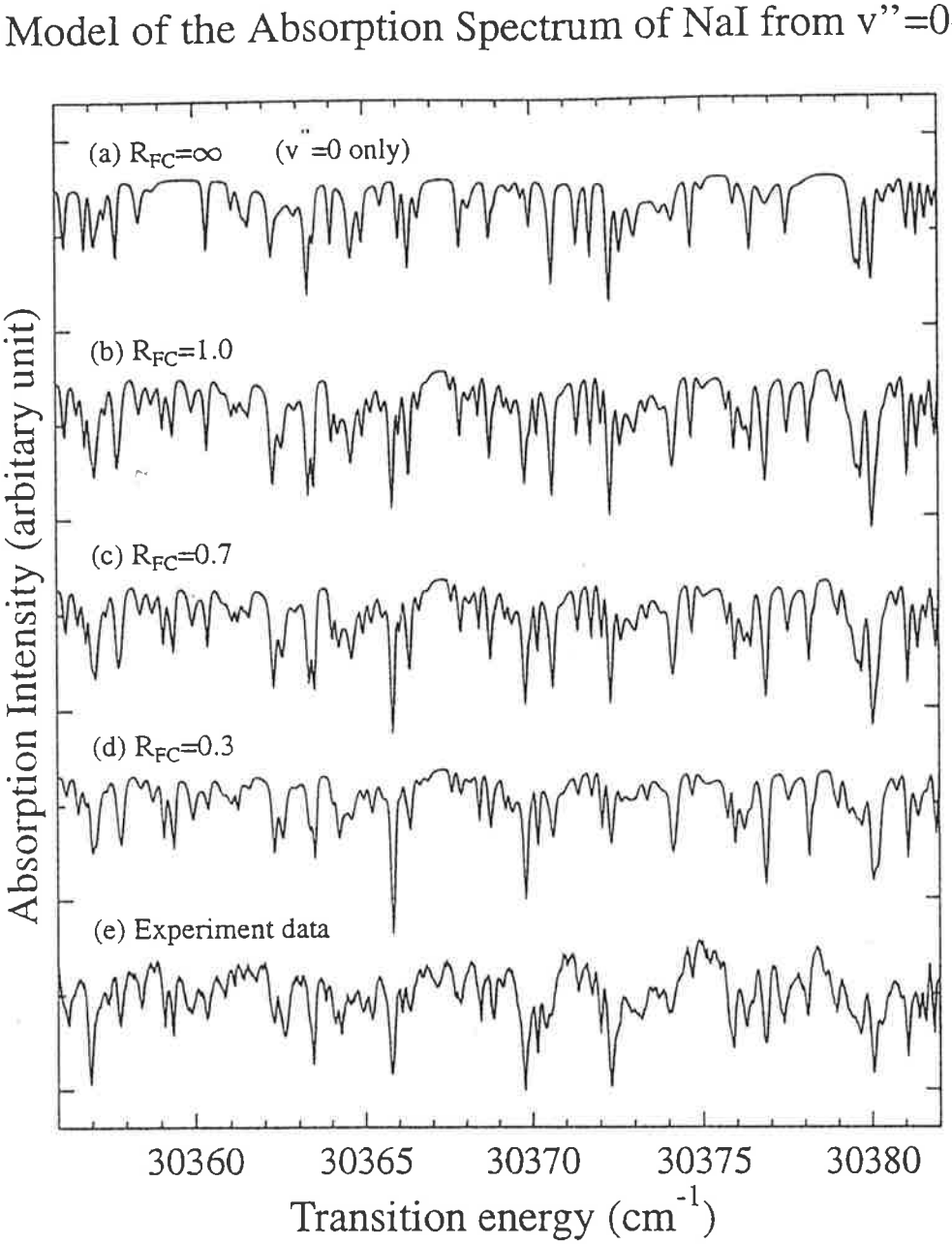

Figure 5.9: Model of the absorption spectrum of NaI according to the calculation of Eq. (5.17) for transitions from $v'' = 0 - 1$ (a-d) with different contribution from the $v'' = 1$ vibrational level. The recorded absorption spectrum of this study is shown in (e). R_{FC} is the ratio of Franck-Condon factors $FC(v'' = 0)/FC(v'' = 1)$. Because the ratio of Boltzmann factors for these two ground state vibrational levels is about 1.5, the transition strength originating from these two levels is about the same for $R_{FC} = 0.7$.

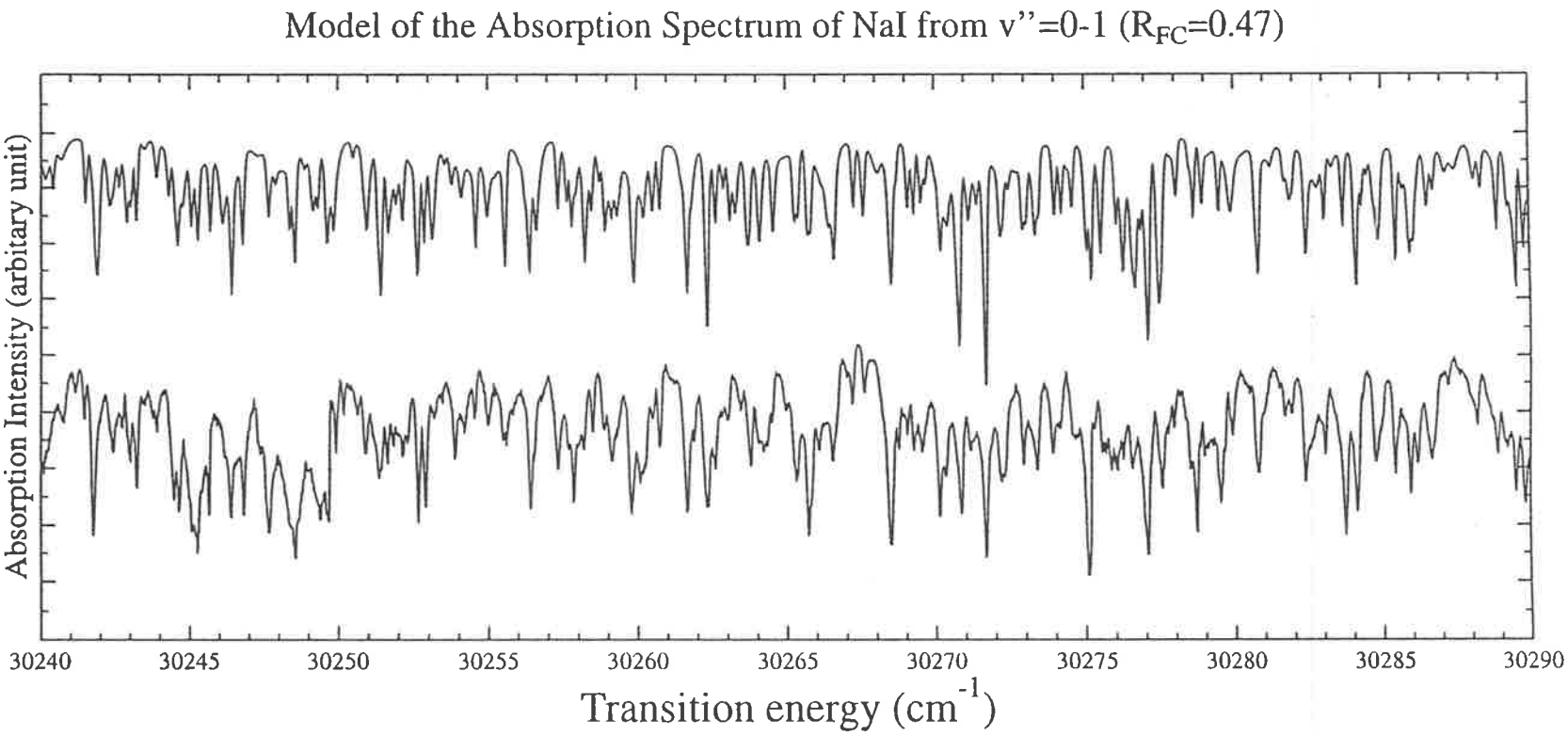

Figure 5.10: Model of the absorption spectrum of NaI according to the calculation of Eq. (5.17) for transitions from v"=0-1(top) and the measured absorption spectrum of the study (bottom). R_{FC} gives the ratio of Franck-Condon factors for FC(v"=0)/FC(v"=1).

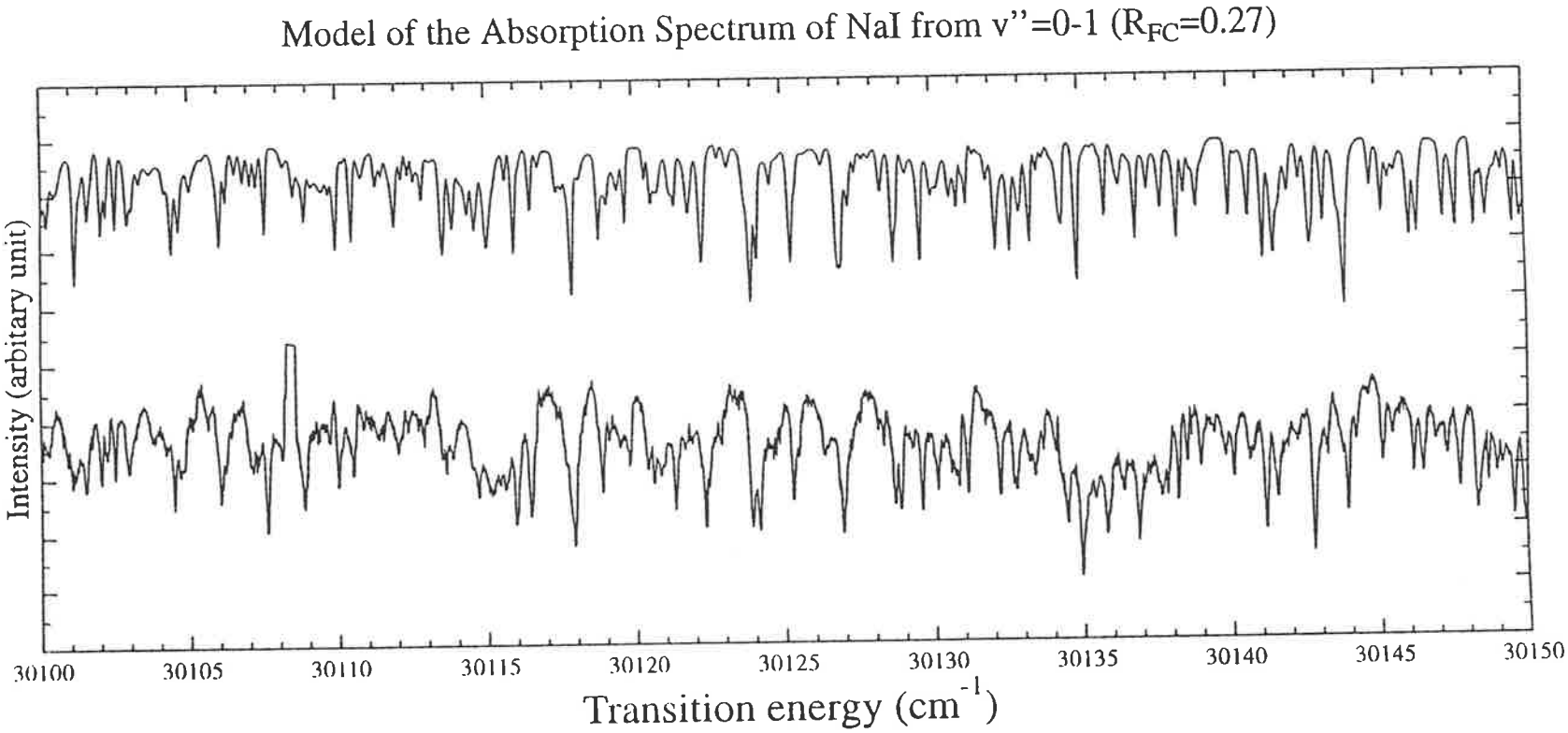

Figure 5.11: Model of the absorption spectrum of NaI according to the calculation of Eq. (5.17) for transitions from v"=0-1 (top) and the measured absorption spectrum of the study (bottom). R_{FC} gives the ratio of Franck-Condon factors for FC(v"=0)/FC(v"=1).

is an approximation for the resonant line structure, the model does not include the changes in the ratio and the predissociation line width due to different the slopes of the diabatic and adiabatic hypothetical levels as seen in Fig. 5.4 for different rotational bands.

Throughout all the analyzed energy regions, only P and R branches and no Q branch lines were observed, which is in agreement with Hund's case (c) coupling. By comparing the model spectrum with the experimental data, it was found that not only all the band fragments observed with the excitation spectrum but also all the other possible band fragments predicted by the Child's theory, as shown in Fig. 5.4, could be observed. The model spectrum accounted for most of the main features. Some weak band fragments are difficult to identify from the fluctuation background. Some weak lines which were not accounted for by the model may originate from lines with $\Delta J > 25$ in the bandfragments or higher vibrational levels in the ground state. However, their contribution to the overall spectrum is very small and they were not included in this study. It is also noted that there are a few reasonably strong lines not accounted for which may originate from superimposed weak lines or perhaps traces of an impurity in the salt.

5.3.4 Transitions from $v'' = 0$ and 1

The model for the absorption spectrum given above uses the Dunham parameters derived from a laser induced molecular fluorescence experiment (Schaefer et al 1984) and their vibrational and rotational assignments (as presented in Fig. 4.2 and Fig. 5.4) to predict the possible bands. It represents the first attempt to analyze the absorption spectrum of NaI and reproduce the main features of the observed spectrum in an energy region from 30000 to 31200 cm^{-1}. With this model, all the possible bands in the experimental region were observed with about 50 lines in each band fragment, compared to only about 7 lines in the fluorescence experiment The results support

some of the spectroscopic data of Schaefer et al, for example the rotational constants B and the rotational assignments J. However, it was found that there is an inconsistency between the Franck-Condon factors for the potential curve that they proposed for the excited state and the dominant vibrational transitions from the ground state.

Calculated Franck-Condon factors for transitions originating from $v'' = 0 - 3$ for the potential curves of van Veen et al (1981) and Schaefer et al (1984) are shown in Fig. 5.12(a) and (b) where the excited state potential curve of Schaefer et al was approximated by the analytical expression obtained in the previous Chapter. It can be seen that the Franck-Condon factor for the potential curve of Schaefer et al increases as v'' increases over the full range of energy of interest, and the Franck-Condon factor for $v'' = 0$ is at least 10 times less than that for $v'' = 1$ in the observed energy region. Furthermore, because of the high temperature, the thermal population (see Table 5.1) decreases much more slowly than the increase in the Franck-Condon factors as the ground vibrational level increases for the potential curve of Schaefer et al. Thus transitions from ground state vibrational levels higher than $v'' = 0$ and 1 should be dominant. This is not in agreement with the model spectrum where transitions originate mainly from $v'' = 0$ in the high energy region and $v'' = 1$ in the lower energy region. In contrast, the potential curve of van Veen et al gives a Franck-Condon factor a few times stronger for $v'' = 0$ than for $v'' = 1$, 2 etc throughout the observed region. Therefore, transitions originating from $v'' = 0$ would be at least 5 times stronger than those from $v'' \geq 1$ by taking account the thermal distribution as well. With such a strong intensity, the transitions from higher vibrational levels ($v'' \geq 1$) would be difficult to observe in the fluctuation background as seen in Fig. 5.6 - Fig. 5.8. However it is clearly apparent that at lower spectral energy the potential curve of van Veen et al gives incorrect Franck-Condon factors because transitions originating from $v'' = 1$ are seen to dominate. Furthermore, as discussed in the previous chapter, the rotational constants of their potential curve are too small to explain the experimental data.

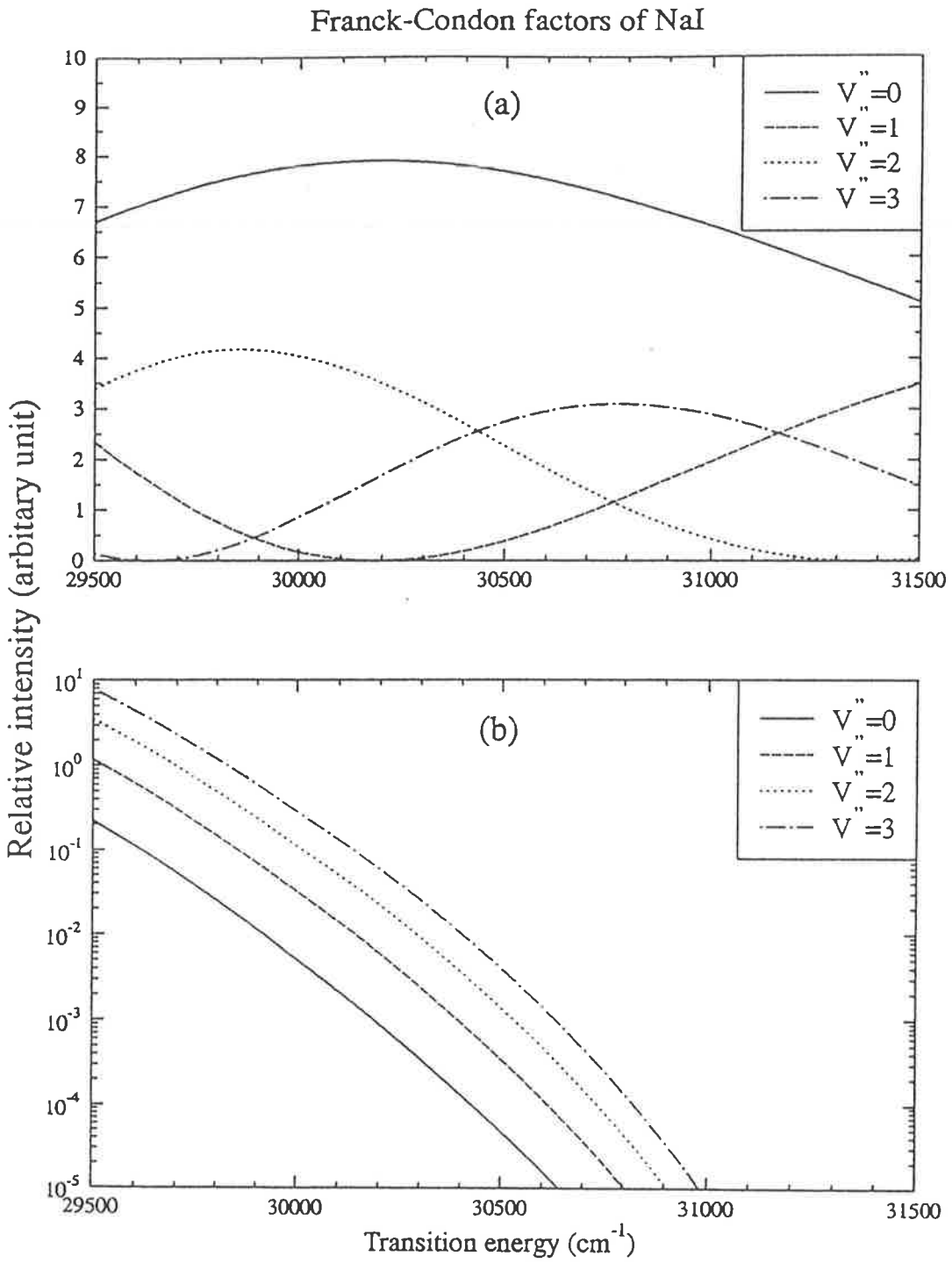

Figure 5.12: Franck-Condon factors for the potential curve of van Veen et al (1981) (a) and the potential curves of Schaefer et al (1984) (b) for transitions from $v'' = 0 - 3$.

The disagreement between the published potential curves and the Franck-Condon factors observed in this study implies that modification in the potential curve or the rotational and vibrational assignments is necessary to explain the absorption spectrum and the controversy between the published potential curves. The absorption spectrum recorded in this study is modeled, as described before, by the Dunham parameters derived from the experimental data of Schaefer et al with their rotational and vibrational assignments. The success of this model to fit most of the absorption feature recorded in this study over a large energy region with all the predicted band fragments suggest that the assignments are correct. Furthermore, since more rotational lines were recorded in each band fragment, the experimental values can be used to confirm the assignments derived from the Dunham parameters, over a larger energy region for each band fragment than was possible in the fluorescence experiment , to prevent any accidental agreement of the line position. The assignments of rotational lines and the ground state vibrational levels from which the transitions originated can be checked with the combination relation between the P and R branches:

$$\Delta_2 F''(J) = R(J-1) - P(J+1), \tag{5.20}$$

which is related only to parameters of the well known ground state levels (Herzberg, 1950 Chapter 4):

$$\Delta_2 F''(J) = (4B_{v''} - 6D_{v''})(J+\frac{1}{2}) - 8D_{v''}(J+\frac{1}{2})^3. \tag{5.21}$$

where $B_{v''}$ and $D_{v''}$ are rotational constants for vibrational level v which can be calculated from the Dunham parameters given in Table 4.1:

$$B_{v''} = \sum_i Y_{i1}(v''+\frac{1}{2})^i \tag{5.22}$$

$$D_{v''} = \sum_i Y_{i2}(v''+\frac{1}{2})^i \tag{5.23}$$

Table 5.2 and Table 5.3 list the calculated results of the $\Delta_2 F''$ values and the experimental values $\Delta_2 F''(exp)$ of this study for part of two rotational bands with

Table 5.2: The observed rotational lines originating from $v'' = 0$ for a band of $n_a = 151$ and $n_d = 271$ and the $\Delta_2 F''$ values

J	P(J)	R(J)	$\Delta_2 F''(exp)$	$\Delta_2 F''_{v''=0}$	$\Delta_2 F''_{v''=1}$	$\Delta_2 F''_{v''=2}$
26	30672.498	30675.472	12.438	12.439	12.370	12.302
27	30667.592	30670.695	12.904	12.907	12.836	12.765
28	30662.568	30665.792	13.235	13.375	13.301	13.228
29	30657.46	30660.644	13.888	13.843	13.767	13.691
30	30651.904	30655.387	14.274	14.311	14.232	14.154
31	30646.37	30649.917	14.843	14.778	14.697	14.616
32	30640.544	30644.237	15.301	15.246	15.162	15.079
33	30634.616	30638.422	15.684	15.713	15.627	15.541
34	30628.553	30632.426	16.188	16.181	16.092	16.003
35	30622.234	30626.215	16.708	16.648	16.556	16.465
36	30615.718	30619.88	17.117	17.115	17.020	16.927
37	30609.098	30613.328	17.589	17.581	17.485	17.388
38	30602.291	30606.579	18.039	18.048	17.949	17.850
39	30595.289	30599.738	18.485	18.514	18.412	18.311
40	30588.094	30592.586	19.015	18.980	18.876	18.772
41	30580.723	30585.379	19.368	19.446	19.339	19.233
42	30573.218	30577.968	19.878	19.912	19.803	19.693
43	30565.501	30570.346	20.4	20.378	20.266	20.154
44	30557.568	30562.592	20.795	20.843	20.728	20.614
45	30549.551	30554.646	21.26	21.308	21.191	21.074
46	30541.332	30546.498	21.817	21.773	21.653	21.534

Table 5.3: The observed rotational lines originating from $v'' = 1$ for the band of $n_a = 145$ and $n_d = 266$ and the $\Delta_2 F''$ values

J	P(J)	R(J)	$\Delta_2 F''(exp)$	$\Delta_2 F''_{v''=0}$	$\Delta_2 F''_{v''=1}$	$\Delta_2 F''_{v''=2}$
18	30246.399	30248.544	8.640	8.689	8.641	8.594
19	30243.000	30245.263	9.161	9.158	9.108	9.057
20	30239.383	30241.794	9.592	9.627	9.574	9.521
21	30235.671	30238.159	10.068	10.096	10.040	9.985
22	30231.726	30234.331	10.525	10.565	10.506	10.449
23	30227.634	30230.361	11.000	11.033	10.973	10.912
24	30223.331	30226.188	11.455	11.502	11.439	11.376
25	30218.906	30221.845	11.889	11.970	11.904	11.839
26	30214.299	30217.372	12.399	12.439	12.370	12.302
27	30209.446	30212.649	12.845	12.907	12.836	12.765
28	30204.527	30207.799	13.326	13.375	13.301	13.228
29	30199.323	30202.803	13.784	13.843	13.767	13.691
30	30194.015	30197.529	14.247	14.311	14.232	14.154
31	30188.556	30192.223	14.708	14.778	14.697	14.616
32	30182.821	30186.564	15.207	15.246	15.162	15.079
33	30177.016	30180.904	15.587	15.713	15.627	15.541
34	30170.977	30174.945	16.180	16.181	16.092	16.003
35	30164.724	30168.845	16.572	16.648	16.556	16.465
36	30158.373	30162.578	17.028	17.115	17.020	16.927
37	30151.817	30156.154	17.481	17.581	17.485	17.388
38	30145.097	30149.518	17.973	18.048	17.949	17.850
39	30138.181	30142.819	18.383	18.514	18.412	18.311

transitions originated from $v'' = 0$ and $v'' = 1$ respectively. The observed absorption lines are located near the calculated value from the Dunham parameters with the corresponding assignments. With the experimental error of less than 0.1 cm^{-1}, both the rotational assignments and the ground state vibrational assignments of the absorption lines are confirmed to be correct. The confirmation of the $v'' = 1$ transitions, together with its relative strength of the Franck-Condon factors, imply that a departure from the published potential curves is necessary to account for the absorption spectrum. It should also be pointed out that although the vibrational assignments of Schaefer et al (1984) were used in this analysis, they may not be correct. It can only be shown that the position of these vibrational levels in the observed energy region is correct. It is always possible to modify the potential curve and change the vibrational assignments but keeping these energy levels at the same position. The validity of the vibrational assignments of Schaefer et al (1984) are questioned in this study and are likely to be incorrect in view of the following discussion.

From Fig. 5.6 - Fig. 5.11, it was found that some lines in the model spectrum are about 0.2 cm^{-1} from the observed position which exceeds the experimental error and results in changes to the intensity and width of some overlapping lines. The model needs to include more accurate information about the position of lines, widths and intensity distribution for each band fragment to give a better fit. Moreover, the model was found to fail when applied to the absorption spectra in higher energy regions measured with other dyes. This implies that there is an error in the vibrational assignments and the Dunham parameters are accurate only in a small energy region corresponding to the most detailed section of the fluorescence excitation spectrum. For higher energy, the model spectrum doesn't shown any similarity to the experimental data, indicating that the error in the Dunham parameters is so large that they failed to predicted many bands. This can be taken as further evidence that the potential curve proposed by Schaefer et al (1984) is incorrect.

5.3.5 The proposed potential curve for $\Omega = 0^+$ state

There exists contradiction between the published potential curves and the experimental data of this study. The potential curve of Schaefer et al gives the correct energy levels and rotational constants in the experimental energy region, but the Franck-Condon factors are greatly different from the experimental values. This implies that the repulsive limb of the potential curve is not located at the correct position. On the other hand, the potential curve of van Veen et al gives the correct Franck-Condon factors only for transition energies higher than 30500 cm^{-1}, and incorrect rotational constants when compared with the experimental data. This implies that a modification of this potential curve in the lower energy region ($E_t < 30500\ cm^{-1}$) is needed to fit the experimental data.

Summarizing the above analysis, it is apparent that the $\Omega = 0^+$ potential curve should account for the following spectroscopic properties in the analyzed energy region.

- The same rotational constants B and vibrational level spacings for the adiabatic state as those given by Schaefer et al (1984), with an error in line position less than the experimental error.
- Similar relationship of the Franck-Condon factors for $v'' = 0$ and $v'' = 1$ to those given by the potential curve of van Veen et al (1981) for transition energies higher than 30500 cm^{-1};
- Larger Franck-Condon factors for $v'' = 1$ than that from $v'' = 0$ for transition energies lower than 30500 cm^{-1}.
- Transitions originating from $v'' > 1$ not strong enough to make an observable contribution to the absorption spectrum.

In the following, a potential curve which meets all these spectroscopic properties is proposed.

In quantum mechanics, the rotational constant B is given by the integral:

$$B = \frac{\hbar^2}{2\mu} < \chi(r)|\frac{1}{r^2}|\chi(r) > \tag{5.24}$$

where r is the internuclear distance and $\chi(r)$ is the vibrational wavefunction. Its value is determined by the location and the shape of the potential curve. The location of the potential curve affects the value of $1/r^2$ while the shape of the potential curve affects the amplitude of the wavefunction. For the potential curves given by Schaefer et al (1984), it is noted that in the observed energy region, as shown in Fig. 4.3, the adiabatic potential curve has a larger B value than the diabatic one although its repulsive limb is located at a greater internuclear distance as shown in Fig. 5.13. This is because to the left of the crossing point the diabatic potential has a very deep well and the wavefunction in this region has a small amplitude. Thus, the integrand of $\chi(r)\frac{1}{r^2}\chi(r)$ is small in that region. On the other hand, the excited adiabatic state has a much shallower well at the same region which leads to a larger amplitude wavefunction and thus a larger integrand in the same region. Since the wavefunctions for both potentials are nearly the same to the right of the crossing point, the integrands to the left of the crossing point will decide which B value is the greater. The excited state potential curve given by van Veen et al (1981) has a smaller B value than that of Schaefer et al since its repulsive limb is located at a larger internuclear distance and they both have about the same depth well. Therefore, the B value of a potential curve can, in principle, be increased by translationally moving the repulsive limb of the potential curve to a smaller internuclear distance, or having a shallower potential well in the repulsive limb region.

It is noted from the previous discussion that the adiabatic potential curve of Schaefer et al (1984) is derived from an RKR method based on their extrapolation to determine the lower energy levels using the Dunham parameters which were found in a much higher energy region. There is no direct experimental evidence for determining the location of the lower energy levels, so that while the position of the high energy

levels have been measured by the experiment data, the actual position of the low energy levels remain unknown. Furthermore, the location of repulsive limb of their potential curve is not uniquely fixed by their experimental data, but by their assumed position of the lower energy levels. The change of the unknown lower energy levels will affect the location and the shape of their "RKR" potential curve. The incorrect Franck-Condon factors of their potential curve suggest that their assumption about the lower vibrational levels are not correct. It follows that an alternative set of energy levels in the lower potential energy region is needed to support a potential curve which fits the known experimental data better.

The potential curve proposed in this study is a modification of the potential curve given by van Veen et al (1981), especially in the lower energy region of the repulsive limb. The location of the repulsive limb of the excited state potential curve, determined by the Franck-Condon factors, is very close to that of van Veen et al for energies higher than 30500 cm^{-1}. However, the only possibility for this potential curve to have rotational constants B very close to those given by Schaefer et al in the experimental energy region, as discussed above, is to have a shallower shape than that of van Veen et al in the repulsive limb region. This is in accordance with the requirement that the slope of the potential curve should become smaller than that of van Veen et al in the lower part of the experimental energy region ($E_t < 30500\ cm^{-1}$) to give the correct ratio of the Franck-Condon factor R_{FC}, as seen in Fig. 5.9 to Fig 5.11. While the repulsive limb of the potential curve is shallow in the low energy region to give the correct rotational constant B in the experimental energy region, it should also smoothly and rapidly approach the dissociation limit as internuclear distance increases due to the nature of a covalent state. Such a potential curve is proposed to be

$$V_1(r) = \left(\frac{12}{r}\right)^3 exp\left(-\left(0.01 + \left(\frac{r}{7.5}\right)^6\right)(r - 2.7) + \left(\frac{2.42}{r}\right)^{15}\right) + 3.18\ \ (ev) \quad (5.25)$$

and is shown in Fig. 5.13. It is an empirical modification based on the potential curve of van Veen et al. The very sharp slope at small internuclear distance is provided

by the $(\frac{12}{r})^3$ coefficient and the exponential of $(\frac{2.42}{r})^5$. The shallower shape above the equilibrium position of the ground state and the fast damping of the potential curve are generated by the exponential of $-(0.01+(r/7.5)^6)(r-2.7)$. The dissociation limit is taken to be 3.18 ev, given by van Veen et al. The electronic coupling strength V_{12} is taken to be 0.055 ev in this study. No attempt was made to obtain a more accurate coupling strength since small modification to this value produces a negligible contribution to the spectroscopic parameters concerned in this study.

Although the proposed potential curve appears different from any of the currently published potential curves in the lower energy region above the equilibrium position of the ground state, as shown in Fig. 5.13, it is consistent with the currently available experimental data. The Franck-Condon factors, which fix the location of the repulsive limb of the potential curve, are in agreement with the broadband absorption experiment of van Veen et al (1981) and are consistent with the high resolution absorption spectrum measurements of this study. Its rotational constants and vibrational spacings in the experimental region are in excellent agreement with those given by Schaefer et al (1984).

The smaller slope of the potential curve makes the transitions from right-hand turning points of the lower state levels stronger than that for van Veen's potential curve, consequently the Franck-Condon factors for transitions originating from $v'' = 1$ are stronger than those from $v'' = 0$ for energies below 30450 cm^{-1}, as illustrated in Fig. 5.14(a). The ratio of Franck-Condon factors for $v'' = 0$ and 1, R_{FC}, for the proposed potential curve are given in Fig. 5.14(b) which are in agreement with the observation in Fig. 5.9 to Fig. 5.11.

The shallower shape of the proposed potential curve also increases the rotational constants B of the adiabatic state when compared with that of van Veen et al providing excellent agreement with the experimental values which are the same as those given by Schaefer et al (1984) over the observed energy region, as shown in Fig. 5.15(a).

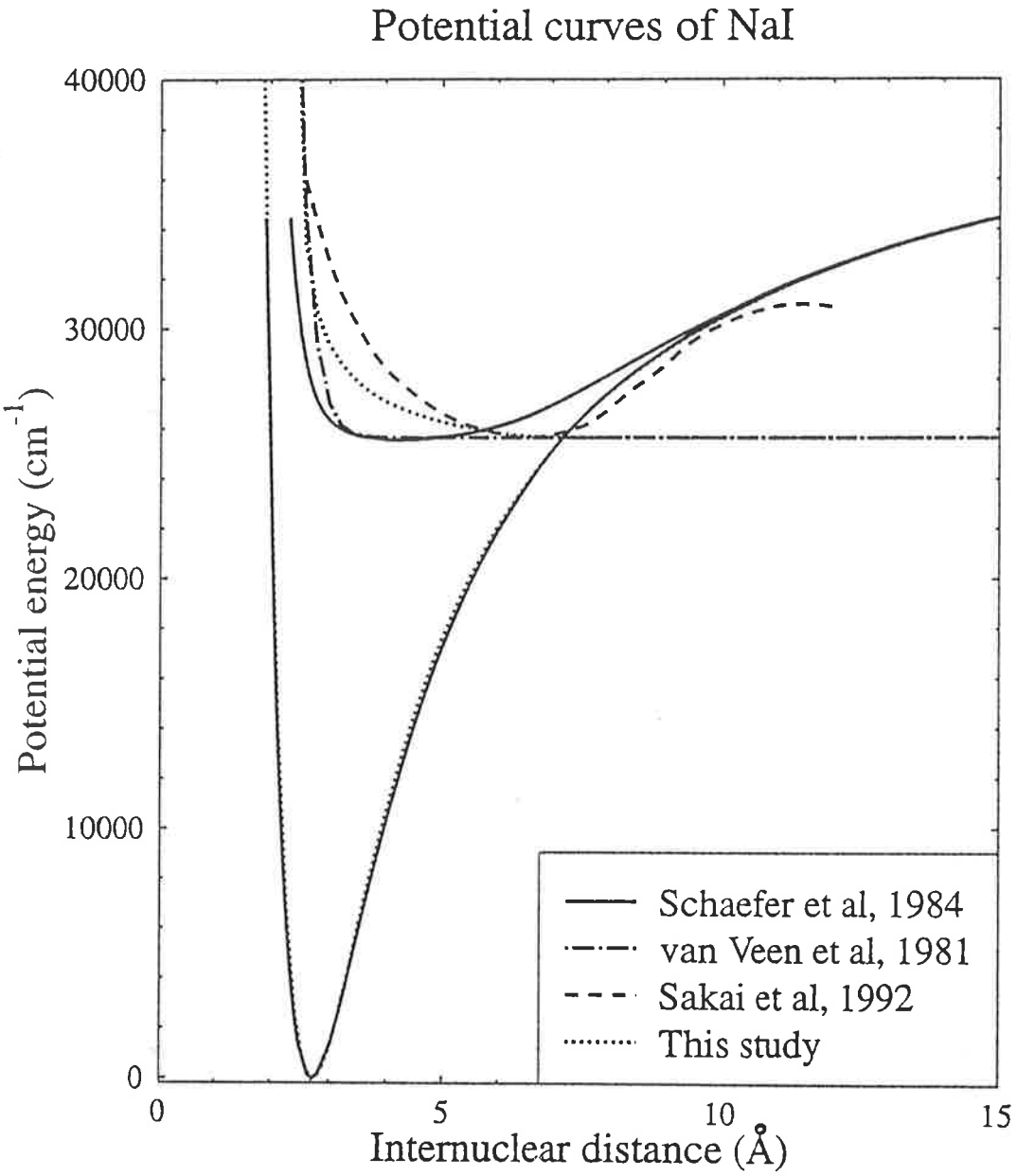

Figure 5.13: Comparison of the proposed potential curve with those of the other authors. Note that the excited state potential curves of Schaefer et al (1984) and Sakai et al (1992) are adiabatic potential curves while the others are diabatic ones.

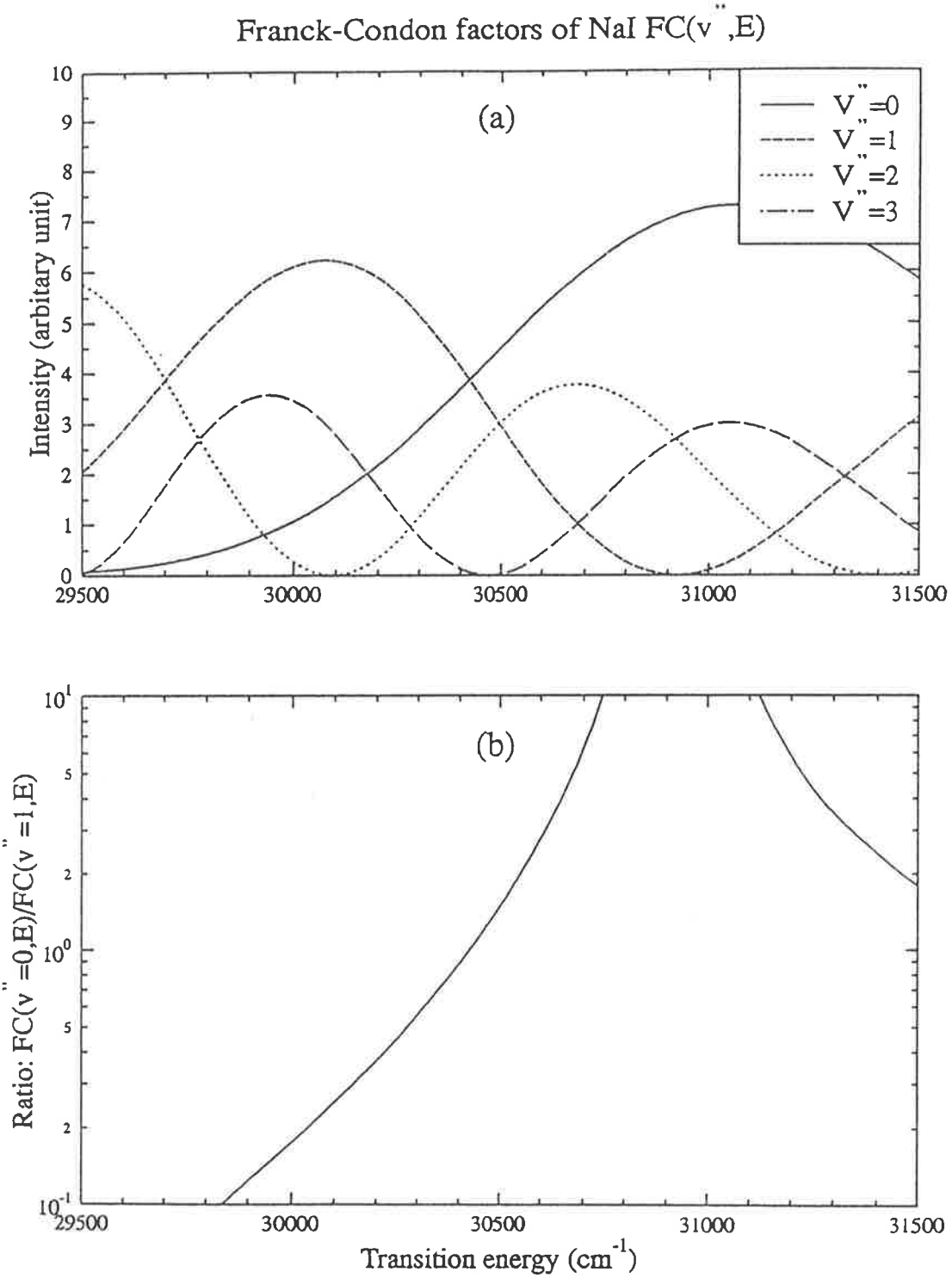

Figure 5.14: Franck-Condon factors of the new potential curve for transitions from $v'' = 0 - 3$ (a) and the ratio of the Franck-Condon factors for $v'' = 0$ and 1 (b).

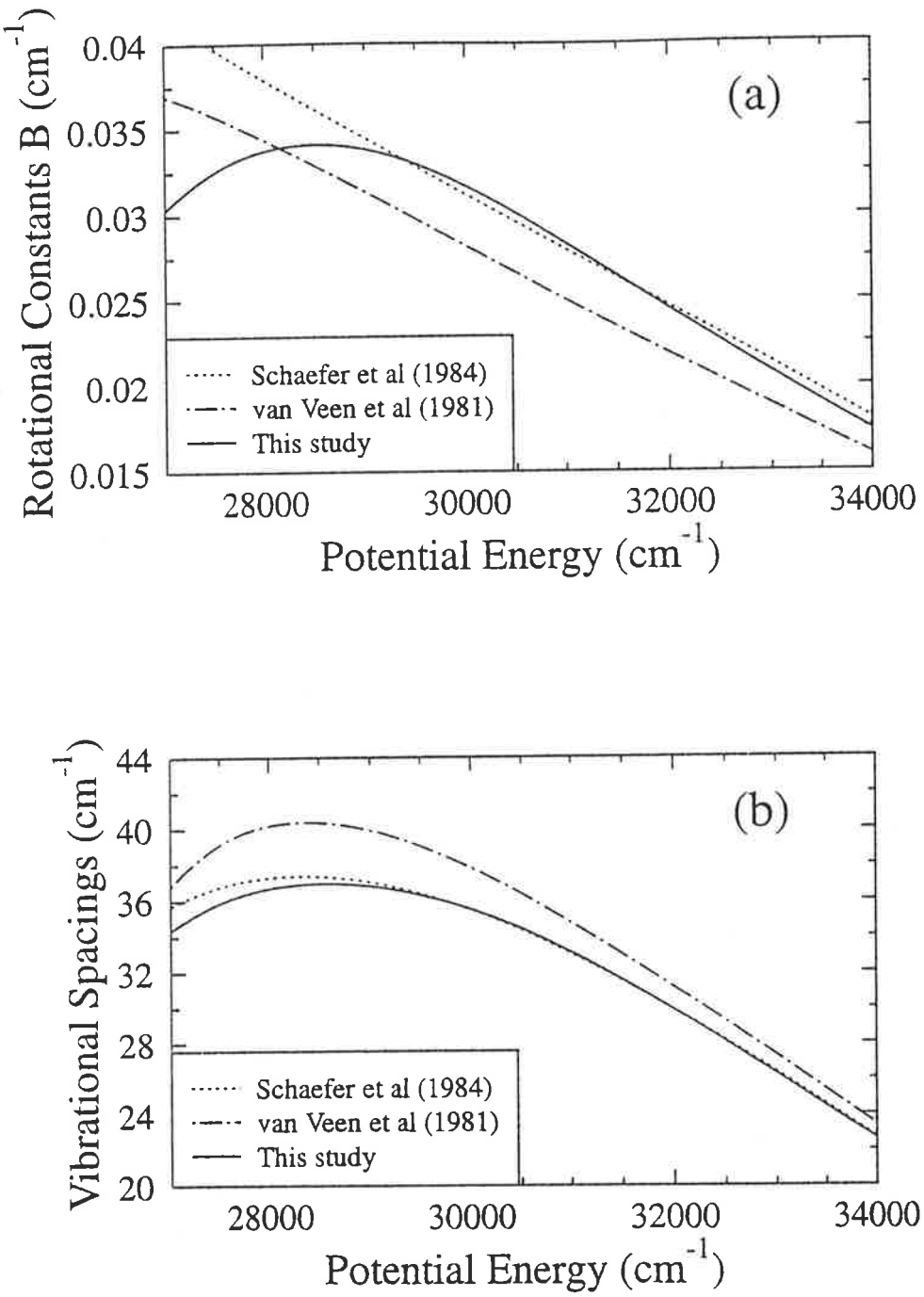

Figure 5.15: Comparison of the rotational constants B (a) and the vibrational spacings (b) of the new potential curve with the published ones.

The outer limb of the $X0^+$ diabatic potential curve obtained in the previous chapter was empirically pushed inward by multiplying a factor

$$\epsilon = 1.0 + 0.01exp\left(-0.7((r-7.5)/3.5)^2\right) \quad for \quad r > 3.5 \tag{5.26}$$

to obtain a good fit for the vibrational spacings of the upper adiabatic state which are shown in Fig. 5.15(b).

The shallower nature of the proposed potential curve is supported by the result of a multireference singly and doubly excited configuration interaction (MRSDCI) calculation (Sakai et al, 1992), as shown in Fig. 5.13. However, the potential curve of MRSDCI calculation is too shallow and its repulsive limb is located at a greater internuclear distance, giving incorrect Franck-Condon factors when compared with the experimental data.

A thorough literature search indicates that there has been no high resolution experimental data published for wavelengths longer than 350 nm. Berg and Skewes (1969) stated that bandlike groups of lines regularly spaced by about 36 cm^{-1} appear throughout the region from 2945 to 5400 Å. Accordingly it was proposed that the upper state has a potential well much deeper than a van der Waals well with a vibrational spacing of about 36 cm^{-1}, although no analysis was provided which supported this suggestion. Both the potential curve of Schaefer et al and the newly proposed potential curve have vibrational spacings of about 36 cm^{-1} over a large lower energy region, as seen in Fig. 5.15(b). However, careful examination of the spectrum throughout all the experimental regions does not indicate a regular 36 cm^{-1} band spectrum grouping. Furthermore, such 36 cm^{-1} bandhead-like structure can not be explained with the new potential curve, or with the potential curves of Schaefer et al (1984) or van Veen et al (1981). Some of the conflicting aspects of these bands observed by Berg and Skewes (1969) at wavelength longer than 3500 Å are:

1. A suggestion by Berry (1979) that these 36 cm^{-1} regularities that are supposed to be associated with the vibrational frequency of the upper state are really

nothing but quasi-periodic coincidence of complex overlapping bands. None of these bandhead like groups were observed in the present high resolution absorption spectrum or reported by any other authors. It is also impossible to reproduce such bandheads from the P and R branches with the present model as the lines of these branches are separated over a large energy region due to the large difference between the B values of the ground state and the upper state.

2. There is no evidence that the $\Omega = 0^+$ state is responsible for this behavior. Perhaps it could be caused by the $\Omega = 1$ state if it has a shallow well. If this is true, the Q branches may be able to reproduce the bandhead like structure with the B values of the $\Omega = 1$ state very close to those of the ground state. However this is unlikely since a shallow well will not give an extended region of 36 cm^{-1} spacing of the "bands". In addition, the spacing of 36 cm^{-1} requires a broad well giving a small B value very different from the ground state.

At present, these "band" like structures occurring at wavelength greater than 400 nm appear to be an unresolved problem concerning the absorption spectrum of NaI.

Finally, it must be pointed out that the shape of the proposed potential curve is determined by the experimental data and is not a theoretical extrapolation or assumption. This is due to the fact that the repulsive limb of the potential curve in the experimental region is fixed by the Franck-Condon factors. The shallow shape in the lower energy region of the repulsive limb is required to match the rotational constants in the experimental energy region and provide stronger transitions originated from $v'' = 1$ than that from $v'' = 0$ in the lower part of the experimental energy region. The covalent nature of the potential curve requires its repulsive limb approach the dissociation limit rapidly as internuclear distance increase, so that the shallow shape of the repulsive limb cannot extend to large internuclear distance. Thus the shape of the proposed potential curve is uniquely determined by the experimental data, although

the parameters of the potential curve need refining to reproduce the observed band fragments. This will require accurate location of more bands in a wider energy region to determine the Dunham parameters.

5.4 Conclusion

The absorption spectrum of NaI in the energy region 30000 - 31200 cm^{-1} was modeled for the first time with a set of Dunham parameters derived from a molecular fluorescence experiment (Schaefer et al 1984). The model spectrum, with transitions from $v'' = 0$ and 1, reproduced most of the absorption feature recorded by the high resolution laser experiment in this energy region, which corresponds to the most detailed part of the fluorescence experiment. As a result of this analysis, a diabatic potential curve for the $A0^+$ excited state is proposed. Unlike other currently published potential curves for this state, the potential curve is consistent with the known experimental data, it provides the correct rotational constants B, vibrational spacings and the Franck-Condon factors in the observed energy region.

Further high resolution spectroscopic investigations at higher and lower energy regions is suggested to extend this study. Spectroscopic data in the lower energy region can verify the shallow well of the newly proposed potential curve and may help to explain the 36 cm^{-1} bandhead like structure claimed by Berg and Skewes (1969). More fluorescent band fragments are required to be identified in the higher energy region to determine improved Dunham parameters to model the absorption measurement in this region.

It is suggested that the vibrational assignments of Schaefer et al (1984) be modified to get a better set of Dunham parameters which covers a larger energy region. The potential curve proposed in this study can be used as a reference to provide vibrational quantum numbers, rotational constants and the position for the lower en-

ergy levels. By adjusting these parameters to fit the experimental data, more accurate Dunham parameters can be obtained and applied to a wider range of energy. Improved potential curves can then be constructed using the RKR method.

Chapter 6

Intermediate Coupling Strength Pre-dissociation of Diatomic Molecules: Transition from Diabatic to Adiabatic Case

6.1 Introduction

The crossing of an attractive molecular potential curve with a repulsive curve can produce interesting spectroscopic features if the interacting diabatic states are of the same symmetry. As described in Chapter 2, analytical expressions for the energy shift and line width for pre-dissociation were given by Child on the basis of semiclassical theory but only apply to sharp resonances, or near the diabatic or adiabatic limit. Möhlenkamp and Korsch (1986) presented a semiclassical calculation based on the complex energy quantization method to investigate the intermediate coupling region. Several novel features were discovered but were not fully understood, as reviewed in the following section. It is the purpose of this study to give a better physical understanding

of the resonance behaviour in this region.

In this study, two methods have been used based on the coupled Schrödinger equations, to investigate the resonance behaviour in the intermediate coupling region. The first is similar to that of Möhlenkamp and Korsch (1986) but uses an integral solution of the coupled Schrödinger equations with the complex scaling method (Lefebvre 1990, Atabek and Lefebvre 1980, 1981, Brandas 1987). The second method is similar to the internal amplitude approach for shape resonance (Allision 1969, Jackson and Wyatt 1970) which was adapted to a two channel curve crossing system.

Unlike the absorption spectrum, the resonance spectrum contains only information about the excited states and is independent of the position of the ground state which, through the Franck-Condon factor, significantly changes the absorption spectrum.

6.2 The Semiclassical Complex Energy Quantization Method

Based on the Child's semiclassical theory for Feshbach resonance and predissociation, Korsch (1984, 1986, 1987, Möhlenkamp and Korsch, 1986) presented a semiclassical complex energy quantization study for a curve crossing system. In particular a model MgH system was examined and the position of resonances in the predissociating region were computed for a range of coupling strength. A simple and intuitively appealing semiclassical description of resonances for coupled-state (Feshbach) resonance was given. A brief review of Korsch's work is presented in this section and a further investigation on the MgH model system is made in the following sections.

6.2.1 Semiclassical quantization of predissociating states

The semiclassical complex energy quantization condition is based on the diagrammatic technique developed by Child as described in §2.3. Therefore the semiclassical waves have the same properties in free propagation, reflection from a classical turning point and connection matrix for the amplitudes on passage through a curve crossing as those described in Chapter 2. It is noted that the phase change for passage through a curve crossing took a slightly different form in Korsch's formula (Möhlenkamp and Korsch, 1986):

$$\begin{pmatrix} Q'_+ \\ Q'_- \end{pmatrix} = \begin{pmatrix} B^-, & -e^{-\pi\nu} \\ e^{-\pi\nu} & B^+ \end{pmatrix} \begin{pmatrix} P'_+ \\ P'_- \end{pmatrix} \tag{6.1}$$

$$\begin{pmatrix} P''_+ \\ P''_- \end{pmatrix} = \begin{pmatrix} B^-, & e^{-\pi\nu} \\ -e^{-\pi\nu} & B^+ \end{pmatrix} \begin{pmatrix} Q''_+ \\ Q''_- \end{pmatrix} \tag{6.2}$$

(6.3)

where

$$\begin{aligned} B^{\pm} &= \frac{\sqrt{\pm 2\pi\nu i}}{\Gamma(1 \pm i\nu)} e^{-(\pi/2)\nu \mp i(\nu - \nu ln\nu)} \\ \nu &= -\frac{i}{2\pi}\left(\int_{r_-}^{r_+} [k_-(r) - k_+(r)]dr\right) \\ k_{\pm}(r) &= [2\mu(E - V_{\pm}(r))]^{1/2}/\hbar \end{aligned}$$

and r_+ and r_- are the complex crossing points of the adiabatic upper V_+ and lower V_- potential curves in the complex coordinate plane. The difference in the phase may originate from the methods of deriving the connection matrix (Korsch 1984). With this connection matrix, Eq. (2.37) of Chapter 2 becomes :

$$[(B^-)^2 e^{2\alpha_+} + e^{-2\pi\nu + 2i\alpha_-}]e^{2i\beta_+} = -1. \tag{6.4}$$

This equation is the quantization condition which determines the complex resonance energies. Korsch then introduced the quantum number function

$$N_x(E) = \frac{1}{\pi}\{\beta_+ + \frac{1}{2i} ln[(B^-)^2 e^{2i\alpha_+} + e^{-2\pi\nu + 2i\alpha_-}]\} \tag{6.5}$$

for curve crossing predissociation system so that Eq.(6.4) can be rewritten as

$$N_x(E_n) = n + \frac{1}{2} \tag{6.6}$$

with integer values of n.

Such expressions are in accordance with the WKB quantization in the two limiting cases. In the diabatic limit, the coupling strength goes to zero resulting in a vanishing phase integral ν, which imposes $B^- \to 0$ and

$$N_x \to \frac{1}{\pi}(\alpha_- + \beta_+) = \frac{1}{\pi}\int_{a_-}^{b_+} k_2(r)dr. \tag{6.7}$$

In the opposite limit of large coupling strength, we have $e^{-2\pi\nu} \to 0$, $B^- \to 1$, and

$$N_x \to \frac{1}{\pi}(\alpha_+ + \beta_+) = \frac{1}{\pi}\int_{a_+}^{b_+} k_+(r)dr. \tag{6.8}$$

Eq.(6.7) and Eq.(6.8), together with Eq. (6.6), are the same WKB quantization condition for bound states in the diabatic potential V_2 (Eq. 2.38) and the upper adiabatic potential V_+ (Eq. 2.39). In Eq. (6.6), the semiclassical resonance states are numbered by an integer value n. There are two classifications for the numbering scheme. The adiabatic quantum number n_a defined by the numbering in the adiabatic limit when the coupling strength is very strong; and the diabatic quantum number n_d for the diabatic limit. Therefore the numbering of the resonance is not unique in the intermediate coupling region. A resonance state can be numbered by a diabatic quantum number as well as an adiabatic quantum number.

6.2.2 Application of the semiclassical quantization

Numerical calculations were performed for the above semiclassical complex energy quantization theory for a model curve crossing system of MgH (Möhlenkamp and Korsch 1986) with the potential curves

$$V_1(r) = 95817.22\ exp(-0.7872477r) + 5859.824\ \ cm^{-1} \tag{6.9}$$

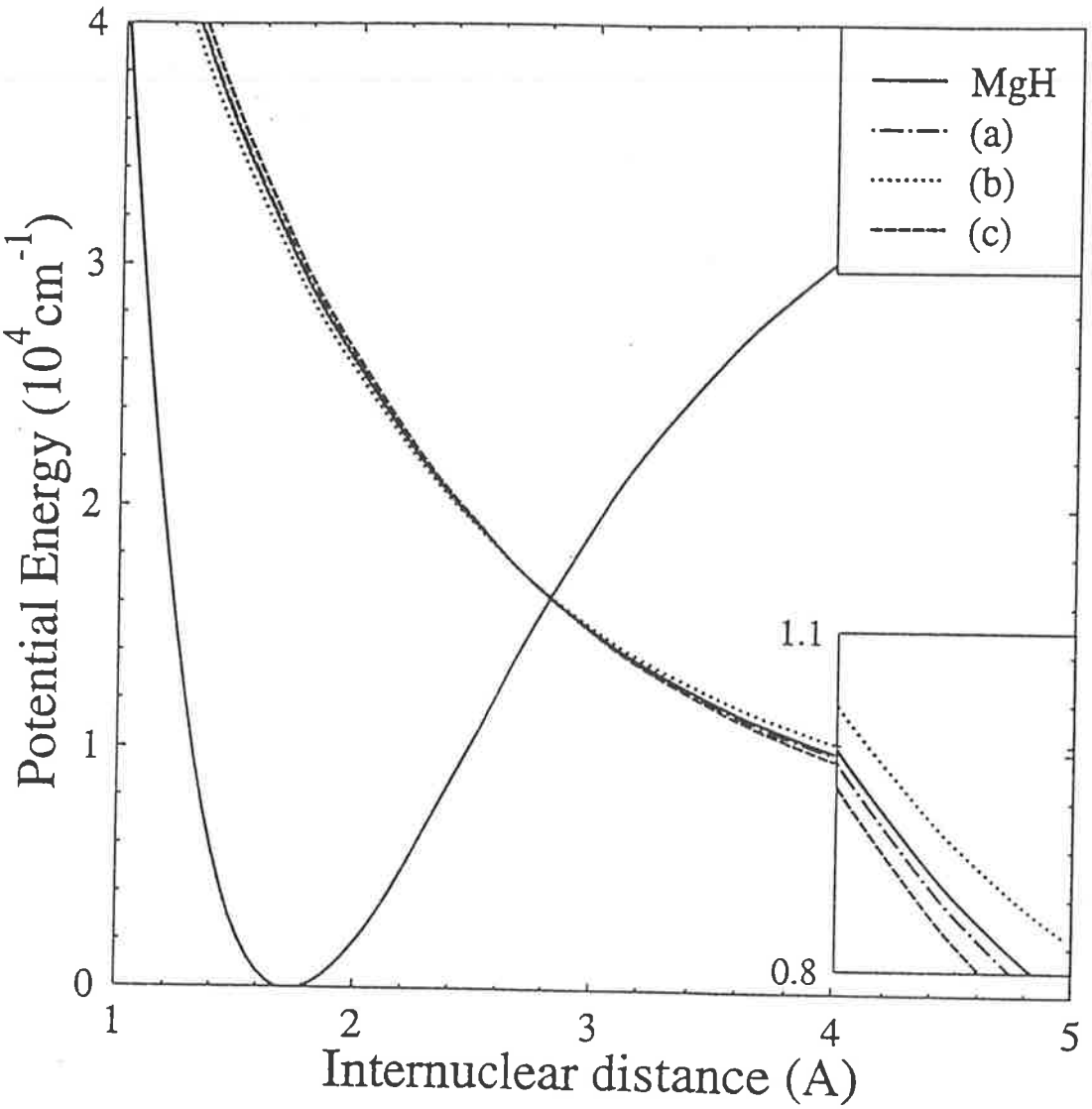

Figure 6.1: Model potential curves for MgH (solid lines) and the modified dissociative potential curves a, b and c which are used to investigate the effect of the relative resonance position of the diabatic and adiabatic components on the overall resonance.

$$V_2(r) = 38339.19(1 - exp(-0.9766027(r - 1.736154)))^2 - 100.2809 \ cm^{-1} \quad (6.10)$$

$$V_{12}(r) = A_{int} exp(-(r - 2.824)^2) \quad (6.11)$$

which are shown in Fig. 6.1 as the solid lines with the internuclear distance r in $\mathring{A}$. The reduced mass was $\mu = 1763.0698$ a.u. The realistic value of the coupling strength for MgH is $A_{int} = 6822.694\ cm^{-1}$ or 0.031 a.u. which is almost in the adiabatic limit. In order to study the influence of the coupling strength on resonance spectrum, A_{int} was varied from values near the diabatic limit to values near the adiabatic limit. The calculated results of Möhlenkamp and Korsch (1986) are reproduced in Fig. 6.2 and Fig. 6.3. These results shown that

1. In the diabatic or adiabatic limits, the system decouples and there are bound states in the diabatic or adiabatic potentials V_2 or V_+.

2. With increasing coupling strength, all the predissociating semiclassical resonances approach the bound states of the upper adiabatic potential V_+ with vanishing line width.

3. With decreasing coupling strength, most of the semiclassical resonances approach the bound states of the diabatic potential V_2 with vanishing line width. However, there is an unexpected exception for the resonance state of $n_a = 18$. The resonance positions (or the real part of the resonance eigenvalues) for resonance states $n_a = 17$ and $n_a = 18$ both approach the same position as the diabatic resonance $n_d = 30$. The width of the state $n_a = 18$ goes to infinity resulting in the vanishing of the resonance state while the line width of state $n_a = 17$ goes to zero.

4. Some of the resonance states are very insensitive to the variation of the coupling strength while others are extremely sensitive and show pronounced changes in resonance positions and widths in the intermediate coupling region.

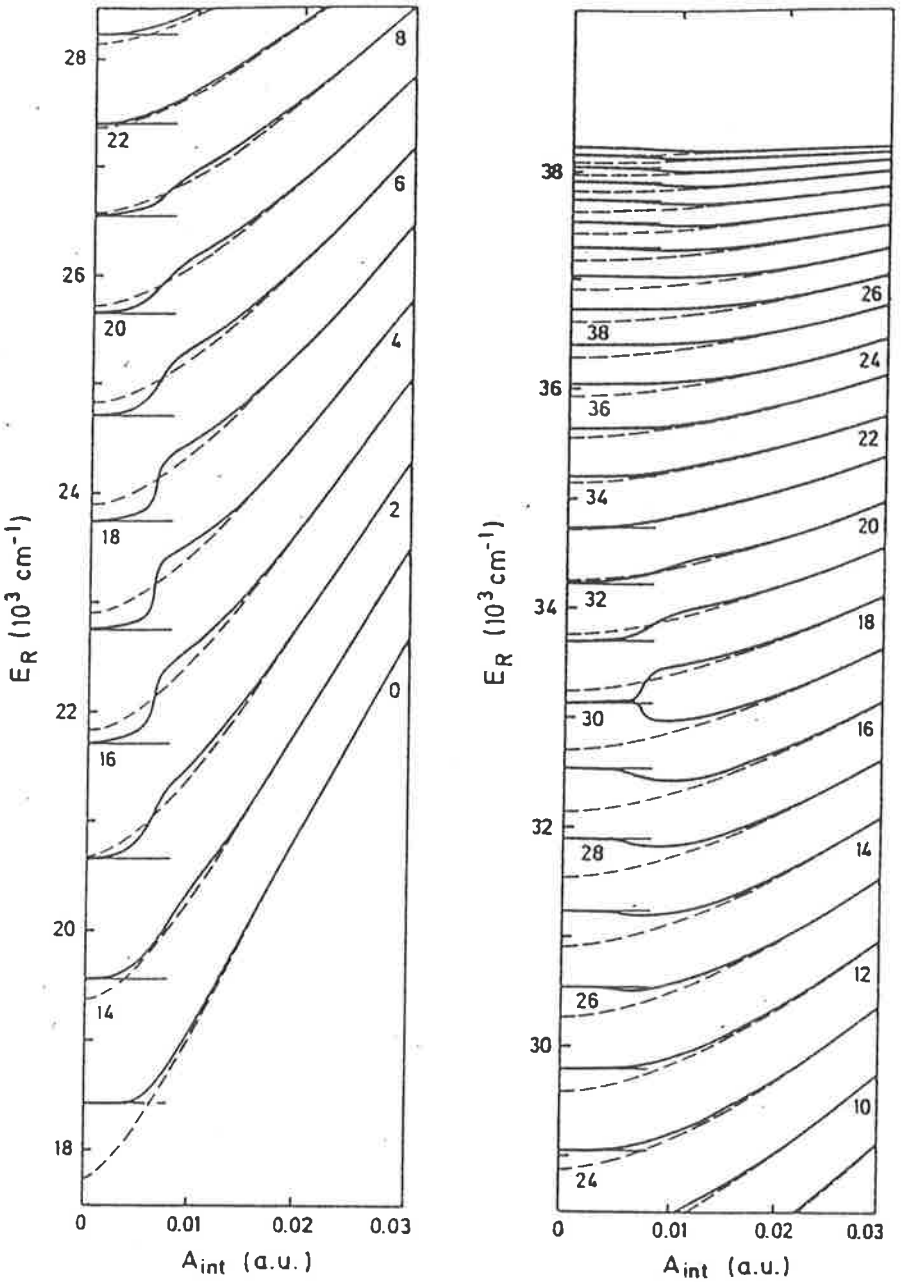

Figure 6.2: Variation of semiclassical resonance positions as a function of coupling strength (solid lines). The thin lines on the left mark the diabatic eigenvalues for V_1 and the dotted lines indicate the adiabatic eigenvalues for V_+ as a function of coupling strength. The diabatic quantum numbers are given on the left of the trajectories while the adiabatic ones are given on the right (After Möhlenkamp and Korsch, 1986).

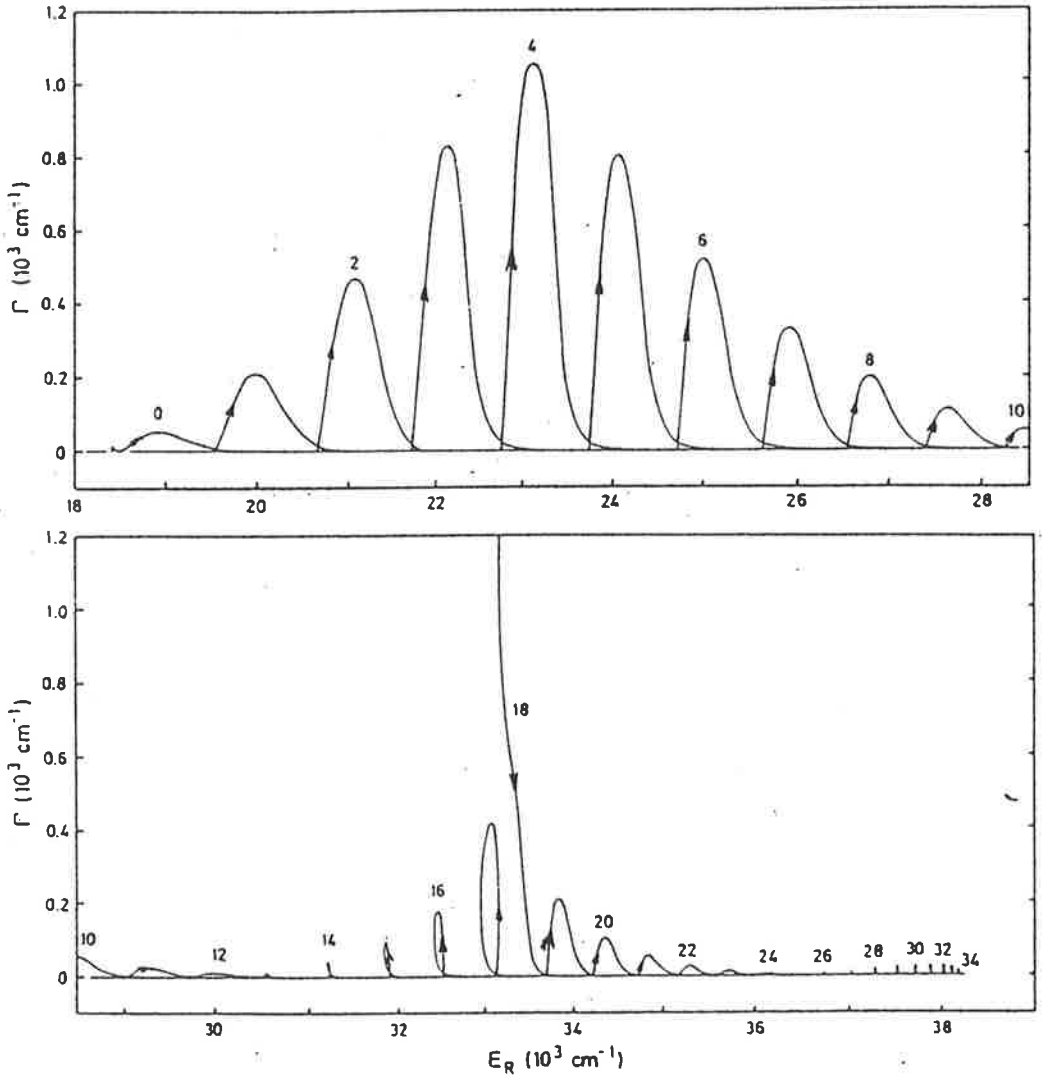

Figure 6.3: Variation of semiclassical resonance energy and width of the semiclassical resonances shown in Fig. 6.2 with the variation of the coupling strength. The numbers denote the adiabatic quantum numbers. The arrows indicate increasing coupling strength (After Möhlenkamp and Korsch, 1986).

5. The transition from the diabatic to adiabatic regime occurs in a small well localized coupling region, where all the curves show more or less pronounced changes.

6. The resonance energy vs width trajectories show various types of behavior such as humps and loops.

Although some of the properties such as (1) and (2) are expected, the reason for the behaviour of some of the resonant trajectories, for example $n_a = 17$ and 18, is not evident from their analysis.

6.3 The Complex Scaling Method

Möhlenkomp and Korsch (1986) commented that the appearance or disappearance of resonant states may be an artifact of the semiclassical solution, so to verify that the semiclassical behavior can also be observed in the numerical integration of the coupled Schrödinger equation with the complex scaling methods was carried out and is presented in this section. The same potential curves Eq. (6.9) - (6.11) adopted by Möhlenkomp and Korsch (1986) were used and the coupling strength A_{int} was also varied over the intermediate coupling region.

The complex energy eigenvalues of the coupled equations were calculated using the method as presented in Chapter 2 and Appendix D. Complex rotation of coordinates was applied only where $|r| > r_0$ with $r \rightarrow r_0 + (r - r_0)exp(i\theta)$, $r_0 = 0.07\mathring{A}$ and $\theta = 0.07$ rad. This is the exterior scaling transformation which has better numerical stability (Brandas *et al* 1987). Johnson's renormalized Numerov method (Johnson 1978) is used to solve the complex coupled equations. Calculations of the complex energy eigenvalues were begun at the diabatic or adiabatic limit where the bound state eigenvalue could be used as the starting approximation. Then, as the coupling strength was changed by successive increment, the previous solution was used as the starting

approximation. The variation of the energy of each resonance is represented by a continuous trajectory as a function of coupling strength. In this way, the resonance state can also be numbered by the quantum numbers n_d or n_a and a continuous trajectory linking the diabatic or adiabatic limiting cases can be traced.

Calculated results are shown in Fig. 6.4 and Fig. 6.5 which are in good agreement with those given by the semiclassical method (Möhlenkamp and Korsch, 1986) except for resonance states of very large width which probably arise from the extreme sensitivity of resonant character to the potential curves and therefore the wavefunctions, as described later.

As expected, the resonances approach the eigenvalues of the diabatic or adiabatic bound potential with decreasing or increasing coupling strength respectively, with the widths reducing to zero. There is interesting behaviour in the intermediate coupling region where the transition from weak to strong coupling occurs. Some resonances show pronounced shifts and there are regions where adjacent resonances can merge or split as the coupling strength changes. Since the number of resonance states in the diabatic limit are generally not the same as those in the adiabatic limit in their respective energy region, it follows that some resonance states have to vanish or appear in the intermediate coupling region as the coupling strength changes to match the resonance states in the other limit (Fig. 6.2 and Fig. 6.4). The complex scaling method, as well as the semiclassical quantization method, only determines resonance positions and widths and is therefore unable to give a satisfactory description for the origin of these changes as well as the rapid and pronounced shift in resonance positions that sometimes occur. It can only be demonstrated that the semiclassical behaviour described in the previous section also occurs in the integrated solution. A better understanding of its origin is presented in the following sections where a novel interpretation is presented for the change in resonance states from diabatic bound states to adiabatic resonance states as the coupling strength is increased.

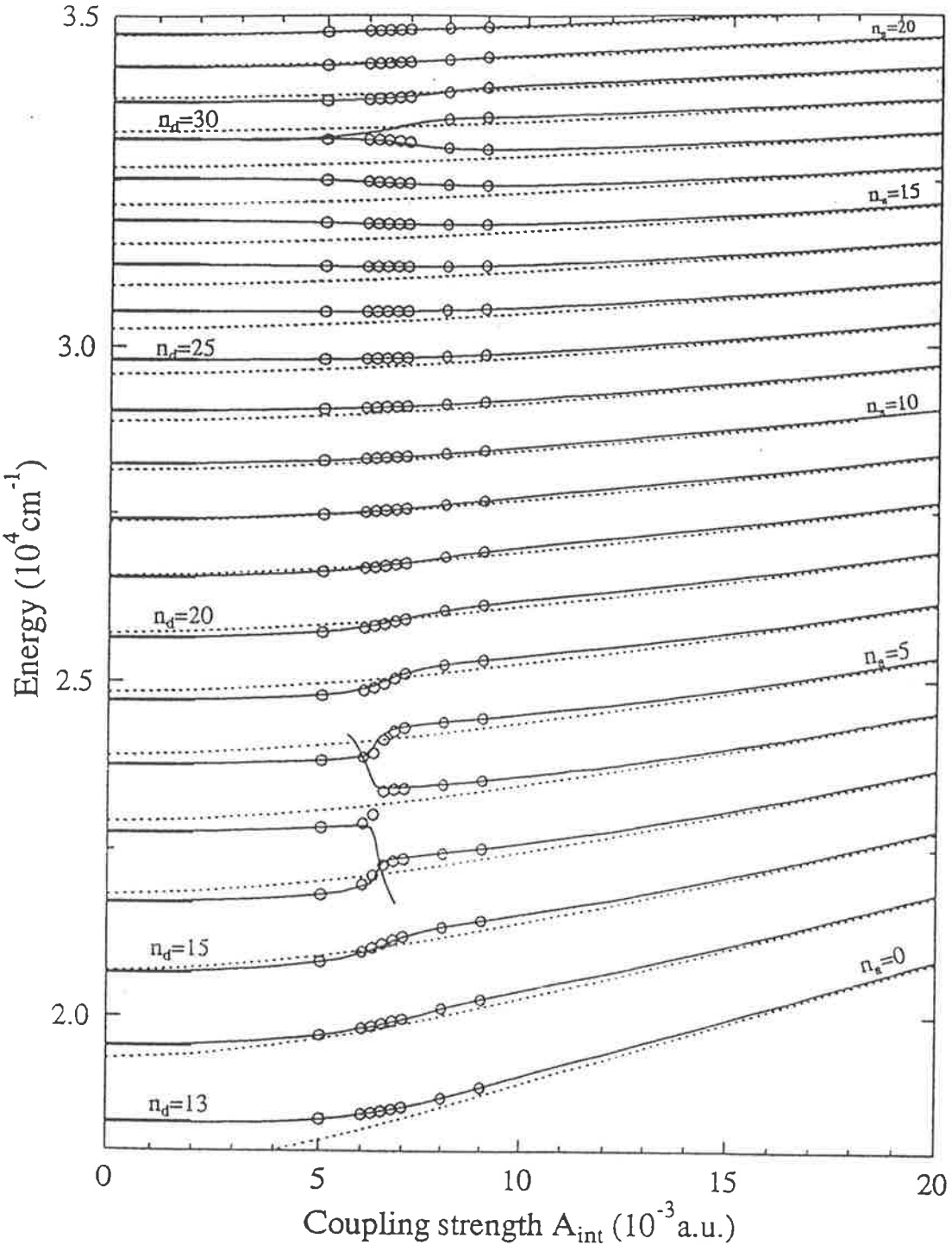

Figure 6.4: Resonance trajectories, calculated by the complex scaling method, as a function of coupling strength for the potential curves of MgH (solid lines). The thick lines on the left mark the diabatic eigenvalues for V_2 and the dotted lines indicate the adiabatic eigenvalues for V_+ as a function of A_{int}. The o indicates the peak positions of the resonance spectrum in Fig. 6.7.

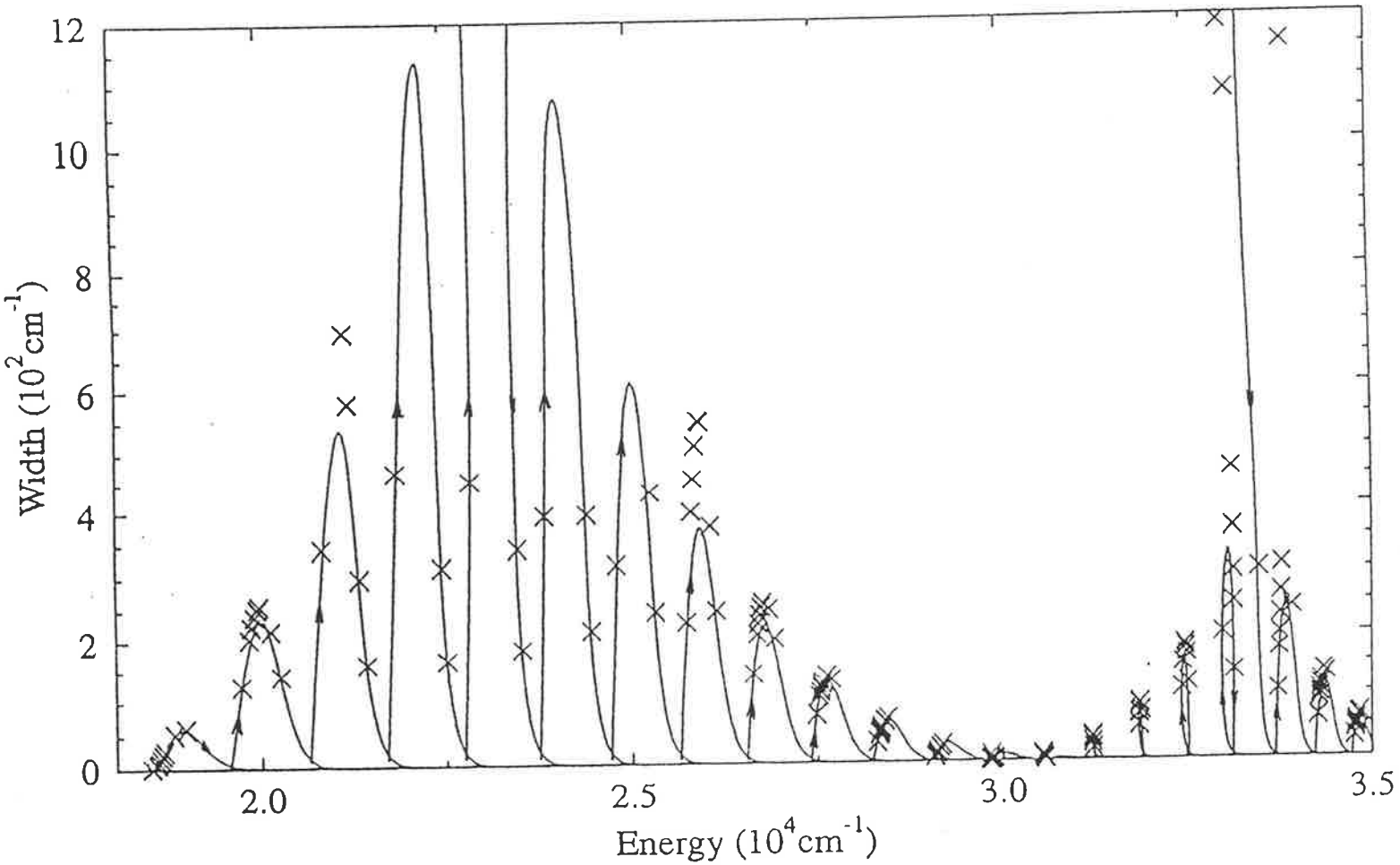

Figure 6.5: Comparison of the variation of resonance energy and width as the coupling strength is changed for complex quantization theory (solid lines) and internal wavefunction method (×) which are measured from Fig. 6.7. The arrows indicate increasing A_{int}.

6.4 The Maximum "Internal Amplitude" Method

The second method to investigate the resonance behaviour in the intermediate coupling region is similar to the internal amplitude approach for shape resonances (Allison 1969, Jackson and Wyatt 1970) in which the resonant position of a quasibound state can be determined as that energy at which the internal amplitude of the wavefunction, normalized by its asymptotic amplitude, reaches a maximum. This idea was adopted for the two channel spectrum where the maximum amplitude of the closed channel wavefunction, normalized by the asymptotic amplitude of the open channel wavefunction, was used to identify the resonances of a curve crossing system when the coupling strength is near the diabatic limit (Lefebvre 1990). It is proposed that in the strong coupling limit a similar procedure can be used to identify the resonance states. In this case the adiabatic potentials are used with the adiabatic bound state normalized by the open channel wavefunction.

However, in the intermediate coupling region, the closed channel is not readily identified. Examples of the diabatic and adiabatic bound state (bold lines) and continuum state (dashed lines) wavefunctions together with the potential curves (dotted lines) for some special cases are shown in Fig. 6.6. The four special cases are: (i) A_{int} = 0.0065 a.u., E=23800.0 cm^{-1}: the bound state is on resonance in the diabatic representation and off resonance in the adiabatic representations (as discussed later). (ii) A_{int} = 0.0065 a.u., E=24245.0 cm^{-1}: the bound state is on resonance in the adiabatic representation and off resonance in the diabatic representations. (iii) A_{int} = 0.0065 a.u., E=29829.66 cm^{-1}: the bound state is on resonance in both representations. (iv) A_{int}=0.0065 a.u., E=18790.0 cm^{-1}: the bound state is off resonance in both representations. It appears in Fig. 6.6 that the total wavefunction has both diabatic and adiabatic character. Even in the intermediate coupling region, when the bound state wave functions reach their maximum values (on resonance), their form is very close to that of the eigenfunctions of a single channel bound state showing strong

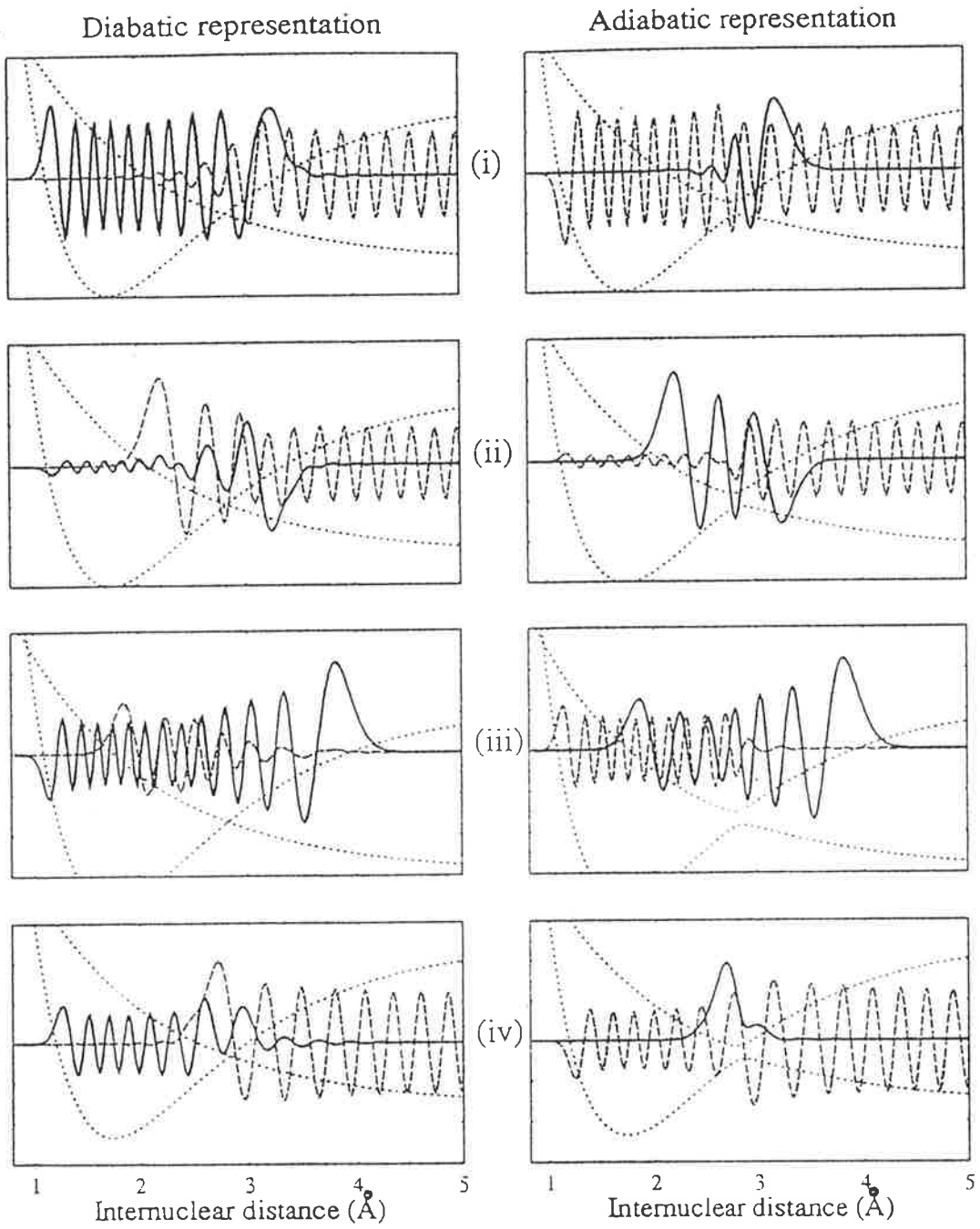

Figure 6.6: Examples of the diabatic and adiabatic bound state (bold lines) and continuum state (dashed lines) wavefunctions together with the potential curves (dotted lines) for some special cases (see text). Note that the wavefunction scale is not the same in (i) to (iv), which is evident from the different amplitudes of the open channel wavefunction at large internuclear distance.

bound character while the wavefunctions for off resonance states have strong mixed character. It is therefore useful to investigate this transition using an approach which separates out the diabatic and adiabatic contributions to the resonance. In this study, it is assumed that the change from the diabatic to the adiabatic limit as the coupling strength increases is smoothly continuous and the contribution to the resonant state can be considered as part diabatic and part adiabatic. An "internal amplitude" which uses both the diabatic and adiabatic bound states is proposed as a criterion for the resonance which is given by

$$P = P^d + P^a \tag{6.12}$$

where

$$\begin{aligned} P^d &= \int_0^\infty |\chi_b^d(r)|^2 dr \\ P^a &= \int_0^\infty |\chi_b^a(r)|^2 dr \end{aligned} \tag{6.13}$$

with $\chi_b^d(r)$ and $\chi_b^a(r)$ the diabatic and adiabatic bound state wavefunctions normalized by the asymptotic amplitudes of the continuum states.

This definition provides a useful explanation for resonance behaviour in the intermediate region although a full theoretical examination of the reason that the bound state components of the two different basis can be added and show consistent results needs to be investigated.

The spectrum P(E)/2 defined by Eq. (6.12) is shown in Fig. 6.7 together with P^d and P^a for a range of coupling strength. The peak positions of the resonance spectrum were located and marked in Fig. 6.4 and widths at the half maximum were measured and shown in Fig. 6.5 where they are compared with the results of complex energy quantization method. Resonance positions given by the maximum value of this "internal amplitude" and the widths measured at its full width at half maximum are found to be in good agreement with calculations by the complex scaling method. A discrepancy occurs for widths approaching infinity, but it is very small when compared with the width and is within the uncertainty originating from overlapping wings of neighboring resonances. As Child (1991) has pointed out for the case of shape reso-

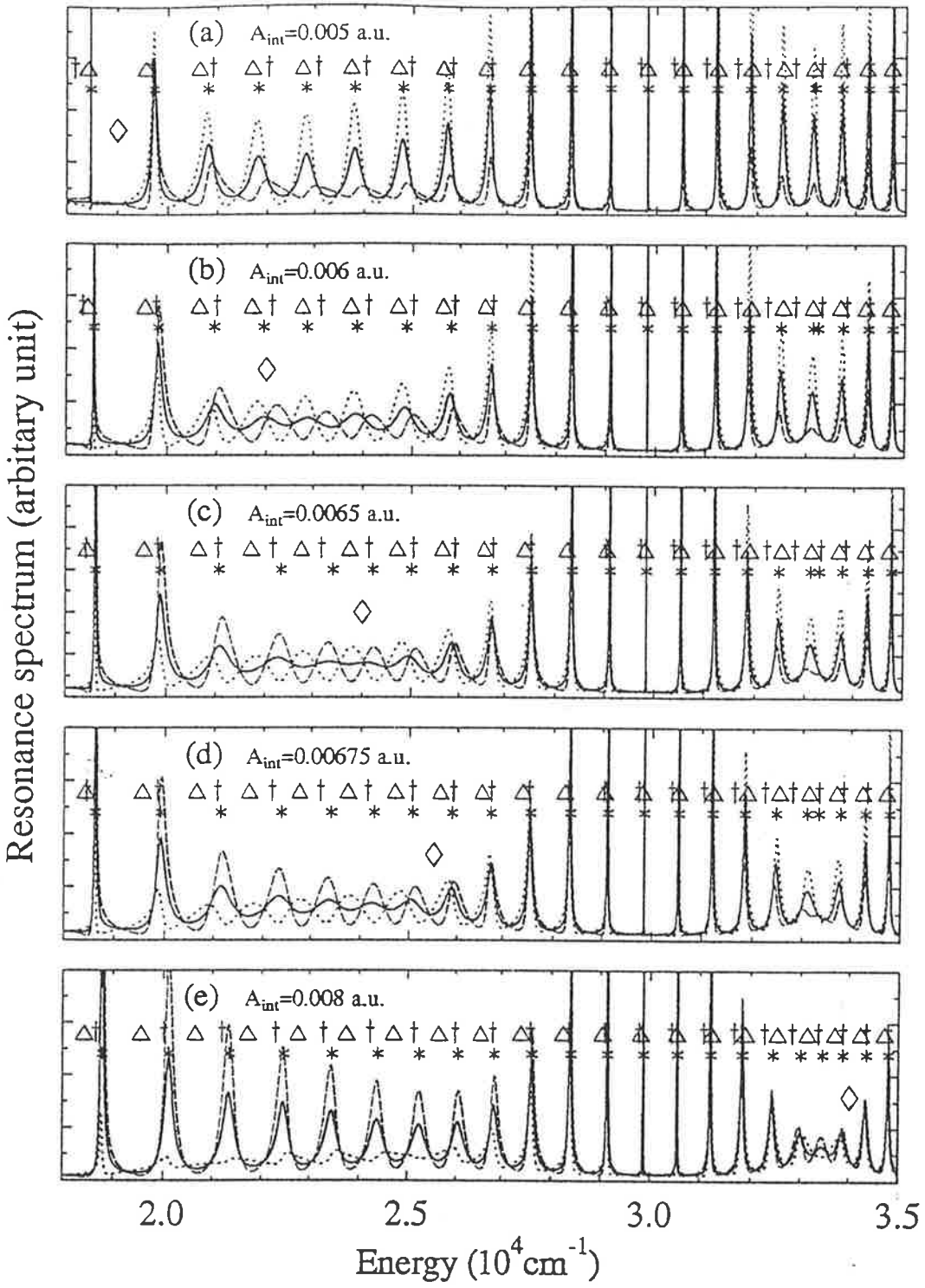

Figure 6.7: Resonance spectrum P/2 (bold lines), P^d (dash lines) and P^a (dotted lines) for a range of coupling strengths A_{int}. The symbols $(*)$, $(\triangle)$ and $(\dagger)$ indicate the resonance positions from complex quantization method and the eigenvalues for the diabatic and adiabatic bound states respectively. The diabatic states $(\triangle)$ range from $n_d = 13$ at the left to $n_d = 33$ at the right. The energies at which $P_{l_z} = 0.5$ are marked as $\diamond$, shifting from lower to higher energy as the coupling strength increases.

nances and tunneling pre-dissociation, the precise equivalence between the resonance positions and width associated with different resonance definitions such as maximum internal amplitude, Siegert eigenvalue, and phase shift can be expected only in the sharp resonance limit.

6.5 Interpretation of the Intermediate Coupling Region

With the "internal amplitude" defined in the previous section, the origin of the behaviour in the intermediate coupling region is readily interpreted. The summation of diabatic (P^d) and adiabatic (P^a) resonant spectrum in Fig. 6.7 demonstrates how the total resonance spectrum (P) changes in the intermediate coupling region from near diabatic to near adiabatic case as coupling strength increases. When adiabatic and diabatic resonant states coincide, the resonance is exceptionally sharp, conversely, when they are not coincident all the diabatic and adiabatic resonances as well as the total resonance are broad.

As the coupling strength is increased from the diabatic limit, the spectral changes in Fig. 6.7 in the region of broad resonances are due to the adiabatic character of the spectrum becoming more apparent and the resulting resonances having a large phase shift relative to the diabatic resonances. Thus, the resonance position undergoes a rapid shift from near diabatic (P^d) toward near adiabatic (P^a) resonance location. The splitting of $n_d = 30$ or the vanishing of $n_a = 18$ is also evident. As illustrated in Fig. 6.7, a weak peak in P^a starts to appear as the coupling strength A_{int} increases to 0.0065 a.u. However, since the diabatic resonance still dominates, there is no additional resonance in the total spectrum until $A_{int} = 0.008$ a.u. when the adiabatic resonance starts to become the dominant component. From the adiabatic limit, this can also be interpreted as the process by which the combined resonances which are

Table 6.1: Potential Parameters for V_2

Curves	B (cm^{-1})	C (cm^{-1})	a	r_0 (Å)
(a)	95817.22	5273.829	0.78	0.04
(b)	95817.22	5609.829	0.78	0.003
(c)	93000.0	6561.0	0.80	0

antiphase at the spectral region of 33500 cm^{-1} cancel at $A_{int} \simeq 0.0079$ a.u. causing the width of one of the resonance states to approach infinity and the resonance state to vanish. It is expected that such a region would be very sensitive to any change in the shape of the potential curves. In an attempt to investigate the effect of the relative resonance positions of the two components on the development of resonance trajectories, the repulsive potential curve

$$V_1(r) = B\ exp(-a(r - r_0)) + C \tag{6.14}$$

was changed slightly to give different adiabatic level spacings while at the same time keeping the adiabatic ground state in the same position as the coupling strength approaches zero. The parameters for different potential curves are listed in Table 6.1 and the corresponding potential curves are shown in Fig. 6.1 in comparison with the potential curves of MgH.

The resonance trajectories as a function of coupling strength for different repulsive potential curves (a, b and c in Fig. 6.1) in the lower energy region of Fig. 6.4 are shown in Fig. 6.8 as (a), (b) and (c). It is noticed that for potential curves with greater adiabatic level spacings than MgH (Fig. 6.8(a)) there is a vanishing of the adiabatic resonance $n_a = 7$ (or splitting of the diabatic resonance $n_d = 21$) in the higher energy region and a vanishing of the diabatic resonance $n_d = 15$ (or splitting of $n_a = 2$) in the lower energy region. As the adiabatic level spacings decrease, the vanishing states approach in energy as shown in Fig. 6.8(b). For the potential curves of MgH where the adiabatic level spacings are further decreased, the vanishing resonant

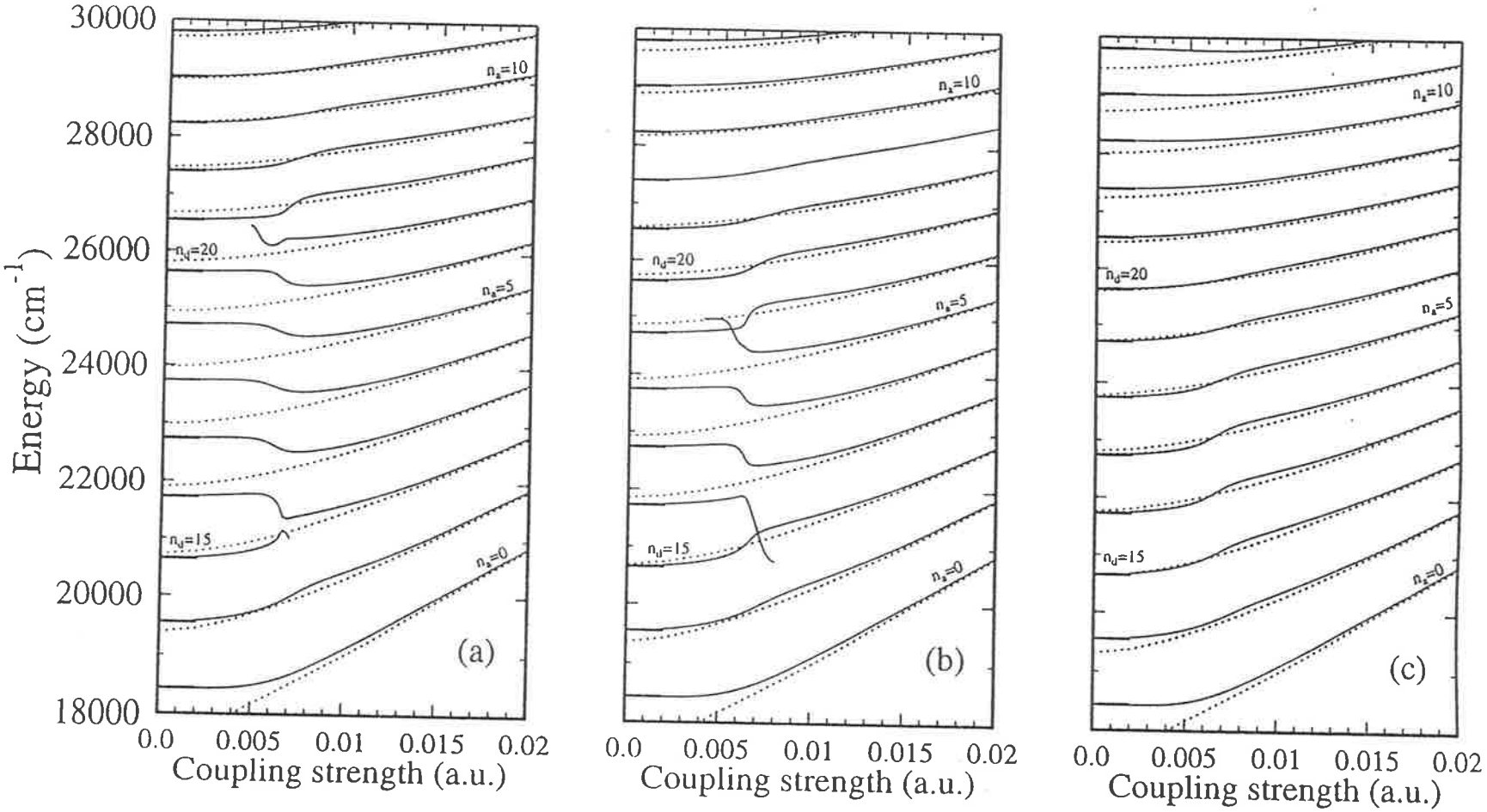

Figure 6.8: Resonance trajectories as a function of coupling strength (solid lines) for different dissociative potential curves (a), (b) and (c) as shown in Fig.6.1.

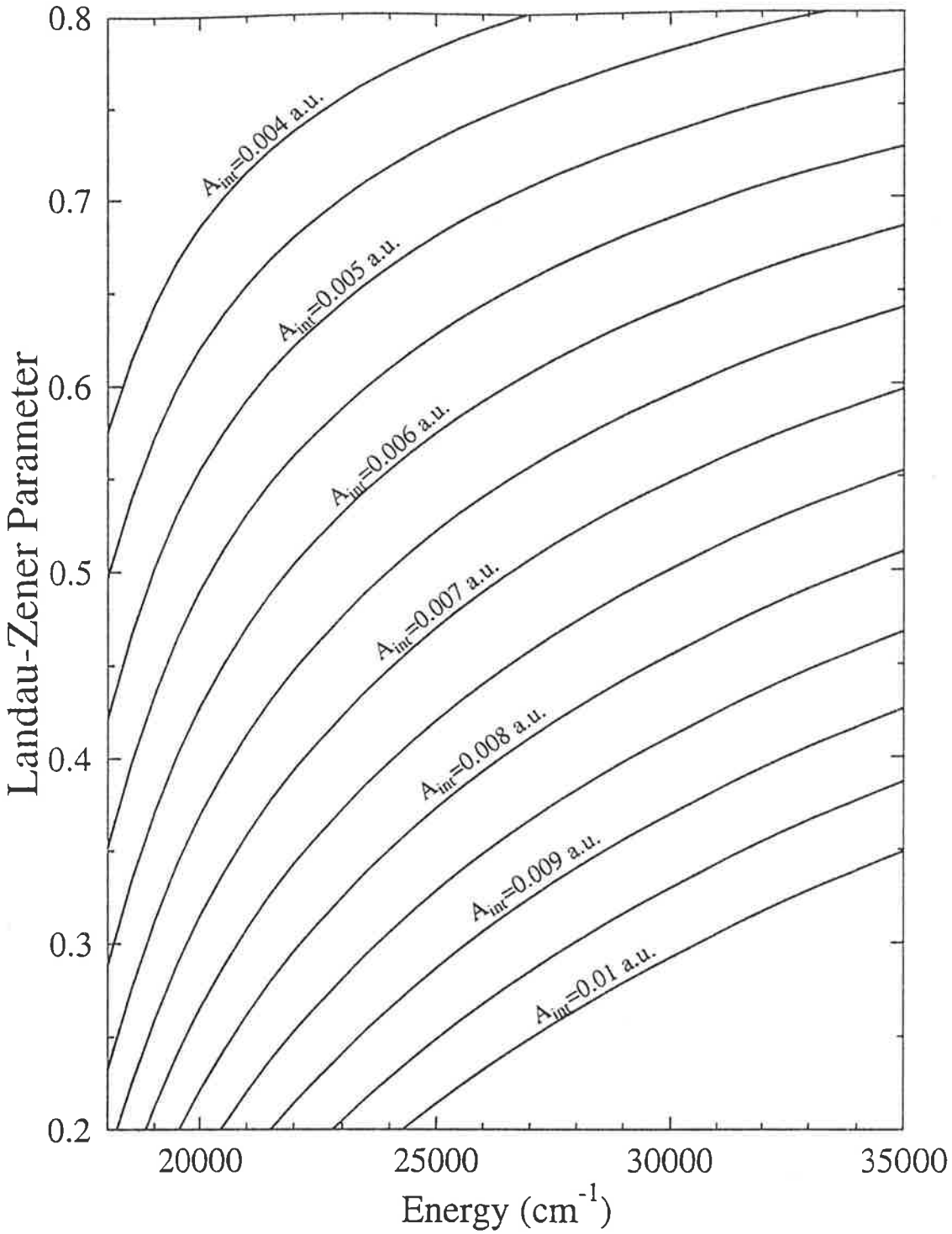

Figure 6.9: Variation of Landau-Zener nonadiabatic transition probability for the potential curves of MgH as a function of energy for different coupling strengths. The change in coupling strength is 0.005 a.u. for neighboring curves.

states ($n_a = 4$ and $n_d = 17$) are at the same energy as shown in Fig.6.4. At smaller adiabatic level spacings than those of MgH, these two splitting merge resulting in a less pronounced change in the diabatic-adiabatic transition region and a smooth transition as shown in Fig. 6.8(c). Thus we see that for the four situations considered above, the number of resonant states in the diabatic limit are the same as those in the adiabatic limit in the respective energy region. However, a change in the number of resonance states can still occur because in smaller energy regions the number of resonance states of the two contributing components may not be the same. As the adiabatic level spacings change such regions also change and can merge and then vanish as shown in Fig. 6.8. These examples illustrate the extreme sensitivity of the shape of the resonance spectrum to the shape of potential curves in the intermediate coupling region. This also explains the small discrepancy between the semiclassical and coupled equation methods in these regions stated earlier. The employment of approximate wavefunctions in the semiclassical calculation can be regarded as equivalent to a small change in the potential curves in the coupled equations method which significantly affects the behaviour of broad resonances.

Fig. 6.9 shows the variation of Landau-Zener parameter P_{lz} with energy for different values of the coupling strength. We find that $P_{lz} = 0.5$ for $A_{int} = 0.00625$ a.u. at E=23000 cm^{-1} and for $A_{int} = 0.008$ a.u. at E=33500 cm^{-1} where it can be seen from Fig. 6.7 that clear transitions occur in the spectrum. Thus the agreement with the prediction of the Landau-Zener parameter in the calculation of nonadiabatic transition between the two adiabatic states is clearly evident.

The results of this study also show that outside a narrow intermediate coupling strength region near $P_{lz} = 0.5$ the diabatic (P^d) or the adiabatic (P^a) resonance spectrum alone gives a very good approximation for the overall resonance position and width. Near $P_{lz} = 0.5$ the "bound state" is not obvious and it is necessary to consider the combined effects of the diabatic and adiabatic bound states to determined the total

resonance.

6.6 A Study of a Different Curve Crossing System

In this section, the proposed "internal amplitude" method is applied to another model curve crossing system which has been studied by different authors (Child and Lefebvre 1978, Lefebvre 1990). The potential curves are given as:

$$V_1(r) = 18154.95\ exp[-2.2039(r-2.48)] - 8000\ \ cm^{-1} \tag{6.15}$$

$$V_2(r) = 15000\,[1 - exp(-1.9685(r-1.6))]^2\ \ cm^{-1} \tag{6.16}$$

and shown in Fig. 6.10. The coupling strength V_{12} is taken to be independent of the internuclear distance and is also varied over the intermediate coupling strength. The reduced mass is 8 atomic mass units.

Fig. 6.11 and Fig. 6.12 display the corresponding calculated results for this curve crossing system. The "internal amplitude" method again shows good agreement with the complex scaling method. The splitting or vanishing of resonance states in the intermediate coupling region are clearly identified and can be explained in the same way as that described in the previous section.

The Landau-Zener parameters for this predissociative system are shown in Fig. 6.13. Unlike the MgH model, it was found that the transition between the diabatic and adiabatic case for this curve crossing system, with the complex scaling method as well as the "internal amplitude" method, does not occur near a coupling strength where the Landau-Zener parameter $P_{lz} = 0.5$! This may be caused by the difference between the vibrational spacing of the diabatic and adiabatic states. As can be seen in Fig. 6.13 that the adiabatic vibrational spacing is about twice of the diabatic one, whereas they were about the same for MgH. It is found in this study that the mixing

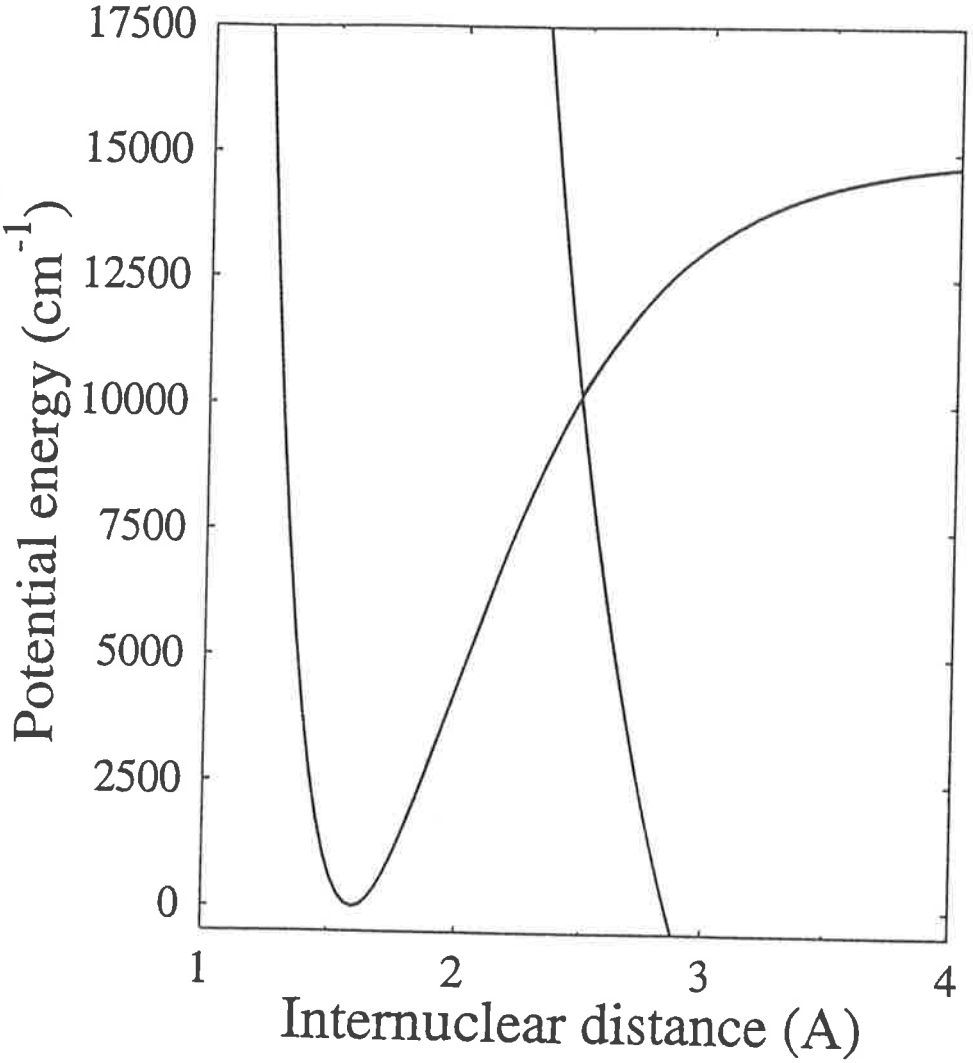

Figure 6.10: The predissociative potential curves of Eq. (6.15) and Eq. (6.16).

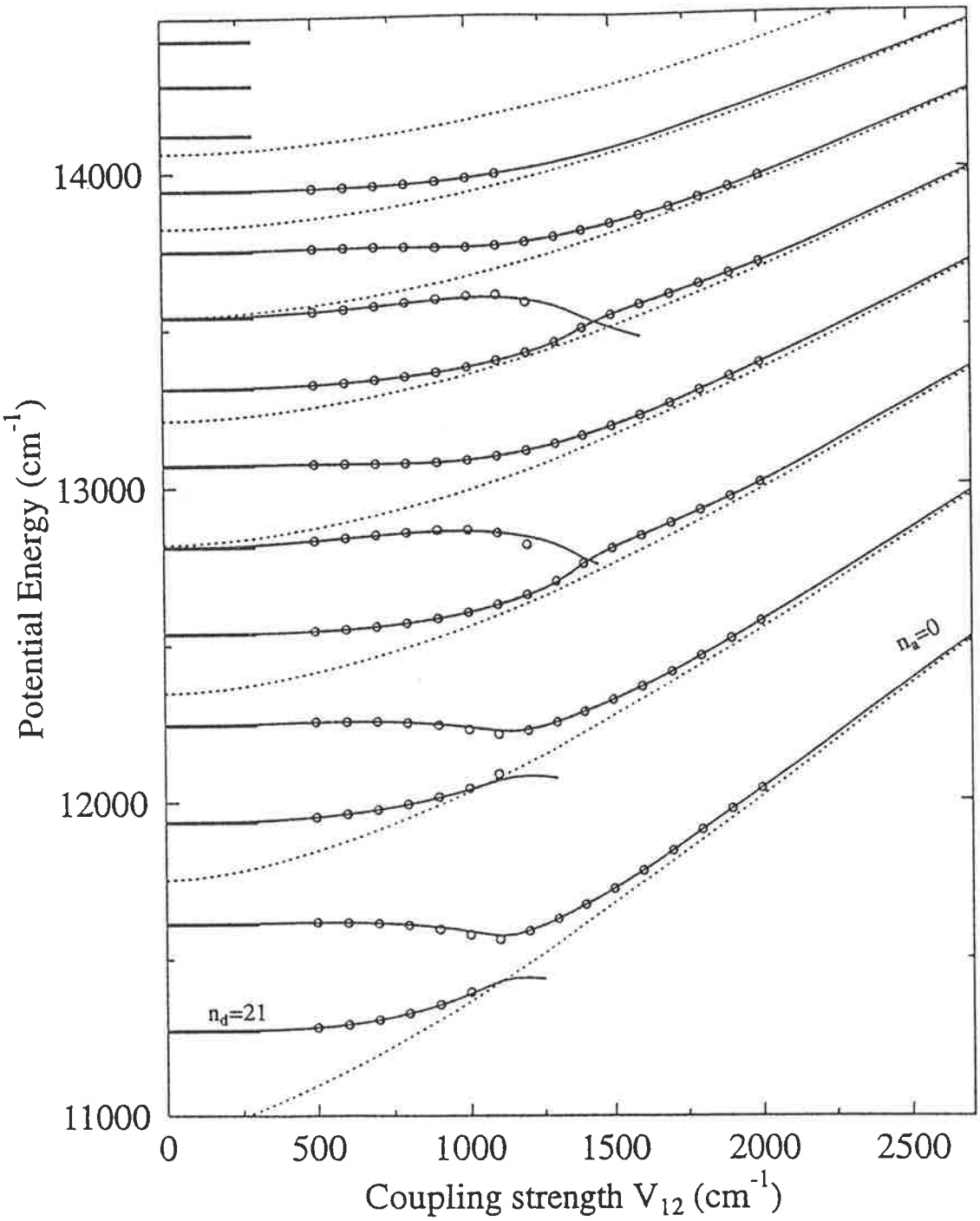

Figure 6.11: Resonance trajectories as a function of coupling strength (solid lines) for the dissociative potential curves shown in Fig.6.10.

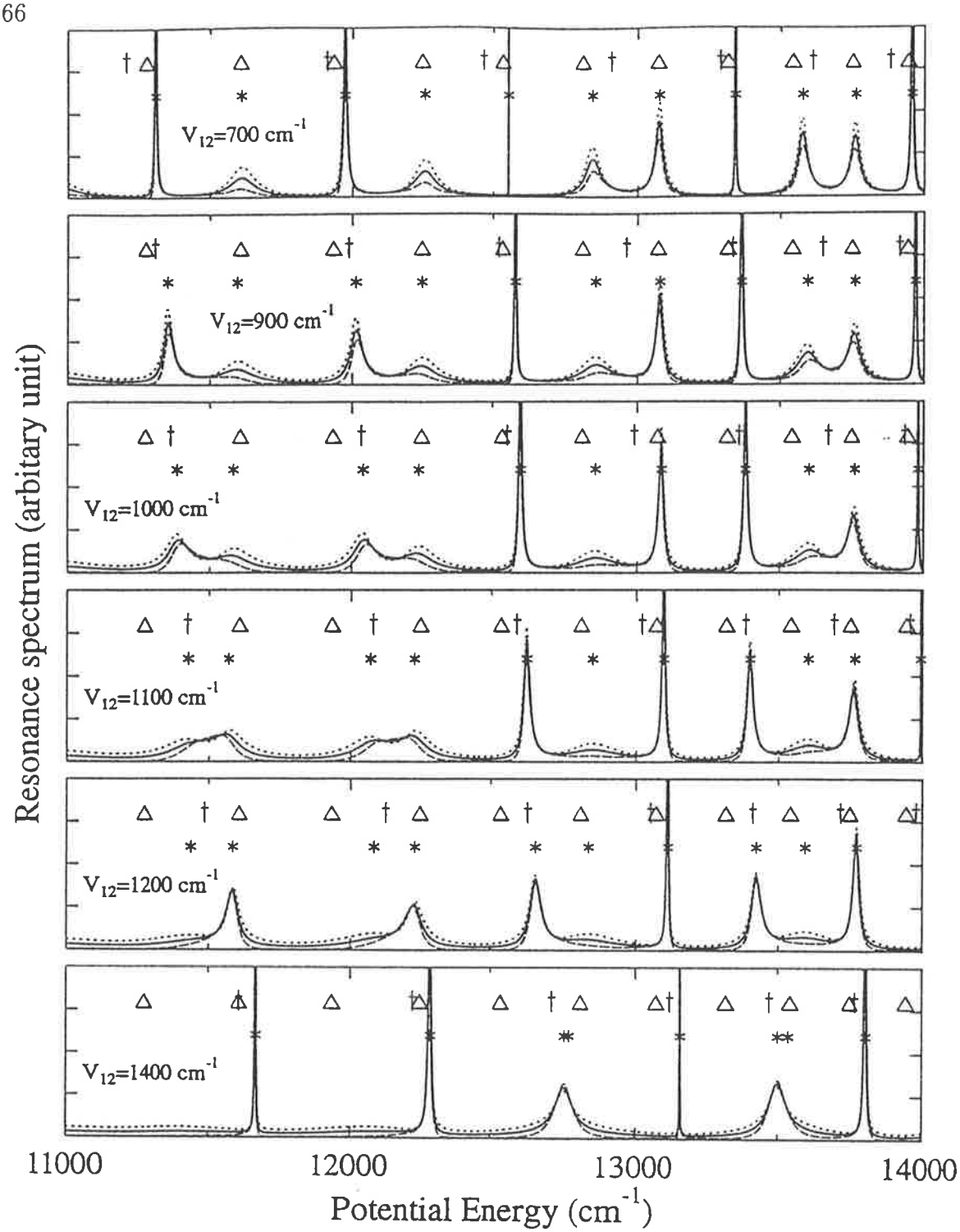

Figure 6.12: Resonance spectrum P/2 (bold lines), P^d (dash lines) and P^a (dotted lines) for a range of coupling strengths for the predissociative potential curves shown in Fig. 6.10. The symbols (∗), (△) and (†) indicate the resonance positions from complex quantization method and the eigenvalues for the diabatic and adiabatic bound states respectively. The diabatic states (△) range from $n_d = 21$ at the left to $n_d = 31$ at the right.

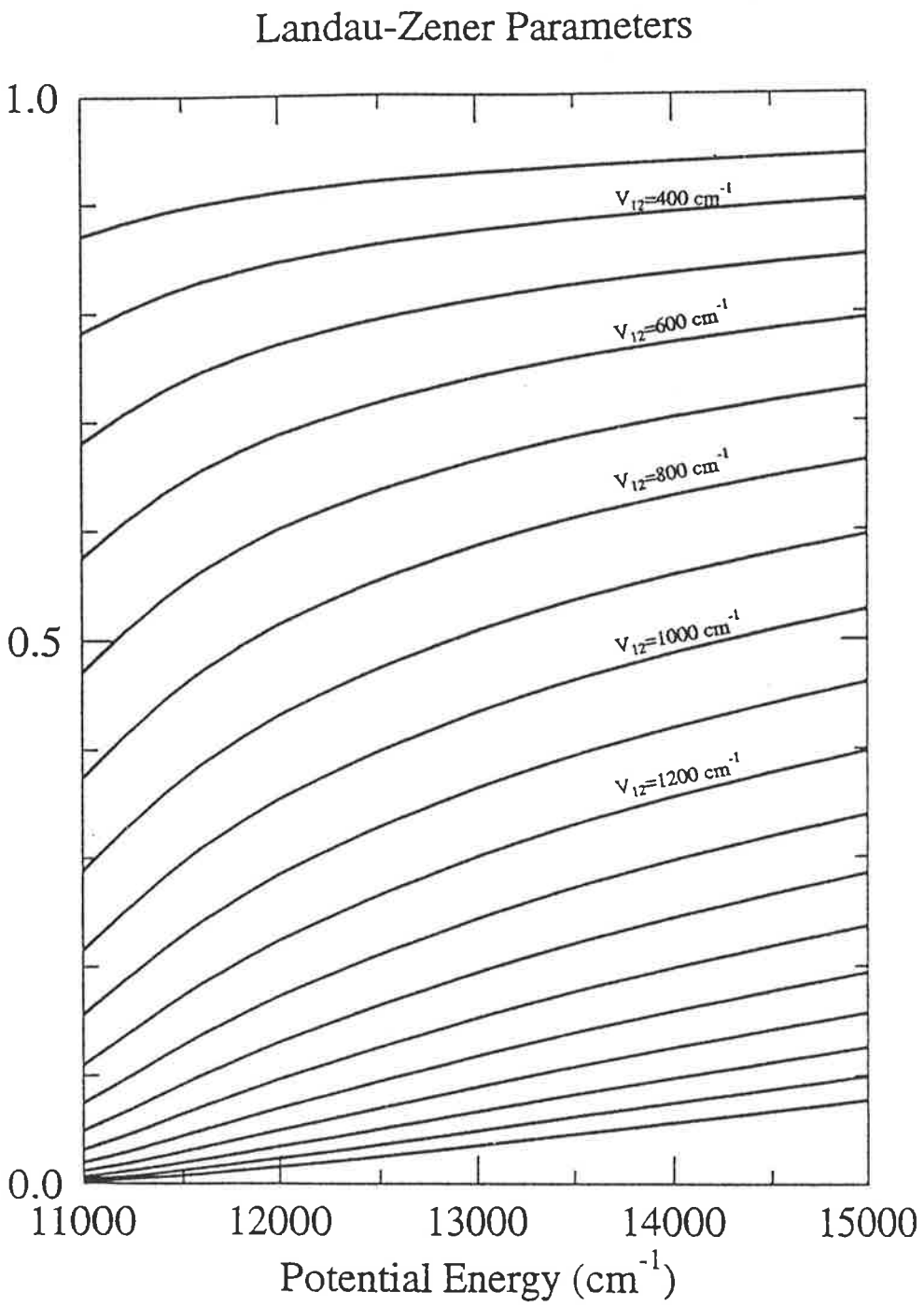

Figure 6.13: Variation of Landau-Zener nonadiabatic transition probability for the potential curves of Fig. 6.10.

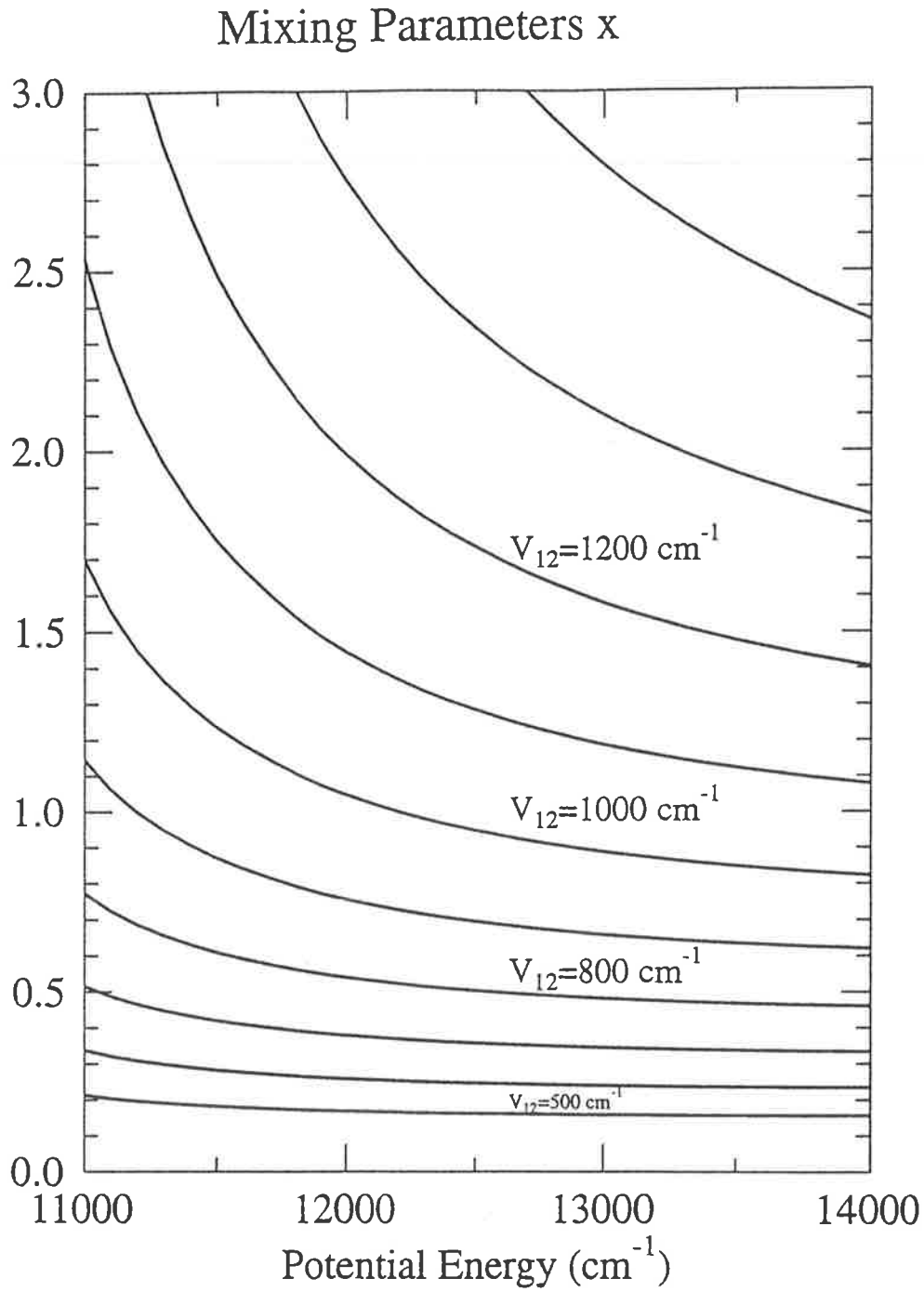

Figure 6.14: Variation of mixing parameters x for the potential curves of Fig. 6.10.

parameter of the diabatic and adiabatic character x given by (Child 1976):

$$x = u\hbar\bar{\omega}_2/\hbar\bar{\omega}_+ \tag{6.17}$$

as shown in Fig. 6.14, would be a better measure for the location of transition. $\hbar\bar{\omega}_2$ and $\hbar\bar{\omega}_+$ are the vibrational spacings of the diabatic and adiabatic states and

$$u = \frac{1}{P_{lz}} - 1. \tag{6.18}$$

Referring to Fig. 6.11 and Fig. 6.12, it can be seen that the transition between the diabatic and adiabatic case occurs at $x = 1$. This is also true for the MgH model since the two level spacings are nearly equal at the intermediate coupling region, so that $x = 1$ for $P_{lz} = 0.5$.

It is apparent that the transition located at $x = 1$ rather than $P_{lz} = 0.5$ would have a strong relationship with the amplitude of the semiclassical wave function at the left turning points of a curve crossing system (Child 1976), ie. when the two amplitude are equal:

$$A_1 = \frac{x}{(1+x)}\left[\frac{\Gamma/2\pi}{(E-\bar{E})^2+\Gamma^2/4}\right], \tag{6.19}$$

$$A_2 = \frac{1}{(1+x)}\left[\frac{\Gamma/2\pi}{(E-\bar{E})^2+\Gamma^2/4}\right]. \tag{6.20}$$

The physics of this relationship is still not clear and is under investigation.

6.7 Summary

The maximum value of the "internal amplitude" P obtained by summing the contributions from the diabatic and adiabatic bound states is proposed as a criterion for locating a resonance and the spectrum of P has been used to evaluate resonance widths. This method has been used to investigate the transition from the near diabatic to the near adiabatic case where the mixing parameter $x = 1$. The method gives resonance positions and widths which are in excellent agreement with those calculated by the complex

energy quantization method. The complex changes in the resonance spectrum, such as the splitting or vanishing of resonances, is explained by considering the contributions from the diabatic and adiabatic bound states. In these regions, the broad diabatic P^d and adiabatic P^d resonance can be out of phase and as their relative amplitudes change there may be cancellation and/or rapid movement of their summed peak. It is also shown in the resonance spectrum that outside a small region where $x \simeq 1$ the diabatic (P^d) or the adiabatic (P^a) resonance spectrum provides a very good approximation for the overall resonance spectrum and thus the resonance positions and widths. Theoretical justification for adding the bound components of two different basis, however, needs further investigation.

Appendix A

Solution of the Schrödinger Equations

Solution of the Schrödinger equation provides a full description of a quantum mechanical system. However exact analytical solutions can only be obtained for a few simple systems. Methods for numerical solutions of the equations for central fields exist for single or multi-channel cases (Cooley 1961; Shapiro 1972; Norcross and Seaton 1973; Johnson 1977, 1978; Goorvich and Galant 1992). Among them Johnson's renormalized Numerov method (1977, 1978) has the advantages of efficient computer time and ease of programming. The calculation of wavefunctions and eigenvalues for single channel as well as multi-channel cases can share the same program. It is the best method for the purpose of this study and a brief review of the method is given in this appendix. The application of this method for complex scaling method is given in Appendix C.

A.1 Solution of the coupled equations

For a two channel case, the diabatic coupled equations can be written in a compact matrix notion:

$$\left[\mathbf{I}\frac{d^2}{dr^2} + \mathbf{Q}(r)\right]\varphi(r) = 0 \tag{A.1}$$

where

$$\mathbf{Q}(r) = \frac{2\mu}{\hbar^2}[E\mathbf{I} - \mathbf{V}(r)], \tag{A.2}$$

$\mathbf{V}(r)$ is the electronic Hamiltonian matrix

$$\mathbf{V(r)} = \begin{pmatrix} V_{11}(r) & V_{12}(r) \\ V_{21}(r) & V_{22}(r) \end{pmatrix}, \tag{A.3}$$

$\mathbf{I}$ is the unit matrix and

$$\varphi = \begin{pmatrix} \chi_1 \\ \chi_2 \end{pmatrix}. \tag{A.4}$$

The renormalized Numerov method (Johnson 1977, 1978) has proved to be a very efficient method for numerical solution of the Schrödinger equation. It makes use of the three term recurrence relation

$$[\mathbf{I} - \mathbf{T}_{n+1}]\varphi_{n+1} - [2\mathbf{I} + 10\mathbf{T}_n]\varphi_n + [\mathbf{I} - \mathbf{T}_{n-1}]\varphi_{n-1} = 0 \tag{A.5}$$

where $\varphi_n = \varphi(r_n)$ and $\mathbf{T}_n = -\frac{l^2}{12}\mathbf{Q}(r_n)$ with l the grid spacing. Defining the matrix

$$\mathbf{F}_n = [\mathbf{I} - \mathbf{T}_n]\varphi_n \tag{A.6}$$

and substitute into Eq.(A.5) gives

$$\mathbf{F}_{n+1} - \mathbf{U}_n\mathbf{F}_n + \mathbf{F}_{n-1} = 0 \tag{A.7}$$

where

$$\mathbf{U}_n = (\mathbf{I} - \mathbf{T}_n)^{-1}(2\mathbf{I} + 10\mathbf{T}_n). \tag{A.8}$$

Introduce the ratio matrix

$$\mathbf{R}_n^o = \mathbf{F}_{n+1}\mathbf{F}_n^{-1} \tag{A.9}$$

as the outward propagation matrix, and

$$\mathbf{R}_n^i = \mathbf{F}_{n-1}\mathbf{F}_n^{-1} \tag{A.10}$$

as the inward propagation matrix. The wave function can be obtained as

$$\varphi_n = [\mathbf{R}_n^o(\mathbf{I} - \mathbf{T}_n)]^{-1}(\mathbf{I} - \mathbf{T}_{n-1})\varphi_{n-1} \tag{A.11}$$

by iterating outward; or

$$\varphi_n = [\mathbf{R}_n^i(\mathbf{I} - \mathbf{T}_n)]^{-1}(\mathbf{I} - \mathbf{T}_{n+1})\varphi_{n+1} \tag{A.12}$$

by iterating inward with the basic recurrence relation of the propagation matrix

$$\mathbf{R}_n^o = (\mathbf{I} - \mathbf{T}_n)^{-1}(2\mathbf{I} + 10\mathbf{T}_n) - (\mathbf{R}_{n-1}^o)^{-1} \tag{A.13}$$

$$\mathbf{R}_n^i = (\mathbf{I} - \mathbf{T}_n)^{-1}(2\mathbf{I} + 10\mathbf{T}_n) - (\mathbf{R}_{n+1}^i)^{-1} \tag{A.14}$$

which can be calculated first using the boundary conditions. The initial condition for $(\mathbf{R}_0^o)^{-1}$ is obtained by considering the fact that the wave functions approach zero at the inner boundary (the classical forbidden region). Therefore it is reasonable to make $\varphi_0 = 0$ while $\varphi_1 \neq 0$. It follows from Eq.(A.6) and Eq.(A.9) that $(\mathbf{R}_0^o)^{-1} = 0$.

For an attractive electronic bound state coupled with a continuum state, a non-zero solution of the Schrödinger equations exist for energies above the dissociation limit. Therefore the propagation matrix $\mathbf{R}_n^o$ can be calculated outward up to a sufficiently large value of $r = r_n$ where the amplitude of the continuum wave function is constant and the amplitude of the bound states wave function approaches zero. At this point the appropriate boundary condition for the wave function is

$$\varphi_n = \begin{pmatrix} 0 \\ a \end{pmatrix} \tag{A.15}$$

where a is a non-zero value to be decided by normalization.

Normalization is performed for the continuum wave function

$$(hc)^{-1}\int_0^\infty \chi_{2,\lambda'}(r)\chi_{2,\lambda}(r)dr = \delta(\lambda' - \lambda). \tag{A.16}$$

which requires the amplitude of the continuum wave function χ_2 at r_n to be normalized to $(8\mu c^2/(E - V_c(r_n))$. Such a normalization will also affect the amplitude of the bound state wave function.

The adiabatic coupled equation can be solved by the Rung-Kutta method for second order differential equations. However it has been proved that it is more efficient to solve the diabatic coupled equations using the above method and obtain the adiabatic nuclear wave functions by the transformation Eq. (2.18) (Wang, 1989).

A.2 Eigenvalue and Eigenfunction for a Bound State

The same procedure can also be applied for the bound eigenvalue problem. The following discussion will be restricted to the single channel bound state so that the matrices discussed above become scalars. For a bound potential eigenfunctions exist only at eigenvalues and the initial condition at the outer boundary is the same as that at the inner boundary. To find an eigenvalue it is assumed that the eigenvalue is located between E_L and E_H where $E_L < E_H$. An initial energy of

$$E = 0.5(E_L + E_H) \tag{A.17}$$

is used to calculate the propagators R^o outward and R^i inward. They are matched in the classical allowed region near one of the turning points. If E is the eigenvalue, the solution calculated inward and outward should be the same at the matching point. It is an advantage to choose the matching point where the wave function has its maximum or minimum values and to avoid the node positions. The nodes of the wave function can be counted by counting the conditions that $R_n < 0$, which implies the wave function crosses zero inside the classical region. If the nodes M_E are greater than the require vibrational quantum number v, the energy for the calculation is too high so set $E_H = E$,

otherwise set $E_L = E$. Then the next energy $E = 0.5(E_H + E_L)$ is used for the calculation. If $M_E = v$, then $D(E)$ defined as

$$D(E) = (R^i_{m+1})^{-1} - R^o_m, \tag{A.18}$$

is a well behaved function of E that it is zero at the eigenvalue and has a positive slope. Set $E_H = E$ for $D(E) > 0$, or $E_L = E$ for $D(E) < 0$ to start the next calculation. This procedure converges linearly and is iterated until $E_H - E_L$ is smaller than the accuracy required.

The matching procedure ensures that the eigenfunction is the same for integration of the Schrödinger equation inward and outward.

The eigenfunction is obtained by setting $\varphi_m = 1$ so that Eq. A.11 and Eq. A.12 can be used to calculate the wave function. Its absolute value $\varphi_r(r_n)$ is obtained by normalization to unity.

$$\varphi_r(r_n) = \varphi(r_n) / \int |\varphi(r)|^2 dr \tag{A.19}$$

Examples of the bound state wavefunctions are shown in Fig.2.5. Also shown in Fig.2.5 are comparisons of the bound state wave functions with the closed channel on resonance wave functions.

Appendix B

The Connection Matrix

A very attractive feature in Child's semiclassical theory for a curve crossing system is that *the theory is readily cast into a diagrammatic form. This serves both to underline the common physical feature of a diverse range of observed effects, and to facilitate the mathematical argument, because each linkage in the diagram is reflected by a matrix product* (Child 1974b). The general method relies on the changes in the coefficients (P and Q as in Eq. (2.26) and Eq. (2.27) in the nonclassical region. The basic elements of the connection matrix related to this study are given in the following section.

(i) Free propagation of the semiclassical wave from r_1 to r_2 leads to a phase change

$$\begin{pmatrix} Q' \\ Q' \end{pmatrix} = \begin{pmatrix} e^{i\gamma}, & 0 \\ 0 & e^{-i\gamma} \end{pmatrix} \begin{pmatrix} P' \\ P' \end{pmatrix} \tag{B.1}$$

where

$$\gamma = \int_{r_1}^{r_2} k(r)dr \tag{B.2}$$

(ii) Reflection from a classical turning point will cause a phase change of $-\frac{\pi}{2}$.

(iii) Passing through a curve crossing. The coupled equations are solve in the crossing region (Bandrauk and Child 1970, Child, 1974) to bridge the wave functions

Table B.1: Numerical values of the phase corrections χ.

ν	χ	ν	χ	ν	χ	ν	χ
0.0	-0.785	0.3	-0.287	0.6	-0.152	0.9	-0.098
0.1	-0.512	0.4	-0.226	0.7	-0.129	1.0	-0.090
0.2	-0.376	0.5	-0.183	0.8	-0.111		

between the crossing region.

$$\begin{pmatrix} Q'_+ \\ Q'_- \end{pmatrix} = \begin{pmatrix} (1-\lambda^2)^{1/2}e^{i\chi}, & -\lambda \\ \lambda & (1-\lambda^2)^{1/2}e^{-i\chi} \end{pmatrix} \begin{pmatrix} P'_+ \\ P'_- \end{pmatrix} \tag{B.3}$$

$$\begin{pmatrix} P''_+ \\ P''_- \end{pmatrix} = \begin{pmatrix} (1-\lambda^2)^{1/2}e^{i\chi}, & \lambda \\ -\lambda & (1-\lambda^2)^{1/2}e^{-i\chi} \end{pmatrix} \begin{pmatrix} Q''_+ \\ Q''_- \end{pmatrix} \tag{B.4}$$

where

$$\lambda = exp(-\pi\nu) \tag{B.5}$$

$$\nu = -\frac{i}{2\pi}\left(\int_{r_-}^{r_+}[k_-(r) - k_+(r)]dr\right) \tag{B.6}$$

$$k_\pm(r) = [2\mu(E - V_\pm(r))]^{1/2}/\hbar \tag{B.7}$$

$$\chi = arg\Gamma(i\nu) - \nu ln\nu + \nu + \pi/4 \tag{B.8}$$

where r_+ and r_- are the complex crossing points of the adiabatic upper V_+ and lower V_- potential curves in the complex coordinate plane. χ is a phase shift caused by the curve crossing. Table B.1 list some of its values.

Applying the curve crossing connection formulas to the wave functions following

the diagram in Fig. 2.5 one finds that

$$\begin{pmatrix} Q'_+ \\ Q'_- \end{pmatrix} = \begin{pmatrix} (1-\lambda^2)^{1/2}e^{i\chi} & -\lambda \\ \lambda & (1-\lambda^2)^{1/2}e^{-i\chi} \end{pmatrix} \begin{pmatrix} exp(2i\alpha_+ - i\pi/2) & 0 \\ 0 & exp(2i\alpha_- - i\pi/2) \end{pmatrix} \begin{pmatrix} (1-\lambda^2)^{1/2}e^{i\chi} & \lambda \\ -\lambda & (1-\lambda^2)^{1/2}e^{-i\chi} \end{pmatrix} \begin{pmatrix} Q''_+ \\ Q''_- \end{pmatrix}. \tag{B.9}$$

For resonance states the Siegert outgoing wave only boundary condition for resonance requires $Q''_- = 0$, therefore

$$\begin{aligned} \begin{pmatrix} Q'_+ \\ Q'_- \end{pmatrix} &= \begin{pmatrix} (1-\lambda^2)exp(2i\alpha_+ + 2i\chi - i\pi/2) + \lambda^2 exp(2i\alpha_- - i\pi/2) \\ \lambda(1-\lambda^2)^{1/2}exp(-i\pi/2)(exp(2i\alpha_+ + i\chi) - exp(2i\alpha_- - i\chi) \end{pmatrix} Q''_+ \\ &= \begin{pmatrix} (1-\lambda^2)exp(2i\theta_+) + \lambda^2 exp(2i\theta_2) \\ \lambda(1-\lambda^2)^{1/2}exp(-i\chi)(exp(2i\theta_+) - exp(2i\theta_2) \end{pmatrix} (-Q'_+). \end{aligned} \tag{B.10}$$

with the relationship of $Q'_+ = Q''_+ exp(-2i\beta_+ + i\pi/2)$.

The derivation of Child's semiclassical theory is beyond of the scope of this study. For more details one can refer to the original work of Child (1970, 1974, 1976, 1991).

Appendix C

Computation of the Complex Eigenvalues

The complex rotation of coordinates results in boundary conditions for a quasibound system that are the same as a bound state. Therefore the computation technique described in Appendix A can also be used to calculate the complex eigenvalues upon the change $r \rightarrow re^{i\theta}$. Consider a two state problem where the coupled equation are:

$$\left[-\frac{\hbar^2}{2\mu}\frac{d^2}{dr^2} + e^{-2i\theta}(V_{11}^d(re^{i\theta}) - E)\right]\chi_1^d(r,\theta) = -V_{12}^d(re^{i\theta})\chi_2^d(r,\theta) \qquad \text{(C.1)}$$

$$\left[-\frac{\hbar^2}{2\mu}\frac{d^2}{dr^2} + e^{-2i\theta}(V_{22}^d(re^{i\theta}) - E)\right]\chi_2^d(r,\theta) = -V_{12}^d(re^{i\theta})\chi_1^d(r,\theta) \qquad \text{(C.2)}$$

with V_1 the closed channel and V_2 the open channel. The initial condition for inner boundary is the same as in Appendix A:

$$\psi_0 = \begin{pmatrix} 0 \\ 0 \end{pmatrix} \qquad \text{(C.3)}$$

while the outer boundary condition is similar to that of a bound state for sufficiently large r_n in the asymptotic region

$$\psi_n = \begin{pmatrix} 0 \\ 0 \end{pmatrix}. \qquad \text{(C.4)}$$

The propagating and matching procedure for a bound state described in Appendix A is then used to calculate the complex eigenvalues. In the calculation, an initial trail resonance energy E_0 is chosen and the matrix propagated and matched at r_m where the determinant

$$D(E) = |\mathbf{R}_m^o - (\mathbf{R}_{m+1})^{-1}| \tag{C.5}$$

vanishes at each eigenvalue. Convergence to the eigenvalue is achieved by iterating the calculation using the Newton-Raphson method which predicts the next trail energy as

$$E = E_0 - \frac{D(E_0)}{(dD(E_0)/dE)}. \tag{C.6}$$

The calculated results for the resonance energy and line widths using CSM for a curve crossing system proved to be in excellent agreement with those using the real coupled equations, and Child's semiclassical theory (Lefebvre 1990).

The development of complex scaling method (CSM) provides an approach to the direct study of resonance through the introduction of complex variables. The complex coordinate approach treats resonance states as the bound states.

Appendix D

Second Harmonic Generation

With the advent of the intense and coherent light made available by the laser, the optical properties of the medium such as its refractive index become a function of the light intensity. When two or more light waves interfere within the medium, the principle of superposition no longer holds. The polarization of a nonlinear medium by an electric field **E** is usually written as

$$\mathbf{P} = \epsilon_0 \chi \mathbf{E} \tag{D.1}$$

where ϵ_0 is the vacuum permittivity and χ is the susceptibilty of the nonlinear medium given by a power series in the form

$$\chi = \chi_1 + \chi_2 E + \chi_3 E^2 + \cdots \tag{D.2}$$

Therefore the polarization takes the form

$$P = \epsilon_0(\chi_1 + \chi_2 E + \chi_3 E^2 + \cdots)E \tag{D.3}$$

$$= \epsilon_0(\chi_1 E + \chi_2 E^2 + \chi_3 E^3 + \cdots) \tag{D.4}$$

The first term in the above equation represents the linear optics. Although the coefficients of the higher-power terms are usually very small, the high coherence of laser light allows the beam to be focused onto a very small spot size of the order of wavelength,

producing electric fields of the orders of the fields binding electrons to nuclei in the optical medium (10^{10} V/m) which allows the higher-power terms to be appreciable. These effects are referred to as nonlinear effects because they are nonlinear in E.

D.1 Theoretical Review

The second term in Eq.(D.2) represents the most common nonlinear phenomena of second harmonic generation (SHG) and frequency mixing. When two light beam $E_1 = E_{01}cos(\omega_1 t)$ and $E_2 = E_{02}cos(\omega_2 t)$ are incident into a nonlinear medium, the second-order polarization

$$P_2 = \epsilon\chi^{(2)}E^2 \tag{D.5}$$

where

$$\begin{aligned} E^2 &= (E_1 + E_2)^2 && \text{(D.6)} \\ &= E_{01}^2 cos^2\omega_1 t + E_{02}^2 cos\omega_2 t + 2E_{01}E_{02}cos\omega_1 t\ cos\omega_2 t && \text{(D.7)} \\ &= \frac{1}{2}(E_{01}^2 + E_{02}^2) + \frac{1}{2}E_{01}^2 cos2\omega_1 t + \frac{1}{2}E_{02}^2 cos2\omega_2 t + && \text{(D.8)} \\ &\quad E_{01}E_{02}[cos(\omega_1 + \omega_2)t + cos(\omega_1 - \omega_2)t] && \text{(D.9)} \end{aligned}$$

contains a dc polarization and ac components at second harmonic frequencies $2\omega_1$, $2\omega_2$, and sum and difference frequencies $\omega_1 \pm \omega_2$. $\chi^{(2)}$ is the second order susceptibility which is a tensor with components $\chi_{ijk}^{(2)}$ depending on the symmetry properties of the nonlinear crystal.

In general, experiments based on the second order nonlinear susceptibilities are carried out in crystalline media which do not process inversion symmetry in order to have a non-zero $\chi_{ijk}^{(2)}$. Examples of the crystals are KDP, ADP, CDA, $LiNbO_3$, BBO, LBO etc.

D.2 The electromagnetic formulation of the nonlinear interaction

The coupled equations describing the nonlinear interaction of second harmonic generation (SHG) can be derived from the Maxwell equations (Yariv, 1975 and Craxton, 1981) in the form of

$$\frac{dE_1}{dz} = -iKE_1^* E_2 e^{-i\Delta kz} \tag{D.10}$$

$$\frac{dE_2}{dz} = -i2KE_1^2 e^{i\Delta kz} \tag{D.11}$$

where $K = \frac{\omega}{2c}(n_1(\omega)n_2(2\omega))^{1/2}\frac{d_{eff}}{\epsilon_0}$ with n the refractive index, ω the fundamental frequency and d_{eff} the effective nonlinear coefficient. $\Delta k = k(2\omega) - 2k_1(\omega)$ represents the phase matching condition. It is also assumed that the nonlinear medium is transparent to the fundamental and second harmonic radiation so that the absorption effect can be neglected.

The conversion efficiency of frequency doubling is usually quite low, therefore the intensity of the fundamental wave can be regarded as constant in the nonlinear medium so that $dE_1/dz = 0$, and

$$E_2 = -i2KE_1^2 \frac{e^{i\Delta kL} - 1}{i\Delta k}. \tag{D.12}$$

The intensity is (Craxton 1981)

$$I_2 = \frac{\epsilon_0 c}{2}E_2^2 = 2K^2L^2c\mu_0 I_1^2 sinc^2(\frac{1}{2}\Delta kL) \tag{D.13}$$

where I in W/m^2 and E in (V/m), $sinc(x) = \frac{sinx}{x}$, and L is the total length of the nonlinear medium. From the above equation, it is prerequisite for efficient second harmonic generation to have $\Delta k = 0$, that is

$$k(2\omega) = 2k(\omega). \tag{D.14}$$

If $\Delta k \neq 0$, the second harmonic wave generated at different location of the crystal is

not in phase and results in the interference effect described by the factor

$$sinc^2(\frac{1}{2}\Delta kL) \tag{D.15}$$

and characterized by the so called "coherence length"

$$L_c = \frac{2\pi}{\Delta k} \tag{D.16}$$

which gives a measure of the maximum crystal length that is useful in producing the second harmonic power. A longer length than L_c can only produce a negative effect for the total second harmonic power because the second harmonic wave generated after L_c is out of phase with that generated before L_c and the interference effect will decrease the total intensity.

D.3 Phase matching technique

The major difficulty in efficient frequency doubling is the dispersion effect which limits the coherence length and therefore the second harmonic power. The technique that is widely used to satisfy the phase matching condition Eq. (D.14) takes the advantage of the natural birefringence of a anisotropic crystals. In some nonlinear crystals, if the direction of the laser through the crystal is chosen such that $n_{2\omega}$ for the E-ray equals n_ω for the O-ray, the phase matching condition can be satisfied at this direction for the chosen wavelength. The situation is shown in Fig. D.1. The phase matching condition is then limited by the beam divergence and the spectral band width of the laser.

If $\Delta k = 0$ is satisfied, the nonlinear coupled equations can be solved analytically and

$$E_2(L) = E_1(0)tanh(L/l_{SHG}) \tag{D.17}$$

where $l_{SHG} = (\frac{4\pi\omega^2}{k_1 c^2}E_1(0))^{-1}$.

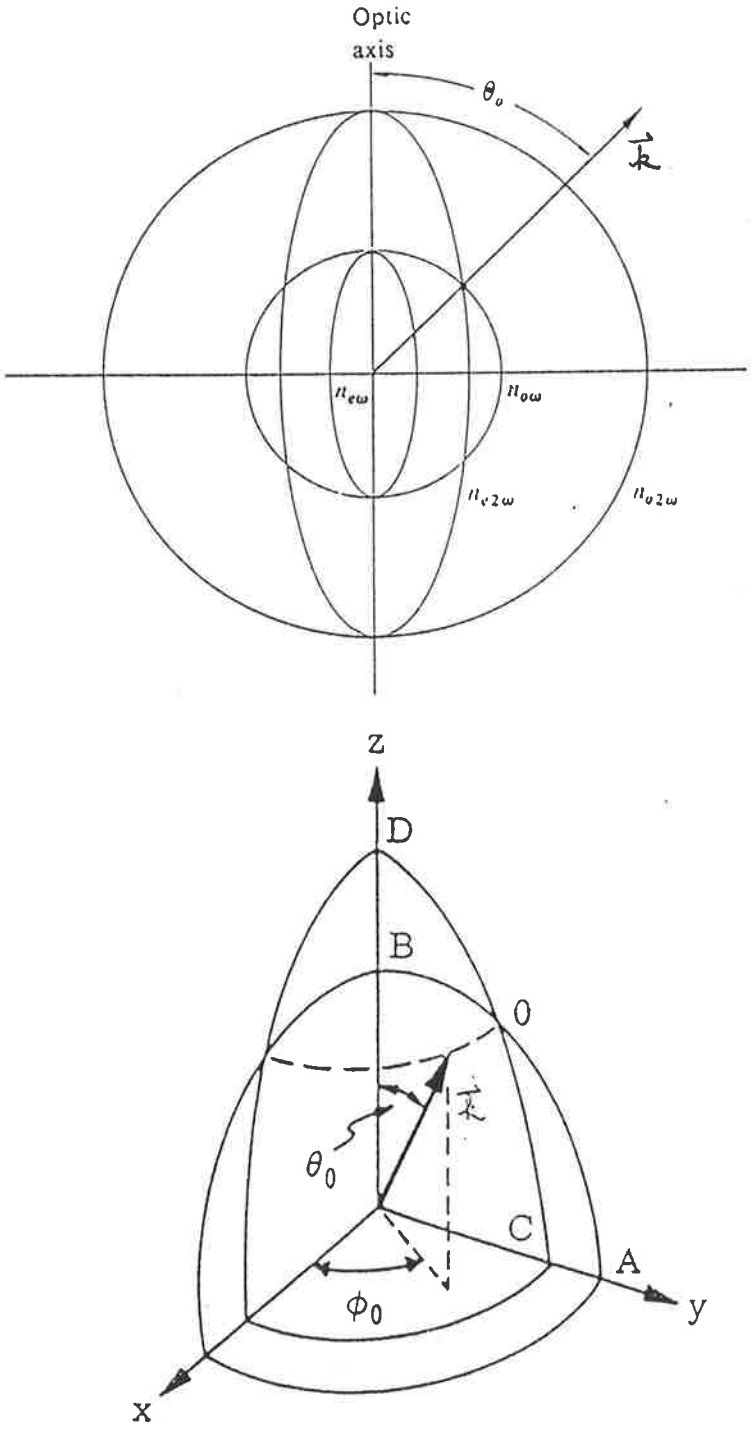

Figure D.1: The phase matching angle in the crystal where k indicates the direction of the laser beam

D.4 Enhancement of the conversion efficiency

From Eq. (D.13), for efficient frequency doubling one has to increase the intensity of the laser, reduce the phase mis-matched Δk, increase the coherence length and the crystal length. Different technique have been developed to improve these parameters.

Focusing is the most common way to increase the laser intensity for frequency doubling and therefore the conversion efficiency. Because the frequency doubler is sensitive to beam divergence in the θ direction and not sensitive in the ϕ direction as indicated in Fig. D.1, focusing using a cylinder lens which focuses in the ϕ direction only can achieve a better result.

For cw laser, the output coupling of the laser cavity is normally very low, about a few percent. Therefore the light intensity inside the cavity is much higher and it is an advantage if the frequency doubler is placed inside the laser oscillator cavity which can also be used as an output coupling and the cavity mirrors can be both 100% reflectivity at the fundamental frequency. Furthermore, with a proper output coupling arrangement, the 2ω wave can pass through the crystal twice before leaving the cavity. This effectively doubles the crystal length and increases the conversion efficiency.

For high laser intensity, the use of two frequency doublers in different combination enables one to obtain high conversion efficient in a large dynamic region. (W. Qin, 1985).

D.5 Characteristics of the BBO crystal

Beta-barium borate (BaB_2O_4) or BBO crystal is a new nonlinear optical material discovered recently (Chen et al. 1984, 1985). It is an interesting material characterized by a wide range of transparency in both UV and infrared. Its large birefringence allows phase matching for second harmonic generation in a large frequency region (189-1750

Table D.1: NLO properties of Type I BBO crystal for SHG at 640 nm (provided by CASTECH)

NLO Coefficient (d_{36}(KDP))	d_{11}=5.8 $d_{31} = 0.05 \times d_{11}$
Phase matching angle (degree)	37.4
Acceptance angle (mrad/cm)	0.4
Walk-off angle (degree)	4.2
Damage threshold (at 530 nm)	1 GW/cm^2 (10 ns); 7 GW/cm^2 (250 ps)

nm) with a large nonlinear coefficient ($5.8 \times d_{36}(KDP)$). These properties indicate that the BBO crystal is potentially useful for many applications, especially in the UV region. The optical, mechanical and thermal properties of the BBO crystal have been summarized by Eimerl et al (1987). For the purpose of this study, Fig. D.2 shows the phase-matching angles and the angular sensitivity for SHG. Some nonlinear optical (NLO) coefficients are listed in Table D.1.

D.6 Conversion efficiency

The BBO crystal used in this study is cut for type I frequency doubling from 580-700 nm, protectively coated with a dimension of $6 \times 4 \times 7\ mm^3$ from CASTECH. The laser beam is weakly focused into the crystal to prevent the divergence of the UV beam because a suitable quartz lens was not available for collimation and the UV power is not a major concern in this study. The tuning angle is controlled by a personal computer in accordance with the tuning of wavelength and is driven by a DC motor (Oriel D.C. Encoder Mike^{TM} Drive) with a linear readout resolution of 0.1 microns.

The effective NLO coefficients for frequency doubling is a function of the crystal

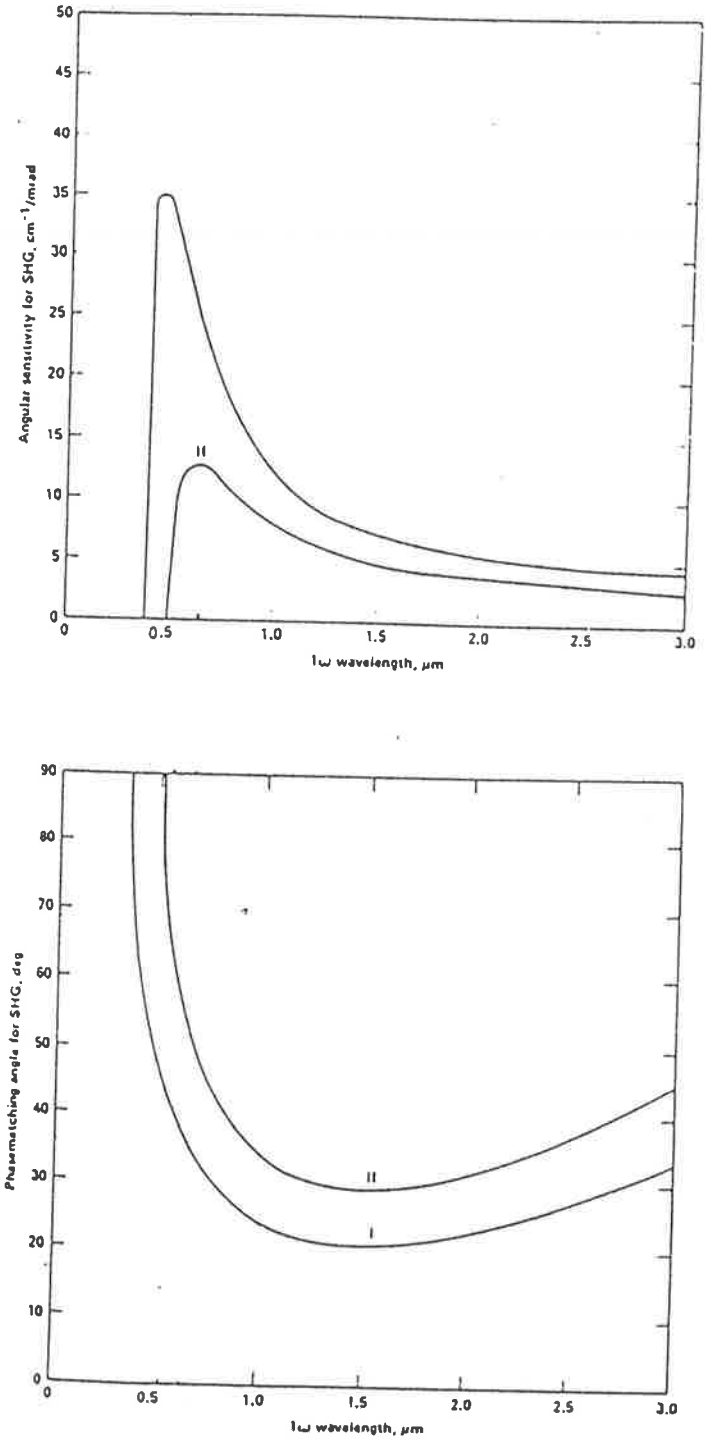

Figure D.2: Characteristic of the BBO crystal for second harmonic generation: (a) angular sensitivity $d\Delta k/d\theta$, and (b) phase-matching angles. (after Eimerl et al, 1987)

orientation and therefore depend on the phase matching angle θ:

$$d_{eff} = d_{31} sin\theta + d_{11} cos\theta. \tag{D.18}$$

At 640 nm $d_{eff} = 4.78 d_{36}(KDP)$ and $d_{36}(KDP)/\epsilon_0 = 0.78 pm/V$ (Craxton R.S. 1981). With $n_o = N_e(\theta) \simeq 1.55$ $K = 9.46 \times 10^{-6}$ V^{-1}. The peak conversion efficiency of the BBO crystal is then

$$\eta_{eff} = 2c\nu_0 K^2 L^2 I_1 sinc^2(\frac{1}{2}\Delta kL) \tag{D.19}$$

$$= 6.78\ L^2 I^2 sinc^2(\frac{1}{2}\Delta kL) \tag{D.20}$$

where L (cm) is the length of the BBO crystal and I_1 (W/cm^2) is the intensity of the fundamental wavelength. For our system L=0.7 cm and assumed perfect phase matched

$$\eta_{eff} = 3.32 \times 10^{-8} I_1. \tag{D.21}$$

Because the Gaussian temporal pulse for the second harmonic becomes narrower by a factor of $\sqrt{2}$ than the fundamental, the overall energy efficiency for such pulse is therefore less than the instantaneous efficiency at the peaks of the pulse by the same factor.

Appendix E

The electronic circuits of the detecting system

The UV pulses have a large energy variation due to the pumped dye laser and the non-linear conversion of the BBO crystal. The electronic circuits, as shown in Fig. E.1 and Fig. E.2, performs a number of functions as follows:

- Uses a peak detector to hold the peak height of pulse (100ns) generated by the pin diodes for the laser radiation. This minimises the contribution of ambient light and noise to the integrate d signal. The peak detector decays to zero in approximately 50 microseconds.

- Stores the peak height of the pulses for both reference and detector in sample and hold circuits "c" and "d" provided the signal is above a minimum threshold detected by the Schmitt trigger "a" and transferred by the sample pulse from the monostable "e".

- Checks the peak height with the threshold Schmitt trigger detector "b" and if greater than a preset level fires a monostable "f" which prevents the transfer pulse from the delay monostables "g" and "h" reaching the second set of sample and

hold circuits "j' and "k" through the action of the AND gate "i". This prevents large pulses which are distorted by the limited voltage range of the peak detector circuits reaching the second set of sample and hold circuits.

- If the intensity of the pulse lies between the required height range, transfers the content of the first pair of sample and hold circuits "c" and "d" to the second pair "j" and "k".

- Uses these voltages at A and B, which are equal to the peak heights of the reference and detector signals and constant between recorded pulses, as input voltages to a pair of integrators "m" and "n".

- When the reference integrator "m" integrates down to a preset level, stores the output of the detector integrator "n" in a sample and hold circuit "r" by the sample pulse from monostable "q".

- The reference and detector integrators "m" and "n" are then simultaneously reset by the MOSFETS "s" and "t" after a short delay through monostables "o" and "p" to commence another integration cycle.

The output signal from the detector sample and hold "C" is thus the ratio of detector to reference signal. Each integration represents the same integrated energy in the reference signal and therefore constant signal to noise ratio. If the intensity of the input signal (ie the intensity of laser radiation) falls, the integration rate is reduced and this produces a stepped output as the wavelength is scanned. This stepped output represents an accurate average ratio of intensities over the wavelength region of the step. The scan is accepted if the wavelength region of the step is less than 0.1 cm^{-1}. Otherwise, either the intensity of the laser radiation is increased or the rate of wavelength scanning is reduced and the scan repeated.

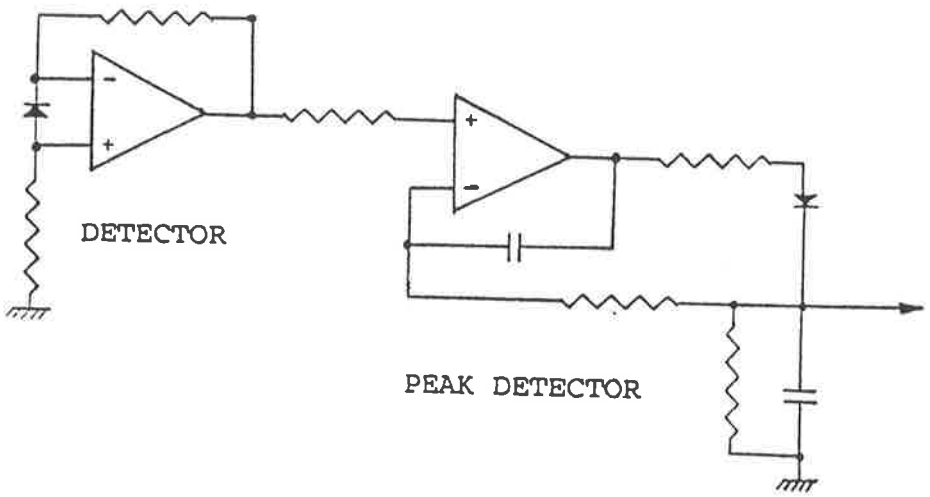

Figure E.1: The electronic circuits for the detector. It consists of a UV enhanced photodiode, a high speed preamplifier and a peak detector which holds the peak level of the laser signal.

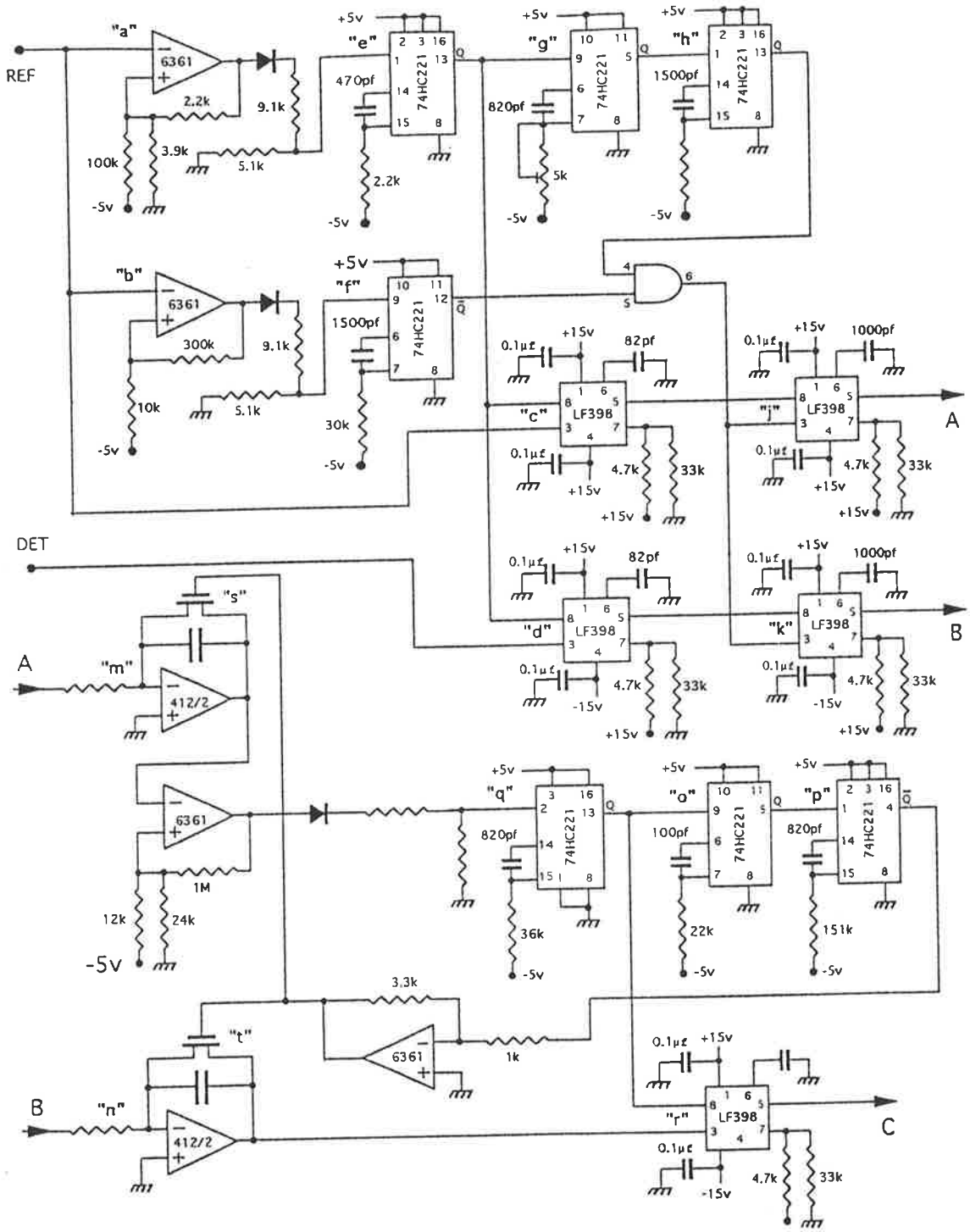

Figure E.2: The electronic circuits of the detecting system.

List of Figures

List of Tables

Bibliography

1. Aguilar J. and Combes J.M. "A class of analytic perturbations for one-body Schrödinger Hamiltonians", *Commun. Math. Phys.*, **22**, 269 (1971).

2. Allison A.C. "Quasi-bound states in H_2", *Chem. Phys. Lett.*, **3**, 371, (1969).

3. Anderson W.R., Wilson B.M., and Rose T.L. "Importance of the perpendicular transition leading to ground state atoms in the photodissociation of NaI", *Chem. Phys. Lett.*, **48**, 284, (1977).

4. Anderson W.R., Wilson B.M., Ormerod R.C. and Rose T.L. "Photodissociation of alkali iodides at 347.1 nm: Experimental angular distribution and dynamic model for their interpretation", *J. Chem. Phys.*, **74**, 3295, (1981).

5. Astadjov D.N., Vuchkov N.K. and Sabotinov N.V. "Parametric study of the CuBr laser with hydrogen additives", *IEEE J. Quant. Electron.*, **QE-24**, 1927, (1988).

6. Atabek O. and Lefebvre R. "Multichannel Siegert quantization with complex rotated coordinates: Application to molecular resonances", *Phys. Rev.*, **A22**, 1817, (1980).

7. Atabek O. and Lefebvre R. "Multichannel quantization for molecular systems. I. Bound states studies", *Chem. Phys.*, **52**, 199, (1980).

8. Atabek O. and Lefebvre R. "Multichannel quantization for molecular systems. II. Resonance studies", *Chem. Phys.*, **55**, 395, (1981).

9. Atabek O. and Lefebvre R. "Multichannel quantization for molecular systems. III. Complex rotation of coordinates", *Chem. Phys.*, **56**, 195, (1981).

10. Atabek O., Lefebvre R. and Requena A. "The wavefunction of the complex coordinate method", *Mole. Phys.*, **40**, 1107, (1980).

11. Bain R.A., Bardsley J.N., Junker B.R. and Sukumar C.V. "Complex coordinate studies of resonant electron-atom scattering", *J. Phys. B: Atom. Molec, Phys.*, **7**, 2189, (1974).

12. Balint-Kurti G.G and Shapiro M. "Quantum theory of molecular photodissociation", in *Photodissociation and Photoionization*, eds. Lawley K.P., John Wiley & Sons Ltd., (1985).

13. Balslev E. and Combes J.M. "Spectral properties of many-body Schrödinger operators with dilatation- analytic interactions", *Commun. Math. Phys.*, **22**, 280 (1971).

14. Bandrauk A.D. and Child M.S. "Analytic predissociation linewidths from scattering theory", *Mol. Phys.*, **19**, 95, (1970).

15. Bardsley J.N. "Complex scaling: An introduction", *Int. J. Quantum Chem.*, **XIV**, P343, (1978).

16. Barker J.R. and Weston R.E., Jr. "Energy-dependent cross sections for quenching of Na($3p^2P$) by several gases", *J. Chem. Phys.*, **65**, 1427, (1976).

17. Berg R.A. and Skewes G.W. "Discrete structure in the spectrum of sodium iodide vapor", *J. Chem. Phys.*, **51**, 5430, (1969).

18. Berkowitz J. "Photoelectron spectroscopy of alkali halide vapors"(in *Alkali Halide Vapors*, eds. Davidovits P. and McFadden D.L. (Academic Press, New York, 1979).

19. Bernhardt A.F. and Rasmussen P. "Design criteria and operating characteristics of a single-mode pulsed dye laser", *Appl. Phys.*, **B26**, 141, (1981).

20. Berry A.J., McKinnie I.T. and King T.A. "Narrow linewidth operation of a pulsed grazing-incidence dye laser", *J. Mod. Optics*, **37**, 463, (1990).

21. Berry R.S. "Interaction of vibrational and electronic motion in alkali halide molecules", *J. Chem. Phys.*, **27**, 1288, (1957).

22. Berry R.S. "Optical spectra of the alkali halide molecules" in *Alkali Halide Vapors*, eds. Davidovits P. and McFadden D.L. (Academic Press, New York, 1979).

23. Berry R.S. and Levy D.H. "Reply to "Comment on 'Fluorescence spectra of NaI molecule'"", *J. Chem. Phys.*, **78**, 6342, (1983).

24. Beutler H. and Levi H. *Elektrochem. Angew. Phys. Chem.*, **8a**, 1, (1931).

25. Bloembergen N. *Nonlinear Optics*, (W.A. Benjamin, Inc. New York, 1965).

26. Bluhm H., Lindner J. and Tiemann E. "High-resolution spectroscopy of NaI around the atomic asymptotes Na $(3p^2P_{1/2,3/2})$ + I $(^2P_{3/2})$", *J. Chem. Phys.*, **93**, 4556, (1990).

27. Born M. and Oppenheimer J.R. "Zur quantentheorie der molekeln", *Ann. Phys.*, **84**, 457, (1927).

28. Borsutzky A., Brünger R., Huang Ch. and Wallenstein R. "Harmonic and sum-frequency generation of pulsed laser radiation in BBO, LBO, and K^*DP", *Appl. Phys. B* **52**, 55, (1991).

29. Bower R.D., Chevrier P., Das P., Foth H.J., Polanyi J.C., Prisant M.G. and Visticot J.P. "Broad-band structured fluorescence from NaI", *J. Chem. Phys.*, **89**, 4478, (1988).

30. Brändas E., Rittby M. and Elander N. "Multichannel complex scaled Titchmarsh Weyl theory a model for diatomic fragmentation", *Lecture Notes in Physics*, **325**, 345, (1987).

31. Brändas E. "The method of complex scaling", *Int. J. Quantum Chem.: Quantum Chem. Symposium*, **20**, 119, (1986).

32. Broyer M. and Chevaleyre J. "CVL-pumped dye laser for spectroscopic application", *Appl. Phys. B*, **35**, 31, (1984).

33. Brumer P. and Karplus M. "Perturbation theory and ionic models for alkali halide systems: I Diatomics", *J. Chem. Phys.*, **58**, 3903, (1973).

34. Chang J.J. "Time-resolved beam-quality characterization of copper-vapor lasers with unstable resonators", *Appl. Opt.* , **33**, 2255, (1994).

35. Chapman S. and Child M.S. "A semiclassical study of long time recurrences in the femtosecond predissociation dynamics of NaI", *J. Phys. Chem.* , **95**, 578, (1991).

36. Chatzidimitriou-Dreismann C.A. 'Complex scaling and dynamical processes in amorphous condensed matter", *Advances in Chemical Physics*, **LXXX**, 201, (1991).

37. Chen C., Wu B., You G. and Huang Y. *Digest of Technical Papers of the XIIIth Internation Quantum Electronics Conference*, 1984, paper MCC5.

38. Chen C., Wu B., You G. and Huang Y. *Sci. Sin.* Ser. **B28**, 235, (1985).

39. Child M.S. (a) "Diatomic predissociation linewidths", *Mol. Spectrosc.*, A specialist report, **2**, 465, (1974).

40. Child M.S. (b) "Semiclassical theory of tunneling and curve-crossing problem: a diagrammatic approach", *J. Mol. Spectrosc.*, **53**, 280, (1974).

41. Child M.S. "Predissociation and photodissociation of IBr: a case of intermediate coupling strength", *Mole. Phys.*, **32**, 1495, (1976).

42. Child M.S. "Separable spectroscopic applications", in *Semiclassical methods in molecular scattering and spectroscopy,* Proceedings of the NATO ASI held in Cambridge, England, in September 1979.

43. Child M.S. "Semiclassical mechanics with molecular applications", Clarendon Press, Oxford, 1991.

44. Child M.S. (a) "A semiclassical study of long time recurrences in the femtosecond predissociation dynamics of NaI", *Phys. Chem.*, **95**, 578, (1991).

45. Child M.S. and Lefebvre R. "Predissociation at intermediate coupling strengths", *Chem. Phys. Lett.*, **55**, 213, (1978).

46. Chu Shih-I "The complex scaling method: application to autoionization, predissociation, and multiphoton resonances", *Int. J. Quantum Chem.: Quantum Chem. Symposium*, **20**, 129, (1986).

47. Cooley J.W. "An improved Eigenvalue corrector formula for solving the Schrödinger equation for central fields". *Math. Comut.*, **15**, 363, (1961).

48. Coutts D.W., Ainsworth M.D. and Piper J.A. "Observation of the temporal evolution of transverse coherence in coper vapor laser", *Opt.Commun.*, **87**, 245, (1992).

49. Coutts D.W., Brown D.J.W. and Piper J.A. "Measurements of the divergence evolution of copper-vapor laser output by using a cylindrical imaging technique", *Appl. Opt.*, **32**, 2058, (1993).

50. Davidovits P. and Brodhead D.C. "Ultraviolet absorption cross sections for the alkali halide vapors", *J. Chem. Phys.*, **46**, 2968, (1967).

51. Delvigne G.A.L. and Los J. "Rainbow, stueckelberg oscillations and rotational coupling on the differential cross section of Na + I $\rightarrow$ $Na^+ + I^-$", *Physica*, **67**. 166, (1973).

52. Duart F.J. and Piper J.A. "Comparison of prism-expander and grazing-incidence grating cavities for copper laser pumped dye lasers", *Appl. Optics*, **21**, 2782, (1982).

53. Dunham J.L. *Phys. Rev.*, **41**, 721, (1932).

54. Dyke T.R. "Microwave and radio-frequency spectroscopy of alkali halide vapors", in *Alkali Halide Vapors*, eds. Davidovits P. and McFadden D.L. (Academic Press, New York, 1979).

55. Earl B.L. and Herm R.R. "Photodissociation of NaBr, NaI, and KI vapors and collisional quenching of Na^* ($3\ ^2P$), K^* ($4\ ^2P$), and K^* ($5\ ^2P$) by foreign gases", *J. Chem. Phys.*, **60**, 4568, (1974).

56. Earl B.L., Herm R.R., Lin S-M. and Mims C.A. "Photodissociation of NaI vapor and the energy dependence of the quenching of $Na^*(3p^2P)$ by foreign gases", *J. Chem. Phys.*, **56**, 867, (1972).

57. Eimerl D., Davis L. and Velsko S. "Optical, mechanical, and thermal properties of barium borate", *J. Appl. Phys.*, **62**, 1968, (1987).

58. El-Kashef H. "New high interferometric quality dye laser jet nozzle", *Optics Comm.*, **100**, 141, (1993).

59. Elkashef H., Hassan G.E. and Tanta "Stability conditions of the dye-laser circulation system", *Acta Phys. Slov.*, **42**, 305, (1992).

60. Engel V. and Metiu H. "A quantum mechanical study of predissociation dynamics of NaI excited by a femtosecond laser pulse", *J. Chem. Phys.*, **90**, 6116, (1989).

61. E. Volker "Summary of the conference and some open problems", *Lecture Notes in Physics*, **211** 351 (1984).

62. Ewing J.J., Milstein R. and Berry R.S. "Curve crossing in collisional dissociation of alkali halide molecules", *J. Chem. Phys.*, **54**, 1752, (1971).

63. Faist M.B. and Levine R.D. "Collisional ionization and elastic scattering in - alkali-halogen atom collisions", *J. Chem. Phys.*, **64**, 2953, (1976).

64. Feshbach H. *Ann. Phys.* (NY), **5**, 357, (1958).

65. Feshbach H. *Ann. Phys.* (NY), **19**, 287, (1962).

66. Flamant P. "Affinement spectral dans les laser á colorants pulsés", *Appl. Optics*, **17**, 955, (1978).

67. Gardner J.L. "Wave-front curvature in a Fizeau wavemeter", *Optics Lett.*, **8**, 91, (1983).

68. Gardner J.L. "Compact Fizeau wavemeter", *Appl. Optics*, **24**, 3570, (1985).

69. Gerstenkorn S. and Luc P. "Atlas du spectre d'absorption de la molecule de l'iode (14800 - 20000 cm^{-1}", Editions du C.N.R.S., Paris, France, (1978).

70. Gerstenkorn S., Luc P. and Perrin A. "Rotational analysis of the 5350 Å band of iodine by means of Fourier transform spectroscopy", *J. Mol. Spectrosc.*, **64**, 56, (1977), and all its references.

71. Gibert R. and Porter R.N. "Nonperturbative calculation of energies and widths of predissociative states of diatomic molecules", *J. Chem. Phys.*, **89**, 3057, (1988).

72. Goorvitch D. and Galant D.C. "The solution of coupled Schrödinger equation using an extrapolation method", *J. Quant. Spectrosc. Radiat. Transfer.*, **47**, 505, (1992).

73. Grice R. and Herschbach D.R. "Long-range configuration interaction of ionic and covalent states", *Mol. Phys.*, **27**, 159, (1974).

74. Grosser J. and Vries A.E.de "Single path transition probabilities in potential-curve crossing phenomena", *Chem. Phys.*, **3**, 180, (1974).

75. Guo Hua "The effect of nonadiabatic coupling in the predissociation dynamics of IBr", *J. Chem. Phys.*, **99**, 1685, (1993).

76. Gurvitz S.A. and Kalbermann G. "Decay width and shift of a quasistationary state", *Phys. Rev. Lett.*, **59**, 262, (1987).

77. Hänsch T.W. "Repetitive pulsed tunable dye laser for high resolution spectroscopy", *Appl. Optics*, **11**, 895, (1972).

78. Hanson H.G. "Quenching of NaI Fluorescence by H_2, HCl, CO, and H_2O", *J. Chem. Phys.*, **23**, 1391, (1955).

79. Hazi A.U. and Taylor H.S. "Stabilization method of calculating resonance energies: Model problem", *Phys. Rev.*, **A1**, 1109, (1970).

80. Hemmati H., Fairbank W.M., Boyer P.K., Jr and Collins G.J. "Spatial-anisotropy and polarized-atomic-fluorescence measurements following molecular photodissociation", *Phys. Rev.*, **A28**, 567, (1983).

81. Herzberg G. "Spectra of diatomic molecules", van Nostrand (1950).

82. Himmelblau D. M. *Applied nonlinear programming*, McGraw-Hill, New York, (1972).

83. Hnilo A.A and Mangano F.A. "Beam expanders for pulsed dye lasers: Comparative study of their performance", *Opt. Commun.*, **55**, 197, (1985).

84. Honig A., Mandel M, Stitch M.L. and Towns C.H. *Phys. Rev.*, **96**, 629, (1954).

85. Huang Z-G. and Namba K. "High power efficient dye laser pumped by a copper vapor laser", *Japanese J. Appl. Phys.*, **20**, 2383, (1981).

86. Jackson J. L. and Wyatt R. E. "Fast determination of resonance states in atomic collisions" *Chem. Phys. Lett.*, **4**, 643. (1970)

87. Janev R.K. "Nonadiabatic transitions between ionic and covalent states", *Adv. At. Mol. Phys.* **12**, 1, (1976).

88. Johnson B.R. "New numerical methods applied to solving the one-dimensional eigenvalue problem", *J. Chem. Phys.* **67**, 4086, (1977).

89. Johnson B.R. "The renormalized Numerov method applied to calculating bound states of the coupled-channel Schrödinger equation", *J. Chem. Phys.* **69**, 4678, (1978).

90. Jordan K.D. "Structure of alkali halide: Theoretical methods", in *Alkali Halide Vapors*, eds. Davidovits P. and McFadden D.L. (Academic Press, New York, 1979).

91. Jordan K.D., Kinsey J.L. and Silbey R. "Use of pade approximations in the construction of diabatic potential energy curves for ionic molecules", *J. Chem. Phys.*, **61**, 911, (1974).

92. Junker B.R. "Recent computational developments in the use of complex scaling in resonance phenomena", *Advances in Molecular Physics*, **18**, 207, (1982).

93. Kaufman K.J., Lawter J.R. and Kinsey J.L. "Differential elastic scattering of potassium atoms by atomic iodine at thermal energies" *J. Chem. Phys.*, **60**, 4016, (1974).

94. Kirby K.P. and van Dishoeck E.F. "Photodissociation processes in diatomic molecules of astrophysical interest", *Adv. Atom. & Mol. Phys.*, **25**, 437, (1988).

95. Kogelnik H.W. "Astigmatically compensated cavities for CW dye lasers", *IEEE J. Quantum Electron.*, **QE-8**, 373, (1972).

96. Korsch H.J. "Semiclassical theory of resonances" *Lecture Notes in Physics*, **211**, 217, (1984).

97. Korsch H.J. "Semiclassical description of resonances" *Lecture Notes in Physics*, **325**, 253, (1987).

98. Korsch H.J., Möhlenkamp R. and Thylwe K-E. "Semiclassical complex energy theory pf orbiting resonances in curve crossing systems", *J. Phys. B*, **19**, 2151, (1986).

99. Kubodera S., Wisoff P.J. and Sauerbrey R. "Absorption spectra of alkali halide molecules in the vacuum ultraviolet", *J. Chem. Phys.*, **92**, 5867, (1990).

100. Lago A., Woehl G.,Jr and Riva R. "A pulsed dye laser with grazing incidence and folded cavity", *Appl. Phys. B*, **49**, 73, (1989).

101. Landau L.D. (a) "A theory of energy transfer on collision", *Phys. Z. Sowjet.*, **1**, 88 (1932).

102. Landau L.D. (b) "A theory of energy transfer II", *Phys. Z. Sowjet.*, **2**, 46 (1932).

103. Landau L.D. and Lifschitz E.M. *Quantum Mechanics, non-relativistic theory*, Pergamon Press.

104. Lavi S., Amit M., Bialolanker G., Miron E. and Levin L.A. "High-repetition-rate high-power variable-bandwidth dye laser", *Appl. Optics*, **24**, 1905, (1985).

105. Lefebvre R. "Resonance widths and normalisation", *J. Phys. B: At. Mol. Opt. Phys.*, **21**, L709, (1988).

106. Lefebvre R. "Diatomic predissociative widths and shifts from multichannel Siegert quantization and asymptotic analysis of resonance wave functions", *J. Chem Phys.*, **92**, 2869, (1990).

107. Lefebvre R. "Resonance wave functions and widths", *AIP Conference Proceedings*, **225**, 175, (1990).

108. Lefebvre R. "Box quantization and resonance determination: the multichannel case", *J. Phys. Chem.*, **89**, 4201, (1985).

109. Lefebvre R. and Child M.S. "Semi-classical analysis of the stabilization method applied to tunneling and curve crossing", *Mol. Phys.*, **66**, 1215, (1989).

110. Levi H. *Inaugural Dissertation*, Friedrich-Wilhelms-University, Berlin. (1934).

111. Lisboa J.A., Ribeiro Teixeira S., Gunha S.L.S. and Francke R.E. "A grazing-incidence dye laser with an intracavity lens", *Optics Comm.*, **44**, 393, (1983).

112. Littman M.G. and Metclaf H.J. "Spectrally narrow pulsed dye laser without beam expander", *Appl. Opt.*, **17**, 2224, (1978).

113. Littman M.G. "Single-mode pulsed tunable dye laser", *Appl. Opt.*, **24**, 4465, (1984).

114. Los J. and Kleyn "Ion-pair formation", in *Alkali Halide Vapors*, eds. Davidovits P. and McFadden D.L. (Academic Press, New York, 1979).

115. Macias A. "Constrained variational procedure for the calculation of autoionization lifetimes", *Phys. Lett.*, **103A**, 377, (1984).

116. Maier C.II., Cederbaum L.S. and Domcke W. "A spherical-box approach to resonances", *J. Phys. B: At. Mol. Opt. Phys.*, **13**, L119, (1980).

117. Maruyama Y., Kato M., Sugiyama A. and Arisawa T. "A narrow linewidth dye laser with double-prism beam expander", *Optics Comm.*, **81**, 67, (1991).

118. Möhlenkamp R. and Korsch H.J. "Semiclassical complex-energy quantization for coupled equations: Feshbach resonances and predissociation", *Phys. Rev.*, **A34**, 4716, (1986).

119. Moiseyev N., Certain P.R. and Weinhold F. "Resonance properties of complex-rotated hamiltonians", *Mol. Phys.*, **36**, 1613, (1978).

120. Morris M.B., Mcllrath T.J. and Snyder J.J. "Fizeau wavemeter for pulsed laser wavelength measurement", *Appl. Optics*, **23**, 3862, (1984).

121. Nair L.G. "Dye Lasers", *Prog. Quant. Electr.*, **7**, 153, (1982).

122. Nicolaides C.A. and Gotsis H.J. "On the calculation of the complex energies of resonances", *J. Phys. B: At. Mol. Opt. Phys.*, **25**, L171, (1992).

123. Niefer R.J. and Atkinson "The design of achromatic prism beam expanders of pulsed dye lasers", *Opt. Commun.*, **67**, 139, (1988).

124. Norcross D.W. and Seaton M.J. "Asymptotic solutions of the coupled equation of electron-atom collision theory for the case of some channels closed", *J. Phys. B: Atom. Molec, Phys.*, **6**, 614, (1973).

125. O'Malley T.F. "Diabatic states of molecules – Quasistationary electronic states", *Adv. At. Mol. Phys.*, **7**, 223, (1971).

126. Padmavathi D.A., Mishra M.K. and Rabitz H. "Role of potential structure in nonadiabatic collisions with applications to $He^+ + Ne(2p^6) \rightarrow He^+ + Ne(2p^5 3s)$ and Na + I $\rightarrow Na^+ + I^-$", *Phys. Rev.*, **A48**, 279, (1993).

127. Peskin U., Moiseysv N. and Lefebvre R. "Partial widths by asymptotic analysis of the complex scaled resonance wave function", *J. Chem. Phys.*, **92**, 2902, (1990).

128. Petrov T.S. and Sabotinov N.V. "Simplified dye jet nozzle construction and interferometric for jet thickness measurement", *Meas. Sci. Technol.*, **2**, 1074, (1991).

129. Petrov T.S., Sabotinov N.V. and Trendafilov S.T. "Efficient dye jet laser pumped by CuBr vapor laser", *Optics Comm.*, **92**, 291, (1992).

130. Qin W. "Nd:glass laser broad band second harmonic generation", *M.Sc. thesis*, The University of Science and Technology of China, (1985).

131. Ragone A.S., Levy D.H. and Berry R.S. "Fluorescence spectra of the NaI molecule", *J. Chem. Phys.*, **77**, 3784, (1982).

132. Reinhardt William P. "Complex coordinates in the theory of atomic and molecular structure and dynamics", *Ann. Rev. Phys. Chem.*,**33**, 223, (1982).

133. Rittner E.S. "Binding energy and dipole moment of alkali halide molecules", *J. Chem. Phys.*, **19**,1030, (1951).

134. Robert J., Roy Le and Liu Wing-Ki "Energies and widths of quasibound levels (orbiting resonances) for spherical potentials", *J. Chem. Phys.*, **69**, 3622, (1978).

135. Rose T.S., Rosker M.J. and Zewail A.H. "Femtosecond real-time observation of wave packet oscillations (resonance) in dissociation reactions" *J. Chem. Phys.*, **88**, 6672, (1988).

136. Rose T.S., Rosker M.J. and Zewail A.H. "Femtosecond real-time probing of reaction. IV. The reactions of alkali halides", *J. Chem. Phys.*, **91**, 7415, (1989).

137. Runge P.K. and Rosenberg R. "Unconfined flowing films for CW dye lasers", *IEEE J. of Quantum Electronics*, **QE-8**, 910, (1972).

138. Rusk J.R. and Gordy W. "Millimeter wave molecular beam spectroscopy: Alkali bromides and iodides", *Phys. Rev.*, **127**, 817, (1962).

139. Sakai Y, Misaku E. and Anno T. "A configuration interaction study of the ground and first excited $^1\Sigma^+$ states of the NaI molecule", *Can. J. Chem.*, **70**, 309, (1992).

140. Schäfer F.P. "Dye Lasers", Springer-Verlag, 1973.

141. Schaefer S.H., Bender D. and Tiemann E. "UV laser spectroscopy on NaI", *Chem. Phys.*, **92**, 273, (1982).

142. Schaefer S.H., Bender D. and Tiemann E. "Comment on "Fluorescence spectra of the NaI molecule"", *J. Chem. Phys.*, **78**, 6341, (1983).

143. Schaefer S.H., Bender D. and Tiemann E. "The predissociation of NaI", *Chem. Phys.*, **89**, 65, (1984).

144. Siegert A.J.F. "On the derivation of the dispersion formula for nuclear reactions", *Phys. Rev.*, **56**, 750, (1939).

145. Siegman A.E. "Lasers", *University Science Books*, Mill Valley, California (1986).

146. Singh S., Dasgupta K., Thattey S.S., Kumar S., Nair L.G. and Chatterjee U.K. "Spectral characteristics of CVL pumped dye lasers", *Optics Commun.*, **97**, 367, (1993).

147. Sink M.L. and Bandrank A.D. "Predissociation linewidth and level shifts for double-curve crossing models". *J. Chem. Phys.*, **66**, 5313, (1977).

148. Shapiro M. "Dynamics of dissociation. I. Computational investigation of unimolecular breakdown processes", *J. Chem. Phys.*, **56**, 2582, (1972).

149. Snyder J.J. "Fizeau wavelength meters", in *Laser Spectroscopy III*, J.L. Hall and J.L. Carsten, Eds, (Springer-Verlag, New York, (1977), p.419.

150. Snyder J.J. "Algorithm for fast digital analysis of interference fringes", *Appl. Opt.*, **19**, 1223, (1980).

151. Sommermeyer K. "The interpretation of a New type of spectrum of the alkali halide vapors", *Z. Phys.*, **56**, 548, (1929).

152. Sorokin P.P. and Lankard J.R. *IBM Jl. Res. Dev.*, **10**, 162, (1966).

153. Stalla L. "An optical technique of dye laser jet stream thickness measurement in real time", *IEEE J Quantum Electron.*, **QE-14**, 565, (1978).

154. Su T-M. R. and Riley S.J. "Alkali halide photofragment spectra. I. Alkali halide bond energies and excited state symmetries at 266 nm", *J. Chem. Phys.*, **71**, 3194, (1979).

155. Sun W., Tang C.S., Zhuge X.B. and Chen M.S. "Theory and experiments of dye lasers longitudinally pumped by copper vapor lasers (CVL)", *Optics Comm.*, **58**, 196, (1986).

156. Sun Y., Du M.L. and Dagarno A. "Amplitude method for multichannel resonances", *J. Chem. Phys.*, **93**, 8840, (1990).

157. Telle H.H. and Tambini A.J. "Photofragmentation of NaI at 355nm: excited-state symmetries", *J. Phys. B: At. Mol. Opt. Phys.*, **22**, L315, (1989).

158. Torop L., McCoy D.G., Blake A.J., Wang J. and Scholz T. "Effects of the close approach of potential curves in photoabsorption by diatomic molecules I. Theory and computational procedures", *J. Quant. Spectrosc. Radiat. Transifer*, **38**, 9, (1987).

159. Tucker S.C. and Truhlar D.G. "Completely L^2 golden rule method for resonance energies and widths", *J. Chem. Phys.*, **86**, 6251, (1987).

160. van Veen N.J.A., de Vries M.S., Sokol J.D., Baller T. and de Veries A.E. "Wavelength dependence of photofragmentation processes of the first excited states of Na and K halides", *Chem. Phys.*, **56**, 81, (1981).

161. Varshni Y.P. and Shukla R.C. "Potential energy functions for alkali halide molecules", *J. Mol. Spectrosc.*, **16**, 63, (1965).

162. von Neumann J. and Wigner E.P. *Z. Phys.*, **30**, 467, (1929).

163. Wang J. "Non-adiabatic dynamics of excited states of molecular oxygen", *PhD Thesis* , The University of Adelaide, (1989).

164. Wang J., Blake A.J. McCoy D.G. and Torop L. "Analytical potential curves for the $X\ ^1\Sigma^+$ and 0^+ states of NaI", *Chem. Phys. Lett.*, **175**, 225, (1990).

165. Watson Deborah K. "Partial widths and resonance normalization", *Phys. Rev.*, **A34**, 1016, (1986).

166. Wellegehausen B., Welling H. and Beigang R. "A Narrowband jet stream dye laser", *Appl. Phys.*, **3**, 387, (1974).

167. Wellegehausen B., Laeppie L. and Welling H. "High power CW dye lasers", *Appl. Phys.*, **6**, 335, (1975).

168. Whetten R.L., Ezra G.S. and Grant E.R. "Molecular dynamics beyond the adiabatic approximation: New experiments and theory", *Ann. Rev. Phys. Chem.*, **36**, 277, (1985).

169. Whiting E E. "An empirical approximation to the Voigt profile", *J. Quant. Spectrosc. Radiat. Transfer.*, **8**, 1379, (1968).

170. Wijn H.W. de "Effect of quenching of polarizations in polar diatomic molecules on nuclear-quadrupole coupling, its vibrational dependence, and molecular dipole moments", *J. Chem. Phys.*, **44**, 810, (1966).

171. Winkler Peter "Siegert's curse: Taming and domesticating divergent wave functions", *AIP Conference Proceedings* **260**, 72, (1991).

172. Yodh A.G., Bai Y. Golub J.E. and Mossberg T.W. "Grazing-incidence dye laser with and without intracavity lenses: a comparative study", *Appl. Opt.*, **23**, 2-46, (1984).

173. Yoichiro Maruyama, Kato M., Sugiyama A. and Arisawa T. "A narrow linewidth dye laser with double-prism beam expander", *Opt. Commun.*, **81**, 67, (1991).

174. Zare R.N. and Herschbach D.R. *J. Mol. Spectrosc.*, **15**, 462, (1965).

175. Zeiri Y. and Balint-Kurti G.G. "Theory of alkali halide photofragmentation: potential energy curves and transition dipole moments", *J. Mol. Spectrosc.*, **99**, 1, (1983).

176. Zener C. "Non-adiabatic crossing of energy levels", *Proc. Roy. Soc.*, **A137**, 696 (1932).

Corrections:

page 3 line 2 from bottom, FTS should read: "femtosecond transition state spectrum (FTS)"

page 6 line 5 from bottom, after ... the RKR method (Schaefer et al 1984). add: "The RKR (Rydberg-Klein-Rees) method is a semiclassical method to construct the potential energy curve from term energies and the rotational constants of vibrational states."

page 137 Figure 5.15 caption, add: "The experimental data of the rotational constants and vibrational spacings in this study coincide with those of Schaefer et al (1984) calculated with their Dunham parameters in the experimental energy region (30000 – 31200 cm^{-1})."

page 153 Figure 6.5 caption, add: "An explanation of the large width occurring near the energy near 33500 cm^{-1} is given in §6.5."

page 158 line 5 of §6.5, after ... as coupling strength increases. add: "It also displays the reason for the occurrence of the large widths shown in Fig. 6.5."

page 159 line 3, to vanish. should read: "to vanish as shown in Fig. 6.4 and Fig. 6.5."